MESOSCALE INTERACTION IN ELECTRODES FOR ENERGY STORAGE

A Dissertation

by

ZHIXIAO LIU

Submitted to the Office of Graduate and Professional Studies of
Texas A&M University
in partial fulfillment of the requirements for the degree of

DOCTOR OF PHILOSOPHY

Chair of Committee,	Partha P. Mukherjee
Committee Members,	Debjyoti Banerjee
	Perla B. Balbuena
	Raymundo Arroyave
Head of Department,	Andreas Polycarpou

August 2016

Major Subject: Mechanical Engineering

ABSTRACT

The electrode microstructure in rechargeable lithium batteries, particularly Lithium-ion battery and Lithium-sulfur batteries, plays an important role in determining the adhesive strength and electrochemical performance of the battery. The overall objective of the present research is to develop mesoscale computational models to understand the effects of mesoscale interactions on electrode structure evolution.

For Lithium-ion battery, the electrode microstructure is significantly affected by the multiphase slurry properties and solvent evaporation. The most important slurry properties are nanoparticle loading, interparticle interactions, and the shape and the size of nanoparticles. Computational results from the present study indicate that the small-sized active material nanoparticles are beneficial to improve the electronic conductivity of electrode microstructure due to its high conductive interfacial area ratio, and high evaporation rate is harmful for achieving good cooperation between the active material and conductive additives. The mixing sequence also affects electrode microstructure. It is found that stepwise mixing sequence can significantly increase the conductive interfacial area ratio in the electrode microstructure to reduce resistance.

A severe challenge for Lithium-sulfur battery is that the discharge product Li_2S is an insulator for both electrons and Li ions. The precipitation of Li_2S varies porosity and tortuosity of cathode microstructure and corresponding electrochemical properties. In this research, it is proposed to develop a mesoscale modeling strategy to investigate Li_2S precipitation-electrode interactions. A first-principle study is performed to

fundamentally understand the interaction mechanism between polysulfides and solid Li_2S substrate. Results reveal that Li_2S molecule direct deposition is energetically favored over the Li_2S_2 molecule deposition/reduction process. Li_2S film formation on graphene is also studied by the first-principles approach and it is found that Li_2S molecule adsorption on graphene is weaker than adsorption on crystalline Li_2S surface. Atomic structure evolution of Li_2S film formation on graphene is also studied by first-principle calculation. It is found that Li_2S (111) layer on the graphene is energetically favored. Based on results from first-principles calculations, a coarse-grained model accompanied by kinetic Monte Carlo algorithm is developed to study cathode surface passivation caused by Li_2S precipitation, which is affected by reactants concentrations, electrode porosity, electrolyte/solid interfacial area, and operating temperature.

ACKNOWLEDGEMENTS

I would like to thank my Ph. D advisor and mentor, Prof. Mukherjee, for his continuous encouragement as well as technical and financial support during my Ph. D career. I would also like to thank my committee members, Prof. Banerjee, Prof. Balbuena and Prof. Arroyave, for their guidance and support through the course of this research.

Thanks also go to my friends and colleagues and the department faculty and staff for making my time at Texas A&M University a great experience. I want to extend my gratitude to the Texas A&M University faculty research initiation grant for providing financial support to my Ph. D research. I also acknowledge financial support from the Department of Energy, Office of Energy Efficiency and Renewable Energy, grant DE-EE0006832.

Finally, thanks to my parents and my wife for their encouragement, patience, and love.

TABLE OF CONTENTS

Page

LIST OF FIGURES

Page

LIST OF TABLES

Page

CHAPTER I

INTRODUCTION, BACKGROUND AND SIGNIFICANCE

Nowadays the Earth suffers from the energy crisis and pollution caused by traditional fuel combustion. It is an important requirement from modern society that is to reduce the use of fossil fuels for ground transportation and achieve vehicle electrification. Electric vehicles requires the development of new sources of sustainable energy. Very impressive progress in the development of sustainable energy technologies, including photovoltaic cells[1], fuel cells[2], and wind turbines[3], has been witnessed in recent years, but the technology for energy storage is far away to meet the requirement for sustainable energy application. Taking EVs for instance, fuel cells may provide the highest energy density, however problems in hydrogen storage prevent fuel cells from practical EVs application[2]. In the visible future, lithium-ion battery (LIB) is the best candidate for vehicle electrification[4].Other lithium-ion based electrochemical energy systems are also very important candidates to drive EVs[5, 6].

1.1 Lithium-Ion Battery

In the family of rechargeable batteries, the lithium-ion battery (LIB) is widely used in mobile phone, camera, laptop and other portable devices. In a LIB, lithium ions move from anode to the cathode during discharge and move back during charge. Materials with layered structures are usually used for Li^+ storage because they are easy for Li^+ intercalation.

For vehicle electrification, improved performance, life and safety are critical determinants for LIBs [4, 7-9]. In this regard, there has been significant advancement in nanomaterial development for improved performance. In the aspect of anode material, conventional carbon-based anode is a limitation due to the low theoretical specific capacity, 372 mAh/g, according to LiC_6. To avoid this problem, researches on LIB anode focus on developing new materials that have high specific capacity, stable cycling behavior and economical synthetic method to replace the carbon-based materials [10-13]. Tin (Sn), which is abundant and cheap, is an interesting and competitive candidate as LIB anode material because of its high theoretical specific capacity, 994 mAh/g, according to $Li_{4.4}Sn$[14]. However, Sn anode has not been commercialized because the volume change during the lithiation/delithiation cycling destroys anode structure. Several schemes have been developed to synthesis innovative Sn nanostructures to tolerate the volume variation and capacity fading [15-18]. Nowadays, synthesis novel nanostructured materials is an effective way to improve the performance of energy storage devices [19-21]. Sn-based materials with layered crystalline, especially tin disulfide (SnS_2), attract a lot of interest as lithium storage materials because the layered structure can minimize the volume change during lithiation/delithiation cycling[22] and improve the Li mobility[23]. In the aspect of cathode material, active materials are usually transitional metal oxides. The most common active material in cathode side is $LiCoO_2$, which has a layered structure with alternating CoO_2 and Li planes. Lithiation and delithiation take place in Li planes during discharge and charge [24]. Although $LiCoO_2$ cathode has been commercialized, it is necessary to develop new materials for

cathode due to some limitations of $LiCoO_2$. Co metal is more expensive than other transition mental such as Fe, Ni, and Mn. Additionally, $LiCoO_2$ suffers from performance degradation caused by over charge [25], Co dissolution [26] and sharp volume expansion [27].

Another important driver is the electrode processing which plays a critical role in determining electrode microstructure [28, 29]. The processing conditions and concomitant physicochemical attributes are envisioned to pose an intimate bearing on the resultant electrode microstructures and ultimately on the performance.

The processing of the multi-phase slurry, which consists of active particles, conductive additives, binder, and solvent, determines the electrochemical properties and performance of the electrode [30-36]. In the electrode processing, it is necessary to make these components cooperate very well with each other. It is well known that the active material stores lithium ions, the conductive additive is employed to increase the electronic conductivity and the binder links the active material and the conductive additive together to form the robust network [37]. It is important to point out that the role of each component is not independent, and components can be affected by each other. For example, the active materials always suffer from poor electronic conductivity, and the aggregation of active material nanoparticles deteriorates the performance of the electrode because the electric conductivity is further lowered [38-40]. To avoid this problem, a proper processing can make conductive nanoparticles be coated on active nanoparticles and prevent the direct aggregation between active nanoparticles, so conductive additives fill the space between the active materials to form the continuum

network for enhancing the electric conductivity [41, 42]. Additionally, the high surface area of the nanostructured active material raises the risk of the capacity fading, because the solid electrolyte interface (SEI) forming on the active material consumes a lot of Li^+ ions supplied by the cathode, and the dissolution of the transition metal in the SEI film induces the loss of the active material [39, 40]. An effective method to prevent this capacity fading is to make the conductive additive coat on the active material during the processing. The coating film can increase the dissolution barrier of the transition metal, suppress side reactions between the active material and the electrolyte and stabilize the SEI film [41, 43, 44]. The cooperation between the binder and the conductive additive also subtly affects the physicochemical and electrochemical properties of the electrode. Although high electronic conductivity can be achieved by increasing the amount of the conductive additive, lacking the binder brings about a decrease of the electronic conductivity because the physical connection between nanoparticles is destroyed [30, 31].

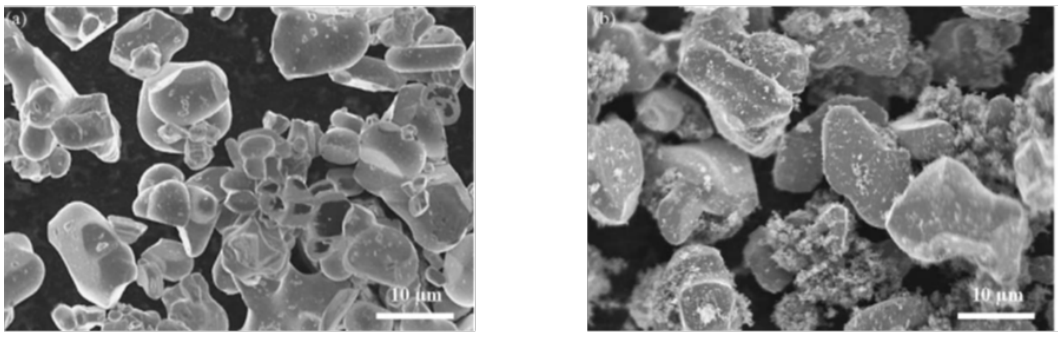

Figure 1.1 SEM images of active nanoparticles (a) without and (b) with carbon coating. The figure is reprinted from Ref [43], Kim, J., et al., Direct carbon-black coating on LiCoO2 cathode using surfactant for high-density Li-ion cell. Journal of Power Sources.

Fundamentally, slurry properties and drying methods mainly determine the microstructure and the performance of the electrode composite. The most important slurry property is the viscosity, which is determined by the concentration and the solid loading of each component, the interaction force among nanoparticles in the slurry, and the properties of active material nanoparticles that include the size of the nanoparticle, size distribution and the surface area [45]. Additionally, the mixing sequence and mixing time also affect the viscosity of the slurry. The slurry needs to be dried after being cast. One common mechanism of the drying process is solvents evaporation from the surface of the substrate. The evaporation induced self-assembly is a quite popular scheme to make nanoparticles form desirable structures [46, 47], and this assembly is controlled by interactions among nanoparticles and solvents [48, 49], evaporation rates [50], the mobility of nanoparticles [51] and the morphology of nanoparticles [52]. Nowadays, multiscale modeling from atomistic level to continuum level becomes a very powerful tool of understanding LIB electrode processing and resulting microstructures as well as electrochemical properties, and Franco makes an exhaustive is this scientific research field [53]. There are some works on the migration of binders during the drying process [54, 55]. However, there is no theoretical research focus on how drying process affects the distribution and cooperation of components in the electrode composite. Optimizing the morphologies of active material nanoparticles is also beneficial to improve the performance of the electrode [56] because morphologies significantly determine arrangement modes of nanoparticles assembly [57], and the interaction force between nanoparticles make the assembly more complicated [58].

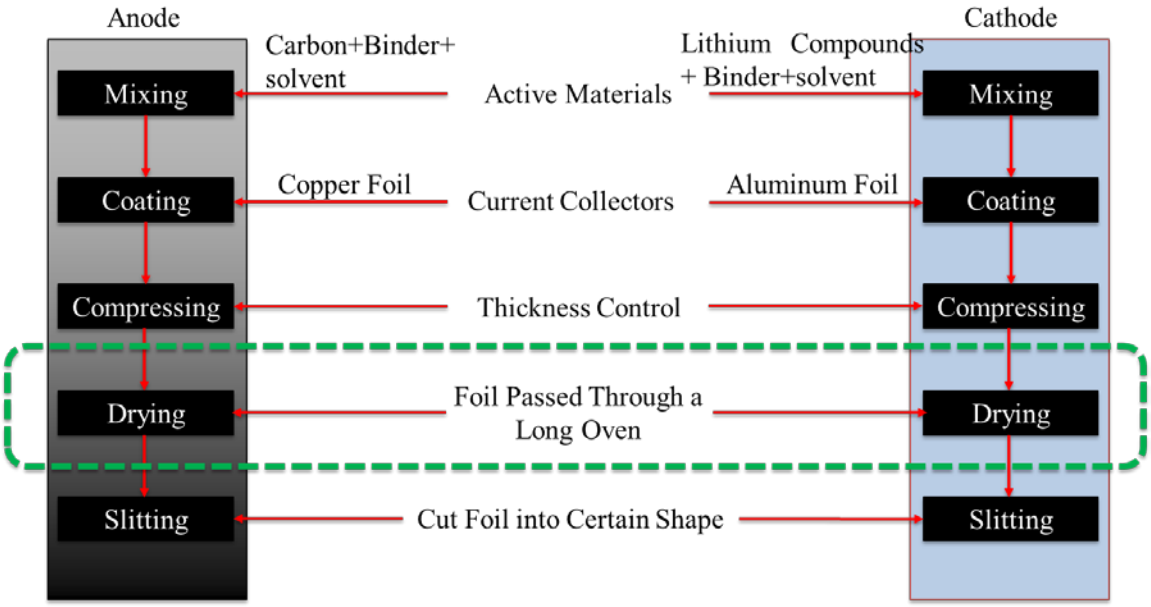

Figure 1.2 Schematic illustration of steps in electrode processing. This research focus on understanding the influence mesoscale interactions on electrode microstructure at the drying step.

A point worth emphasizing is that the mixing sequence plays a critical role in determining the performance of a LIB electrode. Electrode slurries, prepared by different mixing sequences, show different dispersion states of solid particles, even though these slurries are composed of the same materials with the same fraction. Yang *et al.*[59] first reported that changing the mixing method in the negative electrode preparation tripled the cycle life of the LIB. Kim *et al.*[60] designed four mixing sequences for processing $LiCoO_2$ positive electrodes, and demonstrated that pre-mixing dry active material and conductive additive was beneficial for prolonging the life of the LIB. Li *et al.*[61] studied the electrochemical properties of aqueous $LiFePO_4$ slurries, and found that dispersing active material nanoparticles first was beneficial to improve the discharge capacity. The sequence of adding solvent during the slurry preparation also affected the properties of the slurry. Compared with the slurry prepared by adding all solvents to mixed

nanoparticles in one step, the slurry prepared by adding solvents in a stepwise manner had lower viscosity and more homogeneous nanoparticle distribution [62]. However, previous experiments focused on changing mixing sequence before the evaporation step. Recently, Huang *et al.*[63] reported a double carbon coating process to achieve an excellent electrochemical performance of $LiFe_{0.4}Mn_{0.6}PO_4$ electrode. In this experimental work, two different sequences about adding components for carbon coating were investigated during the drying process, and it was found that the step-wise addition is beneficial for coating carbon onto active material.

1.2 Lithium-Sulfur Battery

Sustainable energy presents possibly the greatest challenge, but the greatest potential reward, of our time. The increasing shift towards renewable energy has brought about an urgent need to efficiently store this energy, a need primarily met by lithium-based battery technologies. These batteries, lithium-ion batteries (LIBs) being the most common, benefit from a high energy storage potential compared to other options, due to lithium's low weight and high oxidation potential. In particular, their light weight renders them the best option available for electric vehicles.[64] Lithium-ion batteries are, however, hampered by several drawbacks, such as poor thermal management, low power density, safety concerns, and inadequate stability to charge/discharge cycling, which limit their use. The most prominent issue for their use in electric vehicles is their intrinsically-limited energy density compared to gasoline. These limitations come primarily from the layered metal oxide cathodes utilized in these systems.

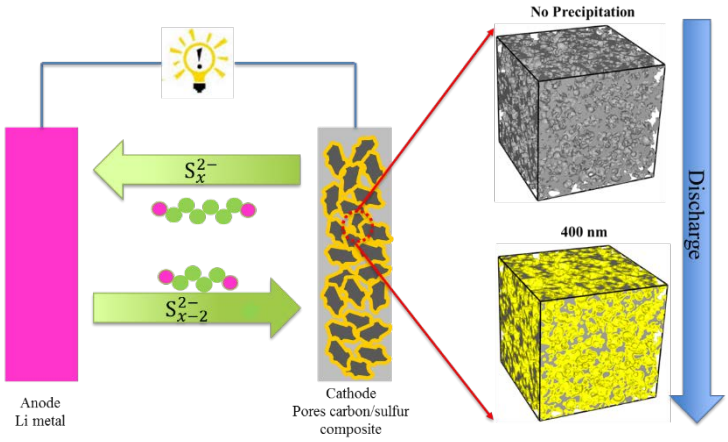

Figure 1.3 Schematic illustration of polysulfides "shuttle effect" and cathode microstructure evolution caused by products precipitation

One potential solution is to change the oxidative element from a metal ion to a non-metal, which results in an entirely new battery system [65, 66]. Sulfur (S) is an attractive option in this regard, as it is also low-weight and relatively abundant in the Earth's crust,[67] meaning that Li-S batteries would be neither prohibitively expensive nor take a large toll on the environment. The Li-S system also has a high theoretical specific energy density, rendering it a good fit for implementation in transportation applications [68, 69]. However, Li-S batteries are far from being ready for commercial use. One of the reasons is that the discharge product lithium sulfide (Li_2S) is an electronic and ionic insulator[70]. The theoretical indirect bandgap of Li_2S is 3.297 eV [71], and its electronic resistivity is larger than 10^{14} cm·Ω. The growth of the insulating product film can cause a sudden death during the discharge process before achieving the theoretical capacity [72]. In order to improve the electrochemical performance of the cathode, some kind of transition metals (TM), such as Fe, Co, Ni, and Cu may be added to the cathode materials to activate the insulating Li_2S [73-77]. Luo *et al.* studied TM-

doped Li_2S by a first-principles approach, and it was found that the electronic conductivity can be increased by Li vacancies, and those dopants can lower the vacancy formation energy [78]. They also pointed out that metal-induced gap states (MIGS) are helpful for electronic conductivity [78]. Unfortunately, it is energetically difficult to introduce doping defects into discharge product Li_2S.

Designing high-quality cathode microstructure is another promising way to improve Li-S battery performance. The cathode architecture plays an important role in determining the performance of the Li-S battery [79]. A wide variety of microstructures has been synthesized to develop the performance of the battery [80-83]. A desirable cathode microstructure should effectively obstruct the dissolution of polysulfide, supply a large conductive area for insulating Li_2S deposition, and facilitate Li^+ ion transport. Furthermore, special microstructure characteristics are required to tolerate the volume expansion induced by lithiation in order to keep the cathode integrity [84].

1.3 Hypothesis

As discussed above, electrode microstructure plays an important role in energy storage devices. For LIB, the electrode microstructure is significantly affected by processing conditions. It is hypothesized that the fractions of constituents in the multiphase slurry, physicochemical interactions between particles, the morphological properties of particles evaporation rate can affect the pattern of assembled particles. In this study, we focus on the cooperation between active materials and conductive additives which is affected by the processing method.

For Li-S battery, the cathode microstructure is directly affected by the precipitation of the insoluble product. The growth of Li_2S is determined by several physicochemical interactions. The reactants concentrations and geometric properties of the local microstructure (pores volume in the solid matrix and solid-electrolyte interfacial area) determine the thickness evolution *vs* time. The diffusion barrier of adsorbed adsorbate on pre-deposited solid phase and operating temperature affect the size of the deposited Li_2S islands.

1.4 Objective 1: Microstructure Evolution in LIB Electrode Processing

The overall objective of the present research is to develop mesoscale models to fundamentally understand the influence of physicochemical interactions on electrode microstructure in energy storage devices.

1.4.1 Influence of Slurry Properties

As discussed above, it is critical to control the distribution of constituent phases (active particle, conductive additive, binder) to achieve good internal microstructure during electrode processing. The salient parameters determining the distribution of electrode compositions in both the slurry preparation step and drying step include the morphology and size of the nanoparticle, the volume fraction of different components, the interaction force between the nanoparticle and the solvent, and the inter-particle interaction force. Additionally, the solvent evaporation dynamics of the slurry is another key factor to determine the microstructural heterogeneity of the electrode. In this work, we present a 2D mesoscale modeling approach in order to investigate the influence of

particle morphology and solvent evaporation dynamics on the constituent phase distribution representative of the typical LIB electrode processing.

1.4.2 Influence of Mixing Sequence on Electrode Microstructure

A series of experiments have been conducted to optimize mixing sequence to improve electrode performance [59-62]. However, previous experiments focused on changing mixing sequence before the evaporation step. This study focuses on elucidating the cooperation between active material and conductive additive during the slurry drying since evaporation critically governs nanoparticle aggregation behavior [46, 47]. In this study, we design different mixing sequences to fundamentally understand the interplay among evaporation, mixing sequence and active particle morphology.

1.4.3 Influence of Binder Length and Drying Temperature on Electrode Film Formation

Binder plays an important role in keeping the integrity of electrode structure. The homogeneous distribution of binder in electrodes is beneficial for the improvement of cohesive force. Additionally, the homogeneous binder distribution can decrease the resistance of the electrode [30, 85]. Polymer-mediated nanoparticle assembly can be a promising method to control over the electrode microstructure [86-88]. However, there are only a few studies focusing on the effect of binder length (binder molecular weight) on electrode microstructure and the relative performance [89, 90]. The solvent evaporation rate also affects the binder distribution in electrode film. However, the previous experiment tuned evaporation rate by changing solvent [85]. The water-based solvent is used to achieve high evaporation rate and the organic-based solvent is used to

achieve low evaporation rate. Thereby, the nanoparticle-solvent interaction, solvent-solvent interaction, and binder-solvent interaction were more or less changed in their experiments. These interactions significantly affect the viscosity of electrode slurry and the final electrode microstructure [45]. In the present study, all interaction parameters are kept as constants to avoid changing the viscosity slurry, and the evaporation rate is tuned by the operating temperature. Additionally, the effect of binder length is assessed in this study.

1.5 Objective 2: Mesoscale Interactions between Polysulfides and Electrode of Li-S Battery

One key challenge for Li-S battery is the internal shuttle effect [91]. During the discharge, solid sulfur is dissolved into the electrolyte as the form of S_8 molecule, and then S_8 is gradually reduced to insoluble Li_2S with dissoluble polysulfides as intermediate discharge products. PSs can diffuse to anode side due to the potential and concentration gradients. PSs can chemically react with Li metal anode to form insulating Li_2S film on the anode surface [92]. The shuttle effect reduces the utilization of active material and leads to an irreversible capacity loss and poor cycling stability.

In order to alleviate shuttle effect, a variety of novel architecture has been fabricated to trap PSs in the porous carbon cathode microstructure.[79, 93-95] Cui and his colleagues rose a concept that the weak PS-carbon interaction is not helpful for PS retention,[96] and they suggested use polarized two-dimensional (2D) materials to immobilize PSs because they have a much stronger affinity to PSs than carbon-based

material.[97] Nazar's group reported that MXene as cathode host material can achieve high specific capacity and good cycling stability.

As discussed above, it is necessary to understand how PSs interact with the electrode surface. One objective of the thesis is to understand PSs interaction with electrode substrate at different scales.

1.5.1 Atomistic Simulation of Adsorption of Polysulfides on Electrode Surface and the Formation of Li_2S Film

The Understanding growth of the Li_2S films is of a guiding significance for the rational design of novel cathode architectures able to improve the performance of Li-S batteries. Atomistic simulations based on a first-principles approach are employed to fundamentally understand the interaction mechanism between PS molecules and electrode surface. The calculated adsorption energies of PSs on different cathode materials can be used to evaluate the capability of the material to retain PSs and alleviate shuttle effect. The atomistic structure evolution during the formation of Li_2S film is also studied and the energetically favored growth direction should be identified.

1.5.2 Mesoscale Modeling of Surface Passivation of Cathode in Li-S Battery

Cathode surface passivation, which is attributed to the deposition of insoluble Li_2S during the discharge process, can reduce the active surface area and negatively affect the electrochemical performance of the battery. It is known that crystalline Li_2S is electronic insulator [70, 98], hence the electrochemical reactions for PSs reduction are difficult to happen at the electrolyte/Li_2S interface. The lateral growth of Li_2S precipitation can reduce the fresh cathode surface which supplies electrons for

electrochemical reactions. Gerber *et al.* reported a method to inhibit the lateral growth of Li_2S film by using benzo[*ghi*]peryleneimide (BPI) as the redox mediator, and the specific capacity is doubled by using the mediator [99].

In this regard, it is necessary to control the precipitation morphology during the discharge process. In the presented study, a mesoscale interfacial model is developed to study how species concentration and temperature affect the Li_2S film growth. This model is expected to provide strategies to defer surface passivation in Li-S battery cathode.

CHAPTER II

EFFECTS OF SLURRY PROPERTIES ON ELECTRODE MICROSTRUCTURE IN LITHIUM-ION BATTERY*

In this particular study, a morphology detailed mesoscale model is developed to investigate the influence of slurry properties on electrode microstructure. Generally, the most important slurry property is the viscosity, which is determined by the concentration and the solid loading of each component, the interaction force among nanoparticles in the slurry, and the properties of active material nanoparticles that include the size and shape of the nanoparticle [45].

2.1 Computational Method

Disparate computational methods, from the atomistic scale to cell scale, has been developed to understand the electrode structure-performance interplay as reported in Franco *et al.*'s review[100]. Kinetic Monte Carlo (KMC) method is a powerful tool to simulate the time evolution of processes occurring in nature. A number of KMC based schemes have been successfully used to study adsorbate diffusion,[101, 102] film growth[103, 104], defect formation[105, 106], cluster morphology,[107, 108] the degradation of nanoparticles in electrochemical energy devices[109], and electrodeposition[110, 111]. Recently, KMC methods have been developed to study physical and chemical properties of electrodes in LIBs. Yu *et al.*[112] studied

* The chapter is reprinted with permission from "Microstructure Evolution in Lithium-Ion Battery Electrode Processing" by Z. Liu and P. P. Mukherjee, 2014. *Journal of Electrochemical Society*, 161, E3248-E3258, Copyright [2014] by The Electrochemical Society.

Li^+/electron-polaron diffusion into nanostructured TiO_2 coated by conductive additive. The study revealed that the total conductivity depended on Li^+ diffusion behavior, and the localized carbon coating on the active material was more beneficial for achieving higher conductivity and capacity than the uniform carbon coating. Methekar *et al.*[113] used a KMC method to explore the SEI formation on the surface of the graphite anode. The effects of exchange current density, charging voltage and temperature on the SEI formation were systematically investigated in this study. However, these works neglect the morphological details of active material particles and the electrode microstructure, although these two factors profoundly affect the performance of the electrode.

Kriston *et al*. developed a pore-scale model accompanied by a stochastic method to mimic the electro-active layer formation process in energy storage devices, and they employed a scaling analysis to reduce the complexity of the system.[114] Their work demonstrated that the interparticle interaction and material loading affected the morphological properties of the electro-active layer. However, their work did not consider multiphase interaction which is important in electrode preparation. Furthermore, the effect of the evaporation was not considered. Additionally, their pore-scale model lacks the morphological properties of particles such as shape and size, which affect the final pattern of assembled particles. In our work, a morphology-detailed mesoscale model is developed to simulate the multiphase electrode microstructure governed by interparticle interaction and evaporation dynamics. The detail of our model will be discussed in the following.

A two-dimensional (2D) coarse-grained lattice-gas model, which was first reported by Rabani *et al.*[51], is employed to represent drying-mediated self-assembly of nanoparticles. Recently we extended this model to track the evolution of ternary mixture of nanoparticles in an electrode slurry in the evaporation processing[115]. The 2D coarse-grained lattice-gas model has successfully predicted the microstructure of evaporation-affected CdSe nanoparticle assembly in hexane[51]. The fractal-like microstructure after drying graphite-water nanofluid can also be reproduced by the 2D model[116]. Our present work focuses on how slurry mixing sequences during the evaporation process affect the cooperation of components, especially the cooperation between active material and conductive additive. Our recent work demonstrated that the 2D model can be employed to investigate the cooperation between active material and conductive additive, and this model can successfully explain phenomena observed in experiments. For example, the experimental study found that the decrease of active material is beneficial for improving the conductivity. Our previous 2D model demonstrated that the interfacial area between active material and conductive additive increases as the amount of active material decreases, which indicated that more paths were created for electrons transferring to active material. In the 2D model, the domain is divided into plenty of identical lattice cells, and the size of each lattice cell approaches the correlation length of the solvent, *ca.* 1 nm. The domain in the present study consists of 500×500 lattice cells, and the edge length of the domain is about 0.5 μm. The period boundary condition is used in the present model to represent a large system. The electrode slurry consists of active material nanoparticles, binder molecules, conductive

additive nanoparticles, and solvent molecules. It is necessary to underline that the multiphase co-existing in one lattice cell is prohibited, which means one cell can only occupied one component. A solvent or vapor molecule only occupy one cell. An active material nanoparticle takes tens to hundreds of cells depending on its shape and size. Several shapes including the polyhedral and the isometric (the cubical and the spherical) are considered for active material nanoparticles because the final microstructure is directly determined by the nanoparticle morphology as mentioned above[57]. A polyhedral nanoparticle is represented by a hexagonal in the present two-dimensional coarse-grained lattice-gas model. The nanoparticle size, which is characterized by the half length of the particle *R*, is an important morphological parameter to determine the behavior of the nanoparticles assembly[117, 118]. In the present study, the small-sized nanoparticle is defined as $R = 6$ lattices, and the large-sized one is defined as $R = 12$ lattices. The size of the active material in the present model is around ten to a hundred nanometers and it can be comparable to the size of $LiFePO_4$ nanoparticle in a cathode[56, 119] and Si nanoparticle in the anode[120]. The shape detail of conductive additive nanoparticle is neglected in the present work because the conductive additive nanoparticle is smaller than the active material nanoparticle. The conductive additive nanoparticle is simplified to a cubic with $R = 2$. The binder molecule is represented by a crisscross with each span occupying 2 lattice cells. The procedure of creating initial microstructure is listed in the following: first, the domain is fully covered by solvent molecules; then active material nanoparticles randomly replace solvent molecules in the domain; and finally conductive additive nanoparticles and binder molecules randomly

substitute solvents molecules between active material nanoparticles. Components are mixed to achieve homogeneous distribution in a non-evaporated slurry and there is no gas phase in the slurry.

The evolution of electrode microstructure is simulated by a kinetic Monte Carlo method. Two dynamic events are implemented in each MC cycle: (i) *M* attempts to move each particle in a random direction, and (ii) convert solvent molecule from liquid phase to gas phase (evaporation) or gas phase to liquid phase (condensation) in turn. The movement of nanoparticles is not absolutely random and complies following rules. One restriction is that the nanoparticle diffusivity is zero in the dry environment[51]. To mimic this behavior, a nanoparticle can move to the neighbor cells which are fully covered by solvent molecules. The solvent mass is conserved during the diffusion. Lattice cells behind the diffused nanoparticle should be refilled by solvent molecules. The number of attempts to move a particle, *M*, relates to nanoparticle diffusivity[121]. Any attempt to move a nanoparticle can change the energy of the system. The energy difference between the current state (before the diffusion) and the candidate state (after the diffusion) is used to calculate the probability of accepting the attempt as shown in Eqn. 2.1. Both physical evaporation and condensation processes are considered in the present study and the evaporation is predominant. A solvent molecule in liquid phase has a negative chemical potential and an attractive interaction with adjacent cells. A solvent molecule in gas phase does not interact with adjacent cells, and its chemical potential is zero. Thereby, the phase transitions of solvent also bring in energy variation. According

to Eqn. 2.1, the energy difference can be employed to judge if the phase transition attempt can be accepted.

In this dynamic simulation, the stochastic state transition is accepted by Metropolis probability as

$$p_{acc} = \min\left[1, e^{-\frac{\Delta E}{\kappa T}}\right], \tag{2.1}$$

where ΔE is the energy difference between the candidate state and the current state, κ is the Boltzmann constant, and T is the temperature. The total energy of each state is estimated by

$$\begin{aligned} E = &-n_{ll}\epsilon_{ll} - n_{al}\epsilon_{al} - n_{bl}\epsilon_{bl} - n_{cl}\epsilon_{cl} - n_{aa}\epsilon_{aa} - n_{ab}\epsilon_{ab} \\ &-n_{ac}\epsilon_{ac} - n_{bb}\epsilon_{bb} - n_{bc}\epsilon_{bc} - n_{cc}\epsilon_{cc} - N\mu. \end{aligned} \tag{2.2}$$

Here *l*, *a*, *b* and *c* denote the liquid solvent, active material, binder and conductive additive, respectively. n_{ij} denotes the number of interaction pair between adjacent component i and component j $(i, j = l, a, b, c)$ and ϵ_{ij} denotes the relative interaction energy. In Eqn. 2.2, only the first nearest interaction is considered and this assumption is accurate enough for simulating the evaporation-affected nanoparticles aggregation[51]. *N* is the number of solvent molecules and μ is its chemical potential in liquid phase. All energetic parameters, including interaction energy (ϵ_{ij}), chemical potential (μ) and κT term are scaled by the interaction energy between two liquid solvent cells ($\epsilon_{ll} = 1$). Interaction energies between nanoparticles should be larger than 1 because nanoparticles tend to aggregation to reduce the surface tension. To mix components well in the electrode slurry, the interaction energy should also be larger than 1 to disperse nanoparticles. It is obviously that there is a competition between nanoparticle-

nanoparticle attraction and nanoparticle-solvent attraction. The competition determines aggregation mechanisms and final electrode microstructures. Evaporation rate depends on chemical potential μ and temperature (represented by κT term in the present study). The critical chemical potential for liquid and gas phases coexisting is -2.0 when all lattice cells are occupied by solvent molecules. Chemical potential below the critical value makes gas phase more stable than liquid phase and a more negative chemical potential corresponds to a higher evaporation rate[121]. Adding nanoparticles into the liquid shifts the critical chemical potential to a more negative value because the nanoparticle-solvent attraction can stabilize liquid phase around nanoparticles[121].

The total volume fraction of the solid phases (active material, conductive additive and binder) is set to 65% in the present computational study. Following Zheng's experiment[33], The volume fraction of the active material is 40% ($\Phi_a = 40\%$), and the volume fraction ratio of binder to conductive additive is 1: 0.8 ($\Phi_b: \Phi_c = 1: 0.8$). The nondimensional solvent chemical potential (μ) is set to -2.2 in all simulations. The nondimensional interaction parameters are $\epsilon_{aa} = \epsilon_{bb} = \epsilon_{cc} = 1.7$, $\epsilon_{ab} = 1.8$, $\epsilon_{bc} = 1.9$, ϵ_{ac}=2.0 and $\epsilon_{al} = \epsilon_{bl} = \epsilon_{cl} = 1.2$. The nondimensional interaction parameter is appropriately adjusted in our simulations. In this regard, we have adopted representative values based on reports in the literature that have successfully predicted patterns due to evaporation induced aggregation of nanoparticles [51, 116], although not in the context of electrode processing. Since the objective of the present work is to understand how slurry mixing sequences and evaporation conditions affect the electrode microstructure formation, we only use one set of representative values mentioned above to simulate the

aggregation behavior of the active material with conductive additive and binder. These values have been successfully employed to investigate the morphology of active material, nanoparticle aggregation mechanism, and evaporation rate interplaying with electrode microstructure in our reported work[115]. Accurate description of material-specific interaction energy can be derived from atomistic calculations. This is planned as a future work.

All computations stop at the 8000^{th} MC cycle because the electrode structure does not change as simulated time increases after the 8000^{th} MC cycle, even though solvents are not completely evaporated. The solvent evaporation actually can further decrease the overall energy of the system till all solvent molecules are transferred to gas phase. However, the present study focuses on the cooperation of solid phases in electrode slurry. The nanoparticles assembly has reached stable structures before the 8000^{th} MC cycle. As shown in Figure 2.1(a), the conducive interfacial area ratio has converged before the 8000^{th} cycle. Increasing MC cycles would not affect the final electrode microstructure. In Figure 2.1(b), curves of overall energy and solid phase interaction energy as a function of normalized time (normalized by 8000 MC cycles) are reported. It is found that the overall energy increases before $time = 0.2$. The energy rising indicates that the liquid-to-gas phase transition needs overcome an energy barrier before the bubble arriving the critical size. After the saddle point, the overall energy decreases because liquid-to-gas phase transition is energetically favored. Due to the low evaporation rate, solvent molecules are not fully converted to vapor at $time = 1$, so that the overall energy does not converge. Solid phase interaction energy continuously

decreases as time increases and converges to a constant before $time = 1$. The rapid decrease of the solid phase interaction energy is attributed to the nanoparticle aggregation. The decrease stops when the solid phase microstructure arrives a stable state. Hence, simulations stop at the 8000th cycle to save the computational resource. The simulated time in this study is normalized by 8000 MC cycles, which means time=1 is equivalent to $iter = 8000$ MC cycles.

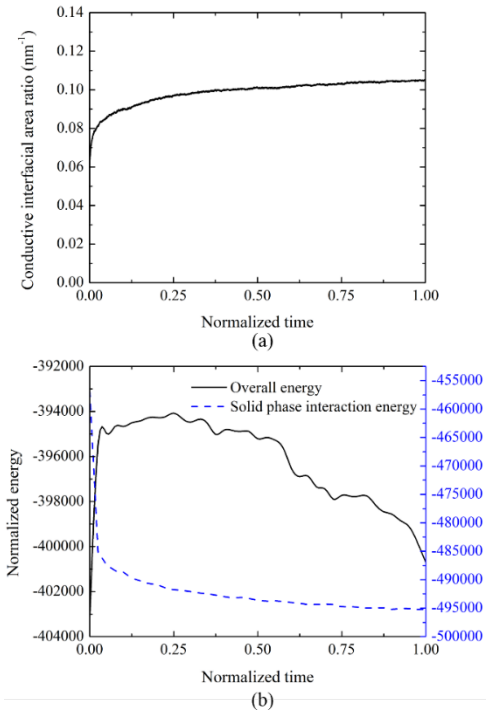

Figure 2.1 (a) Conductive interfacial area ratio as the function of simulation time, and (b) energies as the function of simulation time. The simulation time is normalized by 8000 MC cycles.

2.2 Results and Discussion

As mentioned above, nanoparticle additives affect the critical chemical potential $\tilde{\mu}$ due to the nanoparticle-solvent interaction force, ϵ_{nl}. In the nanoparticle-contained system, $\tilde{\mu}$ can be obtained by the mean-filed argument[50].

$$\tilde{\mu} = -2 - (\epsilon_{nl} - 1) \times \Phi_{tot}. \quad (2.3)$$

The Eqn. (2.3) is feasible when Φ_{tot} is very low (~10%) because it ignored the interaction between nanoparticles. In the present work, the Equation (2.3) is only employed to roughly estimate $\tilde{\mu}$ at the high Φ_{tot} condition with a specified ϵ_{nl}. ϵ_{nl} also significantly affects the aggregation/dispersion of nanoparticles. For a low ϵ_{nl}, the attractive force between nanoparticles is dominant and nanoparticles aggregate spontaneously. Oppositely, for a high ϵ_{nl}, solvents tend to surround additives and nanoparticles are dispersed.

Firstly we discuss the internal microstructure evolution of the slurry during the drying process with $\epsilon_{nl} = 1.2$. According to the Eqn. (2.3), $\tilde{\mu}$ is around-2.13. Here, $\mu = -2.1, -2.2, -2.25\ and\ -2.3$ are considered. To characterize the mixing quality of the electrode structure, we define a conductive interfacial area ratio $R_{c:a}$ as

$$R_{c:a} = \frac{A_{ca}}{\Phi_a}, \quad (2.4)$$

where $A_{ca}$is the area of conductive additive/active material interface, and $\Phi_a$is the volume fraction of the active material. The active materials are always not the good conductor for electron transfer, and the larger $R_{c:a}$ supplies a broader channel for electrons moving from the conductive additive to the active material, leading to reducing the resistance of the electrode.

Figure 2.2 clearly shows that the active material morphology can significantly determine the $R_{c:a}$. For a specified chemical potential, the electrode with cubical active material has the highest $R_{c:a}$, while the electrode with polyhedral active material has the lowest $R_{c:a}$. In the coarse-grained lattice-gas model, the surface of the cubical active

material particle is perfect flat, so the isometric conductive particle can fully stick on the active material. On the contrary, the surface of spherical or polyhedral nanoparticle has a lot of steps, and the conductive particle only partly sticks to the stepped surface, so that the face-to-face contact between active material nanoparticle and the conductive additive nanoparticle are reduced. From Figure 2.2 we can know that reducing the size of the active material nanoparticle is also helpful for increasing the conductive interfacial area ratio. Smaller size means a larger specific surface area (ratio of the surface area to the volume) for a single active material nanoparticle. Thereby, the electrode with smaller active material nanoparticles supplies larger available surface for the conductive additive/active material interaction.

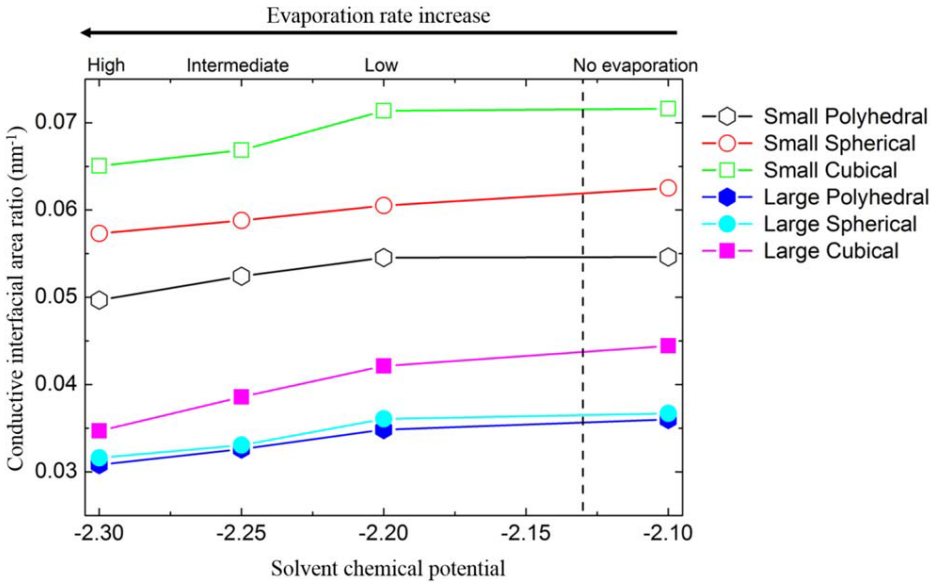

Figure 2.2 The effect of the chemical potential on the conductive interfacial area ratio under the spontaneous aggregation mechanism ($\boldsymbol{\epsilon_{nl} = 1.2}$). The shapes of the active material can be polyhedral, spherical and cubical. The size ratio of the large active material nanoparticle to the small one is 12:6. Each point in the plot is the averaged value of the last 500 MC steps. The vertical dash line at $\boldsymbol{\mu = -2.13}$ represents the critical chemical potential for the liquid/gas phase transition. The total volume fraction of nanoparticles are 65%, and the volume fraction of different compounds are $\boldsymbol{\Phi_a = 50\%, \Phi_c : \Phi_b = 0.8 : 1}$.

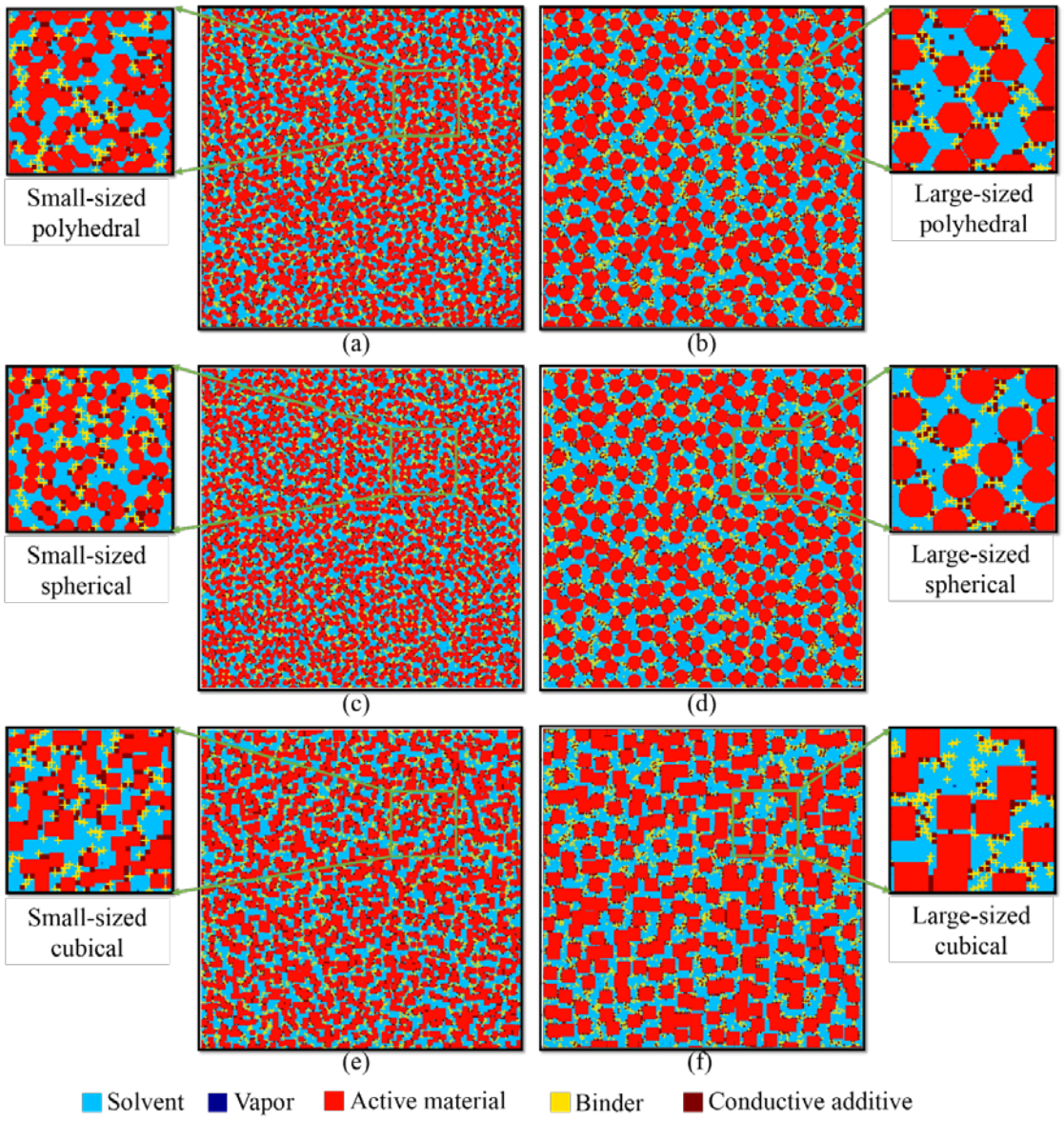

Figure 2.3 Stable structures of the electrode slurry with different active material nanoparticles under the spontaneous aggregation mechanism ($\boldsymbol{\epsilon_{nl} = 1.2}$). $\boldsymbol{\mu = -2.1}$ is used in all cases. (a) & (b) hexagonal nanoparticle, (c) & (d) sphere nanoparticle, (e) & (f) square particle. The size of the nanoparticle is small in the left column and large in the right. The total volume fraction of nanoparticles is 65%, and the volume fraction of different compounds are $\boldsymbol{\Phi_a = 50\%, \Phi_c : \Phi_b = 0.8 : 1}$.

Figure 2.3 shows internal structures with different active material nanoparticles.

If the active material is the small sized nanoparticle (left column in Figure 2.3),

conductive nanoparticles can be dispersed very well and bind with active materials as much as possible. Oppositely, in the electrode with large active material nanoparticles, the surface area of the active material is reduced, leading to decreasing the probability of conductive additive interacting with active material. Consequently, the probability of the conductive additive interacting with the binder relatively increases. It is obvious that more conductive nanoparticles are trapped by the binder network (right column in Figure 2.3), and can never stick to the active material surface. Physically, the larger surface area always corresponds to higher surface energy. To release the surface tension and stabilize the internal structure, smaller active nanoparticles is more ready to aggregate with conductive additives. In our computations, the size ratio of conductive nanoparticle to the small sized active nanoparticle is 1:3, while the ratio of conductive nanoparticle to the large sized active nanoparticle is 1:6, which means the size of the conductive nanoparticle is more comparable to the small sized active material nanoparticle. Experimentally, Hong *et al.*[122] found that poor mixing between conducting agent and active material is attributed to the significant difference in size of these two components. Using Brownian dynamics simulation, Zhu *et al.*[123] investigated the aggregation behavior of particles in the cathode, and their results showed that the larger active material particle can increase the fraction if carbon black sticking to the active material because the larger active material particle leads to stronger attraction force. This opposite conclusion can be ascribed to that the attractive force is independent on the size of the nanoparticle in the present coarse-grained lattice-gas model.

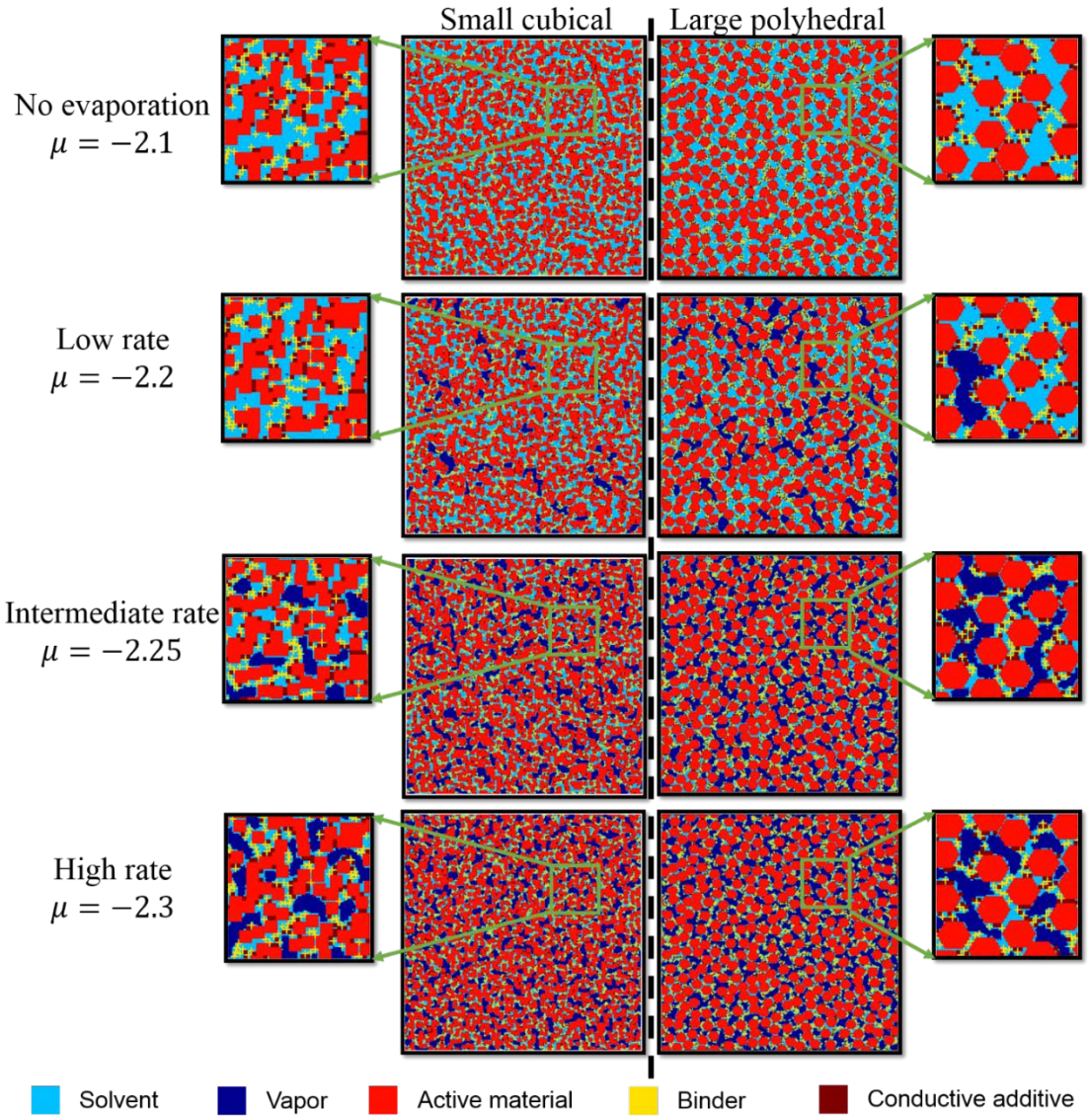

Figure 2.4 Figure 2.4. The left and right panels display the stable structure of the electrode slurry at the different evaporation rate, respectively. The shape of the active material nanoparticle is small sized cubical in the left panel, and the shape is large sized polyhedral in the right panel. These two shapes correlate the highest and lowest conductive interface ratio according to Figure 2, respectively. From the top panels to the bottom panels, the evaporation rate increases due to the decrease of chemical potential. In the internal structure map, the light blue, dark blue, red, yellow and brown denote the solvent, the vapor, the active material, the binder and the conductive additive, respectively.

As mentioned above, small sized active material nanoparticles correlate large surface area, and the electrolyte can be significantly oxidized on the surface of the active material, forming a passive layer and leading to capacity fading [29]. However, the small sized particle is good for high power applications due to the short diffusion length and fast kinetics[33]. Especially, the small sized nanoparticle can reduce the fracture induced by the Li diffusion, further reduce the capacity fading and impedance rising.[124] It was reported that the 70 nm $LiMn_{1.5}Ni_{0.5}O_4$ particle is preferred to maintain capacity than the 1μm particle[125]. For the $LiCr_{0.2}Mn_{1.8}O_4$ particle, 50 nm is the optimum size for preventing capacity fading [126].

The chemical potential of the solvent, which directly determines the evaporation rate, also significantly determines the mixing quality of the electrode. The $R_{\mathrm{a:c}}$ decreases from $\mu = -2.1$ to $\mu = -2.3$. The left panels of Figure 2.4 show the stable structures of the electrode with small cubical active material nanoparticles. We can see that when $\mu = -2.1$, the evaporation does not appear because μ is higher than the critical value. When μ decreases to -2.2, the gas phase appears in the stable structure, and gas bubbles take about 5% space in the domain. The slow evaporation does not affect the $R_{c:a}$ obviously. Although gas bubbles may cover the surface of the active material and block the interaction between the active material and the conductive additive, there is still enough space for conductive particles diffusing to the active material nanoparticles and binding with them. Thereby, low evaporation rate generates similar nanoparticle distribution as no evaporation. When μ is lower than -2.2, more than 15% space are taken by gas phase after 8000 MC steps and lots of gas bubbles appears around active materials. The right

panels of Figure 2.4 also show the internal structures of electrode with the large sized polyhedral active material nanoparticles. Similarly, the solvent cannot be evaporated when the chemical potential is larger than the critical value, and the nanoparticle distribution at the low evaporation rate is not significantly different from the distribution in the non-evaporation case. According to Figure 2.4, in relatively higher evaporation rate cases $\mu < -2.2$, gas bubbles obviously cover the surface of the active material and cut off the pathway for the conductive particle diffusing to the active material, leading to significantly reducing the aggregation of conductive additive with active material or binder nanoparticles. Maul investigated the evaporation rate effect on the nanoparticle assembly by using coarse-grained lattice-gas model, also found that the high evaporation rate can scatter nanoparticles.[127]

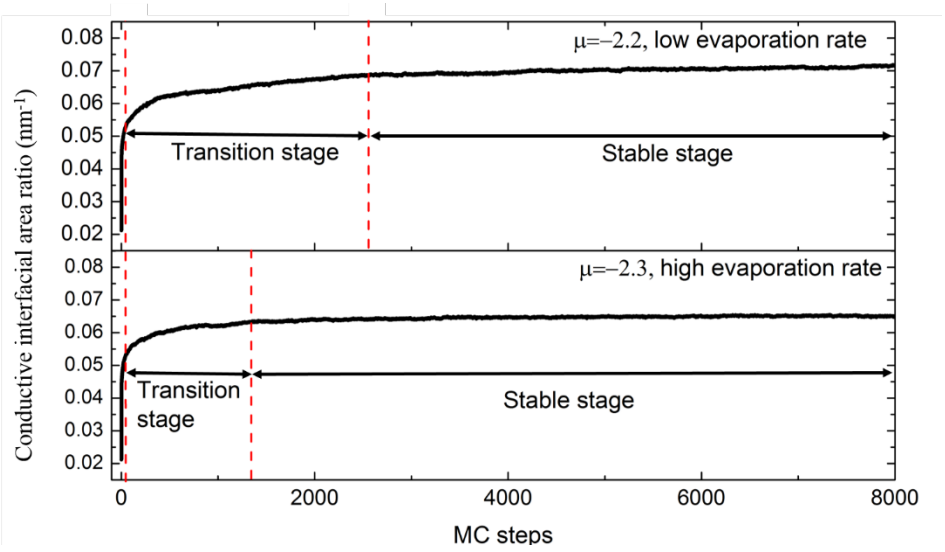

Figure 2.5 Evolution of the conductive interfacial area ratio under the spontaneous aggregation mechanism ($\boldsymbol{\epsilon_{nl} = 1.2}$). The shape of the active nanoparticle is small sized cubical. The total volume fraction of nanoparticles is 65%, and the volume fraction of different compounds are $\boldsymbol{\Phi_a = 50\%, \Phi_c : \Phi_b = 0.8 : 1}$.

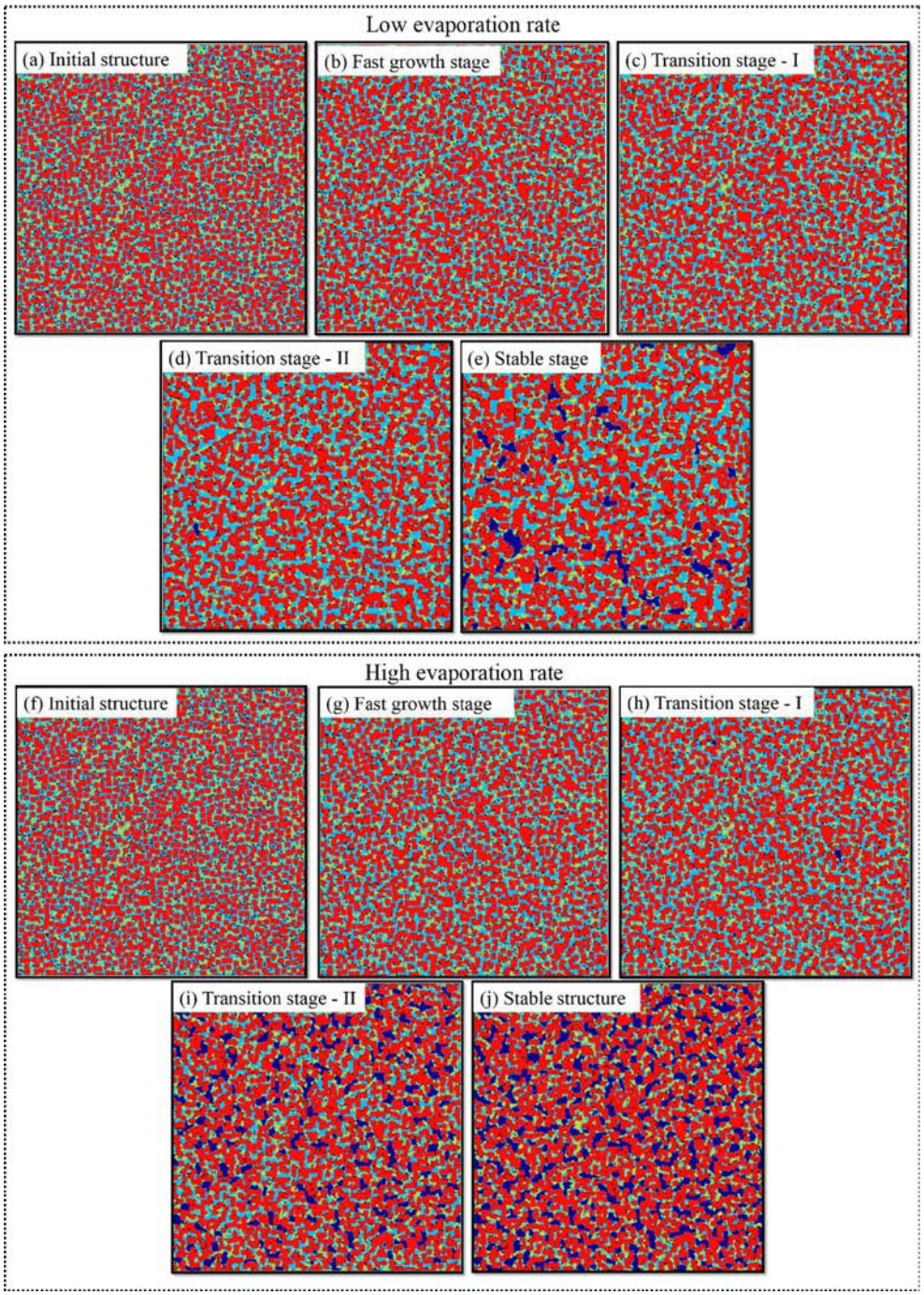

Figure 2.6 Internal structure evolution with time in the low evaporation rate condition (a)-(e), and the high evaporation rate condition (f)-(j).Nanoparticles take a spontaneous aggregation ($\boldsymbol{\epsilon_{nl} = 1.2}$). The total volume fraction of nanoparticles is 65%, and the volume fraction of different compounds are $\boldsymbol{\Phi_a = 50\%, \Phi_c : \Phi_b = 0.8 : 1}$.

Figure 2.5 shows how $R_{c:a}$ increases during the drying process. It is clear that the growth of the $R_{c:a}$ with time can be divided into three stages. Firstly, $R_{c:a}$ increases by about 200% to 300% in the fast growth stage. Then, $R_{c:a}$ curve enters the transition stage. In this transition stage, the slope of the curve continuously decreases and approaches to zero. The last stage is the stable stage, in which the $R_{c:a}$ does not change obviously. The $R_{c:a}$ curve with $\mu = -2.3$ enters the stable stage earlier due to the higher evaporation rate. Figure 6 shows the internal structure evolution with time in the low evaporation rate condition and high evaporation rate condition, respectively. In the fast growth stage, nanoparticles take similar behaviors. Conductive particles near to active material particles rapidly move to the latter, forming the coating film on the surface of the active material (Figure 2.6(b) and (g)), and leading to a significant increase in the $R_{c:a}$. Conductive nanoparticles suspending in the liquid phase tend to interact with binder molecules, forming conductive additive/binder clusters. These clusters are meta-stable, and may decompose and release the conductive nanoparticles. Although the decomposition increases the energy of the system, this behavior can be accepted with the probability calculated in the Eqn. (2.1). The released conductive nanoparticles execute a random walk, and some of them can be captured by the active material due to the strong attractive force between the conductive additive and the active material. As fewer and fewer conductive particles can be released, the slope of the $R_{c:a}$ curve continuously decreases. In the low evaporation rate case, the gas phase appears in the late transition stage (Figure 2.6(d)). At this time, most of conductive particles stick to the active material surface, and the left are trapped in binder cages. Thereby, the appearance of the

gas phase does not affect the distribution of nanoparticles. In the high evaporation rate case, gas bubbles appear in the first 50 MC steps (Figure 2.6(h)), and the area of the gas phase grows up with time increasing. As discussed above, these gas bubbles cut off the pathway for conductive nanoparticles diffusing, so conductive particles released by the conductive additive/binder cluster decomposition cannot diffuse to the active material and are pushed back to the binder by gas bubbles. In the high evaporation rate case, conductive nanoparticles are isolated from active material by gas bubbles and binders after 1500 MC steps, and the $R_{c:a}$ curve enters the stable stage earliest than other cases.

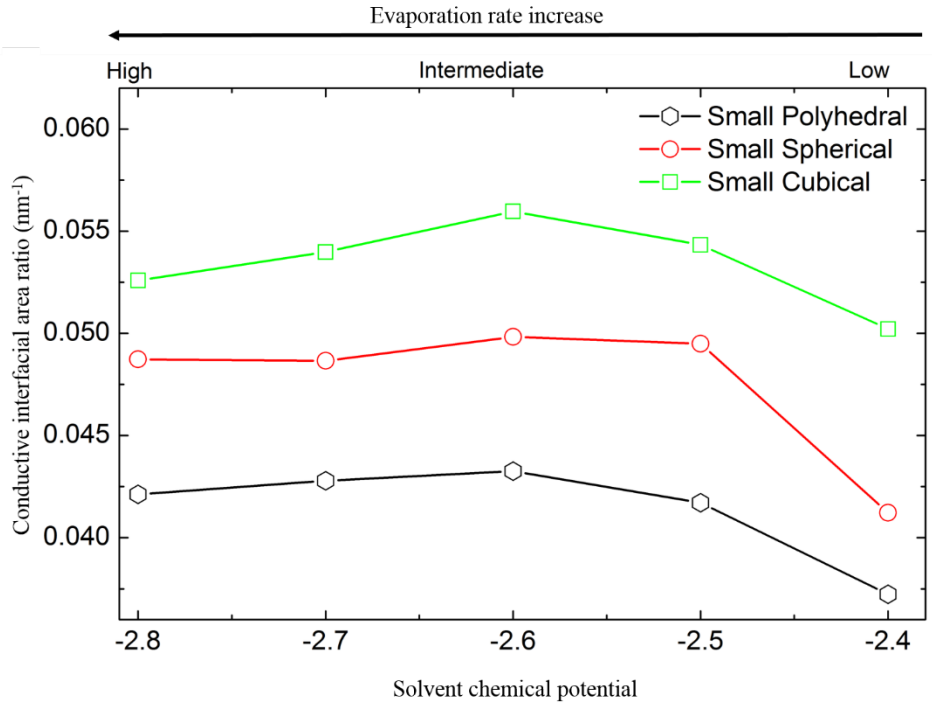

Figure 2.7 The effect of the chemical potential on the conductive interfacial area ratio under the evaporation-induced aggregation mechanism ($\boldsymbol{\epsilon_{nl} = 1.6}$). Only small sized material nanoparticles with different shapes are considered. Each point in the plot is the averaged value of the last 500 MC steps. The total volume fraction of nanoparticles is 65%, and the volume fraction of different compounds are $\boldsymbol{\Phi_a = 50\%, \Phi_c : \Phi_b = 0.8 : 1}$.

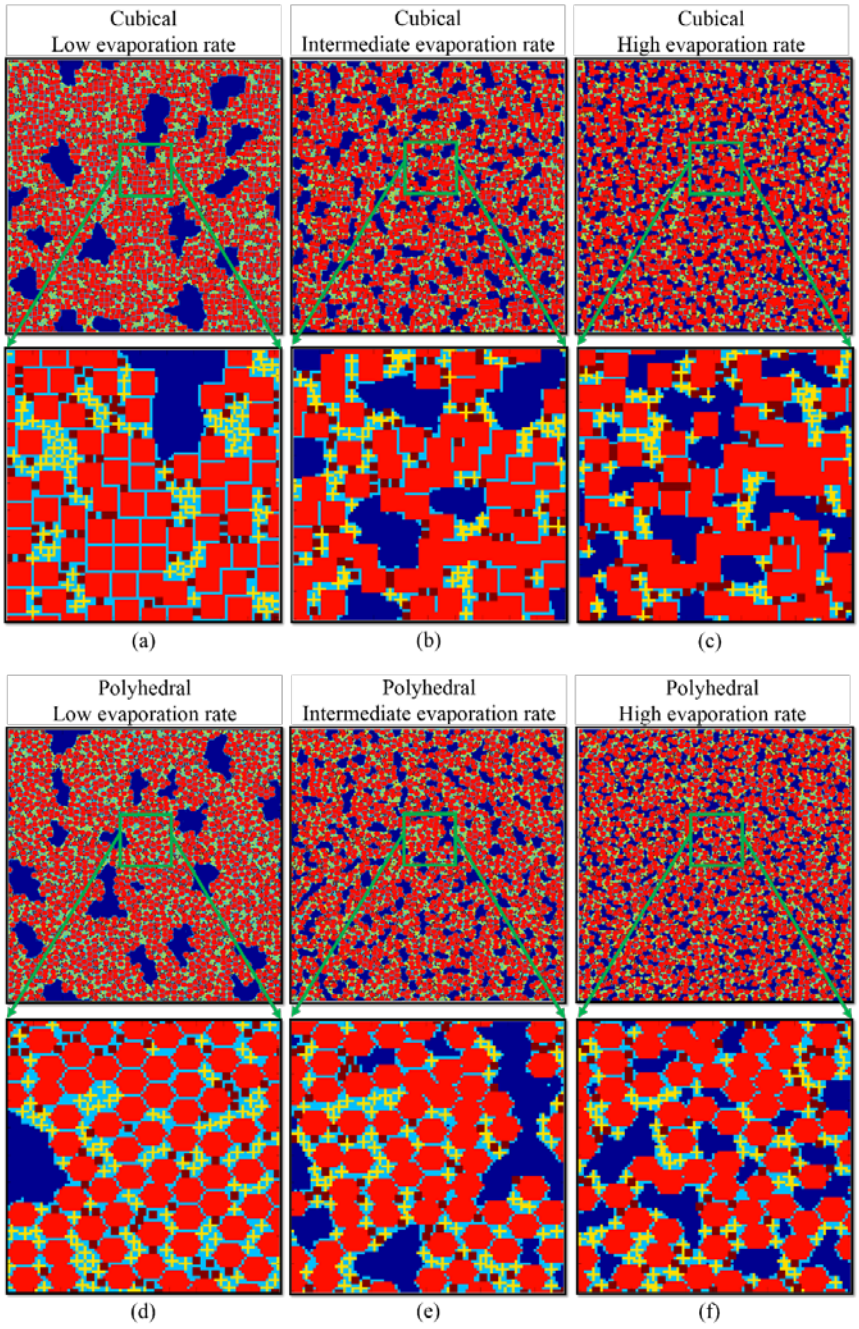

Figure 2.8 The stable structure at different evaporation rates. Nanoparticles in the slurry take the evaporation-induced aggregation($\boldsymbol{\epsilon_{nl} = 1.6}$). Figure (a)-(c) display the internal microstructures of electrode with cubic active nanoparticles, and (d)-(f) display the internal microstructures of electrode with polyhedral active nanoparticles. The total volume fraction of nanoparticles is 65%, and the volume fraction of different compounds are $\boldsymbol{\Phi_a = 50\%, \Phi_c : \Phi_b = 0.8 : 1}$.

The aggregation behavior with high nanoparticle/solvent attractive energy, $\epsilon_{nl} = 1.6$, is quite different from the case of low ϵ_{nl}. In the high ϵ_{nl} condition, the relatively stronger attractive energy between nanoparticles and solvents will have nanoparticles be surrounded by solvents as much as possible, so nanoparticles cannot aggregate spontaneously and the evaporation is the driving force to push them together.

Here only small active materials nanoparticles are considered because the small size is good for getting large $R_{c:a}$. In the high ϵ_{nl} condition, the cubical active material nanoparticle is still the best choice for increasing the conductivity of the electrode, followed by the spherical particle and the polyhedral particle (Figure 2.7). Both high evaporation rate ($\mu = -2.8$) and low evaporation rate ($\mu = -2.4$) reduce the $R_{c:a}$, and the favored condition to generate highest $R_{c:a}$ is an intermediated evaporation rate ($\mu = -2.6$).

Figure 2.8 shows the stable internal microstructure of electrode with small sized cubical nanoparticles (Figure 2.8(a)-(c)) and small sized polyhedral nanoparticles (Figure 2.8(d)-(f)) in the low, mediated and high evaporation rate conditions, respectively. In the low evaporation rate condition, there are only a few large gas bubbles, and active material nanoparticles are separated from each other by very narrow gaps (Figure 2.8(a) & (d)). During the electrode processing, the electrolyte is distributed in the solvent/gas region. In such a configuration, the gas bubble will mainly carry the electrolyte, and the gap between nanoparticles is too narrow to accept the electrolyte. Thereby, the electrolyte cannot mix with active material homogenously and form network for Li^+ ion diffusion. The conductive particles suspended in the liquid phase

cannot stick to the active material because surrounding by solvents is beneficial for lowering the energy of the local structure. In the low evaporation rate condition, a lot of active material nanoparticles are isolated, so Li^+ ion and electrons cannot be transferred to these particles, leading to the capacity loss. With evaporation rate increasing to the intermediate value, the volume per gas bubble decreases but the number of the gas bubble increases (Figure 2.8(b) & (e)). The gas phase is distributed more homogeneously in the domain, and this configuration is beneficial for the electrolyte mixing well with the active material. The volume growth of the gas bubble has the nanoparticle move along the normal direction of the bubble surface. Thereby, these gas bubbles can push nanoparticles together, causing an increase in the aggregation. Due to the aggregation, liquid gaps are eliminated and more nanoparticles anticipate forming network in the electrode for the Li^+ ion and the electron diffusion. However, continuously increasing the evaporation rate will generate more gas bubbles with much smaller size (Figure 2.8 (c) & (f)). These gas bubbles sometimes prevent the connection between the active material and the conductive additive, leading to a decrease of $R_{c:a}$. These small gas bubbles generated by the high evaporation rate can also suppress the formation of the conductive additive/binder composite, thereby reducing the electron-conductive network which would adversely affect the electronic conductivity.

Figure 2.9 shows the internal structure evolution with time under the evaporation induced aggregation ($\epsilon_{nl} = 1.6$). Differently from spontaneous aggregation ($\epsilon_{nl} = 1.2$), the very initial stage (the first 10 MC steps) is a nanoparticle dispersed stage (Figure 2.9(b)), and the $R_{c:a}$ falls down because nanoparticles are ready to be surrounded by

solvents. In this stage, only a few gas bubbles appear and they cannot push nanoparticles together due to the small volume the limited number. From the 10th step, more gas bubbles appear and these bubbles grow up rapidly (Figure 2.9(b) ~ (d)). The growth of gas bubbles compress the space for nanoparticle distribution, so nanoparticles aggregates and the $R_{c:a}$ increases significantly. After 500 steps, the growth of the gas bubble slows down, because high packed nanoparticles cannot make more space for the gas bubble growth (Figure 2.9 (e)), and $R_{c:a}$ curve enters the stable stage at last.

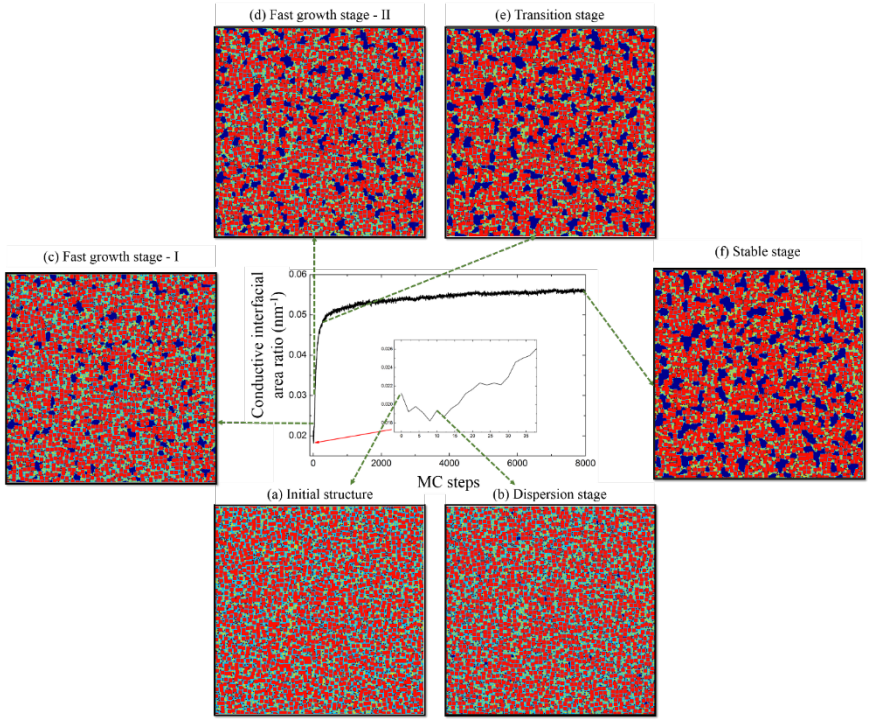

Figure 2.9 Evolution of the conductive interfacial area ratio under the evaporation-induced aggregation mechanism ($\boldsymbol{\epsilon_{nl} = 1.6}$). The Internal microstructure evolution with time is shown from (a) to (f). The active material nanoparticle is the small sized cubical, and the chemical potential is $\boldsymbol{-2.6}$ (intermediate evaporation rate), which generates the highest $\boldsymbol{R_{c:a}}$. The total volume fraction of nanoparticles is 65%, and the volume fraction of different compounds are $\boldsymbol{\Phi_a = 50\%, \Phi_c : \Phi_b = 0.8 : 1}$.

The attractive force between the nanoparticle and the solvent not only determines the evaporation rate of the solvent but also the affects the viscosity of the slurry. For

example, a stronger attractive force corresponds to a higher viscosity. A favorable viscosity can improve the performance of the electrode. Hintennach *et al.*[128] studied the discharge capacity of TiO_2 electrode composite with varying viscosity during the slurry preparation, and found that the capacity monotonically decreases if the viscosity is too high. Our computational prediction shows that the conductive interface ratio is smaller in the slurry with the higher viscosity (larger ϵ_{nl}). In this case, a larger active material surface is exposed to the electrolyte, so that more active material is corroded by side reactions between the electrolyte and the active material surface during the charge/discharge cycling, leading to the capacity fading.

Changing the ratio of conductive nanoparticles to active nanoparticles is also an efficient way to changing the connection between these two kinds of nanoparticles. Brownian dynamics simulation showed that an increase of the mass ratio of conductive nanoparticles to active material nanoparticles is helpful to form pathways for electrons migration.[123] Liu *et al.*[31] found that increasing the mass ratio of the conductive additive (acetylene black) to the polymer binder (polyvinylidene difluoride) improve the conductivity when the ratio is smaller than 0.8:1, and the crack appears in the electrode film when the ratio is beyond 1:1.

In the present work, the influence of conductive additive volume fraction on the conductive interfacial area is also investigated. Here the total volume fraction of nanoparticles, Φ_{tot}, is fixed at 65%, and the volume ratio of conductive additive to binder remains 0.8:1. The volume fraction of active material, Φ_a, is changed from 35% to 55% with a step of 5%. Small sized cubical active material nanoparticles are used in

the followed computations because our previous results show that these particles produce largest interface area between the active material and the conductive additive. We choose a low attractive energy, $\epsilon_{nl} = 1.2$, because spontaneous aggregation is favorable for generating the desirable structure. Low evaporation rate ($\mu = -2.2$) is used to reduce the separation of the conductive additive and active material. Figure 10(a) shows that the conductive interface ratio continuously increases with $\Phi_a$decreasing. However, reducing the Φ_a means a decrease in the active material surface area so that a large $R_{a:c}$ cannot represent a large conductive interface area. It is worth noting that the peak of the conductive interface area locates at $\Phi_a = 40\%$ (Figure 10(b)). Figure 10(c) shows the stable structure having the largest conductive interface area. It is clear that the conductive additive/binder composite forms the network attaching active material nanoparticles and makes the electrode integrated. Hereby, 40% volume fraction is the best choice to get a high conductivity for the electrode in the present simulation. The conductive additive coating can also protect the active material by stabilizing the SEI film,[41, 43, 44] so the capacity fade may be greatly suppressed when $\Phi_a = 40\%$ because the largest surface is coated by conductive nanoparticles in all cases considered in the present work. However, the density of the conductive additive or binder is always lower than the active material, so that increasing the conductivity leads to lowering the volumetric energy density. To avoid this problem and achieve high performance, Liu *et al.*[30] suggested that a decrease in the conductive additive/binder ratio will lower the impedance for electrodes with high active material loading. For instance, our study suggests that a decrease of active material volume fraction leads to an increase of conductive interfacial area, which

is beneficial for increasing the electronic conductivity. This corroborates with the experimental results reported in Ref. [14]. The experimental investigation of the influence of evaporation in the drying step of the electrode slurry preparation and the resultant implications on the microstructure formation is currently underway in our laboratory and will be reported in the forthcoming publications.

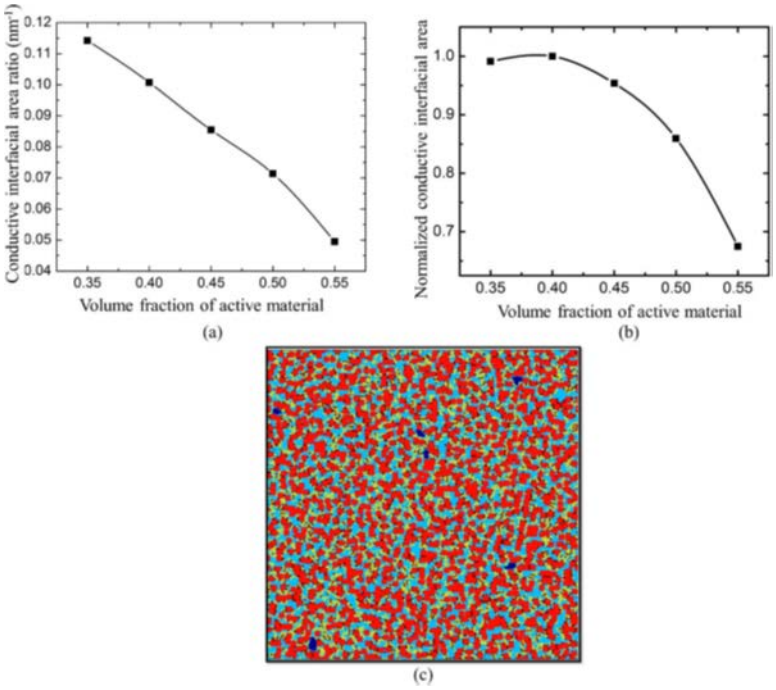

Figure 2.10 Effect of the variation of the active material volume fraction, $\boldsymbol{\Phi_a}$, on conductive additive/active material connection: (a) the conductive interfacial area ratio vs. active material volume fraction, and (b) normalized conductive interfacial area vs. active material volume fraction. In the 2D model, the area is in the unit of nm. The total volume fraction of nanoparticles is fixed at 65%, and the volume ratio of the conductive additive to binder is fixed at 0.8:1. The stable structure with largest conductive interface area is shown in (c).

2.3 Conclusions

A mesoscale computational model has been developed in order to investigate the influence of processing attributes on the microstructure evolution representative of a

typical lithium-ion battery electrode. In particular, the impact of active nanoparticle morphology, solvent evaporation and the nanoparticle/solvent interaction on the resultant electrode microstructure has been assessed. Based on our computational results, a morphology-evaporation rate phase map (Figure 2.11) is generated to help us understand which factors affect the performance of the electrode. The phase map suggests that the small-sized cubical active nanoparticle can be a preferred morphology to generate the large conductive interfacial area ratio owing. The dispersion of active nanoparticles depends significantly on the interaction with the conductive additives, which shows the formation of electrode microstructures with favorable conductive pathway and hence its influence on improved electronic conductivity. The effect of the evaporation rate on the microstructure has been investigated which suggests the existence of distinct aggregation mechanisms. It is found that the spontaneous aggregation with a low evaporation rate is the optimum processing strategy to get the high quality microstructure, and this strategy requires a strong nanoparticle/solvent attractive force. If the nanoparticle/solvent attractive interaction is weak, nanoparticles tend to be isolated by solvents and the evaporation is the only driving force to make an integral conductive network in the electrode. In this case, the evaporation rate plays a subtle role of determining the microstructure because both high and low evaporation rate reduce the conductive interfacial area ratio. The volume fraction of the active material has been shown to affect the conductive pathway formation between the active material and conductive additive.

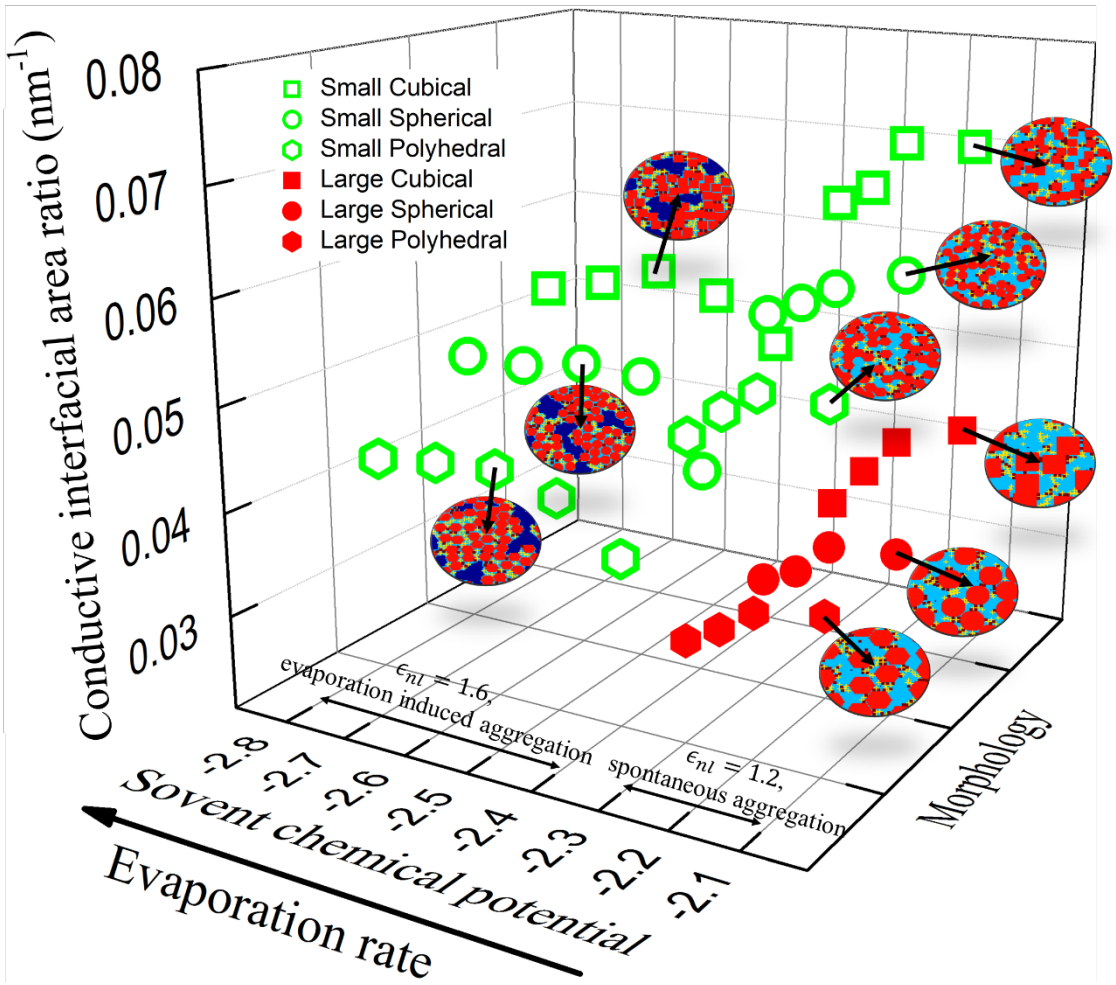

Figure 2.11 3D phase map describing the relationship of conductive interfacial area ratio with processing parameters. The solid hexagonal, circle and square represent the large-sized polyhedral active nanoparticle, spherical active nanoparticle and cubical active nanoparticle, respectively. The hollow hexagonal, circle and square represent the small-sized active nanoparticles. For each point in the figure, the volume fraction of active material is $\boldsymbol{\Phi_a = 50\%}$, and the conductive additive to binder ratio is $\boldsymbol{\Phi_c : \Phi_b = 0.8 : 1}$.

CHAPTER III

EFFECTS OF MIXING SEQUENCE ON ELECTRODE MICROSTRUCTURE IN LITHIUM-ION BATTERY*

A point worth emphasizing is that the mixing sequence plays a critical role in determining the performance of an LIB electrode. Electrode slurries, prepared by different mixing sequences, show different dispersion states of solid particles, even though these slurries are composed of the same materials with the same fraction. Yang *et al.*[59] first reported that changing the mixing method in the negative electrode preparation tripled the cycle life of the LIB. Kim *et al.*[60] designed four mixing sequences for processing $LiCoO_2$ positive electrodes, and demonstrated that pre-mixing dry active material and conductive additive was beneficial for prolonging the life of the LIB. Li *et al.*[61] studied the electrochemical properties of aqueous $LiFePO_4$ slurries, and found that dispersing active material nanoparticles first was beneficial to improve the discharge capacity. The sequence of adding solvent during the slurry preparation also affected the properties of the slurry. Compared with the slurry prepared by adding all solvents to mixed nanoparticles in one step, the slurry prepared by adding solvents in a stepwise manner had lower viscosity and more homogeneous nanoparticle distribution[62]. However, previous experiments focused on changing mixing sequence before the evaporation step. Recently, Huang *et al.*[63] reported a double carbon coating

* The chapter is reprinted with permission from "Mesoscale Elucidation of the Influence of Mixing Sequence in Electrode Processing" by Z. Liu, V. S. Battaglia, P. P. Mukherjee, 2014. *Langmuir*, 30, 15102-15113, Copyright [2014] by American Chemical Society.

process to achieve excellent electrochemical performance of $LiFe_{0.4}Mn_{0.6}PO_4$ electrode. In this experimental work, two different sequences about adding component for carbon coating were investigated during the drying process, and it was found that the step-wise addition is beneficial for coating carbon onto active material. Our present study focuses on elucidating the cooperation between active material and conductive additive during the slurry drying since evaporation critically governs nanoparticle aggregation behavior [46, 47]. In this study, we design different mixing sequences to fundamentally understand the interplay among evaporation, mixing sequence and active particle morphology.

3.1 Computational Method

The mesoscale model presented in CHAPTER II is employed to study the influence of mixing sequence on electrode microstructure during processing. In the present study, four different mixing sequences are designed (Figure 3.1). For all mixing sequences studied in the present work, the evaporation does not stop until $time = 1$. For the one-step mixing sequence, all constituents are mixed together at $time = 0$. For the two-step mixing sequence, active material nanoparticles and conductive additive nanoparticles are mixed in solvents at $time = 0$; then binders and solvents are added to the system at $time = 0.5$. For the multi-step-1 mixing sequence, half of the active material nanoparticles and half of the conductive additive nanoparticles are mixed in solvents at $time = 0$; then solvents and the remaining half of the active material nanoparticles as well as conductive additive nanoparticles are added to the system at $time = 0.125$; finally solvents and binders are added to the system at $time = 0.5$. For the multi-step-2 mixing sequence, all active material nanoparticles and half of the

conductive additive nanoparticles are mixed in solvents at $time = 0$; then solvents and the remaining half of the conductive additive nanoparticles are added to the system at $time = 0.125$; finally, solvents and binders are added to the system at $time = 0.5$.

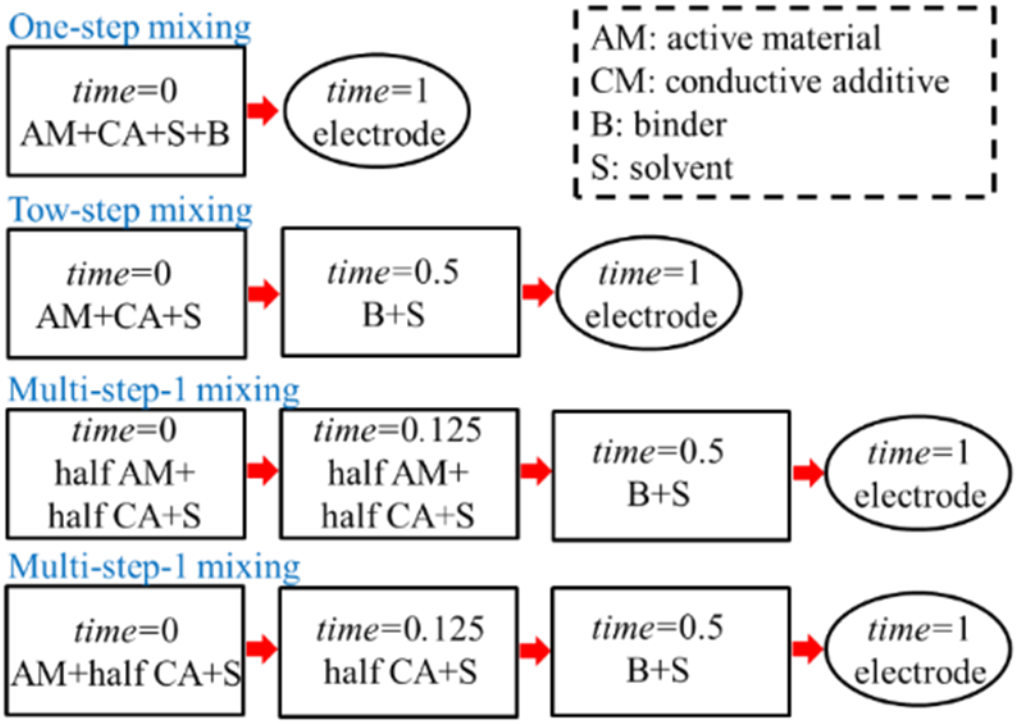

Figure 3.1 Mixing sequences designed in the present study. The red arrow means drying the slurry.

The binder distribution in the electrode also determines the performance of the electrode because a more inhomogeneous distribution causes a higher electrical resistance [85]. Experimentally, energy-dispersive X-ray spectroscopy (EDX) can detect the binder distribution (Figure 3.2(a)).In the present simulations, to characterize the quality of the binder distribution, a homogeneity index (H_b) is defined as

$$H_b = \left(\frac{1}{m \times n}\sum_{m,n}\left(\phi_{m,n} - \Phi_b\right)^2\right)^{\frac{1}{2}}. \quad (3.1)$$

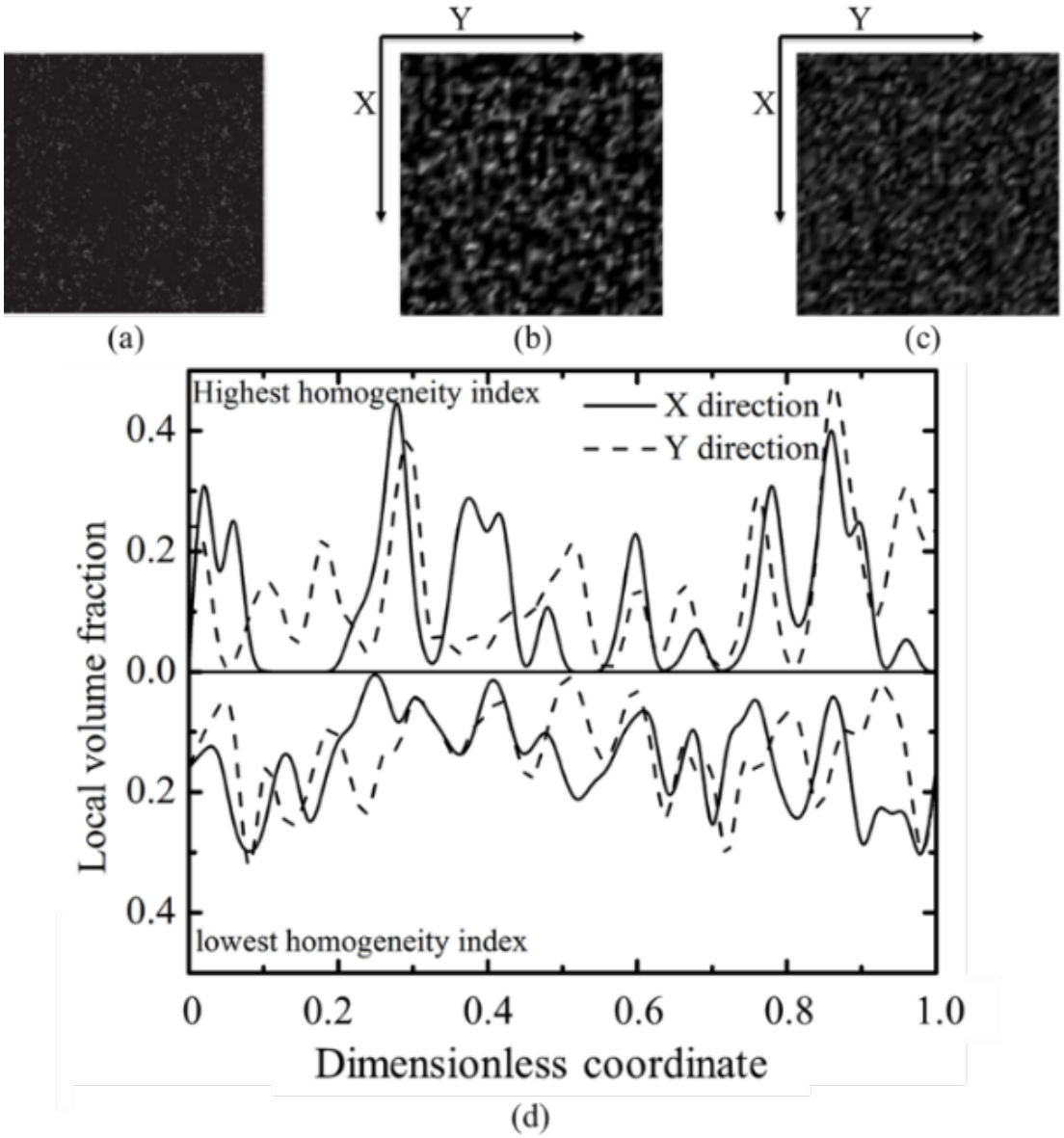

Figure 3.2 Binder distribution detected by Energy-dispersive X-ray spectroscopy (a) and present simulations (b & c). Figure (b) shows the binder distribution with the highest homogeneity (large-sized cubical active nanoparticles, two-step mixing sequence). Figure (c) shows the binder distribution with the lowest homogeneity index (small-sized spherical active nanoparticles, multi-step-2 mixing sequence). In Figure (b) and (c), the white represents the binder-rich region, and the black represents the binder-poor region. Figure (d) shows the 1-D the local binder distribution of left edge along X direction and top edge along Y direction. Figure (a) is adapted from Figure 9(g) in Ref. [32], G. Liu, H. Zheng, X. Song, and V. S. Battaglia, "Particles and Polymer Binder Interaction: A Controlling Factor in Lithium-Ion Electrode Performance", Journal of Electrochemistry Society, 159, A214, 2012.

To calculate the H_b, the domain is uniformly divided into $m \times n$ subdomains, and $m = 50$ and $n = 50$ are used in the present study. In Eqn. (3.1), the $\phi_{m,n}$ denotes the local binder volume fraction in the (m, n) subdomain. The local binder volume fraction can reflect the binder distribution (Figure 3.2(b) & (c)). A lower H_b means a more homogenous binder distribution. Figure 3.2(b) & (c) show the binder distribution maps with the highest homogeneity index (the most inhomogeneous binder distribution) and the lowest homogeneity index (the most homogeneous binder distribution), respectively. In the map with the highest index (Figure 3.2(b)), lots of white spots, which represent the high local binder volume fraction, are observed apparently. In the map with the lowest homogeneity index (Figure 3.2(c)), binder molecules distribute more uniformly and it is hard to observe the white region. Figure 3.2(d) shows the local binder volume fraction of left edge along X direction and top edge along Y direction. It is found that the oscillation of local binder distribution curve is weaker if binder molecules distribute more homogeneously.

Two evaporation conditions, constant temperature condition, and temperature-increasing condition are applied in the simulation of the drying process. In the constant temperature condition, the thermal energy term κT is fixed at 0.3 during the simulation. In the temperature-increasing condition, the thermal energy is defined as a linear function of the MC cycles as

$$\kappa T(iter) = 0.2 + \frac{iter}{8000} \times 0.2, \tag{3.2}$$

where *iter* represents the MC cycle during the simulation. In the temperature-increasing condition, the averaged thermal energy, $\overline{\kappa T} = \frac{\sum_{iter=1}^{8000} \kappa T(inter)}{8000}$, equals to 0.3. All computations stop at the 8000th MC cycle because the electrode structure does not change as simulated time increases after the 8000th MC cycle, even though solvents are not completely evaporated.

3.2 Results and Discussion

First, we will discuss the electrode microstructure evolution in the constant temperature condition. As mentioned above, electrode samples are prepared by four different mixing sequences. Figure 3.3 clearly shows that the stepwise mixing sequence is an effective method to widen the pathway for electrons transferring from conductive additive to active material. Compared with the one-step mixing, stepwise mixing sequences can increase the conductive interfacial area ratio by more than 30%. Compared with the two-step mixing sequence, multi-step mixing sequences do not apparently affect the conductive interfacial area ratio. Small-sized active material nanoparticles are always beneficial for increasing the conductive interfacial area ratio, no matter what the mixing sequence is. The cubic is the favored morphology to broaden the electron-transferring pathway, followed by the sphere and the polyhedral.

Experimentally, for spherical $LiFe_{0.4}Mn_{0.6}PO_4$ particles, a stepwise carbon coating process during slurry evaporation can significantly improve the electrochemical performance of the electrode due to the increase in the electronic conductivity [63]. The experimental result coincides with our simulation predictions: stepwise adding conductive additive nanoparticles is beneficial for improving the electronic conductivity

of the electrode microstructure. Large conductive interfacial area ratio is beneficial for capacity remaining. The coated conductive additive nanoparticles can alleviate the consequences from SEI formation. Additionally, the conductive additive film can block the dissolution of transitional metal in cathode to electrolyte. Therefore, a large conductive area ratio is desired to avoid losing active material in LIBs. Experimentally, carbon black coating on the LiCoO2 particles can improve the capacity-voltage profile compared with bare LiCoO2 particles, so that the coating can enable producing high-density LIBs [43]. Our previous theoretical study shows that a low evaporation rate is beneficial for achieving large conductive interfacial area ratio [115]. Furthermore, our recent experimental results demonstrate that active materials are better coated by conductive additive and binders when the cast slurry is processed with a low evaporation rate [129]. On the other hand, bare active materials are observed when a high evaporation rate is employed. The electrochemical performance test also shows that the electrode processed using low evaporation rate has lower impedance and retains higher capacity after several cycles. The experimental results prove our simulation prediction. The experimental work is currently being prepared for submission.

Figure 3.4 and 3.5 show side-by-side details of electrode microstructures produced by the one-step mixing sequence and the multi-step-1 mixing sequence for large-sized and small-sized particles, respectively. In electrodes containing large-sized active material nanoparticles (Figure 3.4) and processed by the one-step mixing sequence, quantities of conductive additive nanoparticles are separated from active material nanoparticles and combine with binder molecules, so that the conductive

interfacial area ratio ($R_{c:a}$) is reduced. In electrodes processed by the multi-step-1 mixing sequence, it is obvious that more conductive additive nanoparticles adhere to the surface of the active material nanoparticles and fewer conductive nanoparticles are trapped in the binder network. Fundamentally, the attractive force between nanoparticles is the key to determining the final electrode microstructure. In the one-step mixing sequence, binder molecules can cover the surface of active material due to the attractive force between these two species. In this case, the connection between active material and conductive additive is significantly reduced. In addition, in the one-step mixing sequence, due to the attractive force between conductive additive nanoparticles and binder molecules, these two components can aggregate to form binder/conductive additive composites. Conductive additive nanoparticles are trapped in the composites, which leads to a decrease of conductive interfacial area ratio. However, in stepwise mixing sequences, active material nanoparticles, and conductive material nanoparticles are pre-mixed, so that the obstruction from binder is avoided. Thereby these nanoparticles can be mixed well to increase the conductive interfacial area ratio.

Figure 3.5 shows the detailed microstructures of electrodes containing small-sized active material nanoparticles. Compared with electrodes containing large-sized active material nanoparticles, the number of conductive additive nanoparticles trapped by the binder network is smaller in electrodes containing small-sized active material nanoparticles. In these samples, small-sized active material nanoparticles provide a much larger active surface area, so that conductive additive nanoparticles have more chances to interact with active material nanoparticles. Comparing the electrode structures

produced by the one-step mixing sequence (left panels in Figure 3.5) with those produced by the multi-step-1 mixing sequence (right panels in Figure 3.5), it can be seen that the number of conductive additive nanoparticles trapped by the binder network is decreased by the multi-step-1mixing sequence and more conductive additive nanoparticles coat on the surface of active material.

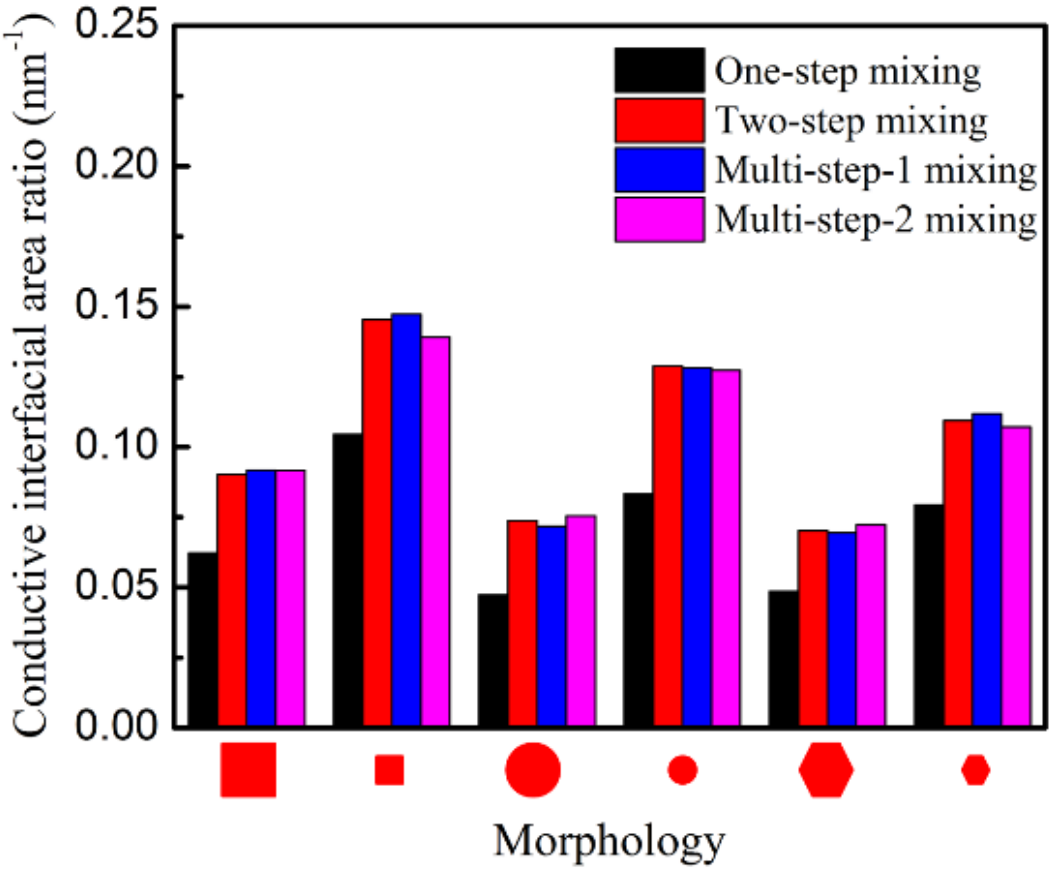

Figure 3.3 Effect of mixing sequence on the conductive interfacial area ratio in the constant temperature condition. The shape of the active material nanoparticle can be cubic, sphere and polyhedral. The size ratio of the large active material nanoparticle to the small one is 12:6. Each data point is the averaged value of the last 500 MC cycles.

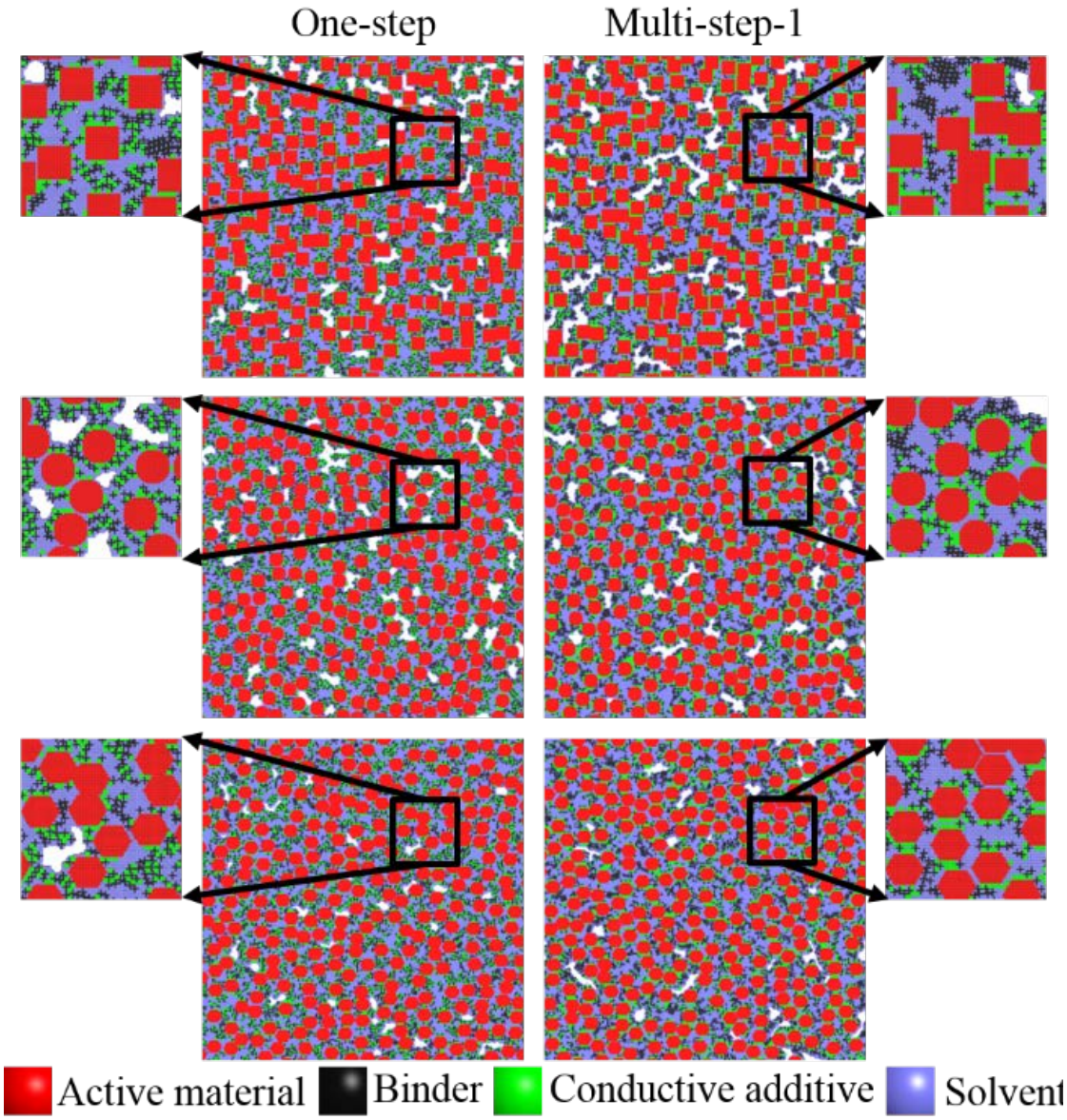

Figure 3.4 Stable microstructure of electrode slurry composed by large sized active nanoparticles and processed by different mixing sequence: (i) one-step mixing in left panels and (ii) multi-step-1 mixing in right panels. All simulations are performed in the constant temperature condition.

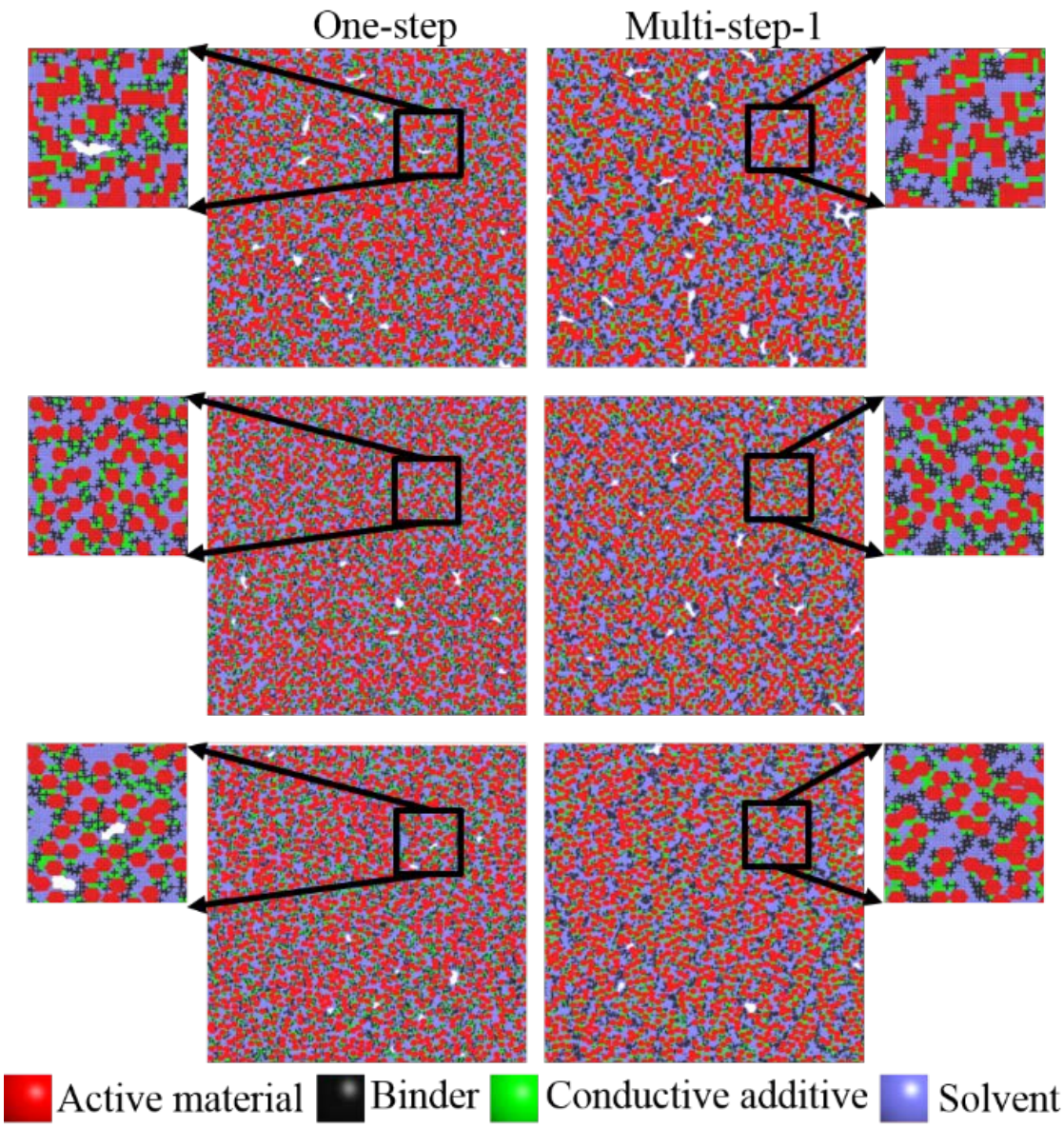

Figure 3.5 Stable microstructure of electrode slurry composed by small sized active nanoparticles processed by different mixing sequence: (i) one-step mixing in left panels and (ii) multi-step-1 mixing in right panels. All simulations are performed in the constant temperature condition.

The evolution of the conductive interfacial area ratios of electrodes processed by the multi-step-1 mixing sequence is shown in Figure 3.6. Here two electrode samples are shown: one is the electrode slurry containing small-sized cubical active material

nanoparticles (corresponding to high conductive interfacial area ratio) and the other one is the electrode slurry containing large-sized spherical active material nanoparticles (corresponding to low conductive interfacial area ratio). It is observed that the conductive interfacial area ratio ($R_{c:a}$) curves rise fast in the time duration (0, 0.0625] due to the aggregation between nanoparticles (Figure 3.7(b) and Figure 3.8(b)). Then the curves enter the first plateau, because most of solvents are evaporated (Figure 3.7(c) and Figure 3.8(c)). $R_{c:a}$ curves rise again after $time = 0.125$ due to the supplementary nanoparticles and solvents, and then they enter the second plateau because of the fast solvent evaporation. $R_{c:a}$ curves fall down a little from $time = 0.5$ because binder molecules are added to the system and they compete against active materials for capturing conductive additive nanoparticles. Although the attractive force between conductive additive and active material (ϵ_{ac}) is much stronger than the force between conductive additive and binder (ϵ_{bc}), conductive additive nanoparticles can still detach from the surface of active material, move to binder, and form conductive additive/binder composites finally. This deaggregation/reaggregation process is energy unfavorable because the conductive additive detachment from active material tends to increase the energy of local structure. Thereby, there is a transition barrier between initial state (a conductive additive nanoparticle adhering on the surface of active material) and final state (that conductive additive nanoparticle binding with the binder network). However this process can be accepted with a transition probability calculated by Eqn. (2.1). Finally, the transfer of conductive additive nanoparticles between active material and

binders reach an equilibrium state and conductive interfacial area ratios do not change significantly any longer, although solvents are not fully evaporated.

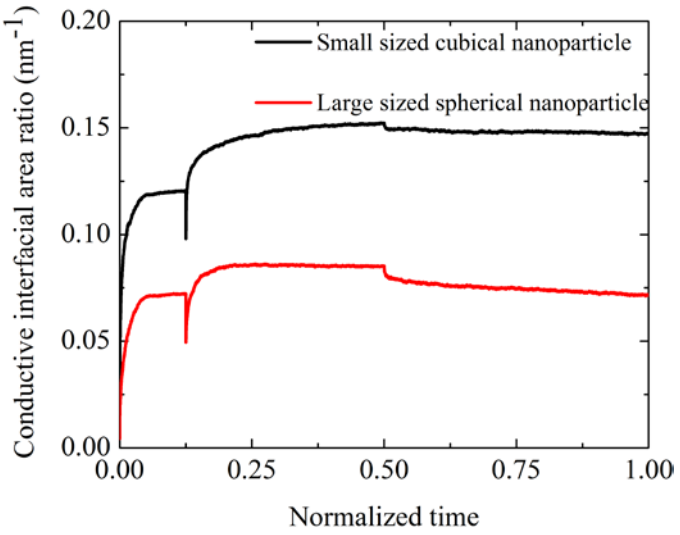

Figure 3.6 Evolution of the conductive interfacial area ratio of electrodes processed by the multi-step-1 mixing sequence. The simulated time is normalized by 8000 MC cycles.

The microstructure evolutions of electrodes during the multi-step-1 mixing sequence processing are shown in Figure 3.7 (small-sized cubical nanoparticles) and Figure 3.8 (large-sized spherical cubical nanoparticles). When processing an electrode that contains small-sized cubical nanoparticles, most of randomly distributed conductive additive nanoparticles combine with active material nanoparticles in time duration (0, 0.0125], and a small amount of conductive additive nanoparticles form clusters in the liquid environment (marked by black circles in Figure 3.7(b)). During the processing, these conductive additive clusters decompose and released nanoparticles that will combine with active material nanoparticles. Meantime, gas bubbles appear in the domain. These bubbles grow up and merge with each other before $time = 0.0625$. Because the domain is dominated by the gas phase, the diffusion of nanoparticles are

stopped, and the conductive interfacial area ratio does not change anymore until new solvents and nanoparticles are added to the domain. After $time = 0.125$, the conductive interfacial area ratio rises again due to the supplement of solvents and nanoparticles. It is worth noting that the evaporation rate becomes lower after $time = 0.125$. The supplement of nanoparticles generates more interaction pairs between solvents and nanoparticles, which can prevent solvents from evaporation because the nanoparticle-solvent attractive force is stronger than the solvent-solvent attractive force.

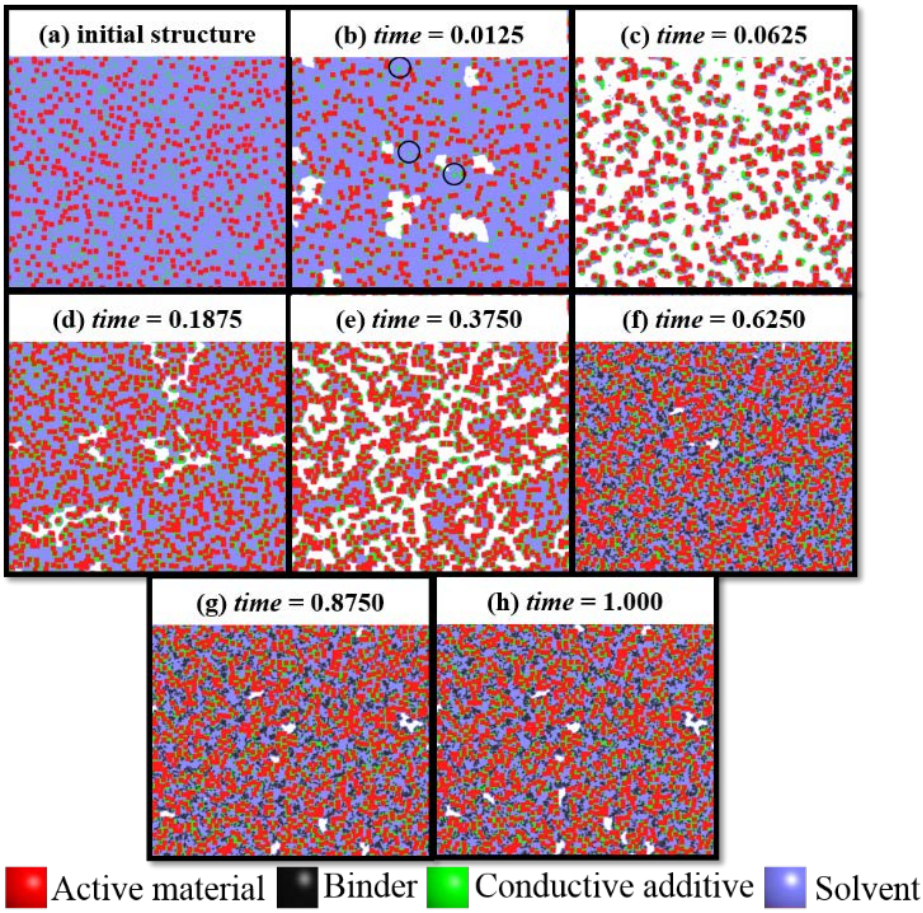

Figure 3.7 Microstructure evolution of electrode slurry under the multi-step-1 mixing sequence in the constant temperature condition. The simulated time is normalized by 8000 MC cycles. The electrode slurry is composited by small-sized cubic active material (red), binder (black), conductive additive (green), solvent (light blue). The solvent can be converted to the vapor (white) by the evaporation.

For the electrode slurry containing large-sized spherical nanoparticles, the microstructure evolution behaves similarly as the electrode slurry containing small-sized cubical nanoparticles when the multi-step-1 mixing sequence is applied (Figure 3.9). In the time duration (0, 0.0625], some of the randomly distributed conductive nanoparticles move to the active material nanoparticles and adhere to them. However, it can be observed that more conductive additive nanoparticles suspend in the solvents at $time = 0.0125$ (Figure 3.8(b)), compared with the electrode slurry containing the small-sized cubical active material nanoparticles (Figure 3.7(b)). At $time = 0.0625$, there are still lots of conductive additive clusters being separated from active material by the gas phase (Figure 3.8(c)), so that the conductive interfacial area ratio ($R_{c:a}$) is significantly reduced. Hence, we can clearly see that the first $R_{c:a}$ plateau of large-sized spherical active nanoparticles is lower than that of small-sized cubical nanoparticles in Figure 3.6. The phenomenon we discussed above is attributed to the smaller specific surface area of the large-sized spherical nanoparticles. The smaller specific surface area of active material decreases the connection between active material and conductive additive, hence the aggregation between conductive additives increases. After $time = 0.125$, the total surface area of the active material increases due to the supplement of nanoparticles, so that the free conductive additive nanoparticles from the decomposition of clusters can be adsorbed on the surface of active material much more easily. Thereby, there is a significant increase of conductive interfacial area ratio after $time = 0.125$.

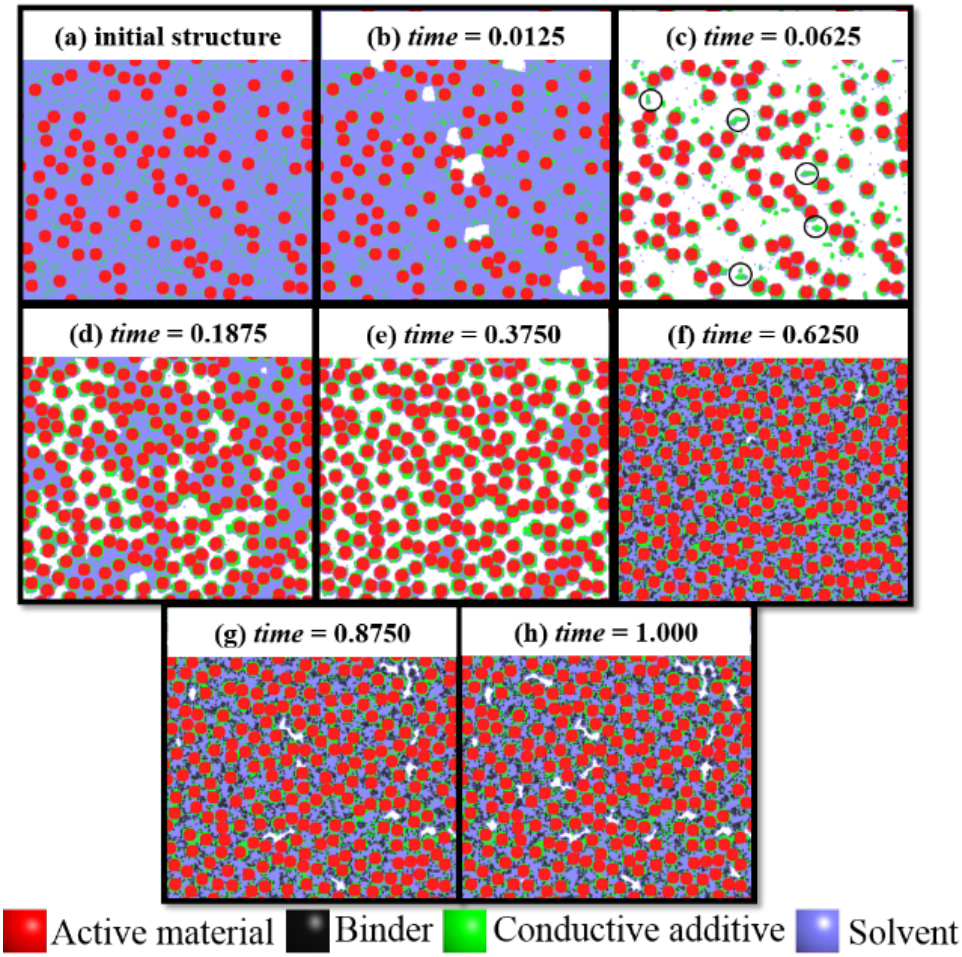

Figure 3.8 Microstructure evolution of electrode slurry under the multi-step-1 mixing sequence in the constant temperature condition. The simulated time is normalized by 8000 MC cycles. The electrode slurry is composited by large-sized sphere active material (red), binder (black), conductive additive (green), solvent (light blue). The solvent can be converted to the vapor (white) by the evaporation.

To lower the electronic resistance, a homogeneous binder distribution is desirable. Homogeneity indices of binder distribution are shown in Figure 3.9(a). Both the morphology and mixing sequence affect the homogeneity of the binder distribution. Generally, smaller sized active material nanoparticles are beneficial to produce a relatively higher quality of binder distribution. The one-step mixing can always make binders distribute homogeneously, although this mixing sequence produces low

conductive interfacial area ratios. Electrodes containing small-sized cubical active nanoparticles can achieve high conductive interfacial area ratios when stepwise mixing sequences are applied. In these three electrodes, only the one processed by two-step mixing sequence has a homogeneous binder distribution. As shown in Figure 3.9(a), one-step mixing can achieve more homogeneous binder distribution than those in the step-wise mixing sequences. In one-step sequence, all components, including binder molecules, are randomly and uniformly distributed in the initial structure before the evaporation. During the evaporation process, the combination between binder molecules and randomly distributed nanoparticles restricts the diffusion and maintains a higher level of homogeneity. In step-wise mixing sequences, binder molecules are added into the system after nanoparticles aggregation. In this case, binder molecules tend to diffuse into the heterogeneously distributed nanoparticle clusters due to the attraction force between binder molecules and nanoparticles. Therefore, binder distribution in step-wise mixing sequence shows lower homogeneity, as suggested by an increase in the distribution index. Furthermore, the present 2D model shows the binder distribution in an ideal horizontal plane, but not the distribution profile along the electrode thickness. A 3D model is planned in our future work which will investigate the spatial distribution of components in the electrode thickness direction. A comprehensive consideration including both the conductive interfacial area ratio and the homogeneity index suggests that mixing small-sized cubical active nanoparticles with other components by the multi-step-1 approach can produce an electrode structure that has high electronic conductivity.

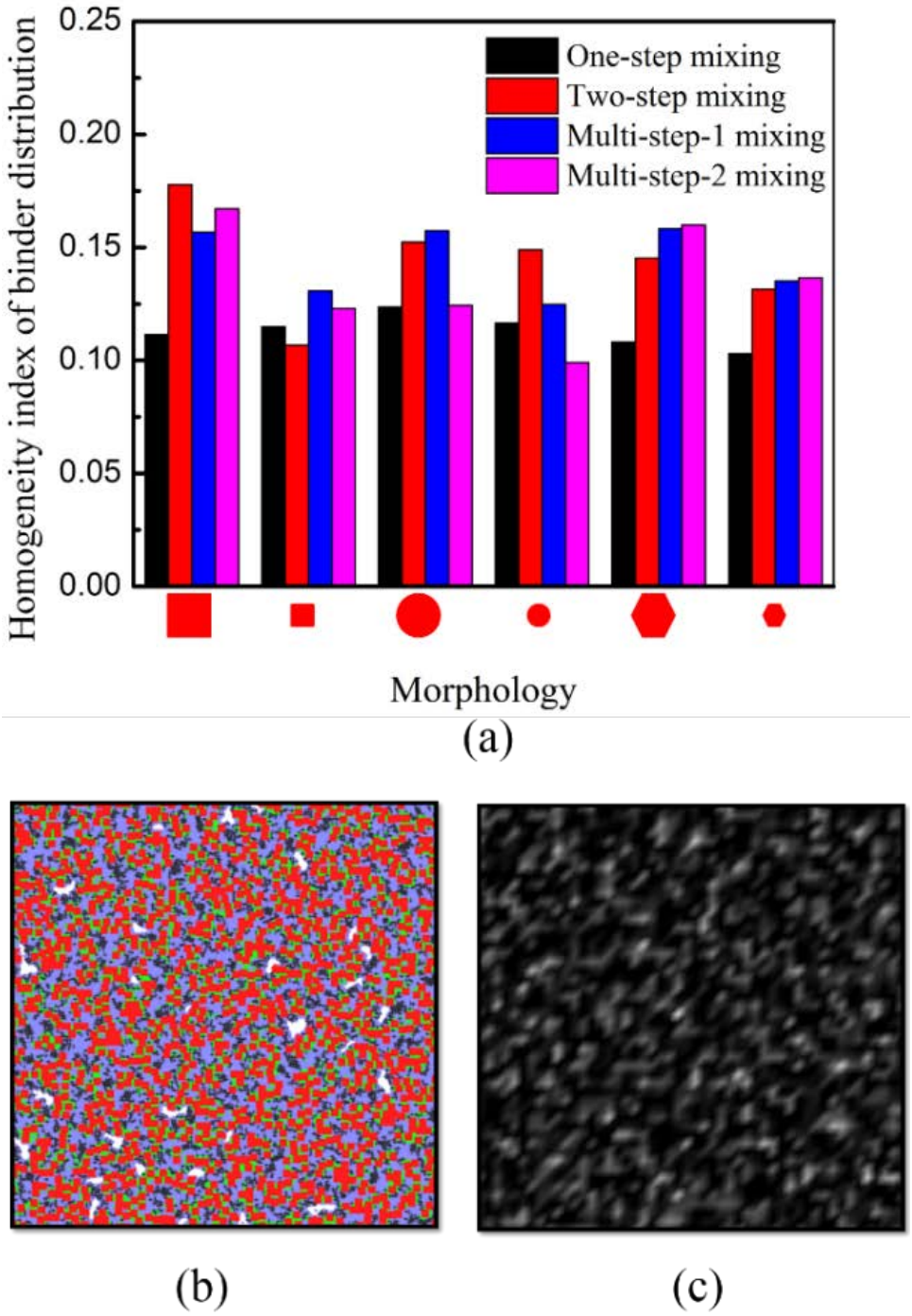

Figure 3.9 Homogeneity index of binder distribution in the constant temperature condition (a). The electrode containing small-sized cubical active nanoparticles and processed by two-step mixing sequence has both high conductive interfacial area ratio and low homogeneity index. The microstructure of this electrode is shown in (b) and the binder distribution is shown in (c).

During the constant temperature condition, solvents are evaporated very fast in the first 4000 MC cycles and the gas phase suppresses the aggregation of active material and conductive additive, especially in the electrode slurry containing large sized nanoparticles. During the active material/conductive additive mixing steps, the fast growth of the gas phase destroys the cooperation between active material and conductive additive. However, after adding the binder, the fast growth of the gas phase may make the binder distribute uniformly. To control the growth of the gas phase, a temperature-increasing condition is performed during the processing simulation. As shown in Eqn. (2.1), for the temperature-increasing condition, the thermal energy term κT is lower than 0.3 in the time duration (0, 0.5], so that the growth of the gas phase is slower than the constant temperature condition; and the κT is higher than 0.3 in the time duration (0.5, 1], so that the growth of gas phase is faster. The purpose of the following simulations is to investigate whether the temperature-increasing condition is practicable to process a better electrode structure than the constant temperature condition.

Same as in the constant temperature condition, small-sized active material nanoparticles produce higher conductive interfacial area ratios than large-sized ones, and the cubic is the optimal morphology to broaden the electronic diffusion pathway, followed by the sphere and then the polyhedral (Figure 3.10).

Compared with the constant temperature condition, the microstructure evolutions during the electrode processing are quite different in the temperature-increasing condition. Figure 3.11 and 3.12 show detailed microstructure evolutions of electrodes containing small-sized cubical nanoparticles and large-sized spherical nanoparticles,

respectively. Both samples are prepared by the multi-step-1 mixing sequence in the temperature-increasing condition. For the electrode slurry containing small-sized cubical nanoparticles, evaporation does not happen in the time duration (0, 0.125]. In this duration, the solvent chemical potential is lower than the critical chemical potential for liquid/gas phase transition, which means the gas phase is thermodynamically more stable than the liquid phase. However, the κT in this duration is too low to activate the evaporation. Thereby, all solvents still remain in the liquid phase. The low κT also affects the behavior of nanoparticles. In the constant temperature condition, all conductive additive clusters have decomposed before the solvents have fully evaporated ($time = 0.0625$, Figure 3.7(c)). However, conductive additive clusters can still be observed at $time = 0.0625$ in the temperature-increasing condition (marked by white circles in Figure 3.11(c)). The reason is that the probability of a conductive additive nanoparticle detached from the cluster is proportional to $e^{-\frac{1}{\kappa T}}$, thereby a low κT is helpful to stabilize the conductive additive cluster and a high κT can break attractive interaction between conductive additive nanoparticles in the cluster. At $time = 0.1875$ (Figure 3.11(d)), conductive additive clusters disappear because the linear increase of κT makes clusters decompose, and the supplement of active materials enlarges the surface area for conductive additive/active material interaction. Figure 3.12 shows the microstructure evolution of electrode slurry containing large-sized spherical nanoparticles and processed by the multi-step-1 mixing sequence. Similar to the microstructure evolution shown in the Figure 3.11, the evaporation is suppressed in the time duration (0, 0.5] due to the low κT. Compared with the electrode containing small-sized cubical active

material nanoparticles, fewer conductive additive nanoparticles aggregate with active material nanoparticles, and lots of free conductive additive nanoparticles and conductive additive clusters suspend in the liquid (Figure 3.12 (b)&(c)) due to the low κT and small specific surface area of large-sized spherical nanoparticles. Even though the supplement of nanoparticles at $time = 0.125$ enlarges the surface area of active materials, we can also observe some conductive additive clusters at $time = 0.1875$. These clusters finally decompose due to the further increase of the temperature (κT).

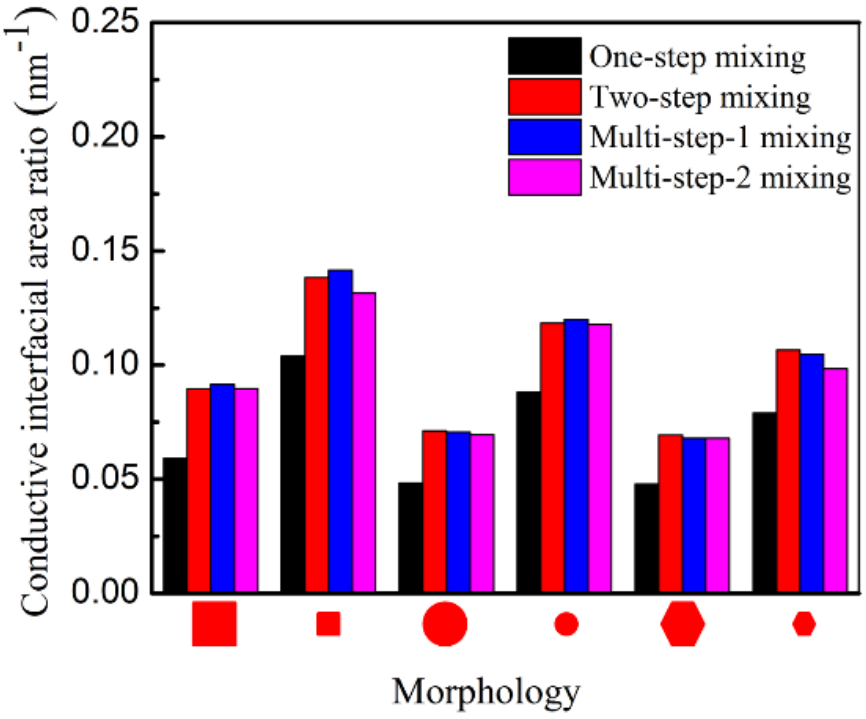

Figure 3.10 Effect of mixing sequence on the conductive interfacial area ratio in the temperature-increasing condition. The shape of the active material nanoparticle can be cubic, sphere and polyhedral. The size ratio of the large active material nanoparticle to the small one is 12:6. Each data point is the averaged value of the last 500 MC steps.

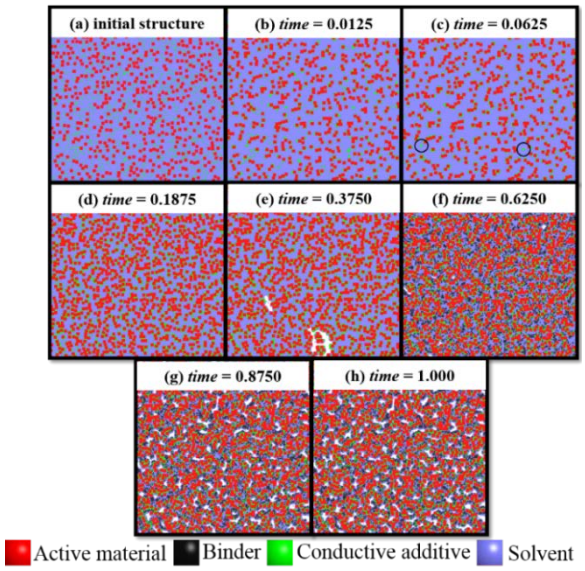

Figure 3.11 Microstructure evolution of electrode slurry under the multi-step-1 mixing sequence in the temperature-increasing condition. The simulated time is normalized by 8000 MC cycles. The electrode slurry is composited by small-sized cubic active material (red), binder (black), conductive additive (green), solvent (light blue). The solvent can be converted to the vapor (white) by the evaporation.

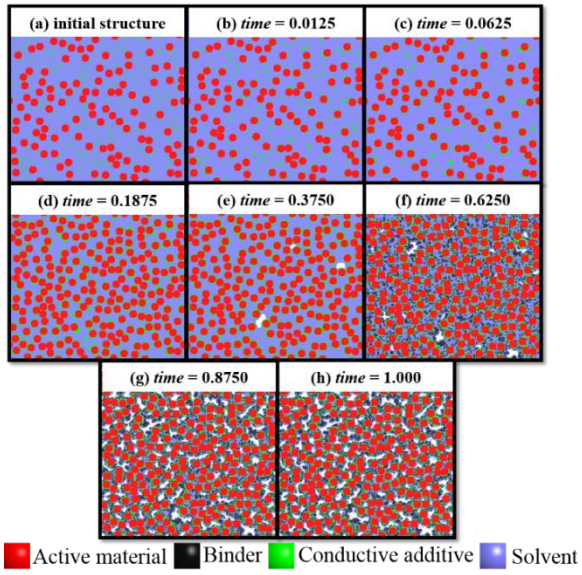

Figure 3.12 Microstructure evolution of electrode slurry under the multi-step-1 mixing sequence in the temperature-increasing condition. The simulated time is normalized by 8000 MC cycles. The electrode slurry is composited by large-sized sphere active material (red), binder (black), conductive additive (green), solvent (light blue). The solvent can be converted to the vapor (white) by the evaporation.

The temperature-increasing condition affects the homogeneity of the binder distribution (Figure 3.13). For electrode samples containing small-sized cubical active nanoparticles, homogeneity indices of the binder distribution is increased by about 30% if samples are processed by two-step or multi-step-2 mixing sequence, and the index does not change obviously if the sample is processed by the multi-step-1 mixing sequence.

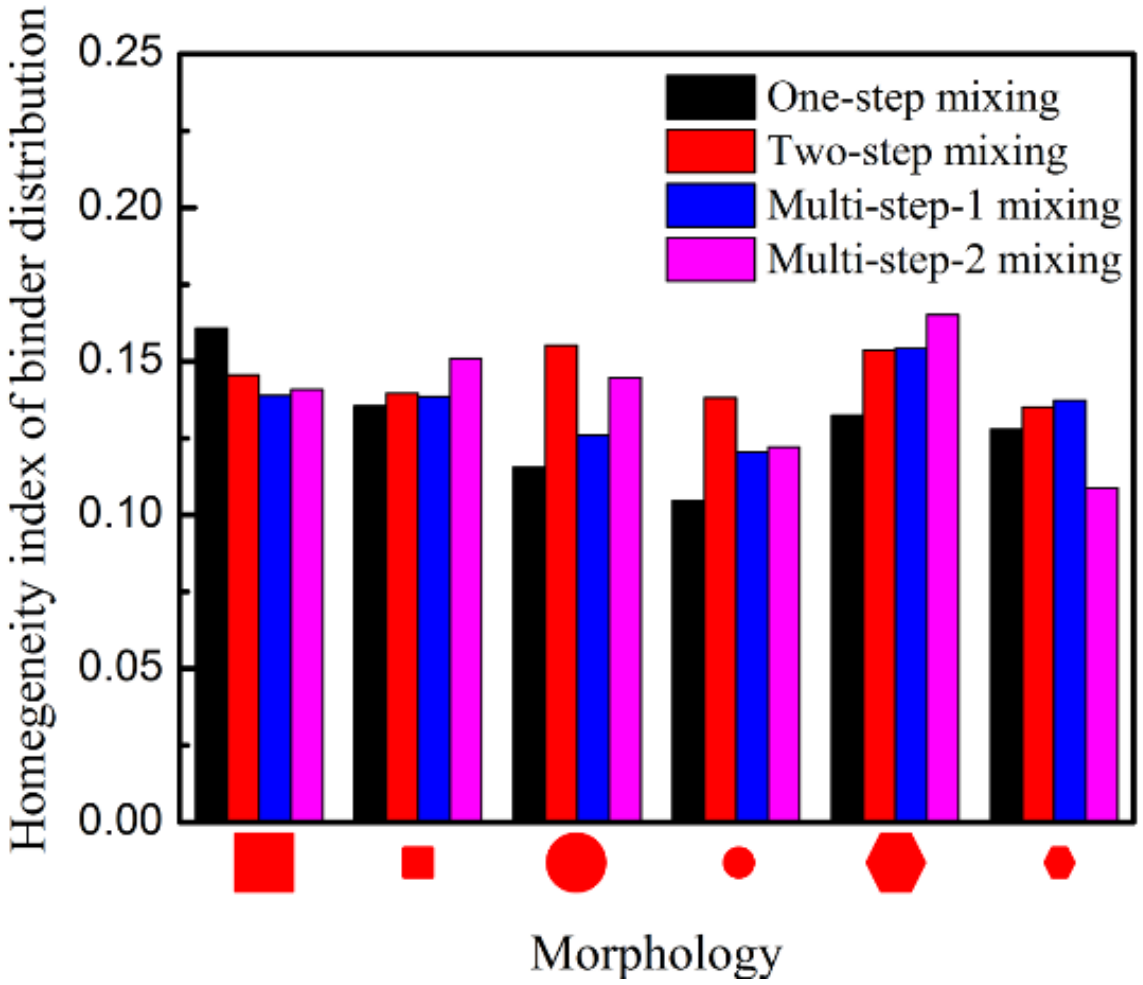

Figure 3.13 Homogeneity index of binder distribution in the temperature-increasing condition

3.3 Conclusions

A mesoscale computational model has been developed in order to investigate the influence of processing attributes on the microstructure evolution of a typical lithium-ion battery electrode. Particularly, the impacts of the slurry mixing sequence, the morphology of active material nanoparticles, and the temperature condition on the resultant electrode microstructure have been assessed. The effects of mixing sequences and nanoparticle morphologies are concluded in the phase map (Figure 3.14). Small-sized nanoparticles are preferred to produce the high conductive interfacial area ratio, and the cubic is the optimal morphology to form a desirable microstructure with a favorable electronic diffusion pathway. The effect of the mixing sequence on the electrode microstructure is investigated. Compared with one-step mixing sequence, stepwise sequences significantly increase the conductive interfacial area ratio. Both the constant temperature condition and temperature-increasing condition are performed in the electrode processing simulation. It is found that the temperature condition does not significantly affect the conductive interfacial area ratio. However, the temperature condition can subtly affect the homogeneity of the binder distribution. Taking conductive interfacial area ratio and binder distribution into consideration, in the constant temperature condition, the two-step mixing sequence is preferred to produce a high-quality microstructure for an electrode slurry composed by small-sized cubical nanoparticles; while in the temperature-increasing condition, the multi-step-1 mixing sequence is preferred to produce a high-quality microstructure for an electrode slurry composed by small-sized cubical nanoparticles.

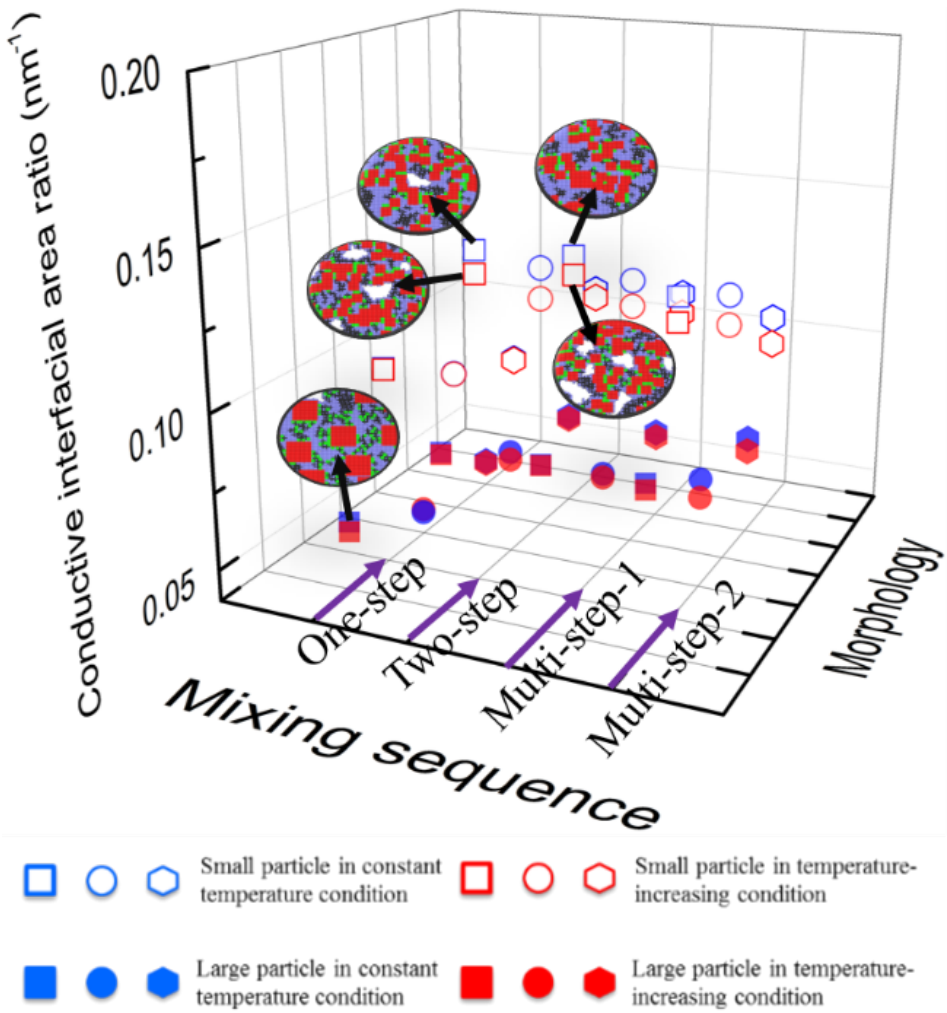

Figure 3.14 3D phase map describing the relationship of conductive interfacial area ratio with processing parameters. The solid hexagonal, circle and square symbols represent the large-sized polyhedral active nanoparticle, spherical active nanoparticle and cubical active nanoparticle, respectively. The hollow hexagonal, circle and square symbols represent the small-sized polyhedral active nanoparticle, spherical active nanoparticle and cubical active nanoparticle, respectively.

CHAPTER IV

EFFECTS OF BINDER LENGTH AND DRYING TEMPERATURE ON ELECTRODE MICROSTRUCTURE IN LITHIUM-ION BATTERY

Polymer-mediated nanoparticle assembly can be a promising method to control over the electrode microstructure [86-88]. However, there are only a few studies focusing on the effect of binder length (binder molecular weight) on electrode microstructure and the relative performance [89, 90]. Additionally, the distribution of components in LIB electrode significantly affects the electrochemical performance of LIB cathode. Our previous 2D LGCG simulations (presented in CHAPTER II and III) focused on nanoparticles and binder distribution in a plane, which cannot be used to study the components distribution and microstructure information along the thickness direction. In this particular study, a (1+1)D CGLG model is developed to illustrate the effect of solvent evaporation on the microstructure of electrode film.

4.1 Computational Method

4.1.1 Lattice-Gas Coarse-Grained Model

Following our previous studies, the CGLG model is employed to describe multiphase electrode slurry. In our present (1+1)D CGLG model, the computational domain consists $W \times H$ lattice cells with $L=200$ and $H=151$. Here W is the width of the domain along the horizontal direction and $H-1$ is the initial thickness of the electrode slurry along the vertical direction. All lattice cells are identical and the magnitude of the cell size is around 1 nanometer (nm), which approximately equals to the correlation

length of a solvent molecule [51]. Electrode slurry consists of active materials nanoparticles, conductive additive nanoparticles, and binder and solvent molecules. It is worth pointing out that each lattice cell can only be occupied by only one component so that multiphase coexisting in one cell is not allowed. In the computational domain, the bottom layer represents the substrate and cells in this layer cannot move or be converted to another component during the simulation. In the present study, a solvent molecule in either liquid or gaseous phase only occupies one lattice cell. An active material nanoparticle occupies tens to hundreds of cells, and the total number of cells is dependent on the size and morphology of the nanoparticle, which are important geometric parameters affecting the microstructure of assembled particles [57, 117, 118, 130]. In the present study, we only consider isometric (cubical and spherical) nanoparticles because they can coordinate better with conductive additive nanoparticles than polyhedral nanoparticles [115, 131]. The half-length (R) of the nanoparticle is used to characterize the nanoparticle size. In this study, the size of both cubical and spherical active nanoparticles equals to 6 lattice units. The nanoparticle size in the present model is about tens nanometers and approaches to the size of $LiFePO_4$ nanoparticle in LIB cathode [56, 119] and that of Si or Sn nanoparticle in LIB anode [120, 132]. Given that the size of primary conductive additive nanoparticle is smaller than that of the active material nanoparticle, we neglect the morphological detail of conductive additive nanoparticle. To simplify the model, a conductive additive nanoparticle is represented by a cubic with $R = 2$ lattice units. Polyvinylidene fluoride (PVDF), which has a single chain structure,

is widely used as binder in LIB. In this study, the binder molecule is represented by a single chain with the length of L = 9, 13, 17, 21, 25 lattice units.

4.1.2 Monte Carlo Dynamics

A KMC method is employed to study the evaporation influenced microstructure evolution and components distribution of electrode film. Both particle/binder movement and solvent phase transition are implemented in each MC cycle. The nanoparticle diffusion should not break the following rules. A nanoparticle can only move to its neighbor cells with a randomly selected direction. The movement is not absolutely random because the nanoparticle diffusivity is zero in a dry local environment.[51] Following this restriction, a nanoparticle can only diffuse to neighbor cells all of which are covered by solvent in liquid phase. To keep the solvent mass conserved during the nanoparticle diffusion, cells behind a nanoparticle should be refilled by solvent molecules after the diffusion. The movement of a binder molecule is described by a slithering-snake algorithm.[133] When we attempt to move a binder molecule, an endpoint of the chain is randomly selected as the leader of the movement. The leader can randomly move to its neighbor cell occupied by liquid solvent, with other monomers in the chain moving ahead along previous conformation and leaving the old tail site being occupied by liquid solvent. The solvent phase transition is also considered in this model to mimic evaporation/condensation dynamics. During the simulation, a lattice cell will be selected randomly, if it is a liquid solvent cell and its top neighbor is a gas cell, the current cell can be evaporated. On the other hand, if the selected cell is occupied by gas and its bottom neighbor is occupied by non-gaseous component, the condensation can

happen. The motivation of this constrain is to avoid an unphysical situation in which nanoparticles suspend in gas.[134]

The state of the computational domain is described by the structure-dependent Hamiltonian as

$$H = -n_{ll}\epsilon_{ll} - n_{al}\epsilon_{al} - n_{bl}\epsilon_{bl} - n_{cl}\epsilon_{cl} - n_{aa}\epsilon_{aa} - n_{ab}\epsilon_{ab} - n_{ac}\epsilon_{ac} - n_{bb}\epsilon_{bb} - n_{bc}\epsilon_{bc} - n_{cc}\epsilon_{cc} - n_{as}\epsilon_{as} - n_{bs}\epsilon_{bs} - n_{cs}\epsilon_{cs} - N\mu. \quad (4.1)$$

In Eqn. (4.1), subscripts *l*, *a*, *b*, *c* and *s* denote solvent molecule in liquid phase, active material, binder, conductive additive and substrate, respectively. Symbol ϵ denotes interaction energy of two adjacent cells and *n* denotes the number of interaction pairs. In this study, only the first nearest neighbors are considered to count interactions pairs, and this is a good assumption for studying evaporation-influenced nanoparticles assembly *via* 2D and 3D lattice-gas models [51, 134]. For the last term $N\mu$ in Eqn. (4.1), *N* is the total number of liquid cell in the computational domain and μ is the solvent chemical potential in liquid phase. The chemical potentials of nanoparticles and binder molecules can be safely neglected because they cannot be evaporated.

Any state transition mentioned above (nanoparticle/binder diffusion and solvent evaporation/condensation) can cause structure change and corresponding Hamiltonian change. Thermodynamically, structure change with Hamiltonian decreasing is always energetically favored. However, structure change with Hamiltonian increasing can also be accepted with Metropolis probability

$$p_{acc} = \min\left[1, \exp\left(-\frac{\Delta H}{\kappa T}\right)\right]. \quad (4.2)$$

Here ΔH is the Hamiltonian of candidate state minus that of the current state. κ is the Boltzmann constant and T is the operating temperature.

4.1.3 Operating Conditions

In this model, all energetic parameters (interaction energy, chemical potential and κT) are in the unit of ϵ_{ll} which value is predefined to 1. To mix components well in the slurry and avoid phase separation, the interaction energy between a nanoparticle (or molecule) cell and a liquid cell should be larger than 1.[135] Nanoparticles tend to aggregate to get a more stable state in the absence of liquid, thereby the attractive interaction between two nanoparticles should be stronger that between a nanoparticle cell and a liquid cell. To make nanoparticles glued to the substrate, nanoparticles should also have strong attractive interactions with substrate. The value of solvent chemical potential determines the volume fraction of liquid phase at the equilibrium state. Dewetting is energetically favored with a negative μ, while wetting is favored with a positive μ [136]. In the present model, the critical solvent chemical potential for liquid-to-gas transition is -2 if the computational domain is completely filled by liquid solvent, and adding other components will shift the critical potential to a more negative value according to mean-field theory.[121] The values of input parameters follow the guidelines of our previous work.[115, 131] The nondimensional solvent chemical potential (μ) is set to -2.4 in all simulations. The nondimensional interaction parameters are $\epsilon_{aa} = \epsilon_{cc} = 1.7$, $\epsilon_{ab} = 1.8$, $\epsilon_{bc} = 1.9$, ϵ_{ac}=2.0, $\epsilon_{al} = \epsilon_{cl} = 1.4$, and $\epsilon_{as} = \epsilon_{cs} = 2.1$. We assume that binder molecules are in good solvent so we predefine that $\epsilon_{bb} = 1$ and $\epsilon_{bl} = 1.4$. All nondimensional interaction parameters are appropriately adjusted in

our simulations. In all simulations, the initial volume fractions of active material, binder and conductive additive are set to 27.0%, 9.3% and 7.3%, respectively.

Simulation in the present study starts from an equilibrium initial structure rather than a nonequilibrium initial structure which is reported in Ref. 127. Step-by-step procedure to create an equilibrium initial structure is listed in the following. At the first step, a $W \times H$ computational domain is created, in which all lattice cells above the substrate layer (bottom layer) are completely filled by liquid solvent. At the second step, the active material and conductive additive nanoparticles are randomly distributed in the domain and replace solvent cells. At the third step, binder molecules are added to space between nanoparticles and the nonequilibrium structure is generated. Then the 5000 MC cycles are conducted without considering Hamiltonian variation and solvent evaporation to get the equilibrium structure for the following evaporation induced aggregation. After generating the equilibrium structure, 3×10^5 MC cycles are performed with considering Hamiltonian variation and solvent evaporation to get the dehydrated film.

4.2 Results and Discussion

We would like to discuss the effects of operating temperature and binder length on the microstructure of electrode film with cubical active material nanoparticles firstly. The mean thickness variation of electrode film is plotted in Figure 4.1(a). The mean thickness is calculated as

$$\bar{\delta} = \frac{\sum_{i=1}^{W} \delta_i}{W}, \tag{4.3}$$

where δ_i is the thickness of the film at column *i*. It is observed that the mean thickness of the electrode film increases linearly as the binder length *L* increases from 9 to 25 with

operating temperature term $\kappa T = 0.3$. However, for the evaporation condition with a higher operating temperature $\kappa T = 0.6$, the mean thickness tends to decrease as the binder length increases. For the dehydrated film which consists of the shortest binder as L = 9, the mean thickness is about 72.77 at the lower operating temperature ($\kappa T = 0.3$) and the thickness is about 73.97 at the higher operating temperature. It is obvious that the film processed by the lower operating temperature is thicker than that processed by the higher operating temperature when the shortest binder (L = 9) is compounded into electrode slurry. On the contrary, for dehydrated films with the longest binder (L = 25), the mean thickness of film with the higher operating temperature is 72.59, which is smaller than that of the film with the lower operating temperature. The crossover of thickness variation *vs.* binder length takes place around binder length equals to 17. Both binder length and operating temperature affect the surface topography of dehydrated electrode film. Figure 4.1(b) shows the surface roughness of electrode films processed in different conditions. The surface roughness is defined as

$$R_q = \left(\frac{1}{W}\sum_{i=1}^{W}\left(\delta_i - \bar{\delta}\right)^2\right)^{0.5}. \tag{4.4}$$

For the same binder length, it is found that the roughness of the film processed by a lower drying temperature is larger than that of the film processed by a higher drying temperature. Additionally, the binder length also affects the surface topography of electrode film according to Figure 4.1(b). For the films processed by the lower operating temperature, it can be seen that the roughness increases as binder length increases from 9 to 21. For the films processed by the higher operating temperature, the surface roughness does not change obviously when the binder length is below 17.

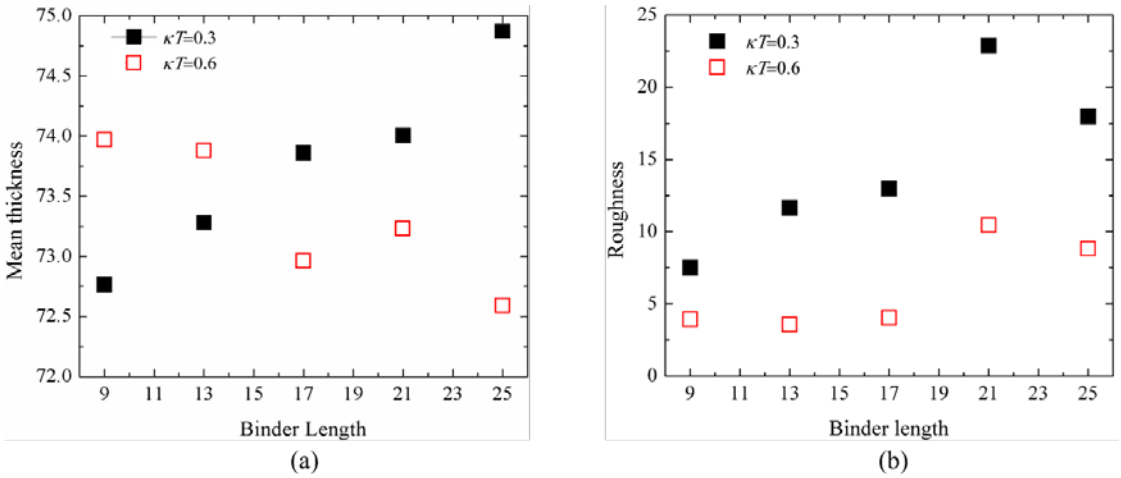

Figure 4.1 Geometric properties of electrode film processed by evaporation with different operating temperature. The mean thickness varies with binder length is shown in (a), and the roughness varies with binder length is shown in (b). The electrode film consists of cubical active material nanoparticles conductive additive nanoparticles and binder.

Figure 4.2 clearly depicts the microstructures of the electrode with different binder length and processed by different drying temperature. According to Figure 4.1, it is learned that a lower drying temperature produces film with a rougher surface. The two topmost panels show the microstructures of films processed by $\kappa T = 0.3$ (Figure 4.2(a)) and $\kappa T = 0.6$ (Figure 4.2(f)) respectively, in both of which the binder length equals to 9. Several micropores are observed on the surface of electrode film processed at the lower drying temperature as shown in Figure 4.2(a). Oppositely, the surface of electrode with the higher drying temperature is smoother and no holes are observed in Figure 4.2(f). According to Figure 4.1(b), it is found that the surface roughness is proportional to the binder length when the lower drying temperature is operated. Figures 4.2(a)~2(e) clearly demonstrate the microstructure evolution of electrode film with different binder length. It is obvious that the surface is craggier when the longer polymer is used as binder in the slurry. The increase of the surface roughness is mainly attributed to the depth of

the surface hole in the electrode film. For instance, the depth of the surface hole is around two nanoparticles in the electrode with binder length equaling to 9 lattice units (Figure 4.2(a)); while the depth of the surface is larger than five nanoparticles in the electrode with binder length equaling to 21 units (Figure 4.2(d)). As shown in Figure 4.1(b), the surface roughness varies inconspicuously with binder length L rising from 9 to 17 when a higher drying temperature ($\kappa T = 0.6$) is operated. Figures 4.2(f)~(h) clearly depict that the film surface is almost flat with $R_q < 5$ when the films consist of binder which length is shorter than 17 lattice cells. The surface becomes undulated when the binder length is longer than 17 lattice units. Although the microstructure which is shown in Figure 4.2(i) has the similar surface roughness R_q as the structure shown in Figure 4.2(b), topographies are quite different. Valleys in Figure 2(b) are deeper and narrower than those in Figure 4.2(i).

Snapshots in Figure 4.2 also depict that binder distribution is affected by operating temperature. It can be observed that more binder molecules appear in the surface region of electrode film. The on-surface binder distribution is plotted in Figure 4.3 to quantitatively demonstrate binder distribution. The on-surface binder distribution is calculated by

$$F_b = \frac{\sum_{i=1}^{W} \sum_{j=\delta_i - 8}^{\delta_i} lattice_{i,j}}{N_b}, \tag{4.5}$$

where $lattice_{i,j}$=1 if the (i, j) cell is a binder cell and $lattice_{i,j}$=0 if the (i, j) cell is occupied by another component and N_b is the total number of binder cells in the computational domain. As shown in Figure 4.3, more binder molecules migrate to the surface region when a higher drying temperature is applied. Additionally, the shorter binder is easier to

migrate to the surface region. According to Figure 4.3, it is found that the fraction of on-surface binder tends to decrease with increasing binder length. A larger fraction of on-surface binder means a more inhomogeneous binder distribution, which is harmful to the adhesive strength of the electrode. According to Figure 4.3, it can be inferred that the increase of binder length is helpful for achieve strong adhesion. Lee *et al.* evaluated the effect of carboxymethyl cellulose molecular weight on $Li_4Ti_5O_{12}$ anodic performance, and found that the adhesive strength increased as molecular weight increased [89]. Li *et al*. investigated binder distribution along drying direction experimentally [85]. They also reported that the high fraction of binder in the surface region destroyed the uniform binder distribution in the electrode. The weak adhesion and high electrical were attributed to the inhomogeneous binder distribution according to the experiment. They found that the low evaporation rate generated the inhomogeneous binder distribution. However, the present simulations demonstrate that the nonuniform binder distribution is attributed to the high evaporation rate. The reason of this conflict can be that Li *et al.* tuned the evaporation rate by changing solvent. They used the water-based solvent to achieve high evaporation rate and organic-based solvent to achieve low evaporation rate. Thereby, the nanoparticle-solvent interaction, solvent-solvent interaction, and binder-solvent interaction were more or less changed in their experiments. These interactions significantly affect the viscosity of electrode slurry and the final electrode microstructure [45]. In the present study, all interaction parameters are kept as constants to avoid changing the viscosity of the slurry, and the evaporation rate is tuned by changing the operating temperature.

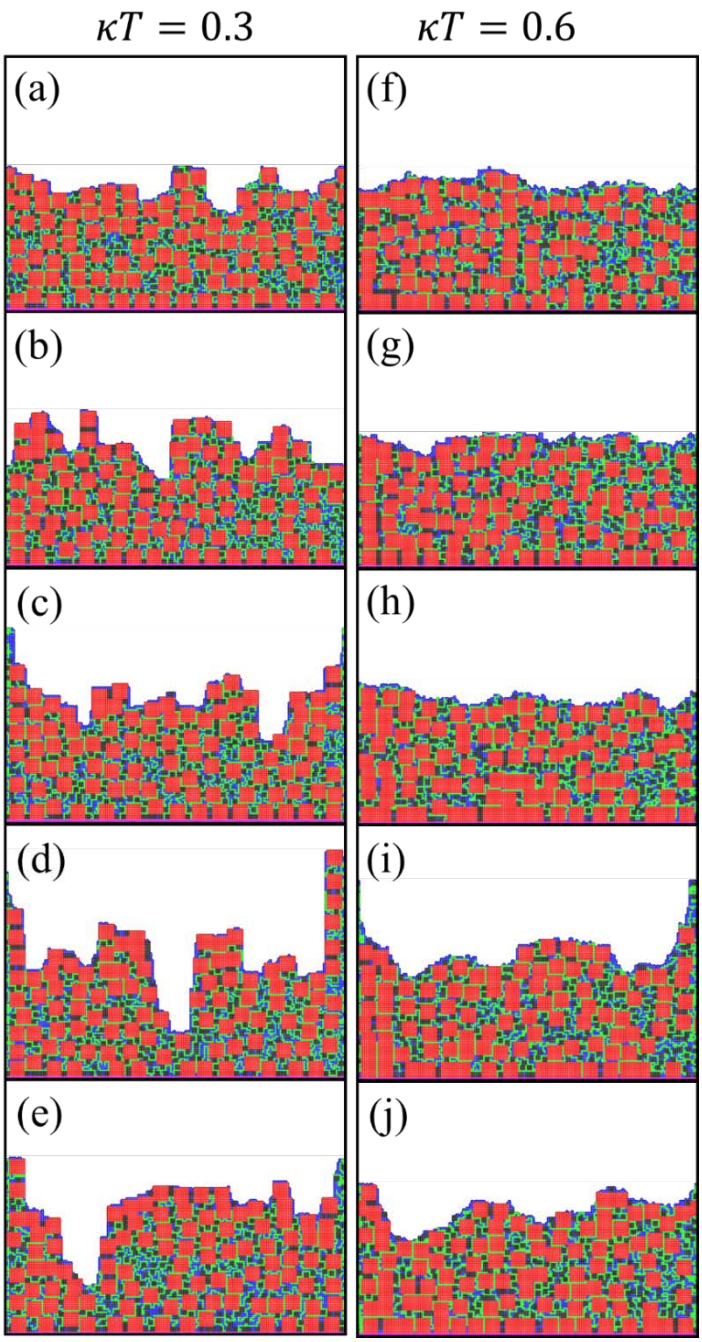

Figure 4.2 Snapshots of electrode films processed by evaporation with (a) ~ (e) low temperature and (f) ~ (g) high temperature. The binder length is increased from 9 cells (top snapshots) to 25 cells (bottom) snapshots. The electrode slurry consists of cubical active material nanoparticles (red), conductive additive nanoparticles (black), semi-flexible binder (green) and solvent molecule (dark blue).

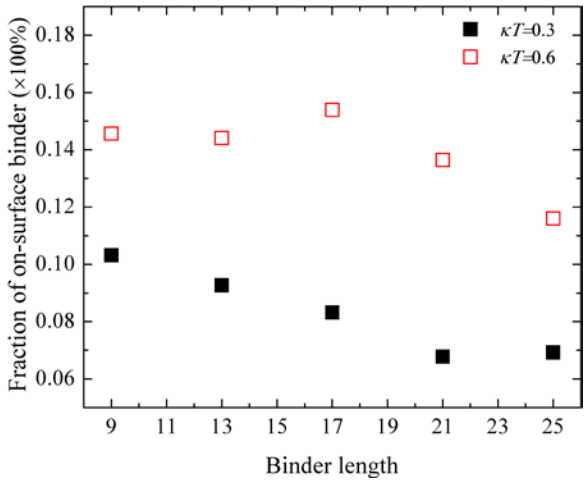

Figure 4.3 Effects of operating temperature and binder length on binder distribution in the electrode film with cubical active material nanoparticles.

The cooperation between active material nanoparticles and conductive additive nanoparticles is a key to improving the performance of electrode. The conductive additive coating on the active material surface can widen the pathway for electrons migrating into active materials. Additionally, the coating can prevent transition metal in active material dissolve into electrolyte and reduce harmful side reaction at the solid/electrolyte interface [41, 43, 44]. The effect of drying temperature on nanoparticle aggregation is investigated in this study. The fraction of interface area on active material is plotted in Figure 4.4. The fraction of active-conductive interface area is defined as the ratio of the interface area between active material and conductive additive to the total surface area of active materials, and the fraction of active-active interface area is defined as the ratio of the interface area between two active nanoparticles to the total surface area of active materials. According to Figure 4.4, it can be seen that the higher active-conductive interface area is obtained when the lower drying temperature is operated.

This phenomenon is also observed in our previous 2D model[115] and experiment[129]. The large active-conductive interface area is beneficial for improving the electronic conductivity of electrode microstructure[115].

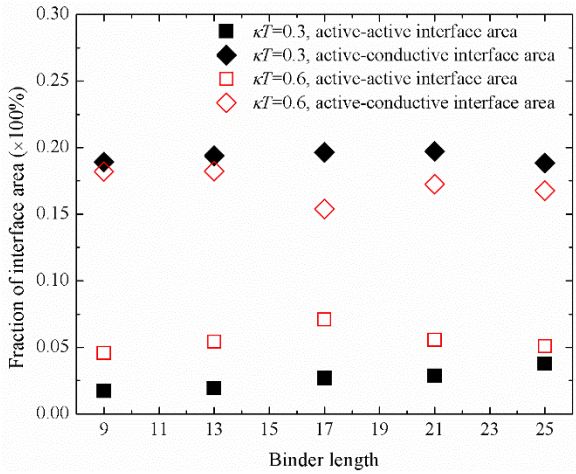

Figure 4.4. The influence of binder length and temperature on nanoparticle aggregation in the electrode film with cubical active material nanoparticles.

Figure 4.4 also demonstrate that aggregation between active material nanoparticles is facilitated by increasing drying temperature. A higher active-active interface area indicates more aggregation between active material nanoparticles. The aggregation is harmful to achieving high performance because the aggregation leads to reducing active surface area for electrochemical reactions. Additionally, the aggregation between active material nanoparticles increase Li diffusion length which leads to a slow kinetics [33]. Based on our simulations, we suggest using a low drying temperature (or evaporation rate) to process electrode with high performance. The nanoparticles aggregation in electrode slurry with different binder length is also studied in this study and demonstrated in Figure 4.4. It is found that the binder length does not significantly affect nanoparticles aggregation.

The conformation of binder in dried film is studied in the present work. The root mean square end-to-end distance $<h^2>^{0.5}$ is usually employed to characterize the conformation of single chain polymer. The end-to-end distance of binder in dried electrode microstructure is plotted in Figure 4.5. The relationship between end-to-end distance $<h^2>^{0.5}$ and binder length L follows the power law

$$< h^2 >^{0.5} = CL^{\alpha}. \tag{4.6}$$

in which C is a numerical constant which depends on the local constrains of the polymer molecule. Fore hindered rotation chain, C is the function of bond angle and α equals to 0.5. For a freely jointed chain, C equals to 1 and α equals 0.5[137]. The values of C and α can be obtained in the present study by fitting Eqn. (4.6) according to end-to-end distance with different binder length. As shown in Figure 4.5, the fitting curve with $\kappa T = 0.3$ almost coincides with the fitting curve with $\kappa T = 0.6$. The numerical constant C approximates to 1.60 and the power α approximates to 0.54 at $\kappa T = 0.3$. If the drying temperature is increased to $\kappa T = 0.6$, C approximates to 1.54 and α approximates to 0.57. Compared with freely jointed chain, the larger C in this study may be attributed to constrain of the LGCG model. In the present model, the bond angle of three consecutive monomers can only be $\frac{n}{2}\pi$ with $n = 1, 2, 3$. However, for a freely jointed chain, the bond angle can be uniformly distributed in the range of (0, 2π) in a 2D space. Additionally, the interaction between binder cell and adjacent nanoparticle cell can also affect the conformation variation of binder. The power α in the present study is larger than 0.5, which indicates that the binder is straightened by nanoparticle due to the attractive force between a nanoparticle cell and a binder cell. Figure 4.5(b) depicts the end-to-end

distance normalized by the binder length L. It is found that the normalized end-to-end distance tends to decrease as binder length increase, which indicates that shorter binder is straighter than longer binder.

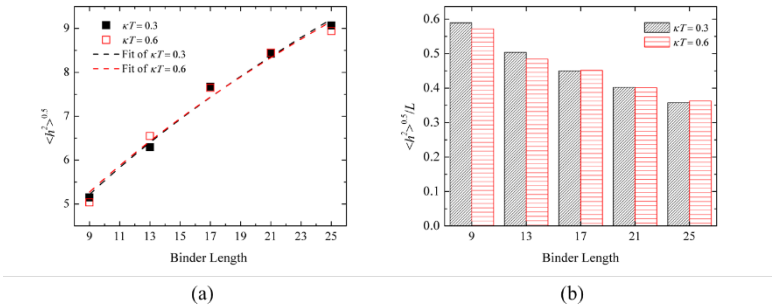

Figure 4.5 Conformation of binder in the dried film with cubical active material nanoparticle: (a) end-to-end distance, and (b) end-to-end distance normalized by binder length.

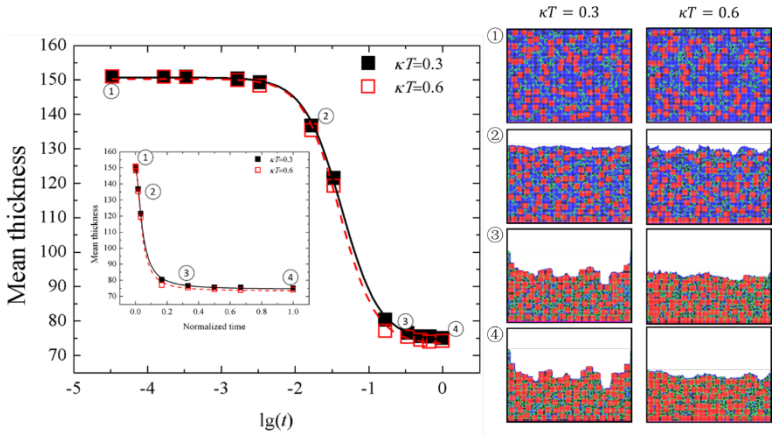

Figure 4.6 The slurry thickness evolution with normalized simulation time and corresponding microstructures. ①, ②, ③ and ④ stand for the normalized simulation time at $\boldsymbol{t = 3.33 \times 10^{-5}}$, $\boldsymbol{t = 1.67 \times 10^{-2}}$, $\boldsymbol{t = 0.33}$ and $\boldsymbol{t = 1.00}$. The slurry consist of cubical active material nanoparticles (red), semi-flexible binder with $\boldsymbol{L = 17}$ (green), conductive additive nanoparticles (black) and solvent molecules (dark blue).

The slurry thickness evolution during the evaporation processing and corresponding microstructures are demonstrated in Figure 4.6. The thickness evolution

during the evaporation process can be divided into three stages. The slurry thickness decreases very fast in the first stage, which is relative to the higher plateau in the thickness-lg(t) space as shown in Figure 4.6. In the first stage, a solvent cell always coordinates with other solvent cells so that it is easy to be evaporated. With evaporation going on, the volume fraction of solvent in the slurry film decreases while the volume fraction of nanoparticles increases. In this case, more solvent cells coordinate with nanoparticle cells, and the strong interaction between nanoparticle and liquid tend to keep solvent in the liquid phase. Thereby, the slurry thickness decreases slower as evaporation time increase in the second stage, which is relative to the transition region between two plateaus in the thickness-lg(t) space. In the third stage, the thickness decreases very slow as shown in Figure 4.6. The reason is that the most of the on-surface solvent molecules are evaporated. In this stage, solvent molecules in the dense film should diffuse to the topmost surface first and then can be evaporated. The slow diffusion of solvent in the dense film limits the evaporation rate, so that the decrease of film thickness cannot be observed apparently.

The influence of nanoparticle morphology on the film microstructure is investigated in the present study. The geometric properties of electrode film that consists of spherical active material nanoparticles are shown in Figure 4.7. Similar to electrode with cubical active material nanoparticles, the thickness of dried film increases as the binder length increases when the lower operating temperature ($\kappa T = 0.3$) is used as shown in Figure 4.7(a). For the higher operating temperature ($\kappa T = 0.6$), the thickness is not affected by binder length obviously when the binder length is less than 21 cells.

Generally, the electrode film with spherical active material nanoparticles is thicker than the film with cubical nanoparticles. For the lower operating temperature, the thickness range of films with cubical nanoparticles is from 72.8 to 74.9, while the thickness range of films with spherical nanoparticles is range from 74.7 to 78.2. Similarly, for the higher operating temperature, the thickness of film with cubical nanoparticles varies from 72.6 to 74.0, and that of film with spherical nanoparticles varies from 75.4 to 76.4. The reason is that the cubical particles can form more compact pattern than the spherical particles with the same total volume of nanoparticles.

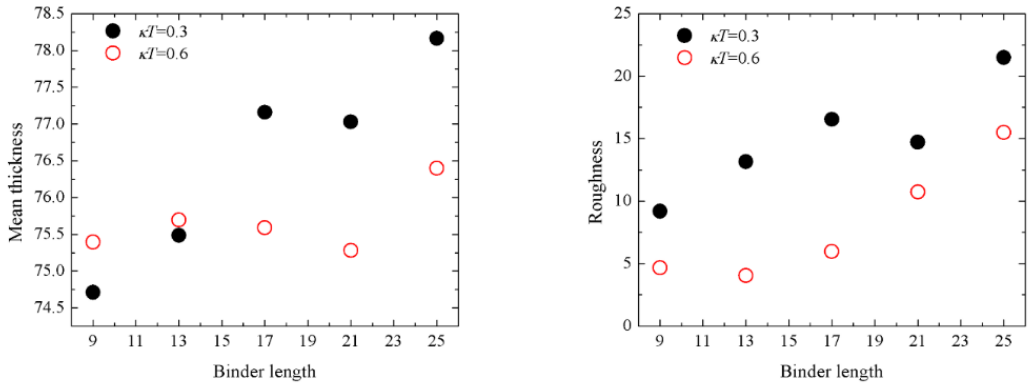

Figure 4.7 Geometric properties of electrode film processed by evaporation with different operating temperature. The mean thickness varies with binder length is shown in (a), and the roughness varies with binder length is shown in (b). The electrode film consists of spherical active material nanoparticles conductive additive nanoparticles and binder.

The surface roughness variation with binder length as well as operating temperature is demonstrated in Figure 4.7(b). It is found that the higher operating temperature processes flatter film that consists of spherical nanoparticles. Additionally, the surface roughness tends to increase as binder length increases at the lower operating temperature, and the surface roughness does not change obviously with $L < 17$ at the

higher operating temperature. All of these phenomena are also observed when the electrode consists of cubical nanoparticles.

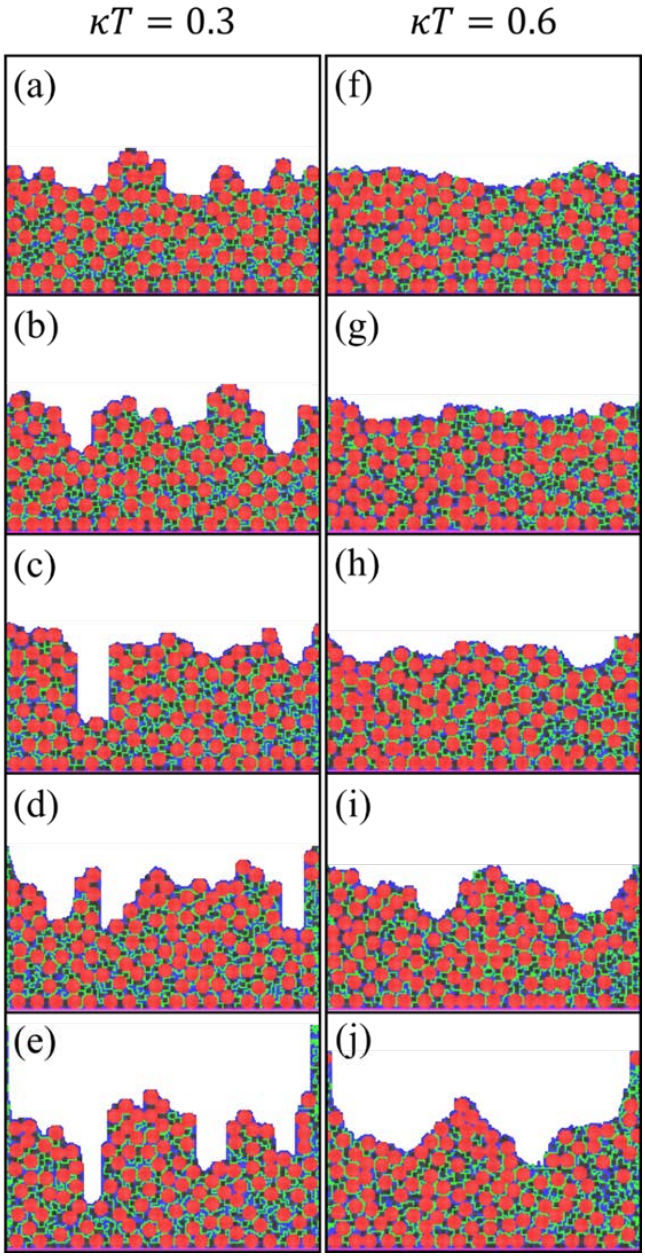

Figure 4.8 Snapshots of electrode films processed by evaporation with (a) ~ (e) low temperature and (f) ~ (g) high temperature. The binder length is increased from 9 cells (top snapshots) to 25 cells (bottom) snapshots. The electrode slurry consists of spherical active material nanoparticles (red), conductive additive nanoparticles (black), semi-flexible binder (green) and solvent molecule (dark blue).

Microstructures of electrode films with spherical nanoparticles are depicted in Figure 4.8. Micropores are observed at the surface of dried film processed by the lower operating temperature ($\kappa T = 0.3$). Figures 4.8(a) ~ (e) clearly demonstrate that the pore depth tends to increases as binder becomes longer, which lead to the increase of surface roughness as shown in Figure 4.7(b). Additionally, the pore diameter in the film with the longer binder (as shown in Figure 4.8(e)) is smaller than that in the film with shorter binder (as shown in Figure 4.8(a)). For electrode processed by the higher operating temperature ($\kappa T = 0.6$), the surface becomes more and more rouged when the binder is longer than 17, which leads to the increase of surface roughness.

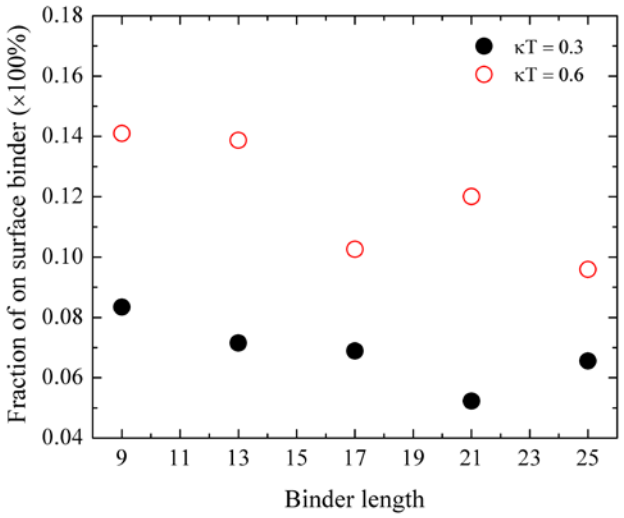

Figure 4.9 Effects of operating temperature and binder length on binder distribution in the electrode film with spherical active material nanoparticles.

The binder distribution along drying direction of electrode film containing spherical active nanoparticles is affected by operating temperature. Similarly to electrode film contacting cubical nanoparticle (Figure 4.3), it is found that fewer binder molecules

migrate to the surface of electrode film when the lower drying temperature is operated as shown in Figure 4.9. Hence, the lower operating temperature is beneficial for keeping more binder molecule in the electrode to improve the mechanical stability of the electrode structure.

The binder conformation in the dried film with spherical nanoparticles is shown in Figure 4.10. It is found that the end-to-end distance *vs*. binder length still follows the power law as shown in Eqn. (4.6). We get $C = 1.67$ and $\alpha = 0.53$ for $\kappa T = 0.3$, and $C = 1.51$ and $\alpha = 0.55$ for $\kappa T = 0.6$. The numerical constant *C* is always larger than 1 because the binder conformation is affected by the nanoparticles in the local microstructure as mentioned above. For the dried film with cubical nanoparticles, the temperature does not affect the *C* constant obviously as shown in Figure 4.6(a). However, for the dried film with spherical temperature, the *C* constant is affected by the temperature more significantly. Thereby, it is observed that the curve with $\kappa T = 0.3$ is higher than the curve with $\kappa T = 0.6$, which indicates that the single chain binder is straighter in the electrode processed by the lower drying temperature. The end-to-end distance normalized by binder length is plotted in Figure 4.10(b). It clearly demonstrates that shorter binder is straighter in the dried film with spherical nanoparticles, which is also observed in the dried film with cubical nanoparticles.

4.3 Conclusions

A morphological-detailed mesoscale (1+1)D CGLG model accompanied by a KMC algorithm is developed to study the influence of processing attributes on microstructure representative of an electrode film in LIB. In particular, the electrode film

microstructure affected by drying temperature and the length of semi-flexible single chain binder is illustrated by the CGLG model. It is found that the geometric properties of the dried film are significantly affected by the operating temperature and the binder length. For electrode film with cubical active material nanoparticles, the mean thickness increases as binder length increases if the film is dried at the lower temperature, but the mean thickness decreases as binder length increases if the film is dried at the higher temperature. It is found that the topography of the film surface is significantly affected by drying temperature and binder length. The film with micropores can be achieved by using the lower drying temperature, and the depth of pores tends to increases as binder length increases. For film processed by the higher drying temperature, the roughness increase can also be obtained by increasing the binder length. However, there are no micropores on the surface of electrode film processed at the higher temperature. The conformation of binder in the dried film is investigated in the present study. The end-to-end distance *vs.* binder length still follows the power law as single chain polymer without interaction with other species. However, the conformation of binder is straightened more or less due to the strong attractive interaction between the nanoparticle and the binder molecule. Additionally, the normalized end-to-end distance demonstrates that the shorter binder is straighter in the dried film. Present computations predict that drying temperature predominantly affects nanoparticle aggregation, and the lower temperature is beneficial for help conductive additive coat on active materials to reduce the electronic conductivity. Additionally, the low drying temperature can restrict binder molecules migrating to the surface of the electrode film, which is helpful for improving the

mechanical stability of the electrode microstructure. The effect of active nanoparticle shape on electrode microstructure is also assessed in the present study. Compared with cubical active nanoparticles, spherical active nanoparticles does not affect the geometric properties of electrode film significantly. For electrode film contacting spherical active nanoparticles, the lower drying temperature is preferred to keep binder molecules in the electrode microstructure to improve the mechanical stability.

CHAPTER V

MECHANISM OF POLYSULFIDES LI_2S_X INTERACTION WITH ELECTRODE SURFACE OF LITHIUM-SULFUR BATTERY*

Sustainable energy presents possibly the greatest challenge, but the greatest potential reward, of our time. The increasing shift towards renewable energy has brought about an urgent need to efficiently store this energy, a need primarily met by lithium-based battery technologies. These batteries, lithium-ion batteries (LIBs) being the most common, benefit from a high energy storage potential compared to other options, due to lithium's low weight and high oxidation potential. In particular, their light weight renders them the best option available for electric vehicles.[64] Lithium-ion batteries are, however, hampered by several drawbacks, such as poor thermal management, low power density, safety concerns, and inadequate stability to charge/discharge cycling, which limit their use. The most prominent issue for their use in electric vehicles is their

* CHAPTER 5 is reprinted with permissions from
(1) "Adsorption of Insoluble Polysulfides Li_2S_x (x= 1, 2) on Li_2S surfaces" by Z. Liu, D. Hubble, P. B. Balbuena, and P. P. Mukherjee, 2015. *Physical Chemistry Chemical Physics*, 17, 9032-9039, Copyright [2015] by The Royal Society of Chemisty.
(2) "Towards Next Generation Lithium-Sulfur Batteries: Non-Conventional Carbon Compartments/Sulfur Electrodes and Multi-Scale Analysis" by A. D. Dysart, J. C. Burgos, A. Mistry, C.F. Chen, and Z. Liu *et al.*, 2016. *Journal of Electrochemical Society*, 163, A730-A741, Copyright [2016] by The Electrochemical Society.
(3) "Evaluating silicene as a potential cathode host to immobilize polysulfides in lithium-sulfur batteries" by Z. Liu, P. P. Balbuena, and P. P. Mukherjee, 2016. *Journal of Coordination Chemistry*, in press (DOI:10.1080/00958972.2016.1184265), Copyright [2016] by Taylor & Francis.
(4) "Li_2S Film Formation on Lithium Anode Surface of Li–S batteries" by Z. Liu, S. Bertolini, P. B. Balbuena, and P. P. Mukherjee, 2016. *ACS Applied Materials & Interfaces*, 2016, 8, 4700-4708, Copyright [2016] by American Chemical Society

intrinsically-limited energy density compared to gasoline. These limitations come primarily from the layered metal oxide cathodes utilized in these systems.

One potential solution is to change the oxidative element from a metal ion to a non-metal, which results in an entirely new battery system.[65, 66] Sulfur (S) is an attractive option in this regard, as it is also low-weight and relatively abundant in the Earth's crust,[67] meaning that Li-S batteries would be neither prohibitively expensive nor take a large toll on the environment. The Li-S system also has a high theoretical specific energy density, rendering it a good fit for implementation in transportation applications.[68, 69] However, Li-S batteries are far from being ready for commercial use. One of the reasons is that the discharge product lithium sulfide (Li_2S) is an electronic and ionic insulator.[70] The theoretical indirect bandgap of Li_2S is 3.297 eV,[71] and its electronic resistivity is larger than 10^{14} cm•Ω. The growth of the insulating product film can cause a sudden death during the discharge process before achieving the theoretical capacity.[72] In order to improve the electrochemical performance of the cathode, some kind of transition metals (TM), such as Fe, Co, Ni, and Cu may be added to the cathode materials to activate the insulating Li_2S.[73-77] Luo *et al.* studied TM-doped Li_2S by a first-principles approach, and it was found that the electronic conductivity can be increased by Li vacancies, and those dopants can lower the vacancy formation energy.[78] They also pointed out that metal-induced gap states (MIGS) are helpful for electronic conductivity.[78] The cathode architecture plays an important role in determining the performance of the Li-S battery.[79] A wide variety of microstructures has been synthesized to develop the performance of the battery.[80-83] A desirable

cathode microstructure should effectively obstruct the dissolution of polysulfide, supply a large conductive area for insulating Li_2S deposition, and facilitate Li^+ ion transport. Furthermore, special microstructure characteristics are required to tolerate the volume expansion induced by lithiation in order to keep the cathode integrity.[84]

The understanding growth of the Li_2S films is of a guiding significance for rational design of novel cathode architectures able to improve the performance of Li-S batteries. The deposition of Li_2S on the substrate affects the porosity of the cathode microstructure, which increases the tortuosity and decreases the effective ionic conductivity and diffusivity.

5.1 Adsorption of Insoluble Polysulfides Li_2S_x (x = 1, 2) on Li_2S Surfaces

In this study, we theoretically investigate the chemical reactions related to the growth of the Li_2S film. The chemical adsorption of insoluble short-chain polysulfide Li_2S_x (x = 1, 2) on crystal Li_2S surfaces and the formation of new Li_2S layer are systematically studied.

5.1.1 Computational Method

In the present work, first-principles calculations are based on density functional theory (DFT)[138, 139] within the plane wave basis set approach [140, 141]. The Vienna *Ab-initio* Simulation Package (VASP)[142, 143] is employed to solve the Kohn-Sham equations, and the projector augmented wave (PAW) method[144, 145] is used to describe the electron-ion interactions. Generalized gradient approximations (GGA) of the Perdew-Burke-Ernzerhof (PBE) functional[146] are used to describe electron-electron exchange correlations. The k-point grid is generated by the Monkhorst-Pack (MP)

technique for the Brillouin zone (BZ) sampling[147]. The energy cut-off for the plane-wave basis set is 500 eV for both the ionic relaxation and static computations, and the Hellman-Feynman forces are less than 0.02 eV/Å for the atomic structure calculation.

The ground state of Li_2S is the antifluorite structure, and the space group is $Fm\bar{3}m$.[71] In a unit cell, S atoms occupy corners and face-centered sites, and Li atoms occupy all tetrahedral sites of the S frame. The atomic structure of the Li_2S unit cell is shown in Figure 5.1(a). All atomic structures are visualized using VESTA[148]. A slab model is used to represent the Li_2S surface. The slab is placed in the middle of a super cell, and 12 Å vacuum is used to remove the influence from the neighbor slab arising from the periodic boundary conditions.

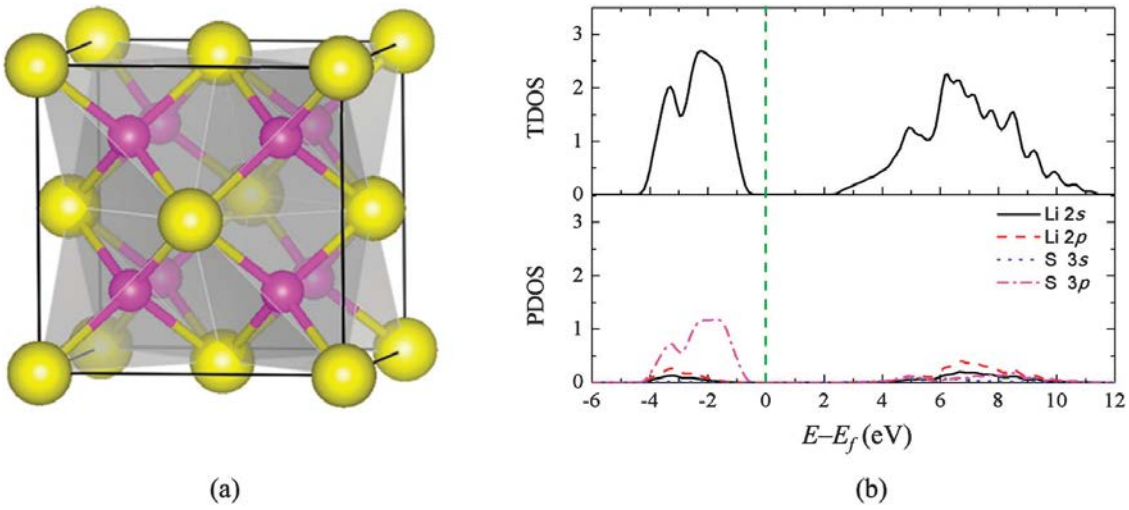

Figure 5.1 (a) Geometric structure and (b) electronic structure of bulk Li_2S. The Fermi level is set to 0 eV in the density of states. Magenta balls in the atomic structure represent Li atoms, and yellow balls represent S atoms.

We calculate the surface Gibbs energy of low index surfaces. For the (001) surface, either a Li layer or an S layer can be the center layer of the slab, and in each case, the termination can also be a Li layer or an S layer. If the (001) surface is terminated

by a Li layer, the ratio of the Li atoms to the S atoms is larger than 2:1, making it a Li-rich structure. If the (001) surface is terminated by an S layer, it is an S-rich structure. For the (110) surface, the ratio of Li to S is always 2:1, so there is only a stoichiometric structure. For the (111) surface, the Li:S ratio is determined by the sequence of the atomic layers, and three structures (stoichiometric structure, Li-rich structure, and S-rich structure) are considered. To find the most stable surface, the surface Gibbs free energy of the each surface structure is calculated. The surface Gibbs energy can be estimated by

$$\gamma = \frac{1}{2A}\left[E^{\text{slab}} - N_s g^{\text{bulk}}_{\text{Li}_2\text{S}} - (N_{\text{Li}} - 2N_{\text{S}}) \times \mu_{\text{Li}}\right]. \quad (5.1)$$

Here E^{slab} represents the total energy of a surface structure, $g^{\text{bulk}}_{\text{Li}_2\text{S}}$ is the energy per Li_2S formula unit in the bulk phase, and μ_{Li} is the energy per Li atom in the *fcc* Li crystal. All of these energies are calculated by the first-principles DFT approach at 0K. In Eqn. (1), *A* represents the surface area of the model, N_S is the number of S atoms in the model and N_{Li} is the number of the Li atoms in the model, respectively. To include realistic battery operation conditions, the applied potential should be considered and Eqn. (1) is rewritten as[149]

$$\gamma = \frac{1}{2A}\left[E^{\text{slab}} - N_s g^{\text{bulk}}_{\text{Li}_2\text{S}} - (N_{\text{Li}} - 2N_{\text{S}}) \times (\mu_{\text{Li}} - eU)\right]. \quad (5.2)$$

Here *U* is the applied potential referenced to the standard Li/Li^+ potential.

The reduction of sulfur is a multistep process during the discharge, and the final product is Li_2S. Generally, solid sulfur (S_8) is reduced to soluble long-chain polysulfides, and then soluble polysulfides are reduced to the insoluble short-chain polysulfides (Li_2S_2 and Li_2S) which deposit on the substrate finally [150]. Solid phase Li_2S_2, as an intermediate product, is converted to Li_2S to lower the total energy of the system [151].

From a thermodynamic aspect, the surface with lowest Gibbs energy per area represents the most stable surface structure. In order to understand the growth of the Li_2S surface, the Gibbs energy difference (adsorption energy) induced by Li atoms and Li_2S_x (x=1, 2) adsorption on stable surfaces is studied in the present work. The Gibbs energy difference is approximated by

$$\Delta G = E(m\mathrm{Li}, n\mathrm{Li_2S_x}) - m\mu_{\mathrm{Li}} - nE_{\mathrm{Li_2S_x}} - E^{\mathrm{slab}}. \quad (3)$$

Here $E(m\mathrm{Li}, n\mathrm{Li_2S_x})$ is the total energy of the substrate with the adsorbate. m and n represent the number of Li atoms and Li_2S_x molecules which are deposited on the substrate, respectively. $E_{\mathrm{Li_2S_x}}$ is the energy of the isolated molecule calculated in a $20 \times 20 \times 20$ Å^3 cubic box. The negative ΔG indicates an exothermic process, which means the chemical reaction happens spontaneously.

5.1.2 Results and Discussion

In the present work, the optimized lattice parameter of crystal Li_2S is 5.72 Å, which is in good agreement with the experimental value of 5.69 Å [152], and with a previous theoretical result 5.71 Å [78]. The single vacancy energy is 3.37 eV, which is the same as Luo's result [78]. The formation energy of bulk Li_2S in our DFT calculation is -8.52 kJ/g. This value is very close to the experimental formation enthalpy -9.40 kJ/g at 298 K [153]. The difference may be in part due to the 0 K temperature used in the DFT calculation. It is well known that Li_2S crystal is an insulator[70] and its indirect bandgap is 3.297 eV [71]. However, no experimental works have been reported related to electronic properties of alkali-metal sulfides. Figure 5.2(b) shows the density of states (DOS) calculated in the present model. It is clear that the difference between the

conduction band minimum (CBM) and valence band maximum (VBM) is about 3.4 eV. Compared to the experimental data and previous theoretical results, it is inferred that the present model is accurate enough to simulate the properties of Li_2S material.

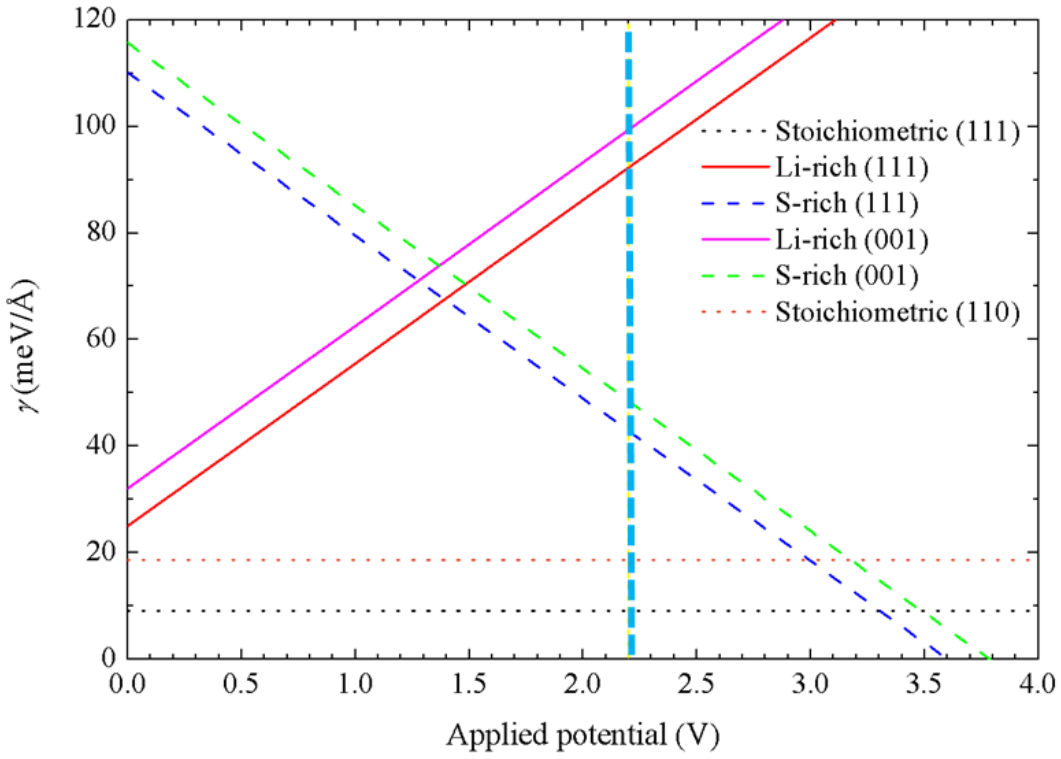

Figure 5.2 . Li_2S surface phase diagram in applied electronic field. The dotted lines represent insulating surfaces, the dashed lines represent p-type conductors, and the solid lines represent metallic-like structures. The vertical line represents the cell voltage of Li-S battery.

The Li_2S surface phase diagram (Figure 5.2) is plotted according to Eqn. (5.2). The phase diagram shows that surface energies of stoichiometric structures are not affected by applied potential because the $(N_{Li} - 2N_S) \times (\mu_{Li} - eU)$ term is zero. It is worth noting that the theoretical cell voltage of the Li-S battery is 2.2 eV [154]. Around this potential, the two most stable surface structures are the stoichiometric (111) and (110) surfaces. This is in agreement with experimental observations. For example, X-

ray diffraction measurements also showed that Li_2S (111) surface and (110) surface had higher intensities than surfaces with other Miller indices [155]. Zhang *et al.* synthesized Li_2S nanoparticles by chemical lithiation, in which the (111) plane with a *d*-spacing of 3.2 Å was observed using high-resolution transmission electron microscopy (HRTEM) [156].

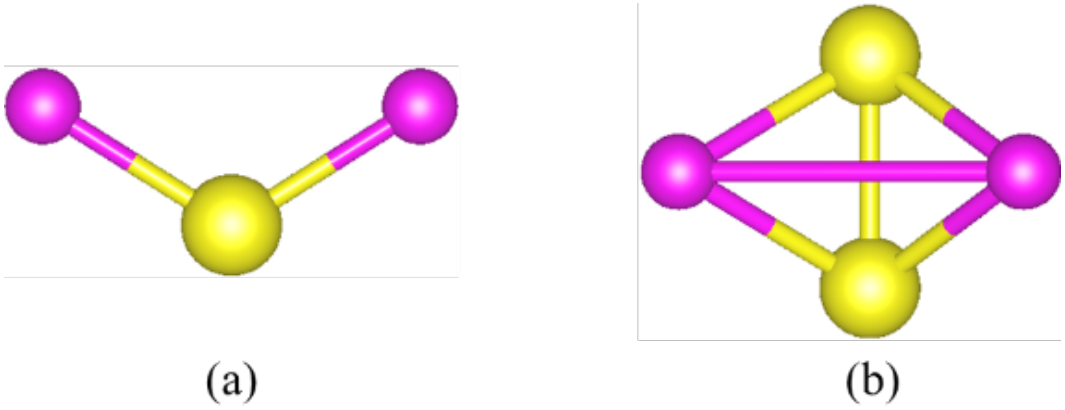

Figure 5.3 Schematic illustration of isolated (a) Li_2S molecule and (b) Li_2S_2 molecule. Violet spheres and yellow spheres represent Li atoms S atoms, respectively.

In order to fundamentally understand the Li_2S growth, we evaluate adsorption of short polysulfide Li_2S_x (x = 1, 2) molecules on the thermodynamically stable surfaces. The molecular structure of isolated Li_2S_x is optimized in a $20 \times 20 \times 20$ $Å^3$ cubic box. The structure of the Li_2S molecule is similar to that of the H_2O molecule (Figure 5.3 (a)). The Li-S bond length of free Li_2S molecule is 2.11 Å and the Li-S-Li bond angle 115.68°. The optimized Li_2S_2 molecule has a tridimensional monocyclic ring structure which point group symmetry is C_s(Figure 3(b)). For optimized Li_2S_2, the Li-S bond length is 2.24 Å, and the S-S bond length is 2.19 Å. The Li-S-S angle is 60.69°, and the dihedral angle with S-S axis is 63.30°. Kao investigated the structures of Li_2S_2 molecule and

related energies by using Gaussian 70, and found that the tridimensional monocyclic ring structure was energetically more stable than other structures[157]. Geometric parameters of Li_2S_2 molecule in the present study agrees well with those in Kao's report. Wang *et al.* studied Li_2S_2 molecular structure with Gaussian 03 [158]. They also found that ground state of Li_2S_2 is a tridimensional monocyclic ring with 2.21 Å Li-S bond length. Geometric parameters of Li_2S_2 molecule in the present study agrees well with those in previous theoretical studies.

First, we would like to discuss the geometric parameters of Li_2S molecule adsorption on the stoichiometric (111) and (110) surfaces. Figure 5.4(a) depicts the optimized configuration of Li_2S adsorption on the (111) surface. The adsorption energy is −1.78 eV. The S atom in the molecule interacts with a Li atom in the top layer of the substrate, and Li atoms in the molecule interact with S atoms in the substrate. The Li-S bond length in the molecule is stretched to 2.18 Å, and the Li-S-Li angle is decreased to 97.55°. The bond length between S in the molecule and Li in the substrate is 2.31Å, which is 0.17 Å shorter than the Li-S bond in the Li_2S crystal. The Li atom in the substrate coordinating with Li_2S molecule is pulled out of the top surface due to the attraction between them. Li atoms in the molecule can also coordinate with S atoms in the substrate, and the related bond length is 2.42 Å. Figure 5.4(b) depicts the optimized configuration of Li_2S molecule adsorption on (110) surface with -2.88 eV adsorption energy. The adsorbed molecule is parallel to the substrate with the Li-S-Li bisector along the $[1\bar{1}0]$ direction. The Li-S bond length of the adsorbed molecule is 2.22 Å, and the Li-S-Li bond angle slightly decreases to 107.18° compared to free Li_2S molecule. The S

atom in the molecule coordinates with two Li atoms in the substrate and the related bond length is 2.38 Å. Li atoms in the molecule also coordinate with S atoms in the substrate with a bond length of 2.34 Å.

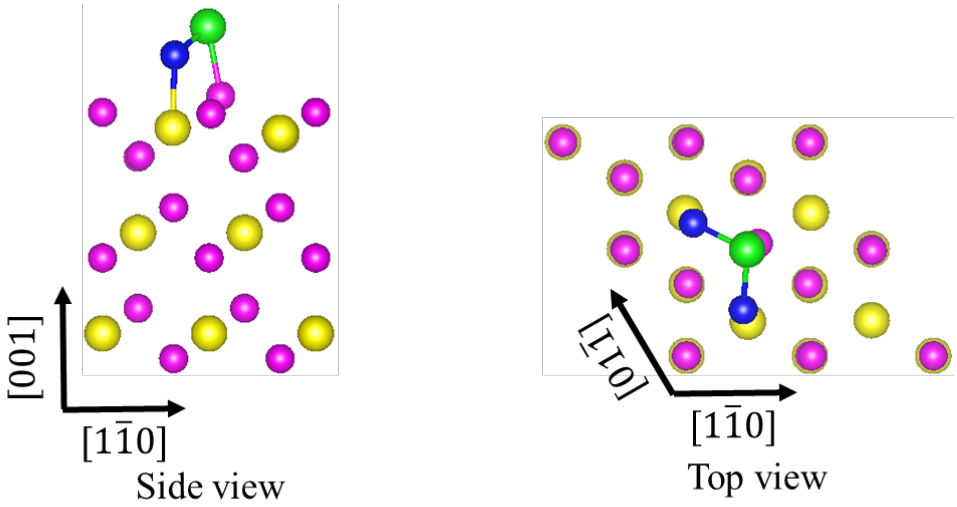

(a) Li_2S molecule adsorption on (111) surface

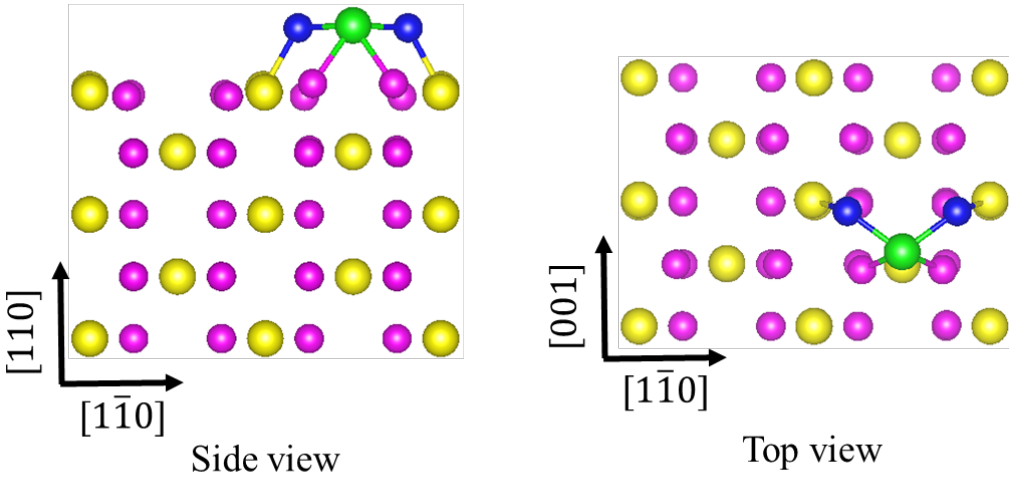

(b) Li_2S molecule adsorption on (110) surface

Figure 5.4 Geometric structures of Li_2S molecule adsorption on (a) (111) surface and (b) (110) surface. Violet spheres and yellow spheres represent Li atoms S atoms in the substrate, respectively. Blue spheres and green spheres represent Li atoms and S atoms in the adsorbate,

Figure 5.5 shows optimized geometric structures of Li_2S_2 molecule adsorption on stoichiometric (111) surface and (110) surface. Li_2S_2 molecule adsorption on (111) surface releases 1.44 eV per molecule. The S-S bond is along $[01\bar{1}]$ direction, and the bond length is 2.16 Å, which approaches S-S bond length (2.19 Å) in free Li_2S_2. The Li atom in the molecule only coordinates with one S atom in the substrate is named Li^{1c} (the blue atom on the left hand of the molecule in Figure 5.5(a), and the other Li atom in the molecule coordinates with two S atoms in the substrate is named Li^{2c} (the blue atom on the right hand of the molecule in Figure 5.5(a)). In the adsorbed Li_2S_2 molecule, Li^{1c}-S bond length is 2.28 Å, and the Li^{2c}-S bond length is 2.32 Å. It is also found that Li^{1c} is much closer to its coordination S atom in the substrate than Li^{2c}. The distance between Li^{1c} and its coordination S atom in the substrate is 2.40 Å, which is shorter than the Li-S bond length 2.48 Å in the bulk phase; while the distance between Li^{2c} and its coordination S atom is longer than 2.74 Å.

For the Li_2S_2 molecule on (110) surface, the adsorption energy is -2.80 eV, which means the (110) surface is more active to accept Li_2S_2 molecule than (111) surface. The optimized configuration of Li_2S_2 adsorption on (110) surface is shown in Figure 5(b). It is interesting that the puckered Li_2S_2 is flattened by the (110) surface. The S-S bond of the adsorbed molecule is along [001] direction with a bond length of 2.17Å. The Li-S bond length in the molecule is stretched to 2.35 Å. Each S atom in the adsorbed molecule coordinates with two Li atoms in the substrate with a Li-S bond length of 2.59 Å, while each Li atom in the adsorbate coordinates with one S atom in the substrate with a Li-S bond length of 2.31 Å.

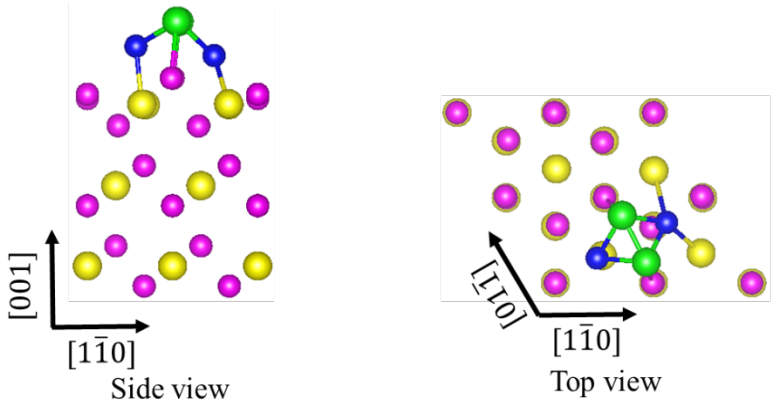

(a) Li_2S_2 molecule adsorption on (111) surface

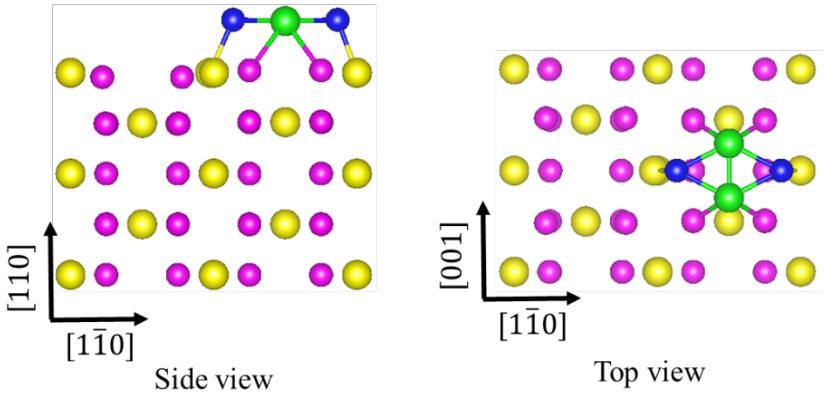

(b) Li_2S_2 molecule adsorption on (110) surface

Figure 5.5 Geometric structures of Li_2S_2 molecule adsorption on (a) (111) surface and (b) (110) surface. Violet spheres and yellow spheres represent Li atoms S atoms in the substrate, respectively. Blue spheres and green spheres represent Li atoms and S atoms in the adsorbate, respectively.

Electronic structures are analyzed in this study to deeply understand the interaction between Li_2S_x and the substrate. Bader Charge Analysis[159] is employed to investigated the amount of charge transferring from the adsorbate to the substrate. Charge transfer induced by adsorption is not observed. The net charge (Q) on adsorbed Li_2S molecules is only about +0.03 |e|, and the adsorbed Li_2S_2 molecules are even

neutral. The slight charge transfer indicates that the adsorbate interacts with the substrate via a strong covalent bond. The charge density difference around adsorbed molecules and their coordination atoms is shown in Figure 5.6. It is obvious that there is an electron accumulation region between a Li (S) atom in the adsorbate and the coordinated S (Li) atom in the substrate, which indicates a typical covalent bond.

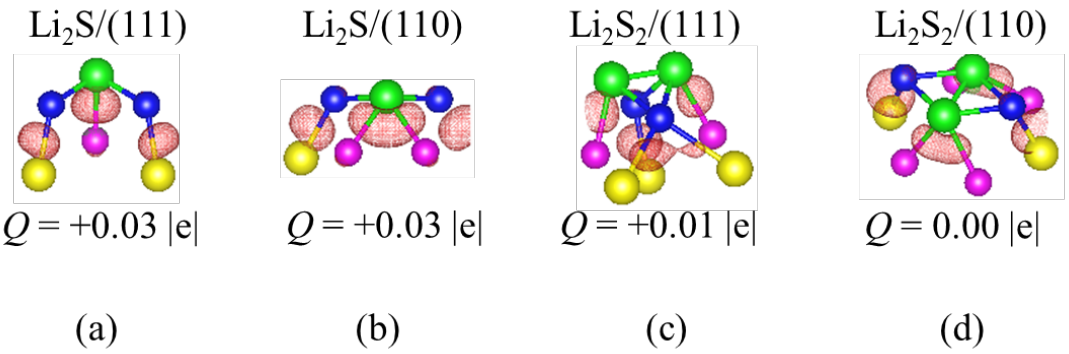

Figure 5.6 Difference charge density of (a) Li_2S molecule adsorption on (111) surface, (b) Li_2S molecule adsorption on (110) surface, (c) Li_2S_2 molecule adsorption on (111) surface and (d) Li_2S_2 molecule adsorption on (111) surface. Violet spheres and yellow spheres represent Li atoms S atoms in the substrate, respectively. Blue spheres and green spheres represent Li atoms and S atoms in the adsorbate, respectively. The red isosurface (0.0035 e/Å^3) represents charge accumulation.

The growth process of the thermodynamically stable surfaces is studied in the present work. To model the growth process, an extra Li-S-Li tri-layer, which follows the layer sequence, is added onto the stoichiometric (111) surface, and a Li_2S monolayer is added onto the stoichiometric (110) surface. For a (2×2) surface unit, both (111) tri-layer and (110) monolayer consists of four Li_2S units. From the initial state to the final state with a new layer, the reaction can be expressed as $8Li+0.5S_8+surface=4Li_2S/surface+\Delta H$. Here ΔH is the energy released during the reaction. Our present calculations predict that the theoretical discharge voltage according

to the reaction is 2.02 eV for both stoichiometric (111) and (110) surfaces. This voltage agrees very well with the lower plateau in the discharge profile of Li/S batteries.[160]

Four reaction paths, shown in Figure 5.7, are designed to deeply understand the growth mechanism of thermodynamically stable surfaces. In Paths (I) and (II), Li_2S_2 molecules and Li atoms are alternatively deposited on the surface. The difference is that Li_2S_2 is first deposited on the surface in Path (I), while Li is first deposited on the surface in Path (II). In Path (III), two Li_2S_2 molecules are deposited on the surface at the first two steps, and then Li_2S_2 deposition is reduced to Li_2S by Li atoms. In Path (IV), Li_2S molecules are deposited on the surface step by step. The Gibbs energy difference (ΔG) of each intermediate state referencing to the initial state is calculated according to Eqn. (3) and shown in Figures 5.9 and 5.10.

(I) Li_2S_2 + surface = Li_2S_2/surface,
$2Li + Li_2S_2/surface = Li_4S_2/surface$,
$Li_2S_2 + Li_4S_2/surface = Li_6S_4/surface$,
$2Li + Li_6S_4/surface = Li_8S_4/surface$;

(II) 2Li + surface = Li_2/surface,
$Li_2S_2 + Li_2/surface = Li_4S_2/surface$,
$2Li + Li_4S_2/surface = Li_6S_2/surface$,
$Li_2S_2 + Li_6S_2/surface = Li_8S_4/surface$;

(III) Li_2S_2 + surface = Li_2S_2 /surface,
$Li_2S_2 + Li_2S_2/surface = Li_4S_4/surface$,
$2Li + Li_4S_4/surface = Li_6S_4/surface$,
$2Li + Li_6S_4/surface = Li_8S_4/surface$;

(IV) Li_2S + surface = Li_2S/surface,
$Li_2S + Li_2S/surface = Li_4S_2/surface$,
$Li_2S + Li_4S_2/surface = Li_6S_3/surface$,
$Li_2S + Li_6S_3/surface = Li_8S_4/surface$;

Figure 5.7 Reaction paths of Li_2S surface growth.

According to Figures 5.9(a) ~ (c), it can be known that Li_2S_2 deposition on the (111) surface at the first step produces a negative Gibbs energy difference, while Li atoms deposition at the first step produces a positive Gibbs energy difference. It is obvious that Path (II) is blocked because Li deposition on the stoichiometric (111)

surface is energetically disfavored. Oppositely, Li_2S_2 can spontaneously adsorb on the stoichiometric surface because of the negative Gibbs energy difference. The Gibbs energy difference between Step 2 and Step 1 in Path (I) is -3.74 eV, which is lower than the difference between Step 2 and Step 1 in Path (III) by 0.57 eV. According to this energy difference, it can be inferred that reducing Li_2S_2 deposition to Li_2S (Path (I)) is energetically more favored than the Li_2S_2 deposition growth (Path (III)). Figure 8(d) shows the Gibbs energy profile of Li_2S molecules deposition on the (111) surface with a stepwise manner (Path (IV)). For Li_2S deposition, the Gibbs energy difference at the first step is -1.78 eV, which is 0.34 eV lower than that of Li_2S_2 deposition at the first step. Additionally, the Gibbs energy difference between the final state and initial state in Path (IV) is also 2 eV lower than that in Path (I).

Figure 5.9 shows the atomic structure of each intermediate state for the (110) surface growth and the corresponding Gibbs energy difference. Similarly to the discussion of (111) surface growth, Path (II) is blocked because Li atoms deposition on the clean (110) surface increases the Gibbs energy of the system as shown in Figure 5.9(b). It is obvious that Li_2S_2 deposition on the clean surface at the first step is energetically favored, and the deposited Li_2S_2 tends to be reduced by Li atoms at the second step (Figure 5.9 (a)). Li_2S deposition on the stoichiometric (110) surface releases 2.88 eV at the first step, which is larger than the energy released by Li_2S_2 deposition at the first step. In addition, the Gibbs energy difference between the final state and initial state in Path (IV) is also 2.08 eV lower than that in Path (I).

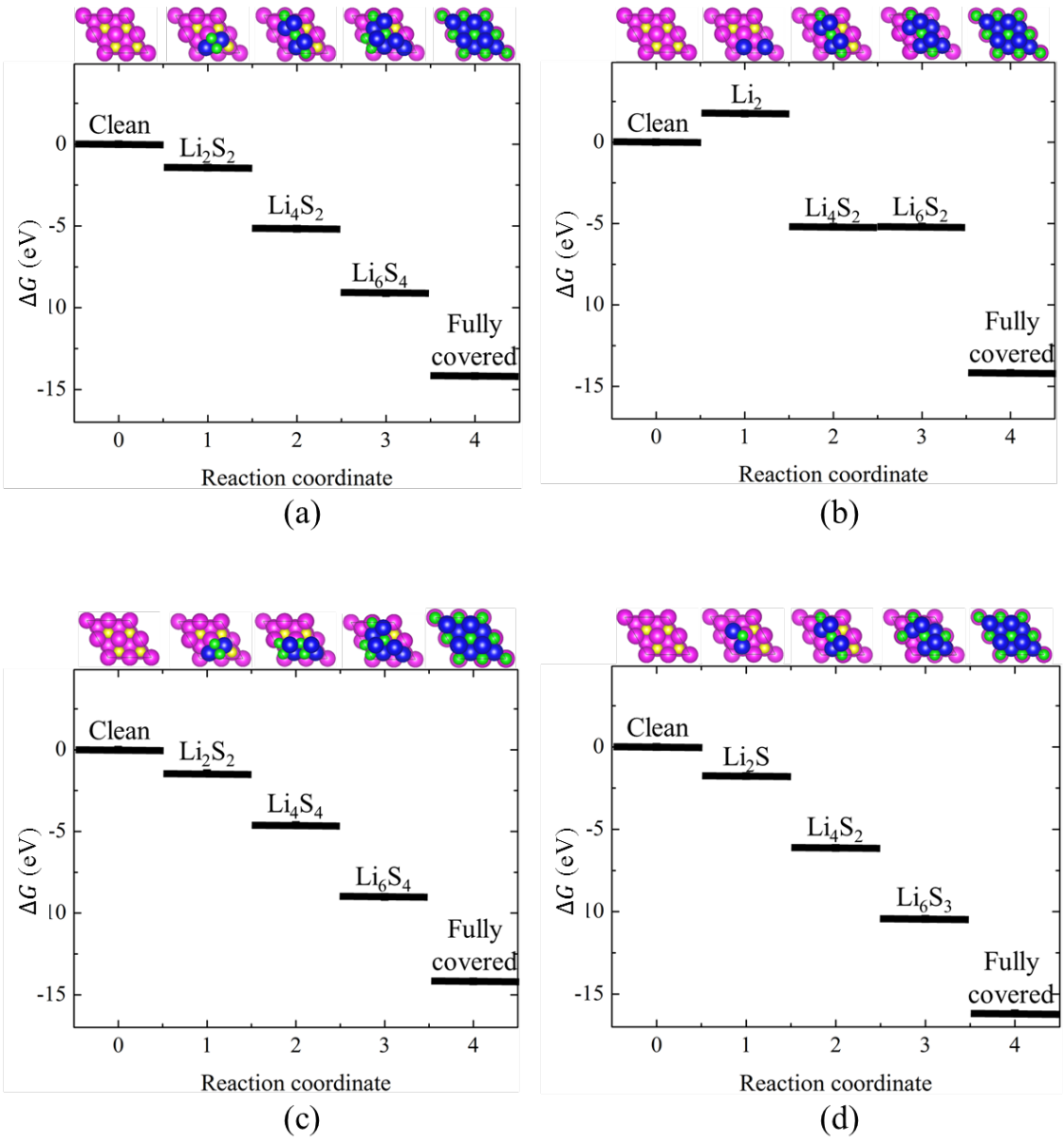

Figure 5.8 Atomic structure of each intermediate state for stoichiometric (111) surface growth and the corresponding Gibbs energy difference referenced to the initial state. Violet spheres and yellow spheres represent Li atoms and S atoms in the substrate, respectively. Blue spheres and green spheres represent Li atoms and S atoms in the deposition.

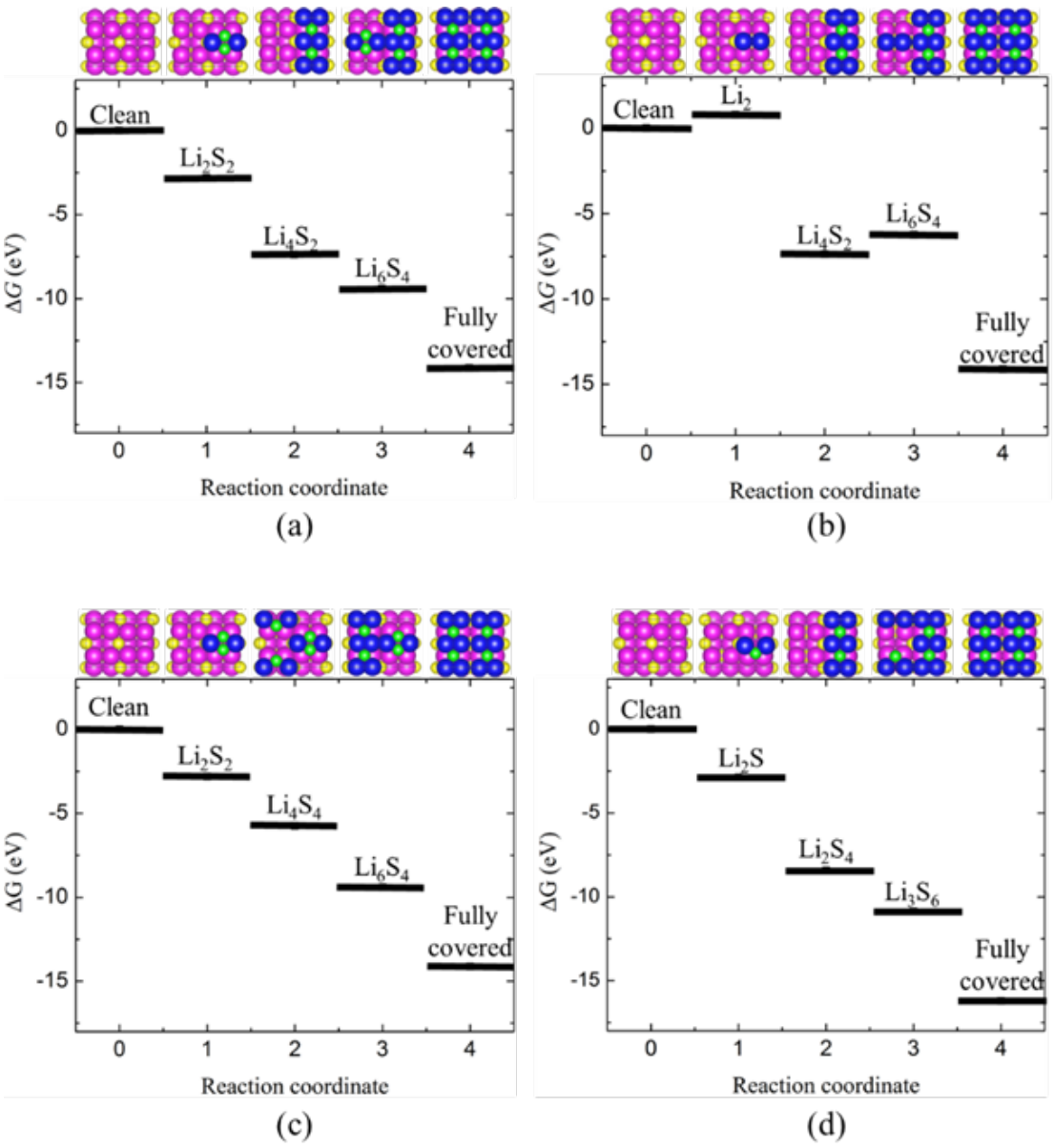

Figure 5.9 Atomic structure of each intermediate state for stoichiometric (110) surface growth and the corresponding Gibbs energy difference referenced to the initial state. Violet spheres and yellow spheres represent Li atoms and S atoms in the substrate, respectively. Blue spheres and green spheres represent Li atoms and S atoms in the deposition.

For the Li_2S surface growing along both (111) direction (Figure 8) and (110) direction (Figure 5.9), the Gibbs energy difference ΔG between the final state (fully

covered structure) and initial state (clean surface and reactants) in Path IV is larger than that of the other three paths. According to Eqn. (5.3), the Gibbs energy difference between final state and initial state is calculated as

$$\Delta G = E_{CV} - \left(E_{CL} + mE_{\mathrm{Li}} + nE_{\mathrm{Li_2S}_x}\right). \quad (5.4)$$

Here E_{CV} is the total energy of the final state (fully covered structure). The summation of terms in the parentheses represents the total energy of initial state. E_{CL} stands for the energy of clean surface, E_{Li} is the energy per atom in pure Li crystal, $E_{\mathrm{Li_2S}_x}$ is the energy of isolated Li_2S_x molecule. Although the final states of these four reaction paths are exactly the same, the initial state of Path IV is different from any other reaction path we considered in the present paper. The reactants in the initial state are four Li_2S molecules in Path IV; while the reactants in other paths are four Li atoms and two Li_2S molecules. Because the full reactions are started from different initial states, different ΔG values are obtained at the final states as shown in Figures 5.9 and 5.10.

In general, our calculations predict that both stoichiometric (111) and (110) surfaces prefer to capture Li_2S_x (x = 1, 2) rather than Li atoms at the first step during the growth. The adsorbed Li_2S_2 tend to be reduced to Li_2S in the following Li adsorption step, because Li adsorption on the Li_2S_2 pre-adsorbed surface releases more energy than Li_2S_2 adsorption on the Li_2S_2 pre-adsorbed surface. In a Lithium sulfur battery, Li_2S_4 can be directly reduced to Li_2S and deposit on the substrate, or it can be reduced to insoluble Li_2S_2 which is reduced to Li_2S in the following reaction [150]. It is reported that direct Li_2S deposition is the predominant reaction and Li_2S_2 deposition/reduction is kinetically slow [150]. This phenomenon is well explained by our theoretical simulation. Although

both Li_2S adsorption and Li_2S_2 adsorption are exothermic reactions, the former one releases more energy. Additionally, the Gibbs energy difference between the final state and the initial state of the direct Li_2S deposition process (Path (IV) in Figure 5.7) is larger than that of the Li_2S_2 deposition/reduction profess (Path (I) in Figure 5.7). From the thermodynamic aspect, the Gibbs energy difference between the products and reactants determines driving for a chemical reaction. Hence, the direct Li_2S deposition is energetically favored due to the larger Gibbs energy difference.

5.1.3 Conclusions

The chemical reactions of insoluble lithium polysulfides on crystal Li_2S surfaces are studied by a first-principles approach. Our simulations demonstrate that stoichiometric (111) and (110) surfaces are the most stable ones around the cell voltage of the Li-S battery. Geometric properties of Li_2S_x molecules adsorption on crystal Li_2S stable surfaces are predicted in this study. It is found that Li_2S_x (x = 1, 2) adsorption on Li_2S surfaces is an exothermic reaction, and Li_2S molecule adsorption releases more energy than Li_2S_2 adsorption. Li_2S (110) surface is more active to interact with Li_2S_x molecules because of the stronger adsorption energy. Electronic structures demonstrate that adsorbates interact with substrates via strong covalent bonds, and the electron transfer from adsorbates to substrates is not observed. The growth mechanism of thermodynamically stable surfaces is investigated in this study. Our result predicts that Li_2S direct deposition on the substrate is energetically more favorable than the Li_2S_2 deposition/reduction process.

5.2 Formation of Li_2S Film on Graphene

5.2.1 Computational Method

The growth of Li_2S film on graphene is studied by a first-principle approach. All calculations ae based on density functional theory (DFT) [138, 139] within the plan wave basis set approach.[140, 141] The Kohn-Sham equations are solved by Vienna *Ab-initio* Simulation Package (VASP).[142, 143] The projector augmented wave (PAW) method[144, 145] is used to describe the electron-ion interactions, and generalized gradient approximations (GGA) of the Perdew-Burke-Ernzerhof (PBE) functional[146] are used to describe electron-electron exchange correlations. The energy cut-off of the plane wave basis set is set to 400 eV. A (3×3) graphene supercell with 16 Å vacuum is used to simulate Li_2S/graphene interaction. The corresponding k-point grid is generated by Monkhorst-Pack (MP) technique for the Brillouin zone (BZ) sampling. The vdW-D3 correction[161] is considered in the present study because van der Waals interaction plays an important role in the interaction between polysulfides molecules and (two-dimensional) substrate.[162]

5.2.2 Results and Discussions

In order to fundamentally understand the Li_2S growth on a carbon substrate, we study the adsorption of polysulfide Li_2S_x (x = 1, 2) molecules on graphene. The adsorption energy (E_{ads}) is calculated to evaluate the attractive interaction between adsorbate and substrate.

$$E_{ads} = E_{Li_2S_x@G} - \left(E_G + E_{Li_2S_x}\right). \tag{5.5}$$

Here $E_{Li_2S_x@G}$ is the total energy of graphene with adsorbed Li_2S_x molecule, E_G is the energy of clean graphene monolayer and $E_{Li_2S_x}$ is the energy of an isolated Li_2S_x molecule. The negative E_{ads} indicates attractive interaction. Our DFT calculations demonstrate that Li_2S molecule adsorption is energetically favored over Li_2S_2 adsorption. The Li_2S adsorption energy is −0.80 eV with considering vdW-D3 correction and −0.55 eV without considering vdW-D3 correction. The ratio of van der Waals interaction (R_{vdW}) is used to estimate its contribution to adsorption energy.[162]

$$R_{vdW} = \frac{E_{ads}^{vdW} - E_{ads}^{no\ vdW}}{E_{ads}^{vdW}}. \quad (5.6)$$

It is found that van der Waals contribution to Li_2S molecule adsorption is about 31%. For Li_2S_2 molecule adsorption on graphene, E_{ads}^{vdW} is −0.76 eV and $E_{ads}^{no\ vdW}$ is −0.39 eV. It is obvious that graphene tends to accept Li_2S molecule rather than Li_2S_2 molecule because Li_2S adsorption releases more energy. The ratio R_{vdW} for Li_2S_2 adsorption is 49%. Thus, it can be inferred that van der Waals interaction makes more contribution to Li_2S_2 adsorption than Li_2S adsorption. Physically this is because the van der Waals contribution is mainly due to S atoms.[162] This trend is also found in case of Lithium polysulfides adsorption on other two-dimensional materials.[162] Our previous study on insoluble polysulfides adsorption on crystalline Li_2S (111) surface demonstrated that Li_2S adsorption releases 1.78 eV,[163] which indicates that crystalline Li_2S surface is more favorable for Li_2S deposition than graphene as substrate.

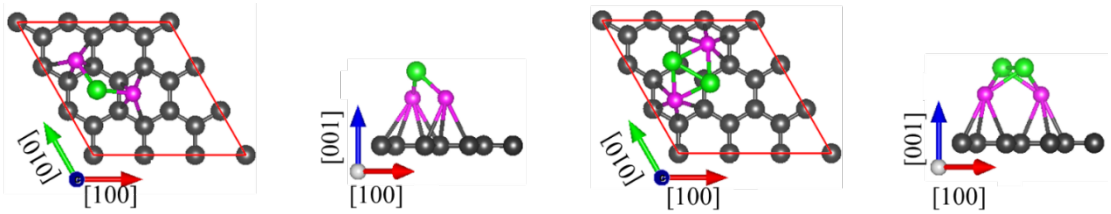

(a) Li_2S adsorption (b) Li_2S_2 adsorption

Figure 5.10 Atomic structures of (a) Li2S molecule and (b) Li2S2 molecule adsorption on graphene. Green, violet and gray spheres represent S, Li and C atoms, respectively.

Table 5.1 Geometric parameters of Li_2S_x on graphene. $\boldsymbol{D_{Li-S}}$ is the Li-S bond length in Li2Sx molecule. $\boldsymbol{D_{S-S}}$is the S-S distance in Li2S2 molecule. ϕ is the Li-S-Li bond angle, and θ is the Li-S-S bond angle. $\boldsymbol{D_{Li-C}}$ is the averaged bond length between Li atoms and their coordinating C atoms.

	D_{Li-S} (Å)	D_{S-S} (Å)	ϕ (°)	θ (°)	D_{Li-C} (Å)
Isolated Li_2S	2.11	--	115.7	--	--
Li_2S@G(3×3)	2.18	--	94.4	--	2.63
Isolated Li_2S_2	2.24	2.19	95.9	60.7	--
Li_2S_2@G(3×3)	2.28	2.11	86.2	62.5	2.68

Atomic structures of Li_2S_x adsorption on (3×3) graphene is depicted in Figure 1. For Li_2S adsorption (Figure 5.10(a)), the Li-S bond length is stretched to 2.18 Å and Li-S-Li bond angle (ϕ) is reduced to 94.4° as shown in Table 5.1. These geometric parameters agree well with the parameters of Li_2S adsorption on crystal Li_2S (111) surface.[163] According to the atomic structure in Figure 5.10(a), it is apparent that Li_2S molecule interacts with graphene via Li-C bond, and the corresponding bond length is 2.63 Å. For Li_2S_2 adsorption (Figure 5.10(b)), the Li-S bond length is stretched to 2.28 Å and the S-S bond is decreased to 2.11 Å due to the interaction with graphene. Similarly

to Li_2S adsorption on graphene, adsorbed Li_2S_2 molecule interacts with graphene via Li-C bond and the corresponding bond length is 2.68 Å.

As mentioned above, the ratio R_{vdW} is less than 50% for Li_2S_x adsorption on graphene. Hence, the chemical interaction is predominant in molecular Li_2S_x-graphene interaction. The electronic structure of Li_2S_x adsorption on graphene is investigated to deeply understand the Li_2S_x-graphene interaction. The distribution of difference charge density induced by Li_2S_x adsorption is demonstrated in Figure 5.11, which is calculated by the following equation

$$\Delta\rho(r) = \rho_{Li_2S_x@G}(r) - \left(\rho_{Li_2S_x}(r) + \rho_G(r)\right), \tag{5.7}$$

where $\rho_{Li_2S_x@G}(r)$ is the charge density in Li_2S_x@graphene system, $\rho_{Li_2S_x}(r)$ is the charge density of isolated Li_2S_x and $\rho_G(r)$ is the charged density of clean graphene with atoms at the same positions as in the in Li_2S_x@graphene system. Electron accumulation regions appear between Li atoms in the adsorbate and C atoms in the substrate as shown in Figure 2. In addition, although interaction with graphene varies charge distribution around S atoms, the electron accumulation region is not observed between S atoms and C atoms. Thereby, it can be inferred that the adsorbate interacts with graphene via strong covalent bonds. The net charge on adsorbed Li_2S_x molecule is estimated by Bader charge analysis.[159] It is found that Li_2S is positively charged by 0.50 |e| after adsorption and Li_2S_2 is positively charged by 0.45 |e|. Hence, the stronger attractive interaction between Li_2S molecule and graphene can also be attributed to the stronger coulomb attraction.

The process of Li_2S layer formation on (3× 3) graphene supercell is simulated by introducing more Li_2S molecules onto the substrate. The Li_2S coverage (Θ) on graphene

in this study is defined as the ratio of the total number of Li and S atoms to the total number of hollow sites in graphene. Hence, $\Theta = \frac{1}{3}$ ML represents a single Li_2S molecule adsorption as discussed in subsection A. $\Theta = \frac{2}{3}$ ML means two Li_2S molecules (or $(Li_2S)_2$) adsorb on graphene and $\Theta = 1$ ML means three Li_2S molecules (or $(Li_2S)_3$) adsorb on graphene.

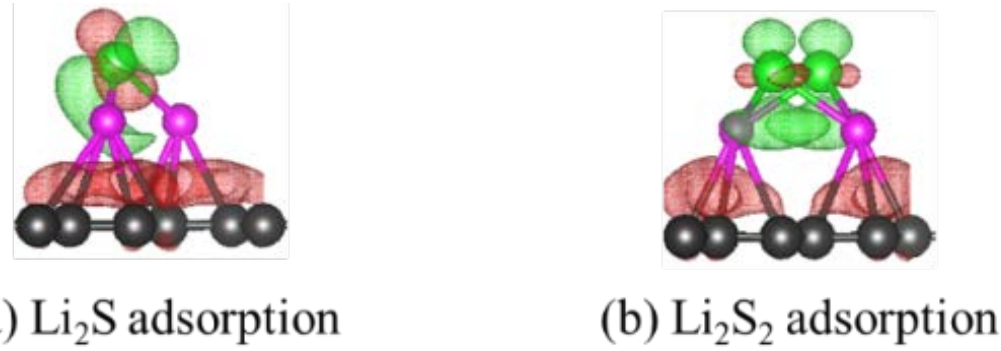

Figure 5.11 Difference charge density induced by (a) Li2S molecule and (b) Li_2S_2 molecule adsorption. Green isosurface indicates electron depletion region and red isosurface indicates electron accumulation region.

For Li_2S adsorption with $\Theta = \frac{2}{3}$, two different configurations are predicted by the present DFT simulations as shown in Figure 5.12, and corresponding energetic and geometric parameters are shown in Table 2. Multiple (3×3) supercells are shown in Figure 5.12(a) to clearly demonstrate the atomic arrangement and periodicity of the resulting structure. It can be seen that S atoms form periodically repeated rectangles, and each S atom is located at the center of small rectangle formed of four Li atoms. From the side view of Structure-I it can be seen that all Li and S atoms are in the same plane, parallel to the graphene monolayer. It is obvious that the atomic structure of Li_2S layer

formed by adsorption with $\Theta = \frac{2}{3}$ is similar to the typical Li_2S (110) layer in Li_2S crystal with anti-fluorite structure (Figure 3(c)). In Structure-I, The Li-S bond length is 2.21 Å, which is 0.27 Å shorter than the Li-S bond in Li_2S crystal according to our previous study.[163] The length of short S-S bridge (D_{S-S}) in Structure-I is 3.70 Å, which is 0.90 Å longer than the S-S distance in typical Li_2S (110) layer. The variation of these geometric parameters is attributed to the lattice parameter mismatch between graphene and Li_2S (110) layer. Multiple (3×3) supercells are shown in Figure 5.12(b) to clearly demonstrate the atomic arrangement and periodicity of the resulting structure. It is interesting that S atoms arrangement in Structure-II is hexagonal, which is similar to S atoms arrangement in typical Li_2S (111) layer (Figure 5.12(d)). In Structure-II, each S atom coordinates with four Li atoms, and the S atom at the center of the S hexagonal disappears compared to the typical Li_2S (111) surface. Hence, Structure-II is a defective Li_2S (111) surface with Li_2S vacancies. The side view of Structure-II also demonstrates that all Li and S atoms are in the same plane parallel to graphene monolayer. In Structure-II, Li-S bond length is 2.24 Å, which is longer than the Li-S bond length in Structure-I, but still shorter than the Li-S bond length in Li_2S crystal. The distance between two neighboring S atoms is about 4.28 Å, which is close to the S-S distance 4.05 Å in typical Li_2S (111) layer.

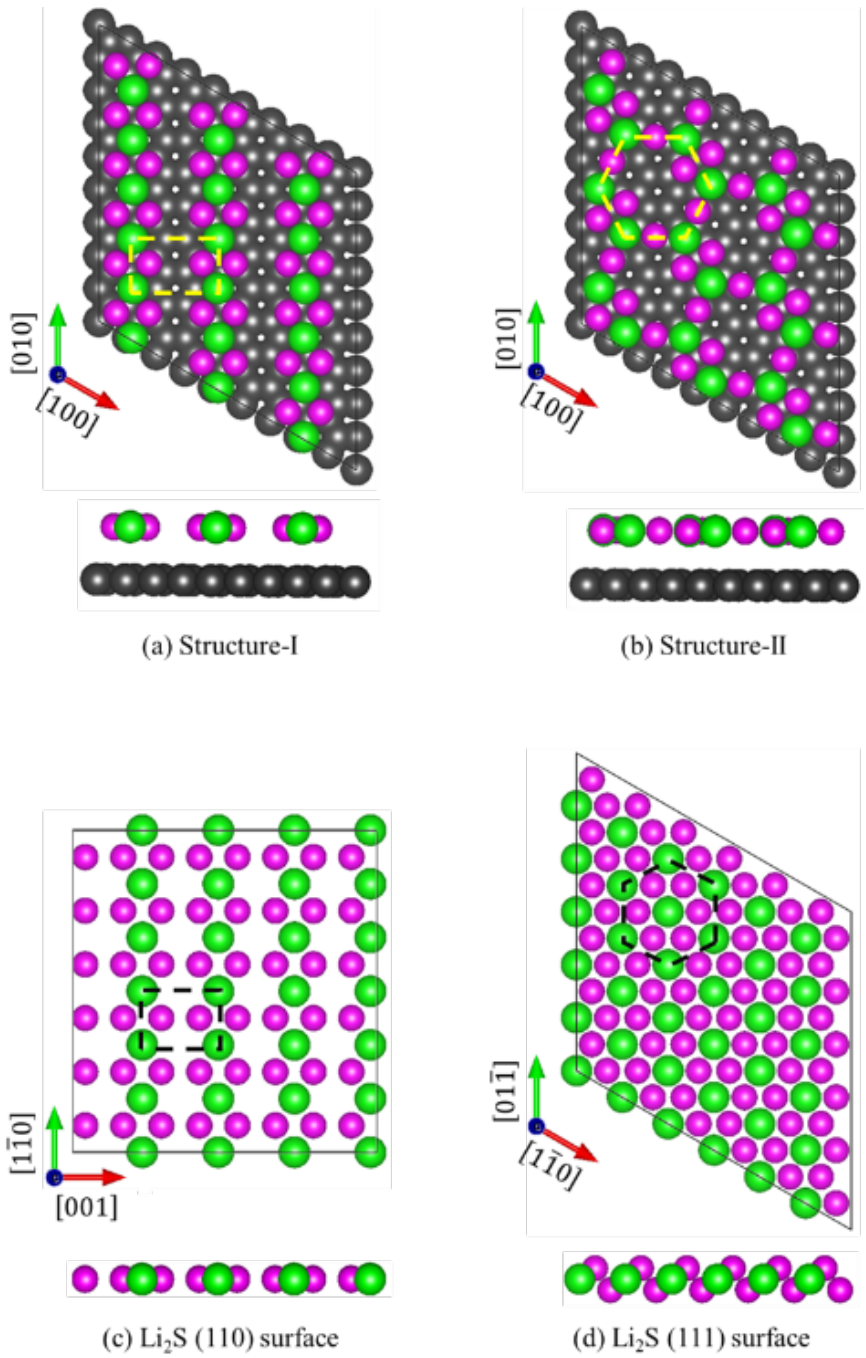

Figure 5.12 Atomic structures of $(Li_2S)_2$ (figures (a) and (b)) on (3×3) graphene supercell and typical Li_2S (110) surface (figure (c)) as well as Li_2S(111) surface (figure (d)). Two structures are observed from computational results. In Structure-I, the arrangement of S atoms is rectangle-like, which is similar to the arrangement of typical Li_2S (110) surface. In Structure-II, the arrangement of S atoms is hexagonal-like, which is similar to the arrangement of typical Li_2S (111) surface.

The thermal stability of Structures-I and II are investigated in the present study. The temperature-dependent Gibbs free energy of a system is calculated by

$$G(T) = H(T) - TS_{vib}(T), \tag{5.8}$$

in which H(T) is the enthalpy and S_{vib} is the vibration entropy which can be estimated by harmonic approximation[164]

$$S_{vib}(T) = \sum_i^{3N-3} \left(\frac{\hbar\omega_i}{\kappa T \cdot exp\left(\frac{\hbar\omega_i}{\kappa T}\right)} - ln\left(1 - exp\left(\frac{-\hbar\omega_i}{\kappa T}\right)\right)\right). \tag{5.9}$$

Here $\hbar$ is the Planck constant normalized by 2π, κ is Boltzmann constant, and $\omega$is the vibration frequency at Gamma point. The temperature-dependent enthalpy is composed by two components as

$$H(T) = E + H_{vib}(T). \tag{5.10}$$

In Eqn. (1.6), E is the total energy of the system calculated by DFT simulation, and H_{vib} is expressed as

$$H_{vib}(T) = \sum_i^{3N-3} \left(\frac{1}{2}\hbar\omega_i + \hbar\omega_i \left(\exp\left(\frac{\hbar\omega_i}{\kappa T}\right) - 1\right)^{-1}\right). \tag{5.11}$$

The Gibbs free energy per unit area is plotted in Figure 5.13. It is can be seen that the Gibbs free energy of Structure-II is lower than that of Structure-I around room temperature (300 K). The energy difference ($\Delta G = G_{II} - G_I$) apparently increases as temperature increases. The Structure-I is only stable at an extremely low temperature (below 100 K).

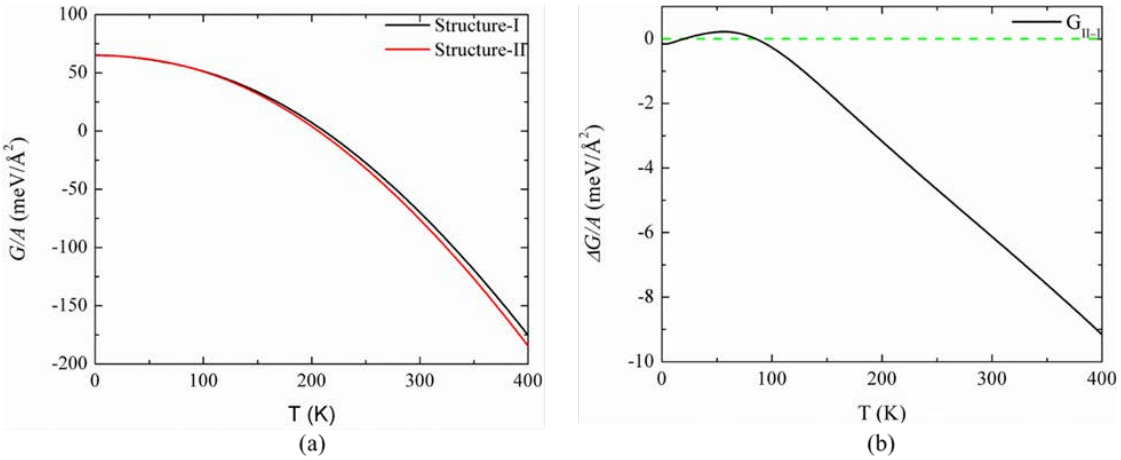

Figure 5.13 Temperature-dependent surface Gibbs free energy of Structure-I and Structure-II.

According to Table 5.2, it is found that the interlayer space between Li_2S layer and graphene in Structure-I is 3.95 Å without considering vdW-D3 correction and 3.49 Å with considering vdW-D3 correction. In Structure-II, the interlayer space is 4.04 Å and with considering vdW-D3 and 3.53 Å without considering vdW-D3. It is obvious that the vdW-D3 correction significant affects the interaction between Li_2S layer and graphene. Interaction energy (E_{inter}) between Li_2S layer and graphene is calculated in the present study to estimate the contribution of van der Waals interaction. The interaction energy is expressed as

$$E_{inter} = E_{(Li_2S)_n@G} - (E_G + E_{(Li_2S)_n}), \tag{5.12}$$

where $E_{(Li_2S)_n@G}$ is the total energy of the system, E_G is the energy of the substrate and $E_{(Li_2S)_n}$ is the energy of the Li_2S layer. According to Table 3, it can be seen that the interaction energy without considering vdW-D3 correction is only -0.03 eV in both Structure-I and Structure-II, which indicates that the chemical interaction between Li_2S layer and graphene is quite weak. However, the interaction energy with vdW-D3

correction is about −0.5 eV, and the ratio of R_{vdW} is about 94%, which indicates that the interaction between Li_2S layer and graphene is dominated by van der Waals interaction.

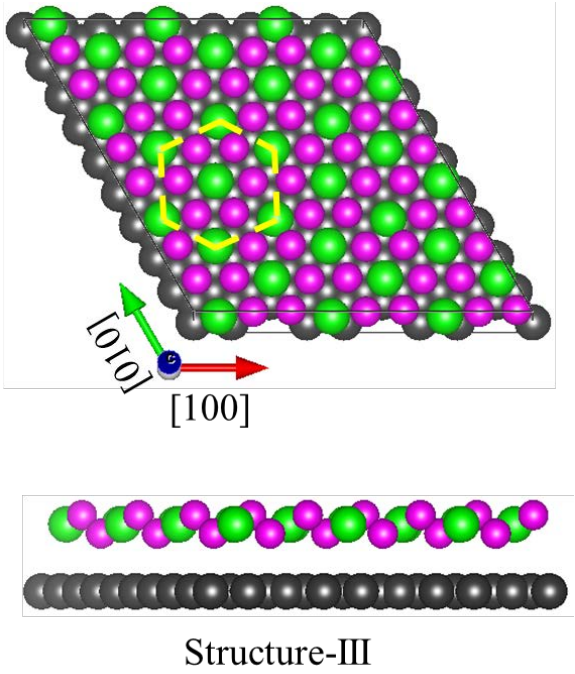

Figure 5.14 Atomic structure of $(Li_2S)_3$ adsorption on (3×3) graphene supercell.

When the Li_2S coverage Θ increases to 1 ML, the complete Li_2S (111) layer named Structure-III appears on graphene as shown in Figure 5.14. It can be seen that the atomic arrangement is exactly the same as the typical Li_2S (111) layer in crystal, and Li atoms are outside S plane. Li-S bond length in Structure-III is about 2.54 Å, which agrees well with Li-S bond length in Li_2S crystal 2.48 Å. The S-S distance in Structure-III is 4.27 Å, which is 0.22 Å longer than that in Li_2S crystal due to the lattice parameter mismatch between graphene and Li_2S (111) layer. According to Table 5.2, it is found that vdW-D3 correction does not affect the geometric parameters, e.g. D_{Li-S} and D_{S-S}, in Li_2S layer. However, the distance between Li_2S layer and graphene in Structure-III is reduced by

0.71 Å with considering vdW-D3 correction. The interaction energy between Li_2S layer and graphene is -0.04 eV without considering van der Waals interaction, which indicates a very weak chemical interaction between the two. However, the interaction energy with considering vdW-D3 correction is -0.66 eV, and the ratio R_{vdW} is 94%.

Table 5.2. Geometric parameters of Li_2S layer on graphene. D_{Li-S} is the Li-S bond length in the Li_2S layer. D_{S-S} is the distance between two neighbor S atoms. H is the interlayer space between graphene and Li_2S layer.

Configuration	D_{Li-S} (Å)		D_{S-S} (Å)		H(Å)	
	No vdW	vdW-D3	No vdW	vdW-D3	No vdW	vdW-D3
Structure-I	2.21	2.22	3.70	3.70	3.95	3.49
Structure-II	2.24	2.25	4.28	4.28	4.04	3.53
Structure-III	2.54	2.53	4.27	4.27	4.41	3.70

[a] $H = \frac{\sum_{i=1}^{M} z_i}{M} - \frac{\sum_{j=1}^{N} z_j}{N}$. z_i is the position of the atom in Li_2S layer, and $z_j$is the position of the atom in graphene. *M* is the total number of atoms in Li_2S layer. *N* is the total number of carbon atoms.

The process of Li_2S (111) formation on graphene is summarized in Figure 5.15 and the corresponding energy profile is plotted. It can be seen that a single Li_2S molecule adsorbs on graphene first with a relative small adsorption energy. The adsorbed Li_2S molecule interacts with graphene via strong covalent Li-C bonds. When introduced one more Li_2S molecule to pre-adsorbed graphene, two configurations, Structure-I and Structure-II, are observed. Structure-I is similar to Li_2S (110) layer and Structure-II is an incomplete Li_2S (111) layer. The thermal stability of Structures-I and II are examined, and it is found that Structure-II is more stable at room temperature. According to Figure

6, it is found that the adsorption energy of introducing one more Li_2S to graphene with pre-adsorbed single Li_2S molecule is more negative than -4 eV. Hence, it can be inferred that the pre-adsorbed single Li_2S molecule is the seed for the formation of Li_2S layer on graphene.

Table 5.3. Interaction energy between Li_2S layer and graphene and the ratio of van der Waals interaction

Configuration	$E_{inter}^{no\ vdW}$	E_{inter}^{vdW}	R
Structure-I	-0.03	-0.52	94%
Structure-II	-0.03	-0.49	94%
Structure-III	-0.04	-0.66	94%

[a] $R = \frac{E_{inter}^{vdW} - E_{inter}^{no\ vdW}}{E_{inter}^{vdW}}$.

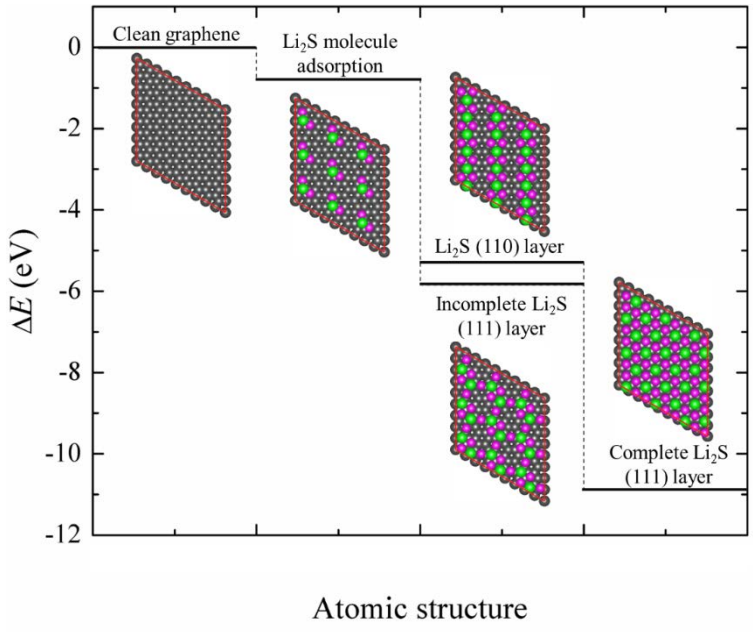

Figure 5.15 Energy profile of Li_2S (111) layer formation on graphene.

5.2.3 Conclusions

The interaction mechanism between Li_2S_x (x = 1,2) and graphene substrate is studied by first-principles calculations. It is found that the adsorption energy of Li_2S molecule on graphene is smaller than that on crystalline Li_2S surface. It can be inferred that Li_2S prefers to adsorb on the pre-deposited Li_2S film in the Li-S battery cathode during the discharge. However, Li_2S adsorption on fresh graphene is still energetically favored. The formation of Li_2S film on the graphene is also studied and the energy profile is calculated. It is found that the formation of Li_2S film is an exothermic process. Defected Li_2S (111) layer will form on the graphene first, and then it will be converted to a perfect Li_2S (111) layer with introducing more Li_2S molecules to the deposited Li_2S layer.

5.3 Silicene as a Promising Host Material in the Cathode of Li-S Battery

In this section, silicone is evaluated as a next generation of cathode host material. In order to improve the performance of Li-S battery, a variety of methods have been developed to inhibit the shuttle effect. In the anode side, alternative anodes are used to replace the metallic Li anode. Zheng *et al.* fabricated a Li-S battery with graphite-based all-carbon anode which achieved 90% Coulombic efficiency for more than 550 cycles, but the discharge voltage was only 1.6 V [165]. Aurbach *et al.* first reported a Li-S battery with Si anode, which achieved a high discharge voltage with poor cycling stability [166]. In addition, Si anode always suffers from extreme volume variation which leads to mechanical degradation. This issue can be mitigated by using nanostructured Si materials as Cui *et al.* suggested [167]. Using electrolyte additives is

an effective way to protect Li metal anode to improve the practical capacity. $LiNO_3$ is a popular additive [168, 169]. It can be reduced to insoluble Li_xNO_y on Li anode surface and oxidize PSs to insoluble Li_xSO_y, both of which serve as protection films to cut off the reactions between Li anode and PSs [170]. However, the protection films grow endlessly with the consumption of the $LiNO_3$ additive, which can increase the electrical resistance [171]. Recently, Wang and his colleagues found that the shuttle effect can be reduced by using fluorinated electrolyte and fluorinated ether as co-solvent [172, 173]. The low solubility of PSs in the fluorinated electrolyte can limit the PSs diffusion from the cathode to the anode, and the fluorinated ether is helpful for a robust protective film formation on electrode surfaces.

In the cathode side, a variety of cathode microstructures has been developed to trap PSs [79, 93-95, 174]. Recently, developing new materials to anchor PSs greatly attracts attentions. A lot of carbon-based materials (*e.g.* porous carbon, graphene nanosheets, and carbon nanotubes) with dopants have been employed to alleviate the shuttle effect because dopant atoms can strongly attract PSs [175-194]. Wang and his colleagues also found that N dopants can activate other functional groups to bind PSs [188, 192-194]. Graphene-based materials are widely used because their two-dimensional (2D) structure can provide large specific surface area for electrochemical reactions. Beyond graphene, 2D polar materials, which have higher PSs affinities, are also applied in Li-S batteries. Nazar and her colleagues used conductive Ti_2C nanosheets as cathode material and achieved high cycling stability [195]. They proposed that the initially adsorbed PSs can be converted to Li_2S with the assistance of electrons

transferred from Ti_2C. Cui and his colleagues achieved a high specific capacity under high rate conditions by using 2D transition metal disulfides as cathode materials [196]. They theoretically investigated the interaction mechanisms between PSs and these 2D substrates by using atomistic simulations, and found that these metal disulfides can strongly attract PSs via chemical bonds [162].

As discussed above, searching materials which have a high specific surface area and strong binding forces with PSs is an effective way to improve the performance of Li-S battery. In the present study, we focus on evaluating silicene as a promising cathode material for Li-S battery. Silicene has a graphene-like 2D structure which has a high specific surface area and zero band gap [197]. A previous theoretical study reported that silicene can facilitate the dissociation of adsorbed O_2 [198]. If silicene can facilitate the dissociation and reduction of PSs, it will be helpful to improve the performance of Li-S battery.

5.3.1 Computational Method

In the present study, all atomistic simulations were performed using Vienna *ab-initio* Simulation Package (VASP) [142, 143] based on density functional theory (DFT) [138, 139] within the plane wave basis set approach [140, 141]. The cut-off energy for the plane wave basis set was set to 400 eV to achieve both the computational accuracy and efficiency. The projector augmented wave (PAW) method [144, 145] was used to describe the electron-ion interactions, and the Perdew–Burke–Ernzerhof (PBE) functional [146] was employed to describe the electron-electron exchange correlations. The *k*-point grids in the Brillouin zone (BZ) were generated by Monkhorst-Pack (MP)

technique [147] with Γ point as the origin. In this study, the silicene (4×4) unit cell with a vacuum of 16 Å thickness was used to study molecular polysulfides Li_2S_x (x = 1, 2, 4) adsorption. The computational experiments to study Li_2S film formation on silicene were conducted on a silicene (2×2) unit cell with 16 Å thickness. The $3 \times 3 \times 1$ k-point grid was generated for (4×4) unit cell and the $6 \times 6 \times 1$ grid was generated for (2×2) unit cell.

Li_2S_x molecules (with x = 1, 2, 4) were considered to study the interaction mechanisms between lithium polysulfides and the silicene substrate. Li_2S is the final discharge product which is insoluble in the electrolyte. Li_2S_2 is an intermediate product which has a low solubility in the electrolyte. Li_2S_4 is a predominant intermediate product with high solubility in the electrolyte. In order to evaluate the strength of interaction between adsorbed PS molecules and silicene, the surface energy was calculated as

$$E_{ads} = \frac{E_{Li_2S_x/surf} - N \times E_{Li_2S_x} - E_{surf}}{N}, \tag{5.13}$$

where $E_{Li_2S_x/surf}$ was the total energy of Li_2S_x adsorption on silicene, $E_{Li_2S_x}$ was the energy of an isolated Li_2S_x molecule calculated in a $20 \times 20 \times 20$ Å^3 cubic box, and E_{surf} was the energy of the clean silicene. According to Eqn. (5.13), a negative adsorption energy E_{ads} indicates an exothermic reaction, and a more negative (or lower) adsorption energy indicates a stronger attractive interaction between the adsorbed Li_2S_x molecule and silicene. The atomistic structure evolution of Li_2S film formation on the silicene was simulated by introducing Li_2S molecules onto silicene (2×2) unit cell with pre-adsorbed Li_2S molecules.

5.3.2 Results and Discussions

Silicene has a honeycomb-like structure which is similar to graphene as shown in Figure 16(a). In the present study, the silicene structure is obtained by optimizing a crystalline silicon (111) monolayer with residual forces less than 0.02 eV/Å on each atom. The optimized lattice parameter for silicene is 3.87 Å and Si-Si bond length is 2.35 Å, which agrees well with previous theoretical results [199, 200]. Figure 5.16(a) depicts that the silicene is buckled because the Si-Si bond is formed by sp^3/sp^2-like hybridization [201]. The silicene lattice can be divided into two sublattices. The sublattice can be identified by Si positions in the *z* direction. Si atoms with higher positions are in sublattice A and atoms with lower positions are in sublattice B. The vertical distance between sublattices A and B is 0.45 Å, which also exactly agrees with previous theoretical results. The conformations of free PSs considered in the present study are shown in Figure 1(b). Geometric properties of these molecules, *e.g.* Li-S bond length and S-S bond length, are also labeled in Figure 5.16(b). These values agree well with results calculated by Gaussian 03 [158].

The effect of dopants on PS-silicene interaction is also studied in this work. Three dopant atoms, nitrogen (N), boron (B) and tin (Sn), are used to substitute Si atoms for generating doped silicene as shown in Figure 5.17. Several experimental studies proved that the performance of Li-S batteries can be improved by N dopants in carbon-based cathodes [184-189]. Recently, experimental studies also found that B-doped graphene as cathode can reduce capacity loss and improve cycling stability because the dopant can

strongly bind with Li_2S [190, 191]. The formation energy for the dopant atom substituting a Si atom is calculated by

$$E_{form} = \left(E_{dp-Silicene} + \mu_{Si}\right) - \left(E_{silicene} + \mu_{dp}\right). \quad (5.14)$$

Here $E_{dp-silicene}$ and $E_{silicene}$ are the energies of doped silicene and pristine silicene. μ_{Si} is the energy per Si atom in the perfect silicene. μ_{dp} is the energy per dopant atom in the stable phase. The formation energies for N, B and Sn substituting are 0.66 eV, 0.71 eV and 1.02 eV, respectively. The positive formation energy indicates a relatively weaker bond between the dopant atom and the adjacent Si atom than the Si-Si bond. The density of states (DOS) of doped silicene is also shown in Figure 5.17. Dopants can induce new peak bridging conduction band and valence band. Hence dopants considered in the present study can increase the electronic conductivity of the substrate.

The energetic and geometric properties of insoluble Li_2S_x (x =1, 2) molecules adsorption on silicene are listed in Table 5.4. Figure 5.18 demonstrates atomistic structures of Li_2S molecule adsorption on pristine and doped silicene sheets. The adsorption energy of Li_2S molecule on pristine silicene is -3.14 eV, which indicates that Li_2S adsorption on silicene releases more energy than adsorption on the crystalline Li_2S surface [98] and graphene [162, 189, 190, 202]. The corresponding atomistic structure demonstrates that the S atom is located at the top of a Si atom in the sublattice A, and two Li atoms are located at the top of two Si atoms in the sublattice B. The Li-S bond is slightly stretched to 2.30 Å. Lin *et al*. studied metal atoms adsorption on silicene, and they found that the single alkaline atom prefers to adsorb at the hollow site [200]. In this

study, we also calculated the adsorption energy with S covering a Si atom in sublattice A and Li covering hollow sites. It is found that the adsorption energy is only 0.1 eV higher than that of the configuration shown in Figure 5.18(a).

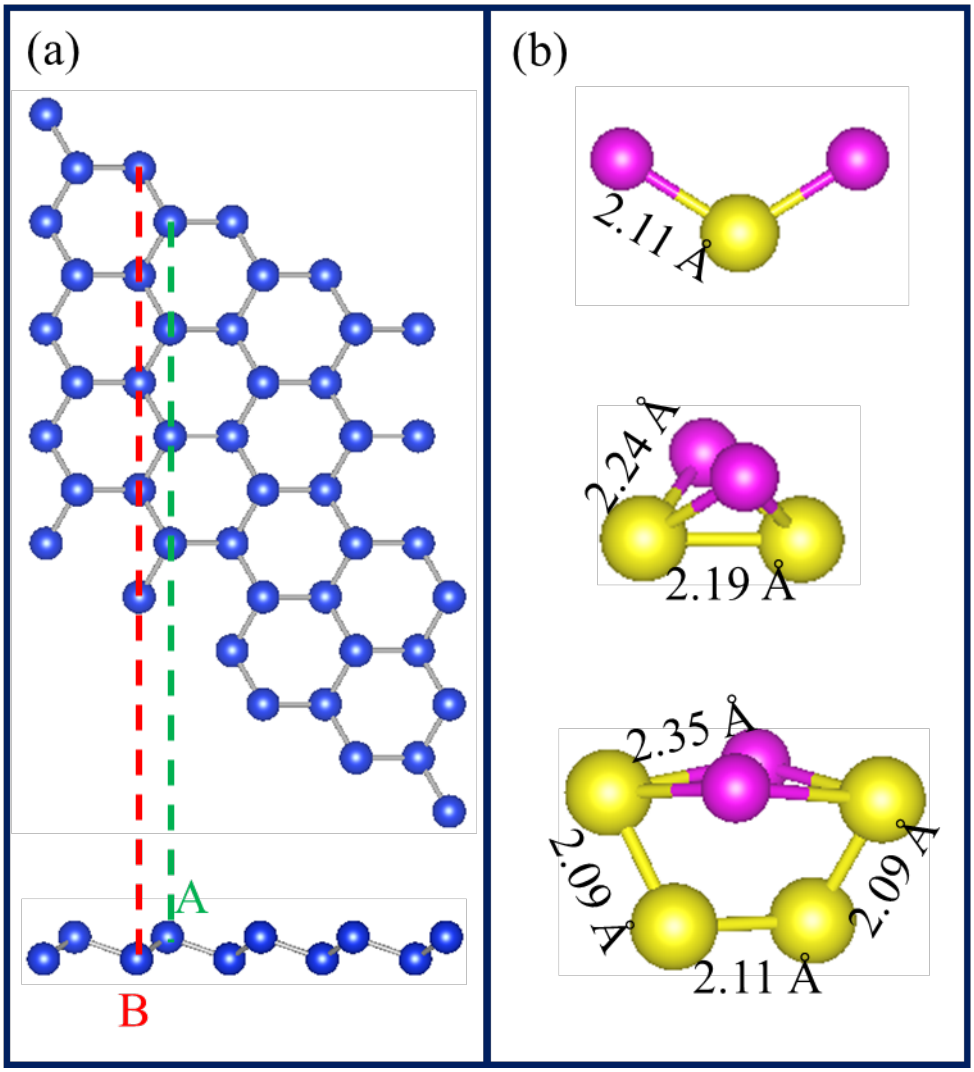

Figure 5.16 Atomistic structures of (a) silicene from top view as well as side view, and (b) free Li_2S_x molecules. Blue balls, violet balls and yellow balls represent silicon atoms, lithium atoms and sulfur atoms, respectively. All atomistic structures in the present paper follow the same color code.

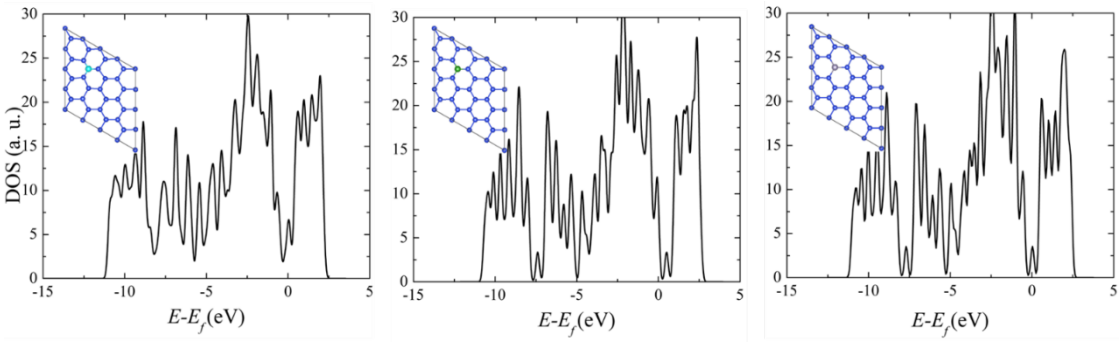

Figure 5.17 Density of states and the atomistic structures of (a) N-doped silicene, (b) B-doped silicene and (c) Sn-doped silicene. The cyan ball, dark green ball and gray ball represent N atom, B atom and Sn atom, respectively. Atomistic structures in the present paper follow the same color code.

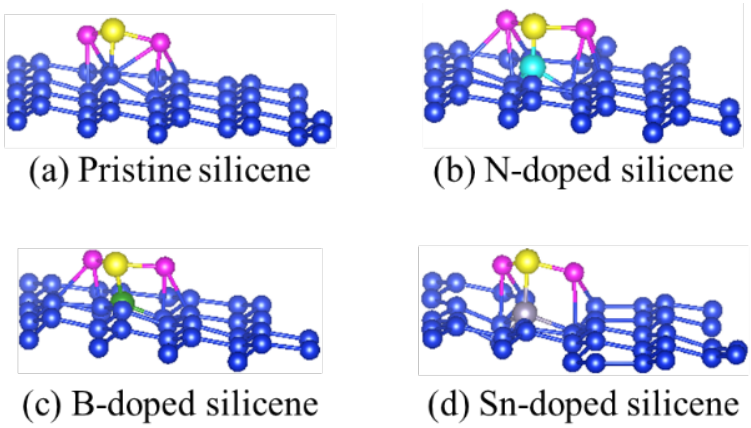

Figure 5.18 Atomistic structures of Li_2S molecule adsorption on (a) pristine silicene, (b) N-doped silicene, (c) B-doped silicecne and (d) Sn-doped silicene. The cyan ball, dark green ball and gray ball represent N atom, B atom and Sn atom, respectively. Atomistic structures in the present paper follow the same color code.

Table 5.4 Energetic and geometric properties of dissoluble Li_2S_x (x=1, 2) adsorption on silicene.

	E_{ads} (eV)	D_{Li-S} (Å)	D_{S-S} (Å)	D_{S-Si} (Å)	D_{S-dp} (Å)
Isolated Li_2S	--	2.11	--	--	--
Li_2S/Silicene	-3.14 (-3.31)	2.30	--	2.15	--
Li_2S/N-Silicene	-0.93 (-1.14)	2.32	--	--	1.84
Li_2S/B-Silicene	-2.63 (-2.92)	2.33	--	--	2.06
Li_2S/Sn-Silicene	-2.82 (-3.02)	2.26	--	--	2.47
Isolated Li_2S_2	--	2.24	2.19	--	--
Li_2S_2/Silicene	-3.09 (-3.45)	2.37	3.80	2.12	--
Li_2S_2/N-Silicene	-4.06 (-4.38)	2.35	4.01	2.12	2.28
Li_2S_2/B-Silicene	-3.32 (-3.49)	2.38	3.76	2.23	2.04
Li_2S_2/Sn-Silicene	-2.69 (-3.06)	2.32	3.84	2.16	2.43

E_{ads} represents the adsorption energy. Numbers in parentheses are the adsorption energies calculated by DFT-D3 approach. D_{i-j} represents the shortest distance between atom *i* and atom *j*. Here *i* and *j* can be either Li, S, Si or dopant atom.

In order to study the effect of dopant on Li_2S adsorption, the Si atom coordinated with S atom is substituted by a dopant atom (N, B or Sn). According to Table 5.4, it is found that substitution atoms weaken the attraction between Li_2S and substrate. For N-doped silicene, the adsorption energy is significantly increased to -0.93 eV. For B-doped silicene and Sn-doped silicene, the adsorption energies are -2.63 eV and -2.82 eV, respectively. The variation of the adsorption energy is dependent on the electronegativity of the dopant. The electronegativity of N is 3.04, followed by B (2.04), Sn (1.96) and Si

(1.90). A higher electronegativity corresponds to a less negative adsorption energy. The dopant atom competes with Li_2S molecule for capturing electron and N can gain more negative charge than other dopant atoms due to its high electronegativity. The Bader charge analysis [203-205] demonstrates that the Li_2S molecule on N-doped silicene is positively charged by 1.33 |e|, followed by Li_2S adsorption on B-doped silicene (positively charged by 0.50 |e|) and Sn-doped silicene (positively charged by 0.08 |e|). It was interesting that there is no obvious electron migration from Li_2S to pristine silicene. The same phenomenon is also observed when Li_2S molecule is adsorbed on crystalline Li_2S surfaces [98].

In order to further understand the interaction between Li_2S molecule and silicene, the charge density difference is calculated to show the adsorption-induced electron redistribution (Figure 5.19). For Li_2S adsorption on pristine silicene, it is clearly observed that an electron accumulation region appears between the S atom and its coordinating Si atom. This electron accumulation indicates a strong S-Si bond. For Li_2S adsorption on Sn-doped silicene, the electron accumulation regions are also observed between S and Sn atoms. However, the volume of the region between S and Sn (Figure 5.19(d)) is smaller than that between S and Si (Figure 5.19(a)). Therefore, the covalent S-Sn bond is weaker than S-Si bond, leading to an increase in adsorption energy. For Li_2S adsorption on N-doped silicene, the electron depletion region is observed between S and N atoms, which indicates a repulsion between S and N atoms (Figure 5.19(b)). Hence Li_2S on N-doped silicene has the highest adsorption energy (-0.93 eV). Electron accumulation regions are observed between Li atoms and Si atoms. Hence Li-Si bonds

also make a contribution for binding Li_2S molecule with silicene. In addition, electron depletion regions appear between Li and S atoms, which indicate that Li-S bond is weakened by the adsorption. Therefor the Li-S bond is stretched after adsorption.

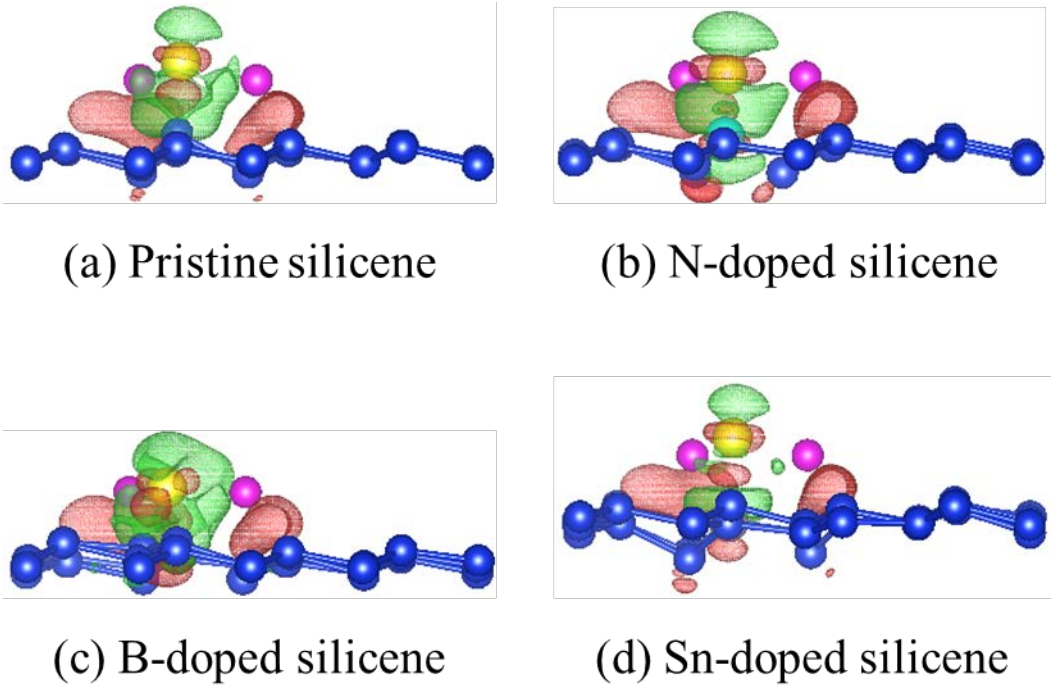

Figure 5.19 Charge density difference of Li_2S molecule adsorption on (a) pristine silicene, (b) N-doped silicene, (c) B-doped silicecne and (d) Sn-doped silicene. The red isosurface (0.003 |e| $Å^{-3}$) indicates the electron accumulation region and the green isosurface (0.003 |e| $Å^{-3}$) indicates the electron depletion region.

The energetic and geometric properties of insoluble Li_2S_2 molecule adsorption on silicene are also listed in Table 5.4. The adsorption energy of Li_2S_2 on pristine silicene is -3.09 eV. The adsorption energy is much lower than Li_2S_2 adsorption on pristine graphene (-0.88 eV) [202]. Li_2S_2 adsorption energy on pristine silicene is slightly higher than Li_2S adsorption on pristine silicene. This trend was also observed when insoluble Li_2S_x (x = 1, 2) adsorbing on pristine graphene [202] and crystalline Li_2S surfaces [98].

The atomistic structure of Li_2S_2 on pristine silicene is depicted in Figure 5(a). Two S atoms are located on the top of two Si atoms in sublattice A. One Li atoms is located on the top of Si in sublatice B, and the other one occupies the hollow site. Li-S bonds are stretched 2.37 Å. As shown in Table 5.4, the S-S distance is 3.80 Å, which is much longer than the S-S bond in a free Li_2S_2 molecule (2.19 Å). It is inferred that S-S bond is broken after Li_2S_2 adsorbing on pristine silicene. Each S atom is negatively charged by 1.9 |e| according to Bader charge analysis. The ion state indicates that S_2^{2-} anion is reduced to two S^{2-} anions by interacting with silicene.

The effect of dopant atoms on Li_2S_2 adsorption is also studied. According to Table 5.4, the N dopant can greatly strengthen the attraction between Li_2S_2 molecule and silicene due to the lowest adsorption energy E_{ads} = -4.06 eV. It is worth noting that the free Li_2S_2 molecule is a closed ring. After Li_2S_2 adsorption on N-doped silicene, the ring is opened as shown in Figure 5.20(b). Li-S bonds are stretched to 2.35 Å ~ 2.43 Å in the adsorbed Li_2S_2 molecule. The distance between the non-connected Li and S atoms is 4.25 Å, which is two times as long as Li-S bond length in a free Li_2S_2 molecule. The S-S distance is 4.04 Å, which indicates that S-S interaction is cut off. It is worth pointing out that there is no S atom directly adsorbed on the top of N-dopant. As show in Figure 5.20(b), one S atom coordinates with two Si atoms and the other S atom coordinate with one Si atom. In this configuration, three Si-S bonds form between the adsorbate and the substrate, which make a major contribution to the significant decrease in adsorption energy. Bader charge analysis shows that S atoms are electron acceptors. The S atom coordinated with two Si atoms is negatively charged by 2.0 |e|, and the S atom

coordinated with one Si atom is negatively charged by 1.9 |e|. According to Table 5.4, it is learned that the B dopant can also decrease the adsorption energy to -3.32 eV. B dopant is also helpful for Li_2S_2 decomposition. As shown in Figure 5.20(c), B dopant can also open the Li_2S_2 ring and cut off the S-S bond. The S atom coordinated with the B dopant is negatively charged by 1.4 |e|. The other S atom coordinated with two Si atoms is negatively charged by -1.9 |e|, which indicates that this S atom capture one electron from the substrate. Similarly with pristine silicene, Sn-doped silicene cannot open Li_2S_2 ring. The S-S interaction is also broken after adsorption, and S atoms accept electrons and are negatively charged by 1.8 |e| ~ 2.0 |e|, which indicates the reduction of S_2^{2-} anion to S^{2-} anions.

Based on the above discussions, we can conclude that silicene is more favorable for binding Li_2S_2 molecules than graphene. In addition, silicene-based material can break the S-S bond and facilitate the reduction of S_2^{2-} to S^{2-}. Among pristine silicene and doped silicene sheets, N-doped silicene is the most attractive candidate for trapping Li_2S_2 because it has the lowest adsorption energy. Additionally, N(or B)-doped silicene can open the Li_2S_2 ring, and facilitate converting Li_2S_2 to Li_2S. The charge density difference is calculated to further understand the interaction mechanism between Li_2S_2 molecule and silicene as shown in Figure 5.21. It can be seen that a significant electron redistribution appears between S atoms and their coordinating Si atoms as well as B/Sn dopants. Electron accumulation regions are observed between S atoms and the substrate. Additionally, electron accumulation regions also appear between Li atoms and Si atoms. Therefore, Li_2S_2 molecules interact with silicene via strong chemical bonds.

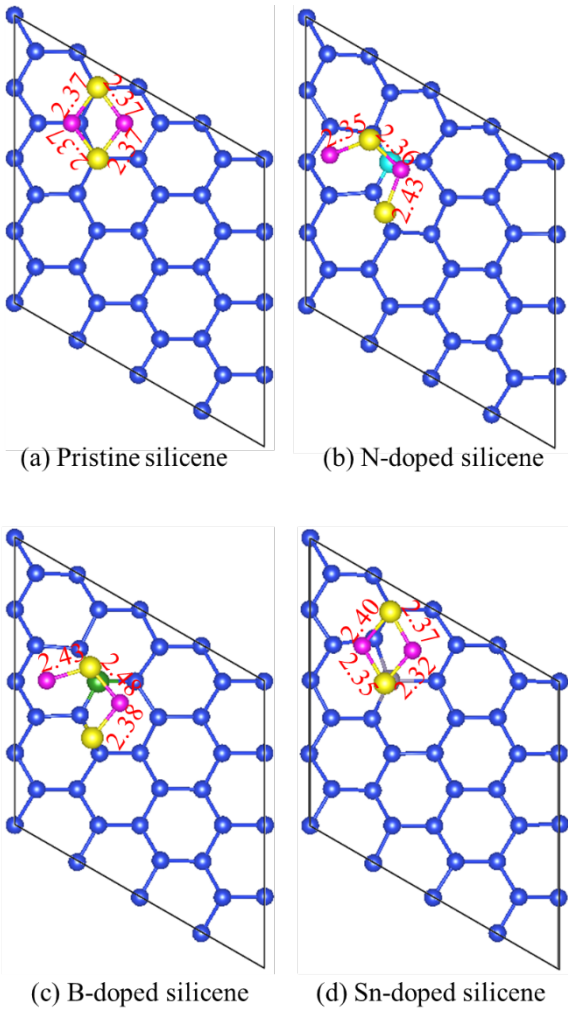

Figure 5.20 Atomistic structures of Li_2S_2 adsorption on (a) pristine silicene, (b) N-doped silicene, (c) B-doped silicene and (d) Sn-doped silicene.

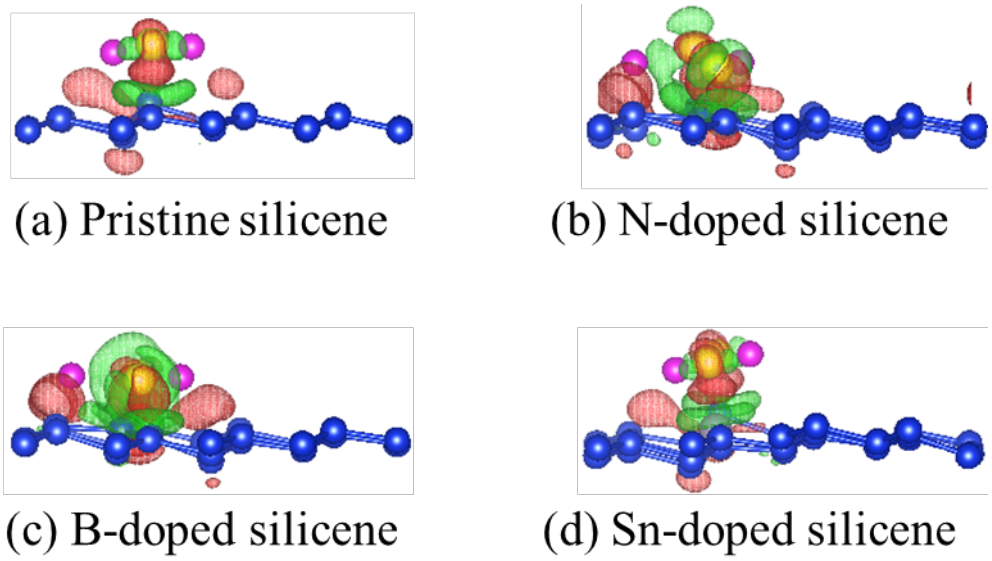

Figure 5.21 Charge density difference of Li_2S_2 molecule adsorption on (a) pristine silicene, (b) N-doped silicene, (c) B-doped silicecne and (d) Sn-doped silicene. The red isosurface (0.003 |e| $Å^{-3}$) indicates the electron accumulation region and the green isosurface (0.003 |e| $Å^{-3}$) indicates the electron depletion region.

The energetic and geometric properties of soluble Li_2S_4 adsorption on silicene are listed in Table 5.5. The adsorption energy of Li_2S_4 on pristine silicene is -1.20 eV. The present simulations demonstrate that the adsorption energy of pristine silicene increases as the number of S atoms in PSs increases. Previous theoretical calculation reported that the adsorption energy of Li_2S_4 on graphene was higher than -1 eV [162]. Hence the silicene can supply stronger attractive force to trap soluble Li_2S_4 in the cathode, which can mitigate the shuttle effect. The atomistic structure of Li_2S_4 adsorption on pristine silicene is shown in Figure 5.22(a). It is interesting that the distance between S_{II} and S_{III} is 3.84 Å, which indicates that the S_4 chain decomposes into two shorter S_2 chains. Li atoms are shared by these two S_2 chains. Bader charge analysis shows that

these two S_2 chains are negatively charged by 1.8 |e|, which indicates the formation of S_2^{2-} anions.

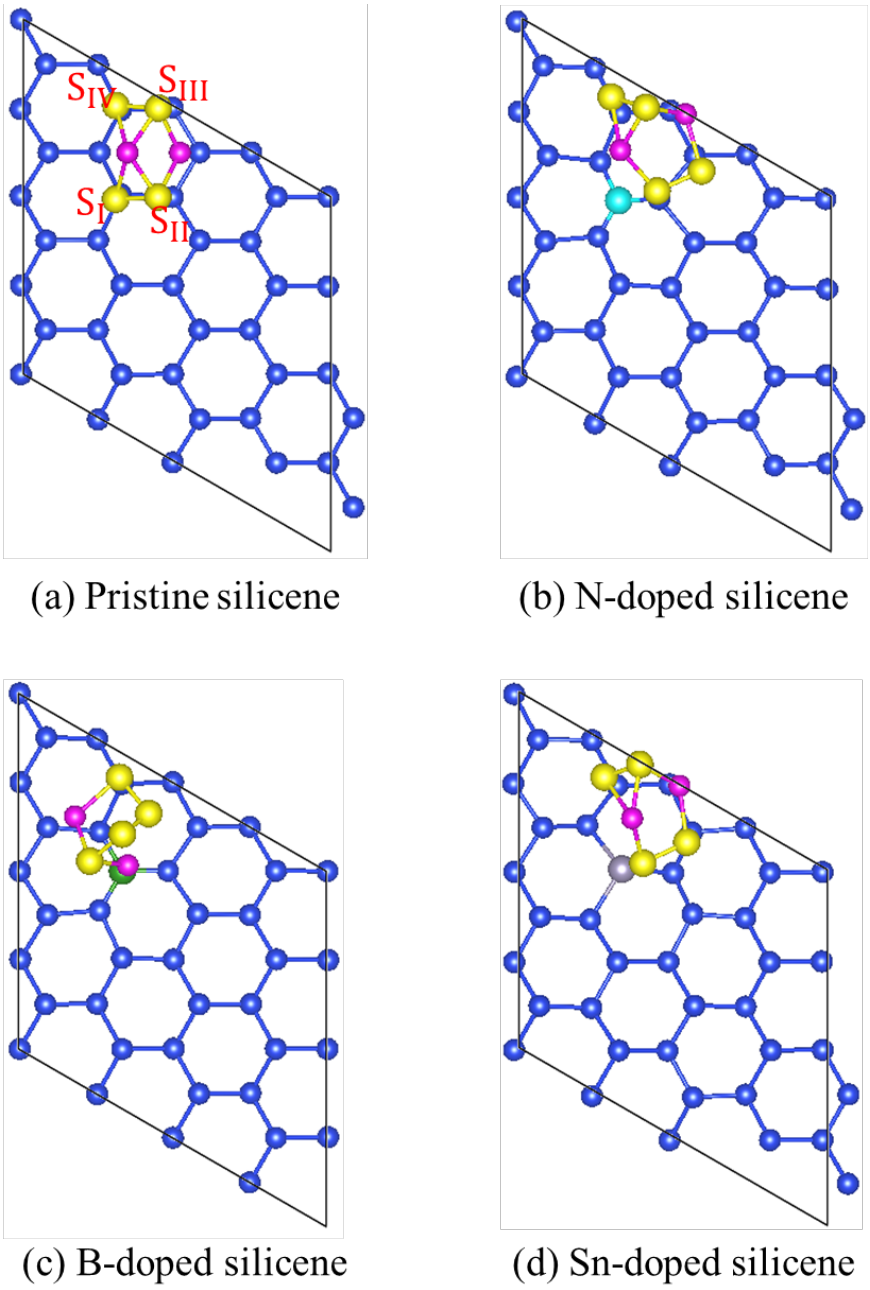

Figure 5.22 Atomistic structures of Li_2S_4 adsorption on (a) pristine silicene, (b) N-doped silicene, (c) B-doped silicene and (d) Sn-doped silicene. S atoms are numbered by Roman numerals from the bottom left one to the top left one in the order of counterclockwise.

Table 5.5 Energetic and geometric properties of dissoluble Li_2S_4 adsorption on silicone.

	E_{ads} (eV)	$D_{S_I-S_{II}}$ (Å)	$D_{S_{II}-S_{III}}$ (Å)	$D_{S_{III}-S_{IV}}$ (Å)
Isolated Li_2S_4	--	2.09	2.11	2.09
Li_2S_4/Silicene	-1.20 (-1.81)	2.07	3.84	2.07
Li_2S_4/N-Silicene	-2.42 (-4.92)	2.11	3.98	2.10
Li_2S_4/B-Silicene	-1.34 (-1.85)	2.07	2.04	2.18
Li_2S_4/Sn-Silicene	-1.92 (-2.59)	2.12	4.12	2.08

E_{ads} represents the adsorption energy. Numbers in parentheses are the adsorption energies calculated by DFT-D3 approach. D_{i-j} represents the shortest distance between atom *i* and atom *j*. Here *i* and *j* can be either Li, S, Si or dopant atom.

Compared with pristine silicene, N-doped silicene doubles the Li_2S_4 adsorption energy. Hence N dopant can further increase the ability to trap the soluble PS. The S_4 chain also decomposes on N-doped silicene because the S_{II}-S_{III} distance rises to 3.98 Å. The S_IS_{II} chain is negatively charged by 2.1 |e|, and the other chain is negatively charged by 2.0 |e|. Sn dopant can decrease the Li_2S_4 adsorption energy to -1.92 eV. On Sn-doped silicene, the S_4 chain also decomposed into two S_2 chains and each of short chains is negatively charged by about 2 |e|. The B dopant can only decrease the Li_2S_4 adsorption to -1.32 eV, and the decomposition of S_4 chain is not observed. Bader charge analysis shows that the sulfur chain still remains as S_4^{2-} anion.

Zhang *et al.* found that van der Waals interaction makes a predominant contribution to the adsorption energies of lithium polysulfides on graphene [162]. In this study, the adsorption energy with the contribution of van der Waals is also calculated by

DFT-D3 method reported by Grimme *et al* [161]. It is found that chemical interactions dominate insoluble polysulfides adsorption on silicene. For Li_2S_4 on N-doped silicene, the adsorption energy with considering van der Waals potential is -4.92 eV. In this case, the chemical interaction and the van der Waals interaction make almost equivalent contributions to the adsorption energy.

The atomistic structure evolution of Li_2S layer formation on pristine silicene is also studied in the present work. The structure evolution is modeled by Li_2S molecules co-adsorption on silicene (2×2) unit cell. Multiple unit cells shown in Figure 8 clearly demonstrate the atom arrangement and periodicity of the resulting structures. Figure 5.23(a) demonstrates the atomistic structure of two Li_2S molecules co-adsorption on silicene (2×2) unit cell and the structure is named Structure-I. In Structure-I, S atoms form periodically repeated rectangles, and each S atom is located at the center of a small rectangle formed of four Li atoms. From the side view of Structure-I, it can be seen that all Li and S atoms are in the same plane which is parallel to the silicene monolayer. It is obvious that the Li_2S layer in Structure-I is similar to the typical Li_2S (110) layer in Li_2S crystal with anti-fluorite structure (Figure 5.23(d)). In Structure-I, the shortest S-S distance is 3.87 Å, which is 0.18 Å shorter than the S-S distance in crystalline Li_2S. The shortest Li-S bond in Structure-I is 2.44 Å, which is also slightly shorter than Li-S bond in crystalline Li_2S. The interfacial energy between Li_2S layer and silicene layer is calculated by

$$E_{intf} = \frac{1}{A}(E_{Li_2S/silicene} - E_{Li_2S}^{layer} - E_{silicene}^{layer}). \quad (5.15)$$

Here A is the interfacial area. $E_{Li_2S/silicene}$ is the total energy of the interface structure. $E_{Li_2S}^{layer}$ is energy of the Li_2S layer, and $E_{silicene}^{layer}$ is the energy of silicene layer. When calculating the energies of Li_2S layer and silicene layer, atoms are in the same positions as in the complete interface structure. The interfacial energy of Structure-I is -77 meV $Å^{-2}$, which indicates that the chemical interaction between Li_2S layer and silicene is much stronger than that between Li_2S layer and graphene [202]. Figure 5.23(b) depicts the atomistic structure of three Li_2S molecules co-adsorption on silicene (2×2) unit cell, which is named Structure-II. It is interesting that S atoms form hexagonal rings which are similar to the arrangement of S atoms in the crystalline Li_2S (111) plane (Figure 8(e)). Compared with a typical Li_2S (111) layer, the Li_2S layer in Structure-II misses a Li_2S unit at the center of the hexagon. Hence the Li_2S layer in Structure-II is a defective Li_2S (111) layer. In this defective layer, the shortest S-S distance is 3.83 Å and the Li-S bond length is about 2.26 Å. The interfacial energy of Structure-II is -74 meV $Å^{-2}$, which is slightly higher than that of Structure-I. Figure 5.23(c) depicts the atomistic structure of four Li_2S molecules adsorption on silicene (2×2) unit cell, which is named Structure-III. In this structure, silicene is completely covered by a Li_2S layer. The arrangement of Li and S atoms in the Li_2S layer exactly follows the arrangement in the crystalline Li_2S (111) layer. The S-S distance in Structure-III is 3.87 Å and the Li-S bond length is 2.35 Å. The interfacial energy of Structure-III is -29 meV Å, which indicates a weaker attractive force between Li_2S (111) layer and silicene than that between Li_2S (110) layer and silicene. The interlayer space between Li_2S layer and silicene layer is also listed in Table 3. It can be found that the interlayer space increases as the interfacial energy

increases. The charge density difference is calculated to analyze the interaction mechanism. Figures 5.25(a) and (b) demonstrate that the Li_2S (110) layer and the defective Li_2S (111) layer chemically interact with silicene via Li-Si bonds and S-Si bonds. However, for the perfect Li_2S (111) layer deposition on silicene, only Li-Si bonds appear in the interlayer space and S-Si bonds disappear. Hence the interfacial energy of Structure-III is higher than the other two cases.

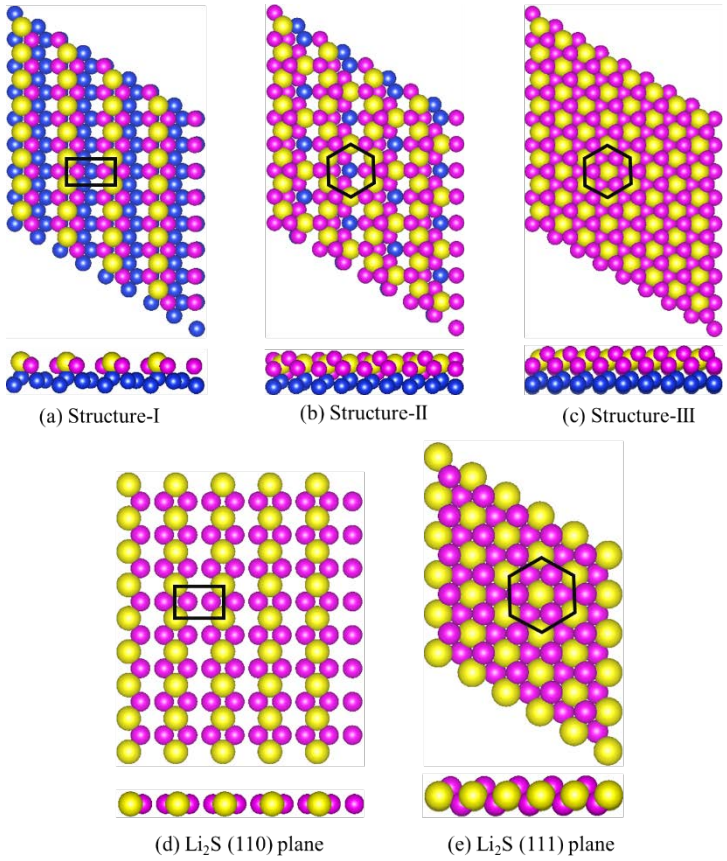

Figure 5.23 Atomistic structure variation of Li_2S layer formation on pristine silicene. (a) Structure-I is modeled by two Li_2S molecules co-adsorption on silicene ($\mathbf{2 \times 2}$) unit cell. (b) Structure-II is modeled by three Li_2S molecules co-adsorption on silicene ($\mathbf{2 \times 2}$) unit cell. (c) Structure-III is modeled by four Li_2S molecules co-adsorption on silicene ($\mathbf{2 \times 2}$) unit cell. The arrangement of Li and S atoms in Structure-I is similar to that in (d) crystalline Li_2S (110) plane. The arrangement of Li and S atoms in Structure-III is similar to that in (e) crystalline Li_2S (111) plane.

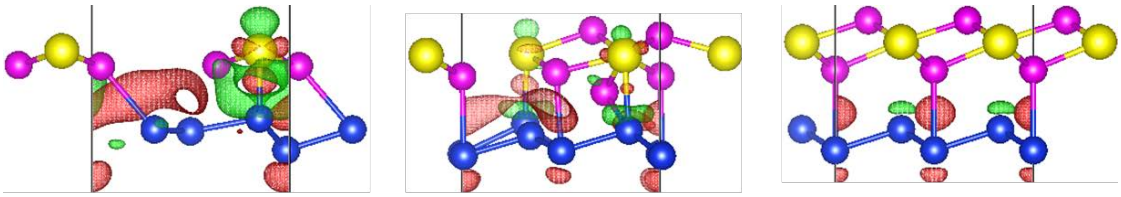

(a) Structure-I (b) Structure-II (c) Structure-III

Figure 5.24 Charge density difference of (a) Structure-I (Li_2S (110) layer on silicene), (b) Structure-II (defective Li_2S (111) layer on silicen) and (c) Structure-III (perfect Li_2S (111) layer on silicene).The red isosurface (0.005 |e| $Å^{-3}$) represents the electron accumulation region and the green isosurface (0.005 |e| $Å^{-3}$) represents the electron depletion region.

Table 5.6 Energetic and geometric properties of Li_2S/silicene interface.

	E_{intf} (meV $Å^2$)	D_{Li-S} (Å)	D_{S-S} (Å)	H (Å)
Structure-I	-77	2.44	3.87	2.41
Structure-II	-74	2.26	3.83	2.65
Structure-III	-29	2.35	3.87	3.22

E_{intf} represents the interfacial energy. Numbers in parentheses are the interfacial energies calculated by DFT-D3 approach. D_{i-j} represents the shortest distance between atom *i* and atom *j*. Here *i* and *j* can be either Li, S, Si or dopant atom.

According to Figure 5.23, it can be inferred that the Li_2S (110) layer will appear on silicene first. With introducing more Li_2S molecules to the substrate, the Li_2S (110) layer will be converted to the Li_2S (111) layer with the defective Li_2S (111) layer as the intermediate state. In Figure 5.24, the energy profile of Li_2S layer formation on silicene is calculated to confirm that the procedure shown in Figures 5.24(a) ~ (c) is energetically favored. The clean silicene is preset as the reference state, and the energy difference ΔE induced by Li_2S deposition is calculated by

$$\Delta E_n = E_n - E_0 - nE_{Li_2S}, \tag{5.16}$$

where n is the number of Li_2S molecules on silicene (2×2) unit cell, E_0 is the energy of the clean silicene, and E_n the energy of silicene with adsorbates. Here n = 1 represents a single Li_2S molecule adsorption on silicene, n = 2 represents the Li_2S (110) layer formation on silicene, n = 3 represents the defective Li_2S (111) layer formation on silicene, and n = 4 represents the perfect Li_2S (111) layer formation on silicene. Figure 5.24 demonstrates that the energy decreases as the number of adsorbed Li_2S molecules increases until the silicene is fully covered. This trend indicates that the formation of Li_2S layer on silicene is an exothermic and thermodynamically favorable process.

5.3.3 Conclusions

In this study, a first-principles approach is used to evaluate silicene as promising cathode material to immobilize discharge products in Li-S batteries. Computational results show that silicene can strongly attract Li_2S_x (x = 1, 2, 4) molecules via chemical bonds. Geometric structures and electronic structures demonstrate that silicene can facilitate the dissociation of PSs and the reduction from S_4^{2-} to S_2^{2-} and S_2^{2-} to S^{2-}. The effect of dopants on PSs adsorption is investigated. It is found that N-doped silicene can further facilitate the adsorption and reduction of intermediate products Li_2S_4 as well as Li_2S_2. Hence silicne-based cathode is an attractive candidate for trapping PSs and mitigating shuttle effect. The atomistic structure evolution of Li_2S layer formation on silicene is also studied. It is found that Li_2S (110) plane first forms on silicene, and then the L_2S (110) layer is converted to Li_2S (111) layer with introducing more Li_2S molecules to the pre-deposited Li_2S layer. The Li_2S layer interacts with silicene via

strong chemical bonds. The energy profile demonstrates that the formation of Li_2S layer on silicene is energetically favorable.

5.4 Li_2S Formation on the Surface of Li Metal Anode

Developing electrolyte additives to protect the Li metal anode surface is another way to improve specific capacity.[206] The most popular additive, $LiNO_3$,[168, 169] is reduced on the Li metal surface to insoluble Li_xNO_y and oxidizes the PSs to insoluble Li_xSO_y, all of which passivate Li anode surface and prevent electron transfer from the Li metal to PSs.[170] However, Zhang reported that the passivation film grows endlessly with the consumption of $LiNO_3$,[171]. In addition $LiNO_3$, can also be irreversibly reduced on the carbon cathode surface, with the products adversely affecting the reversibility and capacity of the battery.

Here we focus on the understanding of Li_2S precipitation on the Li anode surface. We employ a first-principles approach including density functional theory (DFT) to investigate the interaction mechanisms between the insoluble Li_2S molecule and the Li metal surface and the atomic structure evolution during the formation of a Li_2S film on the Li surface.

5.4.1 Computational Method

First-principles calculations are performed using the Vienna *ab initio* Simulation Package (VASP) [142, 143] based on DFT[138, 139] within the plane wave basis set approach.[140, 141] The electron-ion interactions are described by the projector augmented wave (PAW) method,[144, 145] and the electron-electron exchange correlations are described by the Perdew-Burke-Ernzerhof (PBE) functional.[146] The

Monkhorst-Pack (MP) technique[147] is employed to generate k-point grids for the Brillouin zone (BZ) sampling. A 400 eV energy cut-off for the plane-wave basis set is used to achieve both computational accuracy and efficiency. The Hellman-Feynman forces are less than 0.02 eV/Å when optimizing the atomic positions.

For the evaluation of Li_2S adsorption and film formation on the anode surface, slab models with Li (110)-(2×2) surface unit cell (SUC) and Li (111)-(2×2) SUC are employed to represent the Li anode surface. The (110) surface is the close-packed plane of Li crystal with body centered cubic (*bcc*) structure. The (111) surface has a two dimensional hexagonal structure which is similar to the structure of crystalline Li_2S (111) surface. To avoid interactions between consecutive slabs, two adjacent slabs are separated by 16 Å of vacuum. The Li (110) surface model consists of 5 atom layers and the (111) surface model consists of 7 atom layers. The upper three layers are relaxed and the bottom layers are fixed as in the bulk-like positions. Li_2S molecules are placed on the relaxed side of the Li slab where the effect of the induced dipole moment is taken into account by applying a dipole correction.[207]

To evaluate the interaction strength between an adsorbed Li_2S molecule and the Li surface, the surface energy is calculated as

$$E_{ads} = E_{Li_2S@surf} - E_{Li_2S} - E_{surf}, \tag{5.17}$$

where $E_{Li_2S@surf}$ is the total energy of the Li_2S on Li surface, E_{Li_2S} is the energy of an isolated Li_2S molecule calculated in a 20×20×20 $Å^3$ box, and E_{surf} is the energy of the clean surface. A negative E_{ads} represents an exothermic reaction and attractive interaction between the Li_2S molecule and the Li metal surface.

5.4.2 Results and Discussion

Figure 5.25 shows the stable atomic configuration of a Li_2S molecule adsorbed on the Li (110)-(2×2) surface. The atomic structure is visualized by Visualization for Electronic and Structural Analysis (VESTA).[148] Figure 1(a) clearly demonstrates that the Li_2S molecule adsorbs almost parallel to the Li (110) plane. Due to the strong interaction between the Li_2S molecule and the Li substrate, an obvious relaxation of the topmost atom layer of Li (110) surface is observed and the originally flat Li (110) plane is bent. Figure 5.25(b) shows the atom positions projected to the Li (110) surface. It is found that the S atom is located at the bridge site of two adjacent Li atoms in the topmost layer. The bond length between S and Li in the substrate is 2.47 Å (Table 5.7), which agrees well with the 2.48 Å Li-S bond length in crystalline Li_2S.[163] Table 1 also shows the geometric parameters of adsorbed Li_2S on Li (110) surface. It is found that the Li-S bond length of the molecule is stretched to 2.33 Å, and the Li-S-Li bond angle decreases to 86.4°. The adsorption energy of Li_2S on Li (110) surface is -3.22 eV, which is more negative than the adsorption energy of single Li_2S on crystalline Li_2S surface. It can be inferred that the attractive interaction between the Li_2S molecule and the Li (110) surface is stronger than that between the Li_2S molecule and a pre-deposited Li_2S film. This strong attraction between the adsorbate and substrate weakens intramolecular interactions; hence the Li-S bond is stretched.

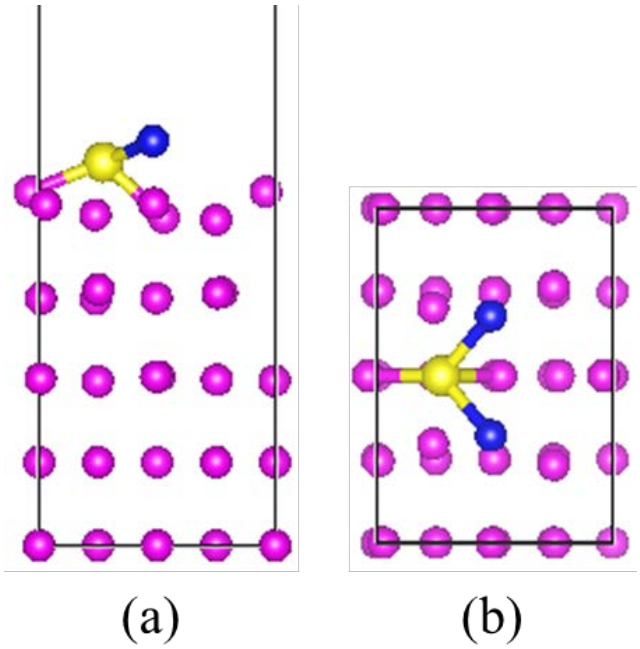

Figure 5.25 (a) Side view and (b) top view of a single Li_2S molecule adsorbed on the Li (110) surface. Yellow spheres represent S atoms. Violet spheres and blue spheres represent Li atoms in the Li metal substrate and adsorbed Li_2S molecules, respectively.

The atomic structure of a Li_2S molecule adsorbed on the Li (111) surface is shown in Figure 5.26. From the side view of the structure it can be seen that the molecule parallels to the substrate (Figure 5.26(a)). Due to the open structure of Li (111) plane, the S atom cannot only interact with Li atoms from the topmost layer but also with a Li atom from the second layer. Figure 5.26(b) clearly shows the positions of atoms in Li_2S projected to Li (111) surface. The S atom is located at the *hcp* hollow site and Li atoms in Li_2S are located at the *fcc* hollow sites. Similarly with Li_2S adsorption on the Li (110) surface, the interaction from the Li (111) surface weakens the intramolecular Li-S bond and stretches the bond to 2.38 Å. The adsorption energy of Li_2S on the Li (111) surface is -3.56 eV, which indicates that the attraction between the Li_2S molecule and the Li

(111) surface is stronger than that on the Li (110) surface. The reason is that the Li (111) plane is not the close-packed plane; hence the Li (111) surface has more dangling bonds which can accept the Li_2S molecule.

It is interesting to compare the adsorption of Li_2S to that of H_2O. Michaelides *et al.* systematically studied single water molecule adsorption on transition and noble metal surfaces, and found that parallel H_2O is the most stable configuration for adsorption on metal surfaces.[208] Since both Li and H are in the first group of the periodic table, and S as well as O belong to the chalcogen group, Li_2S molecule, and H_2O molecule should follow the same mechanism when interacting with metal surfaces. It was found that the molecular orbitals of the adsorbate optimize their mixing with the substrate and become greatly stabilized when the adsorbate lies flat on the metal surface.[208]

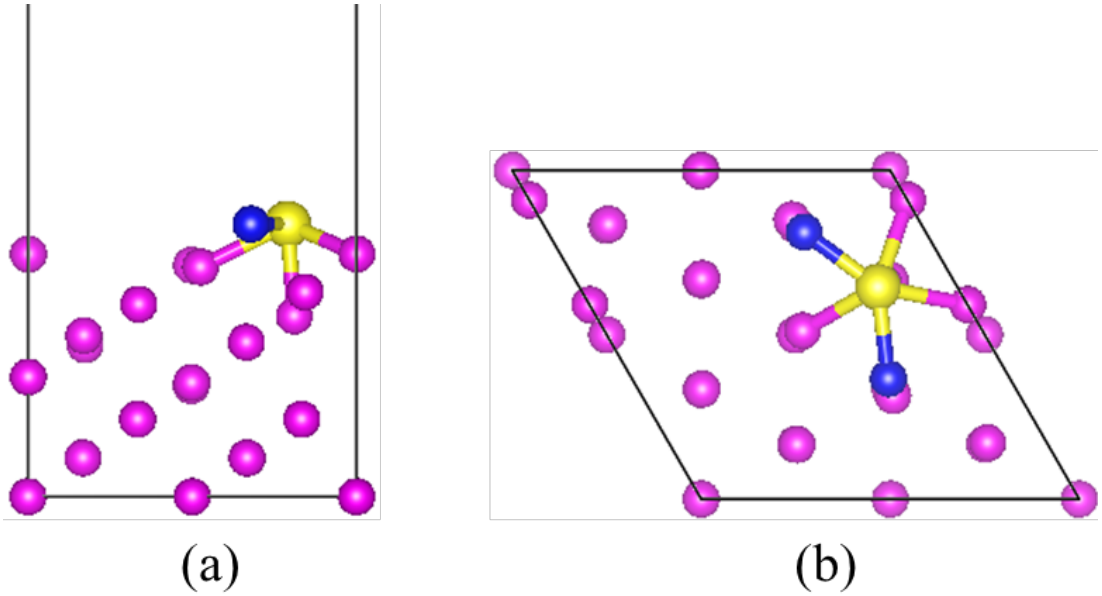

Figure 5.26 (a) Side view and (b) top view of a single Li_2S molecule adsorbed on the Li (111) surface. Yellow spheres represent S atoms.

Table 5.7 Energetic and geometric properties of Li_2S adsorption on Li (110) and (111) surfaces. $\boldsymbol{E_{ads}}$ is the adsorption energy. $\boldsymbol{\theta}$ is the LiSLi bond angle, $\boldsymbol{D^m_{Li-S}}$ is the Li-S bond length in the molecule and $\boldsymbol{D^s_{(Li-S)}}$ is the distance between S and Li atoms of the anode substrate.

Configuration	E_{ads} (eV)	θ (°)	D^m_{Li-S} (Å)	D^s_{Li-S} (Å)
Li_2S@Li(110)	-3.22	85.4	2.33	2.47
Li_2S@Li(111)	-3.57	134.0	2.38	2.47
Li_2S@Li_2S(110)[163]	-2.88	107.2	2.22	2.38
Li_2S@Li_2S(111)[163]	-1.78	97.6	2.18	2.31
Isolated Li_2S[163]	--	115.7	2.11	--

Further analysis of the electronic structures of Li_2S molecule adsorption on the Li metal surface allows a better understanding of the interaction mechanisms. Figure 5.27 depicts the charge density difference of Li_2S adsorption on Li metal surfaces. The charge density difference is calculated by

$$\Delta\rho(r) = \rho_{Li_2S@surf}(r) - \rho_{surf}(r) - \rho_{Li_2S}(r). \quad (5.18)$$

Here $\rho_{Li_2S@surf}(r)$ is the total charge density of the entire system, $\rho_{surf}(r)$ is the charge density of the substrate and $\rho_{Li_2S}(r)$ is the charge density of the substrate. When calculating the charge density of the substrate or adsorbate, atoms are in the same positions as in the complete system. The charge density difference clearly demonstrates that electron accumulation regions appear between S atoms and Li atoms from the substrate. Electron depletion regions also appear between S atom and Li atoms in the adsorbed molecule, which indicate that the intramolecular Li-S bonds are weakened by the Li metal substrate. Electron accumulation indicating strong chemical interactions is

observed between substrate Li atoms and adsorbate Li atoms. According to what we discussed above, it is obvious that both Li and S atoms in the adsorbed Li_2S molecule make contributions to interact with the Li anode surface. In contrast, for the single Li_2S adsorption on graphene, Li_2S only interacts with the substrate via S-C bond, and electron redistribution between Li and C cannot be observed.[209] Bader charge analysis is performed to calculate the net charge of the adsorbate. It is found that the Li_2S molecule acts as the electron donor and the Li metal substrate as the acceptor. For Li_2S adsorption on the Li (110) surface, the adsorbate is negatively charged with 0.39 |e|. On the Li (111) surface, a significant electron migration from the substrate to the adsorbate is observed. The 2*s* orbitals of Li atoms in the adsorbate are fully occupied. This is in contrast with the Li_2S molecule acting as an electron donor when adsorbing on graphene.[209] The different behavior is attributed to the activity of the substrate. The Pauling electronegativity of Li is 0.98 and C is 2.55. Hence, the Li metal is more active to give electrons to the adsorbate than graphene.

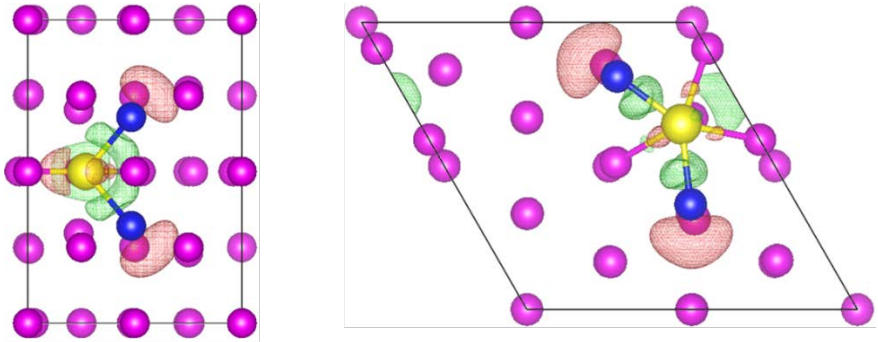

(a) (b)

Figure 5.27 Difference charge density of Li_2S molecule adsorption on (a) Li(110) surface and (b) Li(111) surface. The red isosurface ($\mathbf{3.5 \times 10^{-3}}\ \boldsymbol{e}/\mathrm{Å}^{\mathbf{3}}$) represents electron accumulation and the green isosurface ($\mathbf{3.5 \times 10^{-3}}\ \boldsymbol{e}/\mathrm{Å}^{\mathbf{3}}$) represents electron depletion.

The atomic structure evolution of Li_2S film formation on the Li (110)-(2×2) SUC (shown in Figure 5.28) and on the Li (111)-(2×2) SUC (shown in Figure 5.29) are studied by DFT simulations. The different states during the formation of Li_2S film are represented by co-adsorption of Li_2S molecules. The formation of a Li_2S film on Li (110) surface is discussed first. The stable atomic structure of two Li_2S molecules co-adsorption on the (2×2) SUC is shown in Figure 5.28(a). It can be seen that Li_2S columns appear along the [001] orientation. By periodically extending the atomic structure along the [001] and [$1\bar{1}0$] orientations, we can see that the arrangement of Li and S atoms in the adsorbates is similar to that of a typical Li_2S (110) plane. The Li-S bond length in the Li_2S film is 2.37 Å, and the S-S distance is 3.44 Å, both of which are close to the corresponding values in the crystalline Li_2S (110) plane. However, the distance between two Li_2S columns in Figure 5.19(a) is 9.73 Å, which is 1.7 times of that in a typical Li_2S (110) plane. This significant difference is attributed to the lattice mismatch between the Li (110) and Li_2S (110) planes.

Based on the atomic structure shown in Figure 5.28(a), one more Li_2S molecule is placed on the surface, which means that three Li_2S molecules co-adsorb on the Li (110)-(2×2) SUC. The atom positions after structure optimization are depicted in Figure 4(b). It is interesting that the hexagon consisting of 6 S atoms linked by green lines shown in Figure 5.28(b) appears in the deposited Li_2S film. An S hexagon with an S atom at the center is the feature of the typical crystalline Li_2S (111) plane. The atomic structure shown in Figure 5.28(b) can be an intermediate state during the formation of the Li_2S (111) film. In this intermediate state, the distance between two adjacent S atoms of the

hexagon varies from 3.91 Å to 5.20 Å, and the S-S distance in a perfect crystalline Li_2S (111) plane is 4.05 Å.[209]

Figure 5.28(c) depicts the top view of the stable atomic structure in which four Li_2S molecules are placed on the Li (110)-(2×2) SUC. It is obvious that the S positions projected on to the substrate follow the pattern of S arrangement in the crystalline Li_2S (111) plane as discussed above. In the atomic structure shown in Figure 5.28(c), each S atom is surrounded by six Li atoms and the Li-S distance varies from 2.53 Å to 4.25 Å. The side view of this fully covered Li (110) surface is shown in Figure 5.31. The arrangement of atoms along the normal direction in the deposited Li_2S film is different from crystalline Li_2S (111) plane. In the perfect Li_2S (111) plane, all S atoms are in one layer. However, in the Li_2S film on Li (110) surface, S atoms are distributed into two layers. This Li_2S film can be treated as a Li_2S (111) plane distorted along the normal direction. Previous theoretical and experimental studies demonstrated that the facets of solid Li_2S are dominated by the (111) surface which has the lowest Gibbs free energy.[155, 156, 163, 210] Hence, the distorted Li_2S (111) film formed on the Li (110) surface can be the base for the precipitation of solid Li_2S.

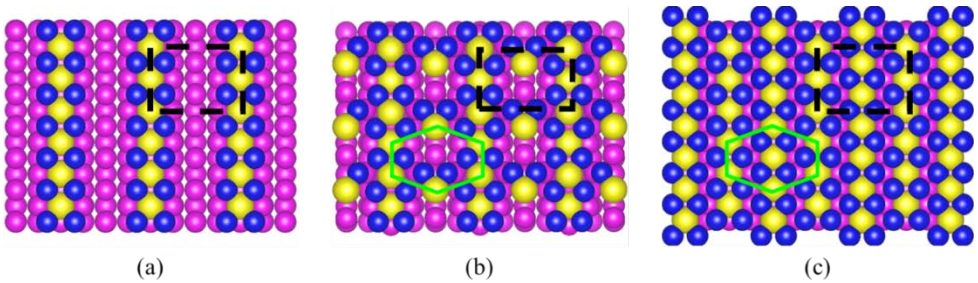

Figure 5.28 Top view of (a) two , (b) three, and (c) four Li_2S molecules adsorption on Li_2S(110)-(2×2) surface unit cell which is marked by a black dash square.

Snapshots in Figure 5.29 demonstrate the mechanism of Li_2S film formation on the Li (111)-(2×2) SUC. Figure 5.20(a) depicts the stable atomic structure of two Li_2S molecules co-adsorption on the surface. It is found that a $(Li_2S)_2$ cluster forms on the Li (111) surface. In the cluster, each Li_2S unit shares one Li atom with its partner, hence each S atom coordinates with 3 Li atoms. The Li-S bond length in the adsorbed $(Li_2S)_2$ varies from 2.30 Å to 2.51Å, which is longer than the Li-S bond length of free Li_2S_x (x = 1, 2) molecule. Figure 5.29(b) depicts the optimized configuration of three Li_2S molecules co-adsorption on Li (111)-(2×2) SUC. In this case, a $(Li_2S)_3$ cluster forms on the anode surface. There are two kinds of S atoms in the cluster: the one coordinated with three Li atoms is named S^{3Li}, and the one coordinated with four Li atoms is named S^{4Li}. Li_2S^{3Li} molecule shares both of its Li atoms with partners, and Li_2S^{4Li} molecules share only one Li with partners. The length of Li-S^{3Li} bonds varies from 2.38 Å to 2.48 Å, and the length of Li-S^{4Li} bonds varies from 2.31 Å to 2.41 Å. Figure 5.29(c) depicts the atomic structure of a fully covered Li (111) surface, which is represented by four Li_2S molecules co-adsorption on the Li (111)-(2×2) SUC. It is clearly shown that the atom positions projected to the surface exactly follow the atomic arrangement in the crystalline Li_2S (111) plane. As evident from Figure 5.29(c), the hexagon consisting of six S atoms can be identified, and the center of the hexagon is occupied by another S atom. Each S atom is surrounded by six Li atoms and the averaged Li-S bond length is around 2.93 Å, which is 0.45 Å longer than the Li-S bond in the Li_2S crystal. The averaged distance between two adjacent S atoms is around 4.86 Å, which is also longer than the S-S distance in the Li_2S crystal by 0.8 Å. These slight differences are attributed

to the lattice mismatch between the Li (111) surface and the Li_2S (111) surface. The atomic positions in the Li_2S film along the normal direction are shown in Figure 5.31(b), which is the side view of Li_2S film/Li (111) interface. It is obvious that the S atoms are in the same layer and the coordinating Li atoms are above and below the S layer alternatively.

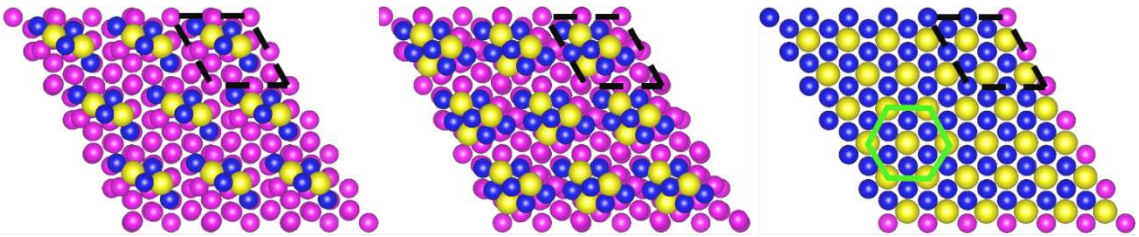

Figure 5.29 Top view of (a) two Li_2S molecules, (b) three molecules, and (c) four Li_2S molecules adsorption on Li_2S(111)-(2×2) surface unit cell which is marked by a black dash parallelogram.

The energy profile of the Li_2S film formation on Li anode is calculated to confirm that the mechanisms shown in Figures 5.28 and 5.29 are thermodynamically favorable. Here the clean surface is preset as the reference state, and the energy difference ΔE induced by Li_2S adsorption is estimated by

$$\Delta E_n = E_n - \left(E_0 + nE_{Li_2S}\right). \quad (5.19)$$

In Eqn. (5.19), E_0 is the energy of the clean surface, E_n is the energy of Li surface with Li_2S adsorbate, and n is the number of adsorbed Li_2S molecules. Here n = 4 represents that the surface is fully covered by the Li_2S film. Figure 5.30 demonstrates that the energy decreases as the number of adsorbed Li_2S molecules increases until the Li surface

is fully covered. This trend indicates that the formation of Li_2S film on Li metal is an exothermic and thermodynamically favorable process. The probability of a Li_2S molecule detachment from the substrate can be estimated by Arrhenius equation

$$P = \exp\left(-\frac{(\Delta E_n - \Delta E_{n+1})}{\kappa T}\right), \tag{5.19}$$

in which κ is Boltzmann constant and T is the temperature. According to the data provided by Figure 5.30, it is found that the detachment probability approaches 10^{-17} at room temperature. This extremely low probability indicates that it is hard to decompose a Li_2S film precipitated on the Li anode surface.

In this study, the interaction between Li_2S film and Li surface is also evaluated by calculating the interfacial binding energy

$$E_{bind} = E_{n=4} - E_0 - E_{Li_2S}^{film}, \tag{5.20}$$

where $E_{Li_2S}^{film}$ is the energy of the Li_2S film. The interfacial binding energy of the distorted Li_2S (111) film on Li (110)-(2×2) SUC is -5.22 eV and that of the Li_2S (111) film on Li (111)-(2×2) SUC is -4.06 eV. These binding energies indicate strong chemical interactions between the Li_2S film and the anode surface. To verify this argument, the difference charge density of Li_2S film/Li anode interface is generated as shown in Figure 5.31. Apparently, electron accumulation regions (red isosurface) appear between Li surface and Li_2S film, and the bonds formed by S atoms and Li atoms in the substrate (violet sphere) penetrate electron accumulation regions. The electronic structures demonstrate that the Li_2S film interacts with the Li anode surface via strong chemical

bonds.

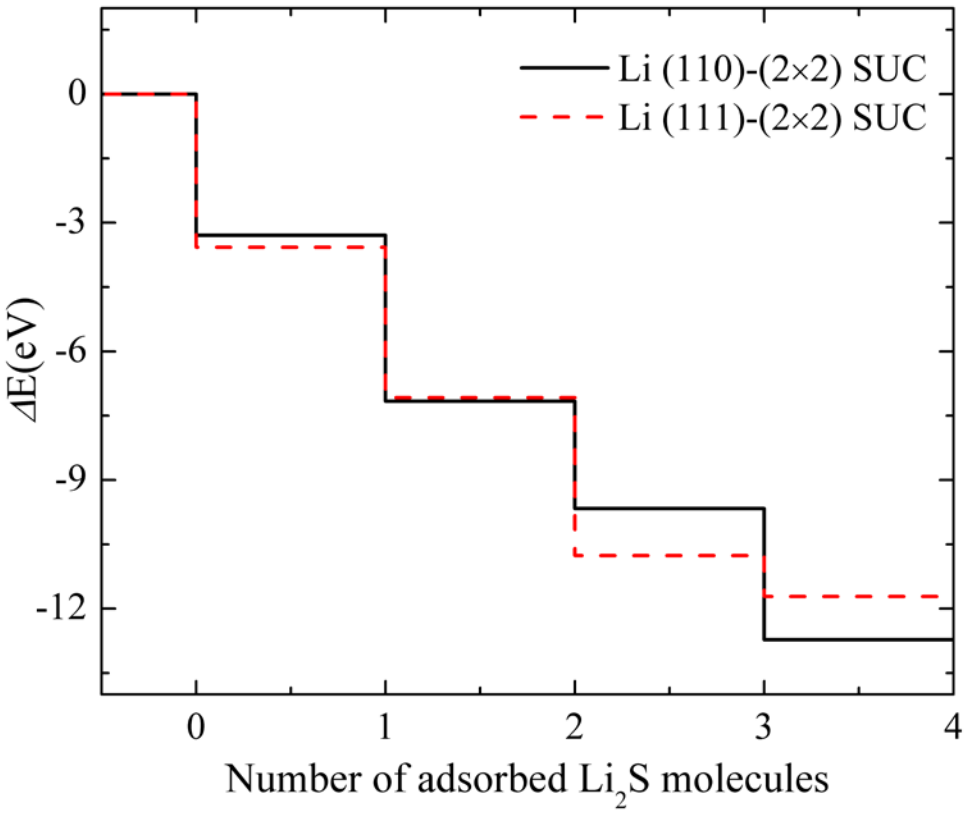

Figure 5.30 Energy profile of Li_2S film formation on Li (110)-(2×2) SUC and Li (111)-(2×2) SUC. The clean surface is set as the reference state with $\boldsymbol{\Delta E}$ = 0 eV.

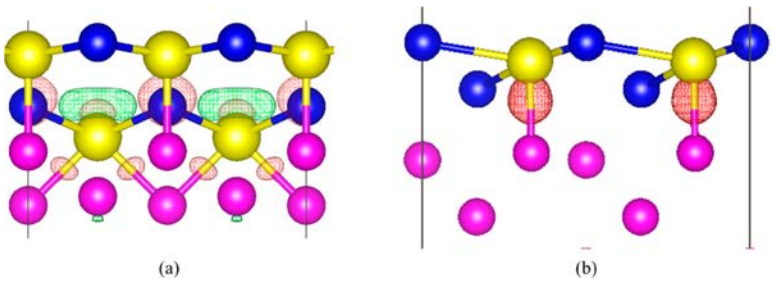

Figure 5.31 Difference charge density of Li_2S film adsorption on (a) Li(110) surface and (b) Li(111) surface. The red isosurface ($\mathbf{3.5 \times 10^{-3}}$ $\boldsymbol{e}$/Å$^{\mathbf{3}}$) represents electron accumulation and the green isosurface ($\mathbf{3.5 \times 10^{-3}}$ $\boldsymbol{e}$/Å$^{\mathbf{3}}$) represents electron depletion.

5.4.3 Conclusions

DFT simulations reveal new insights regarding the formation of a Li_2S film on Li anode surfaces of Li-S batteries. DFT analyses shows details of Li_2S molecular adsorption on Li (110) and Li (111) surfaces with energies of -3.22 eV and -3.57 eV respectively, which denote the strong interaction between adsorbate and substrate also confirmed by the difference charge density that shows chemical bonds formation between S atoms and Li atoms from the anode surface. For the Li (110) surface, a Li_2S film with a Li_2S (110)-like structure is predicted to form first and then the structure of the Li_2S film is converted to a distorted Li_2S (111) plane until the Li (110) surface is fully covered. For the Li (111) surface, $(Li_2S)_n$ clusters form on the surface first and a perfect Li_2S (111) plane appears finally. Both the interaction energy analysis and electronic structure analysis suggest that the Li_2S film interact with the Li anode surface via strong chemical bonds, and the decomposition of Li_2S film is difficult.

CHAPTER VI

A MESOSCALE INTERFACIAL MODEL TO STUDY CATHODE SURFACE PASSIVATION OF LI-S BATTERY

It is known that crystalline Li_2S is an electronic insulator,[70, 98] hence the electrochemical reactions for PSs reduction are difficult to happen at the electrolyte/Li_2S interface. The lateral growth of Li_2S precipitation can reduce the fresh cathode surface which supplies electrons for electrochemical reactions. Gerber *et al.* reported a method to inhibit the lateral growth of Li_2S film by using benzo[*ghi*]peryleneimide (BPI) as the redox mediator, and the specific capacity is doubled by using the mediator.[99]

In this regard, it is necessary to control the precipitation morphology during the discharge process. In the presented study, a mesoscale interfacial model is developed to study how species concentration and temperature affect the Li_2S film growth. This model is expected to provide strategies to defer surface passivation in Li-S battery cathode.

6.1 Computational Method

The formation of Li_2S during discharge undergoes multistep reactions including: [211, 212]

(i) $S_8(s) = S_8(l)$,

(ii) $S_8 + 2e^- = S_8^{2-}$,

(iii) $S_8^{2-} + 2e^- = 2S_4^{2e^-}$,

(iv) $S_4^{2-} + 2e^- = 2S_2^{2-}$,

(v) $S_2^{2-} + 2e^- = 2S^{2-}$.

Reaction (i) represents the dissolution of α-S into electrolyte. Reactions (ii)~(v) represent electrochemical reactions, in which long-chain polysulfides (PSs) are gradually reduced into short-chain PSs. The short-chain PSs are insoluble in the electrolyte, hence they will precipitate onto the substrate when combining with Li^+ ions:

$$\text{(vi)} \quad 2Li^+ + S_2^{2-} = Li_2S_2(\downarrow),$$

$$\text{(vii)} \quad 2Li^+ + S^{2-} = Li_2S(\downarrow).$$

The solid Li_2S_2 can be furtherly reduced to solid Li_2S

$$\text{(viii)} \quad Li_2S_2 + 2Li^+ + 2e^- = 2Li_2S.$$

There is a controversy about the composition of the discharge products in Li-S batteries. Barghamadi *et al.* reported that the direct formation of solid Li_2S is the predominant reaction and the Reaction (viii) is kinetically slow.[150] Xiao *et al.* detected Li_2S_2 by using an in-situ nuclear magnetic resonance (NMR) technique.[213] However, Li_2S_2 is not a thermodynamically stable phase according to experimental observations[214] and the first-principles calculations,[215] and the XRD pattern of the final product matches the crystal structure of Li_2S rather than the structure of Li_2S_2 predicted by the first-principles calculations.[215] Cuisinier *et al.* and Dominko *et al.* independently analyzed products during the discharge/charge cycling by operando X-ray absorption spectroscopy, and they found that Li_2S is the only detectable crystalline phase among discharge products.[211, 216] Cuininier *et al.* also tracked the PSs evolution during discharge with NMR, but they did not detect solid Li_2S_2 as reported by Xiao *et al.*[213] Cañas *et al.* analyzed discharge products by in-situ XRD technique and they did not find

solid Li_2S_2.[217] Cañas *et al*. also found that (111) surface dominates the facets of crystalline Li_2S, which is also confirmed by first-principle calculations.[163, 210, 218]

Based on findings discussed above, a coarse-grained lattice model is developed to represent the Li_2S film structure with the following assumptions.

(1) Li_2S is the only discharge product.

(2) The film grows along the normal direction of Li_2S (111) surface.

(3) The film growth is only attributed to the direct deposition of Li_2S molecules rather than Li_2S_2 deposition and reduction.

(4) The structure of the Li_2S is represented by a coarse-grained model. Each triatomic Li_2S unit is simplified to a lattice site, and the position of a Li_2S unit in the solid phase is represented by the position of the S atom. Hence the antifluorite structure of crystalline Li_2S is converted to a face-centered cubic (*fcc*) structure. The coarse-grained model neglects the geometric parameters (*i.e.* bond length, bond angle and molecule orientation) at the atomic scale.

(5) The adsorption and diffusion of a Li_2S unit on the solid substrate is restricted by a solid-on-solid model,[219] in which an empty cell cannot accept a Li_2S site unless this site coordinates with three occupied sites in the sublayer.

A Kinetic Monte Carlo algorithm is employed to implement transition events taking place at the electrolyte/solid substrate interface. Three transition events are considered in the present model, which are Li_2S adsorption, desorption, and diffusion on the surface. As discussed above, Li_2S adsorption can only happen in an empty site cooperating with

three occupied sites in the sublayer. The adsorption rate of an available site is calculated by

$$R_{ads} = k_0 N_a V \frac{S_a}{S}\left(C_{Li^+}^2 C_{S^{2-}} - \Theta\right). \quad (6.1)$$

In Eqn. (6.11), k_0 is the reaction rate constant, and N_a is the Avogadro constant. V and S are the pore volume and cathode surface area in the porous cathode framework, respectively. S_a is the area of a lattice site projected to Li_2S (111) surface. C_i is the reactant concentration and Θ is the Li_2S solubility term.

$$R_{dif} = \frac{D_0}{d^2}\exp\left(-\frac{E_b}{\kappa T}\right). \quad (6.2)$$

In Eqn. (6.2), R_{dif} is the number of diffusion attempts per second. The term "d" is the distance between two adjacent sites. T is the temperature and κ is the Boltzmann constant. Previous first-principle calculation demonstrated that the chemical adsorption energy (E_{ads}) of a single Li_2S molecule on graphene is only -0.55 eV,[220] hence the desorption of a Li_2S from the cathode surface should be considered and the desorption rate is calculated by

$$R_{des} = \frac{2\kappa T}{h}\exp\left(\frac{E_{ads}}{\kappa T}\right), \quad (6.3)$$

where h represents the Planck constant. Table 6.1 lists the values of input parameters in Eqn. (6.1) ~ (6.3). Previous first-principles calculation showed that there is a strong attractive interaction between a Li_2S molecule and pre-adsorbed Li_2S.[163, 220] Thereby, the adsorbed Li_2S molecule will not implement desorption or diffusion once it coordinates with other Li_2S sites. In KMC simulation, the procedure of Li_2S film growth undergoes the following steps:

(a) *Calculate the total transition rate*. The total adsorption rate (Ω_{ads}), diffusion rate (Ω_{dif}) and desorption rate (Ω_{des}) are calculated based on Eqns (6.4) ~ (6.6).

$$\Omega_{ads} = \sum_{i=1}^{N} R_{ads}^{i}, \tag{6.4}$$

$$\Omega_{dif} = \sum_{i=1}^{N} R_{dif}^{i}, \tag{6.5}$$

$$\Omega_{des} = \sum_{i=1}^{N} R_{des}^{i}, \tag{6.6}$$

$$\Omega_{tot} = \Omega_{ads} + \Omega_{dif} + \Omega_{des}. \tag{6.7}$$

The total transition event rate is the summation of Ω_{ads}, Ω_{dif}, and Ω_{dep}. Here *N* is the total number of lattice site in the simulation domain, and *i* is the i^{th} lattice site.

(b) *Select a transition event*. A random number γ_1 uniformly distributed in (0, 1) is generated. In the condition of $\gamma_1\Omega_{tot} < \Omega_{ads}$, adsorption event will happen; in the case of $\Omega_{ads} \leq \gamma_1\Omega_{tot} < \Omega_{ads} + \Omega_{dif}$, the diffusion event will happen; and in the case of $\Omega_{ads} + \Omega_{dif} \leq \gamma_1\Omega_{tot} < \Omega_{tot}$, the desorption event will happen. After determining the transition event, the position where the event will happen is determined by another random number γ_2. For adsorption event, the position is selected by

$$\sum_{i=1}^{k-1} R_{ads}^{i} < \gamma_2\Omega_{ads} \leq \sum_{i=1}^{k} R_{ads}^{i}. \tag{6.8}$$

For diffusion event, the position is selected by

$$\sum_{i=1}^{k-1} R_{dif}^{i} < \gamma_2\Omega_{dif} \leq \sum_{i=1}^{k} R_{dif}^{i}. \tag{6.9}$$

For desorption event, the position is selected by

$$\sum_{i=1}^{k-1} R_{des}^{i} < \gamma_2\Omega_{des} \leq \sum_{i=1}^{k} R_{des}^{i}. \tag{6.10}$$

Here k indicates the k^{th} lattice site where the transition event happens.

(c) *Update structure and time*. The film structure is updated according to the transition event selected in Step-(c). The time step of the selected event is evaluated by a random number γ_3

$$\delta t = -\frac{1}{\Omega_{tot}} \ln \gamma_3. \tag{6.11}$$

Table 6.1. Input parameters and values of Eqns. (6.1) ~ (6.3) in CG-KMC model.

Symbol		Value
k_0 †	Li_2S deposition rate constant	6.875×10^{-5} $m^6 mol^2$ sec^{-1}
N_a	Avogadro constant	6.02×10^{23} mol^{-1}
V ‡	Total pore volume of cathode microstructure	1.57×10^{-7} m^3
S ‡	Total cathode/electrolyte interfacial area	5.51×10^{-2} m^2
S_a	Area per lattice site	1.41×10^{-19} m^2
E_b	Diffusion barrier of Li_2S molecule on cathode surface	0.01 eV
E_{ads}	Chemical adsorption energy of Li_2S on graphene	-0.55 eV
C_{Li^+} ‡	Concentration of Li^+	10^3 mol m^{-3}
$C_{S^{2-}}$ ‡	Concentration of S^{2-}	10^{-5}~10^{-3} mol m^{-3}
T	Operation temperature	-40 ℃ ~ 80℃
κ	Boltzmann constant	8.617×10^{-5} eV K^{-1}
h	Planck constant	4.136×10^{-15} eV sec^{-1}

In the current CG-KMC model, a period boundary condition is applied along X and Y direction. In this case, an appropriate computational domain size should be selected because the simulation results show significant fluctuation if the domain size is too small to avoid the noise.[221, 222] A set of matrix size (from 50×50 to 250×250) are tested to optimize the simulation domain. In the optimization test, the time for the cathode surface getting 0.3 ML coverage is calculated as shown in Figure 6.1. For each domain size, the simulation is conducted 5 times to get the average value, and the standard deviation is calculated to show the stability of the simulation. Figure 6.1 clearly shows that the average time is converged when the matrix size is larger than 150×150. In addition, the standard deviation decreases significantly after the 150×150 matrix, which indicates a good stability. According to this test, it could be inferred that the 175×175 domain (ca. 4300 nm2) is accurate enough to study the Li2S deposition on cathode surface with using KMC simulation.

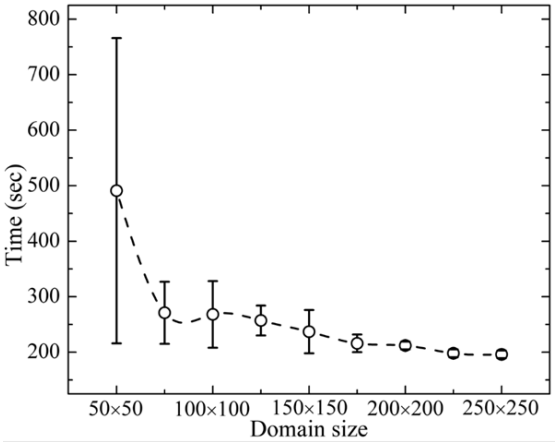

Figure 6.1 Effect of domain size on the time for the substrate getting 0.3 ML coverage. All test simulations are performed with $\mathbf{T = 20\ °C}$, $\mathbf{C_{Li^+} = 10^3}$ mol m^{-3}, $\mathbf{C_{S^{2-}} = 10^{-3}}$ mol m^{-3}

6.2 Results and Discussion

Three stages during the Li_2S film formation are identified by the present mesoscale interfacial model. Figure 6.2(a) shows the Li_2S film coverage variation and thickness variation as a function of time. The simulation in Figure 6.2 is performed with $T = 20$ °C, $C_{Li^+} = 10^3$ mol m^{-3} and $C_{S^{2-}} = 10^{-4}$ mol m^{-3}. The formation of Li_2S film cannot be observed in the first duration (the green region in Figure 6.2(a)). In this stage, Li_2S desorption prohibits other transition events (adsorption and diffusion). The desorption rate dominates the total transition rates. Once a Li_2S molecule is adsorbed on the cathode surface, it does not have enough time to collide with other Li_2S molecules before the desorption happening. When some adsorbed Li_2S get a chance to collide with others, small $(Li_2S)_n$ cluster will form and be stabilized on the electrode surface because the formation of a cluster can significantly increase the adsorption energy according to first-principle calculations.[163, 220] These nuclei act as seeds for Li_2S film growth. As shown in Figure 6.2(a), the coverage keeps increasing in the second stage (pink region) and the third stage (yellow region). The slope of the coverage curve increases in the second stage, which indicates that isolated Li_2S island growth happens at this stage. In the third stage, the slope of the coverage curve, which represent the coverage growth rate, gradually approaches to zero till the substrate is fully covered by the Li_2S film. The decrease of the coverage growth rate is attributed to the coalescence of Li_2S islands. It is worth noting that film thickness growth rate in the second stage is slower than that in the third stage. The reason is that the most of adsorbed Li_2S molecules participate in the lateral growth in the isolated island growth stage. After island coalescence happening,

more Li_2S molecules will precipitate on the pre-deposited solid Li_2S surface. Hence the thickness grows faster and coverage grows slower in the third stage than the second stage. The film thickness grows linearly after the cathode surface being fully covered by the discharge product.

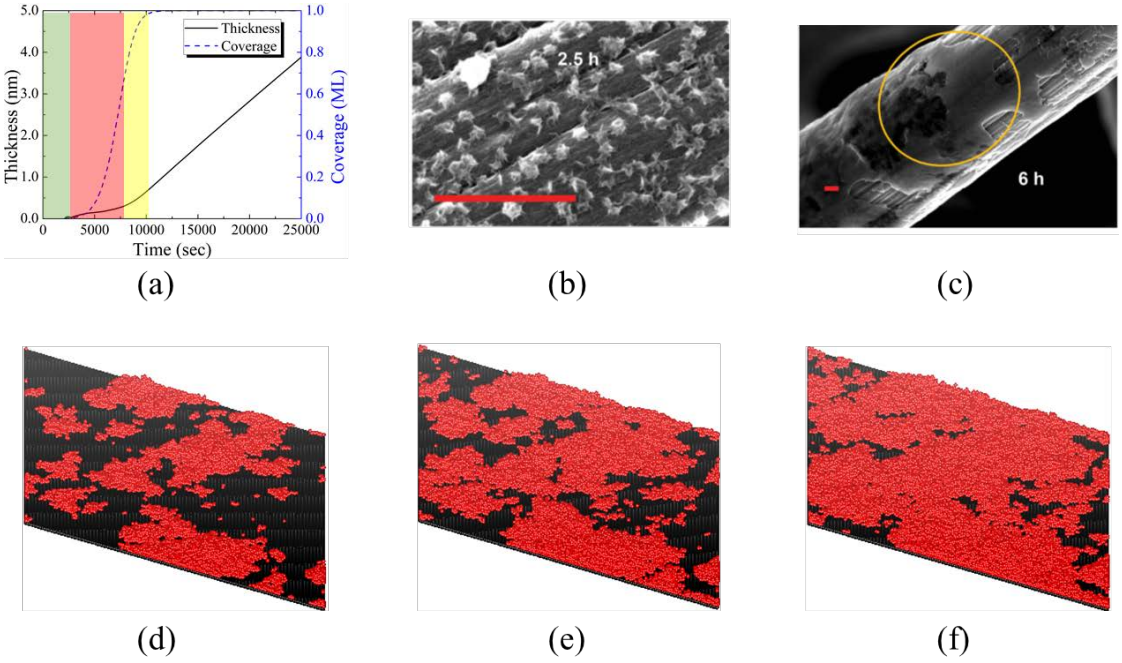

Figure 6.2 (a) Surface coverage as a function of time with constant reaction concentrations ($\mathbf{C_{Li^+} = 10^3}$ mol m^{-3} and $\mathbf{C_{S^{2-}} = 10^{-4}}$ mol m^{-3} and constant operation temperature T = 20 °C. SEM images depict the morphology of precipitated solid Li_2S on carbon fiber cathode after (b) 2.5 h and (c) 6 h with potentiostatic discharge at 2.02 V. Snapshots depict the computational results of Li_2S

The nucleation-island growth-island coalescence process has been observed in the experiment. Fan *et al.* discharged a Li-S battery at constant voltage 2.02 V.[223] The carbon fiber cathode is sparsely covered by Li_2S islands at the time of 2.5 hours (Figure 6.2(b)). At the time of 4 hours, island coalescence happened and thin 2D film is observed

(Figure 6.2(c)). After 6 hours, the completely covering could be observed according to Fan's experiment. Snapshots in Figures 6.2(d) ~ (f) demonstrate the film formation process from the simulation. It is also found that small Li_2S islands form on the cathode surface first (Figure 6.2(d)), then the lateral growth of islands make them coalesce (Figure 6.2(e)) and continuum Li_2S film appears (Figure 6.2(f)).

It is known that Li_2S is insulator and its electronic resistivity is larger than 10^{14} Ω cm.[224] Fan *et al.* believe that the electrochemical reduction of PSs mainly happens at the precipitation-electrolyte-cathode three-phase boundary.[223] In the duration of Li_2S nucleation and isolated island growth (the pink region in Figure 6.2(a)), the three-phase boundary length reaches a maximum and then the boundary disappears due to the island coalescence (the yellow region in Figure 6.2(a)). A recent theoretical study revealed that the Li vacancy (V_{Li}^{-}) is the main charge carrier in crystalline Li_2S,[225] and transition metal doping can increase V_{Li}^{-} concentration.[226] It was also found that transition metal dopant can generate gap states between fully occupied valence band bellow Fermi level and empty conduction band above Fermi level.[226] Fermi level crosses gap states hence transition metal dopants can also facilitate electron migration. The final discharge product Li_2O_2 in Li-air battery is also an electrical insulator, which is similar with discharge product Li_2S in Li-S battery. Theoretical studies also demonstrated that vacancies and dopants can increase the electrical conductivity of crystalline Li_2O_2.[227-229] Beyond point defects, grain boundaries can also increase the electronic conductivity of Li_2O_2.[230] Although there has been no report talking about the role of grain boundaries in Li_2S conductivity, we believe that electrochemical

reductions can happen on the outer surface of Li_2S film because defects in crystal lattice can transport electrons from Li_2S/cathode interface to Li_2S/electrolyte interface. However, the spread of and growth of Li_2S film will generate voltage drop due to Ohm's law. Hence, it is necessary to defer the cathode surface passivation due to Li_2S precipitation.

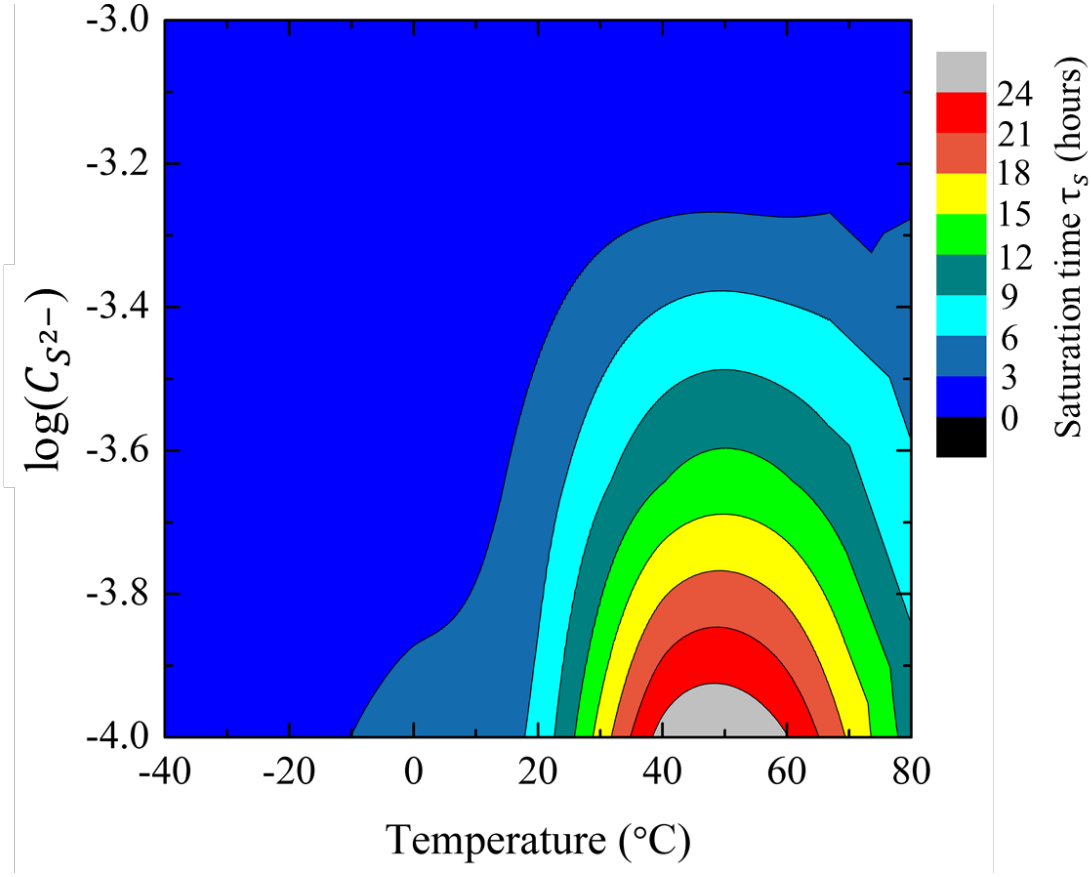

Figure 6.3 Effect of S^{2-} concentration and temperature on surface passivation. The saturation time ($\boldsymbol{\tau_S}$) represent the time for the cathode surface getting completely covered by Li_2S film.

The effects of S^{2-} concentration and temperature on surface passivation are studied by the present mesoscale model. Figure 6.3 shows the saturation time (τ_S), which

is the time for the cathode surface getting completely covered by Li_2S film. It is clear that the saturation time monotonically decreases as S^{2-} decreases. At room temperature (20 °C), the cathode surface will be passivated fast with a high relatively high S^{2-} concentration. Figure 6.4 shows the coverage variation as a function of time. With a high S^{2-} concentration $C_{S^{2-}} = 5 \times 10^{-3}$, the surface coverage almost linearly grows to 1 ML with a large slope. In this case, the zero-coverage stage is not observed, which means that the nucleation happens very fast. A higher S^{2-} concentration indicates that more adsorption events happen per second. Hence, a single adsorbed Li_2S molecule can easily form a stable cluster with another adsorbed Li_2S molecule before desorption event happening. The zero-coverage time duration appears when the concentration is decreased to 1×10^{-3} mol m^{-3}. Since the concentration is reduced, the adsorbed single Li_2S molecule will desorb from the cathode surface before it gets another Li_2S molecule to form a stable cluster. The further decrease in S^{2-} concentration can elongate the zero-coverage duration. Snapshots in Figure 6.5 depict the evolution of precipitation morphology with different S^{2-} concentration at room temperature (T = 20 °C). It can be clearly seen that many small Li_2S islands appear on the cathode surface at 0.1 ML coverage when S^{2-} concentration is 5×10^{3} mol m^{-3}. For the lower S^{2-} concentration, only a few large Li_2S islands are observed at 0.1 ML coverage. At the same surface coverage, smaller islands have more lateral sites than larger islands. Thereby, smaller islands are more beneficial for prohibiting Li_2S desorption and facilitating surface passivation than larger island.

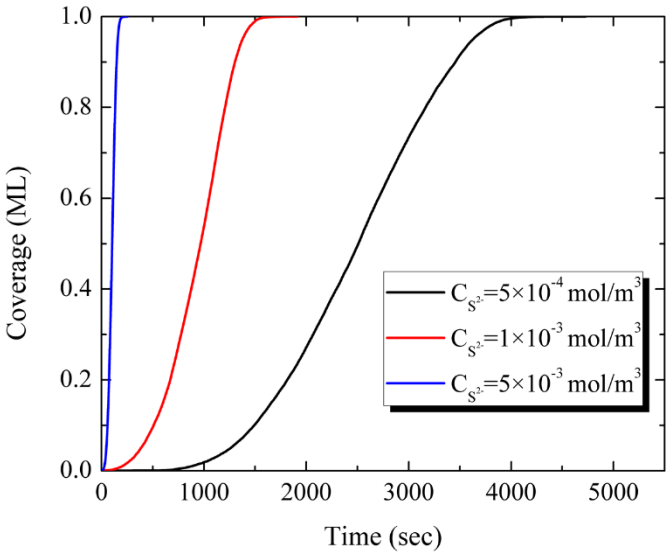

Figure 6.4 Coverage variation vs. time with different S^{2-} concentration at room temperature 20 °C.

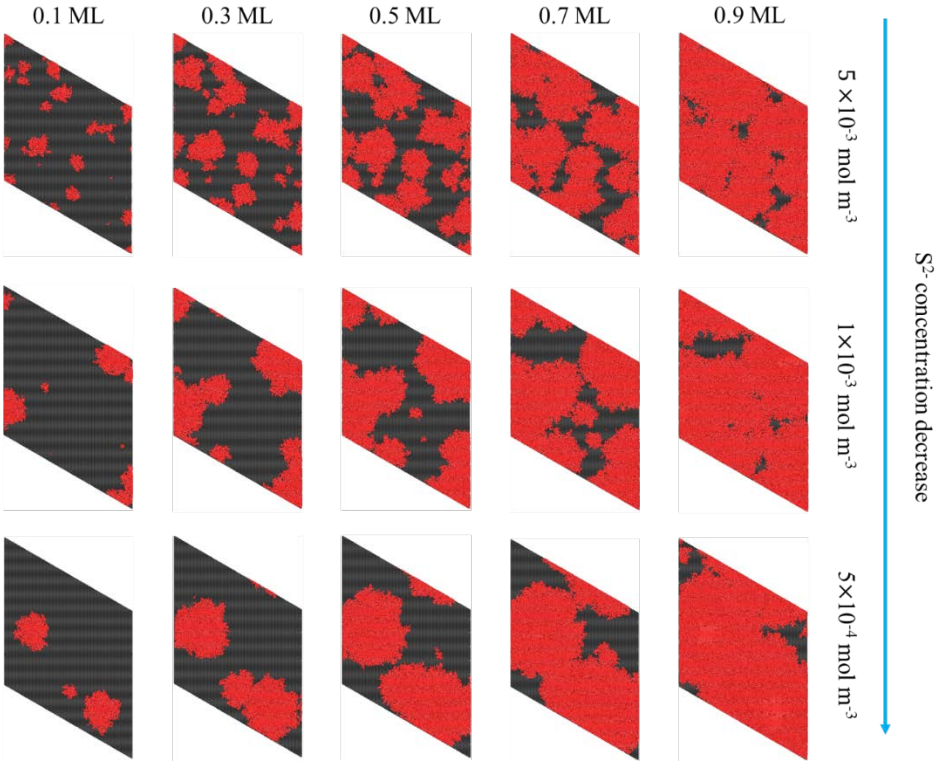

Figure 6.5 Snapshots of Li_2S island formation and growth with different S^{2-} concentration at room temperature 20 °C.

As shown in Figure 6.3, decreasing S^{2-} concentration is a way to defer the surface passivation. One method to reduce S^{2-} concentration is to discharge the battery with a low current density to limit the electrochemical reduction reactions from S_8 to S^{2-}. However, the low discharge current density cannot supply high power density. Another way to reduce S^{2-} concentration is to facilitate the backward reaction of the disproportionation reaction such as

$$S_n^{2-} \Leftrightarrow S^{2-} + S_8.$$

A macroscale model is developed to investigate the effect of disproportionation reaction on battery performance.[231] It is found that the decrease in forward reaction rate (or the increase in backward reaction rate) can lower discharge voltage plateau at the condition of constant discharge density. The reason is that the backward disproportionation reaction consumes active material S_8 and produces long chain PSs S_n^{2-} without making a contribution to electron transfer, hence a large overpotential is required to keep the constant discharge current. In addition, the long chain PSs produced by backward disproportionation reaction can facilitate the shuttle effect, which corrodes Li metal anode and leads to capacity loss. In conclusion, reducing S^{2-} concentration is not a preferred method to defer surface passivation because it will sacrifice discharge voltage.

Another method to defer the surface passivation is discharging the battery at an appropriate temperature. Figure 6.3 shows that the low temperature ($T < -20$ °C) leads to a fast surface passivation ($\tau_S < 3$ hours) even though the S^{2-} concentration is as low as 1×10^{-4} mol m^{-3}. It is found that the saturation time τ_S increases as the temperature increases to T = 60 °C, which means that the surface passivation will be alleviated by

increasing the temperature in an appropriate range. Over this critical temperature point, the further increase in temperature contrarily decreases the saturation time as shown in Figure 6.3.

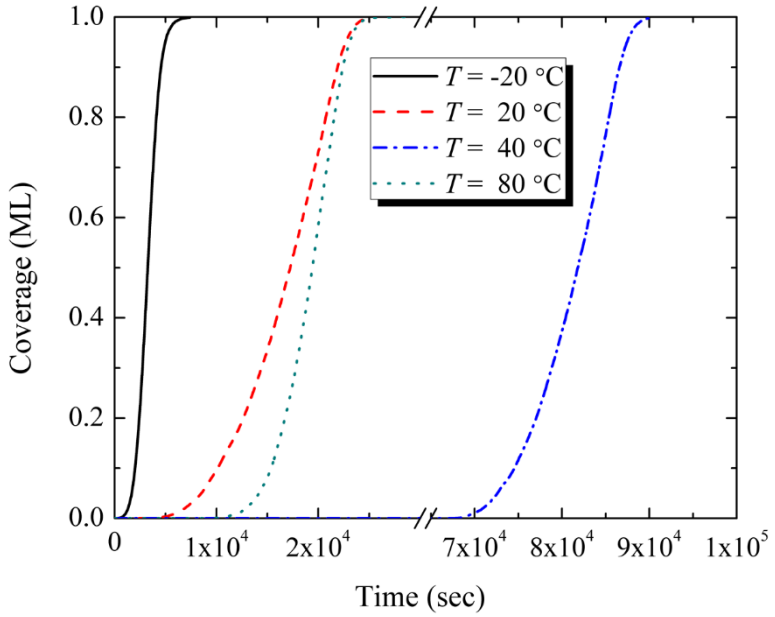

Figure 6.6 Coverage variation vs. time with $\mathbf{C_{S^{2-}} = 1 \times 10^{-4}}$ mol m^{-3} at different temperatures.

Figure 6.6 shows the coverage variation *vs.* time at different temperatures. It is found that the zero-coverage duration is very short at T = -20 °C. The reason is that the adsorbed Li_2S molecules will be frozen on the cathode surface. These molecules are difficult to desorb back into the ambient environment due to low desorption rate at a low-temperature condition. For a given S^{2-} concentration, the adsorption rate is a constant in the present model, and the desorption rate is proportional to $e^{-\frac{1}{T}}$. More desorption event can happen at a relative higher temperature condition, which slows down Li_2S cluster formation. Hence the zero-coverage duration with T = 40 °C is longer than that with T =

-20 °C. However, the further increase in temperature also shortens the zero-coverage duration as shown in Figure 6.6. It is worth noting that the adsorbed Li_2S molecule is more active to diffuse at a higher temperature. Thereby Li_2S molecules have more chances to collide to form clusters at T = 80°C, thus the zero-coverage duration is reduced.

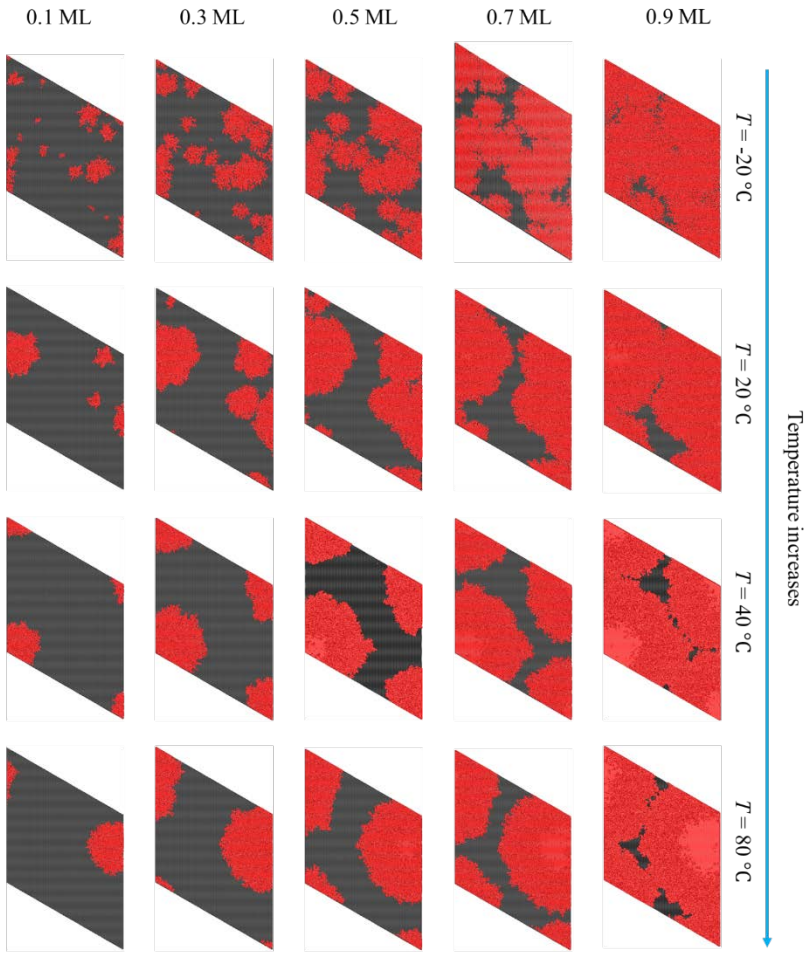

Figure 6.7 Snapshots of Li_2S island formation and growthwith $\mathbf{C_{S^{2-}} = 1 \times 10^{-4}}$ mol m^{-3} at different temperatures.

Snapshots in Figure 6.7 depict morphology evolution during deposition at different temperatures. Snapshots in the first column show the temperature effect on the

Li_2S island distribution at 0.1 ML coverage. It is found that some small Li_2S nanoislands appear on the cathode surface at T = -20 °C, and fewer nanoislands are observed at T = 20 °C. Only one nanoisland is found in the computational domain when the temperature is larger than 40 °C. At low temperature, adsorbed Li_2S molecules can be easily stabilized on the cathode surface due to the low desorption rate. As temperature increases, more pre-adsorbed Li_2S molecules will desorb from the cathode surface to the ambient electrolyte environment, hence the number of island decreases. As shown in Figure 6.7, the temperature affects the morphology variation of the precipitation film. At T = -20 °C and 20 °C, the island coalescence happens at 0.5 ML. When the temperature is above 40 °C, the island coalescence happens after 0.7 ML.

The density of the lateral sites of Li_2S islands is calculated to quantitatively show the morphology evolution of the precipitation. The increase of density corresponds to the isolated island growth and the decrease of density corresponds to the island coalescence. Figure 6.8 clearly shows the island coalescence happens earlier at a lower temperature. For a given coverage in the isolated island growth region, the total perimeter of smaller islands is always larger than that of larger islands. Once a Li_2S molecule is located at a lateral site, it is stabilized on the surface and desorption will not happen. Hence, the cathode surface with smaller islands (larger density of lateral sites) always has a higher coverage growth rate, which leads to a faster surface passivation.

Since the surface passivation is harmful to the electrochemical reactions due to the nature of the solid Li_2S, the Li-S battery need avoid working at a low-temperature condition in order to achieve high performance. Mikhaylik and Akridge firstly studied

the effect of temperature on the discharge performance of Li-S battery with graphite cathode.[232] They found that the discharge capacity and voltage plateau decreased as the temperature decreased from 25 °C to -40 °C, and the Li-S battery working at the higher temperature had a better cycling stability. They also analyzed the discharge profiles at different rates and temperatures, and they proposed that it was cell battery design limited rate capacity rather than chemistry.[233] Huang *et al.* fabricated a cathode with hierarchical porous graphene and tested the high rate performance in the temperature range from -40 °C to 60 °C.[234] They also found that the battery working at 25 °C had the best performance, and the discharge capacity decreased as the temperature decreased. It is interesting that the capacity also decreased if the temperature rose to 60 °C in Huang's experimental study. This phenomenon coincides with our modeling results. Hence, it can be inferred that the temperature-controlled surface passivation affects the battery performance.

Our simulations show that a more heterogeneous film growth taking place at an appropriate temperature is beneficial to defer the surface passivation, and the more homogeneous film growth at a low temperature always facilitates the surface passivation. Recently, Gerber *et al.* reported a method to control Li_2S growth by using benzo[*ghi*]peryleneimide (BPI) as the redox mediator.[99] They found that the discharge capacity was doubled by using BPI to control the morphology of Li_2S precipitation. SEM images demonstrate that BPI can facilitate the Li_2S thickness growth and reduce the lateral growth. Thereby, the surface passivation is alleviated.

Beyond surface passivation, there are other temperature-dependent physicochemical interplays (*i.e.* electrochemical reaction rate and species diffusivity) potentially affect the battery performance. The present mesoscale interfacial model can be coupled with a macroscale performance model and cathode microstructure analysis to identify which are main physical factors determining the battery performance.

6.3 Conclusions

In this work, a mesoscale interfacial model is developed to study the cathode surface passivation due to Li_2S precipitation. The KMC algorithm is employed to implement the Li_2S adsorption, diffusion, and desorption. The effects S^{2-} concentration and temperature on surface passivation are investigated. It is found that the relatively low S^{2-} concentration can differ the surface passivation. The surface passivation can also be deferred by controlling the temperature. At the low-temperature condition, adsorbed Li_2S molecules will be frozen on the cathode surface and desorption events are difficult to happen, in which case the cathode surface will be passivated very fast. As the temperature increases, pre-adsorbed Li_2S molecules are more active to desorb from the surface hence only a few stable nucleation seeds can form on the cathode surface. Compared with the low temperature, the coverage growth rate is slower at a higher temperature. However, if the temperature is over 60 °C, the fast diffusion of Li_2S on cathode surface also speeds up the lateral growth of Li_2S film. Thereby, the cathode surface also suffers from fast surface passivation when the temperature is higher than 60 °C.

CHAPTER VII

CONCLUSIONS AND FUTURE WORK

The modern society urgently demands the development of the techniques of electrochemical energy storage to address energy risks caused by the combustion of fossil fuels. The performance of energy storage devices greatly relies on the microstructures of electrodes [235, 236]. In the present thesis, the mesoscale interactions in the electrode are studied to elucidate their impacts on the electrode microstructure evolution.

7.1 Effects of Mesoscale Interactions on LIB Electrode Processing

A 2D mesoscale computational model has been developed in order to investigate the influence of processing attributes on the microstructure evolution representative of a typical lithium-ion battery electrode. In particular, the impact of active nanoparticle morphology, solvent evaporation and the nanoparticle/solvent interaction on the resultant electrode microstructure has been assessed. Based on our computational results, a morphology-evaporation rate phase map is generated to help us understand which factors affect the performance of the electrode. The phase map suggests that the small-sized cubical active nanoparticle can be a preferred morphology to generate the large conductive interfacial area ratio owing. The dispersion of active nanoparticles depends significantly on the interaction with the conductive additives, which shows the formation of electrode microstructures with favorable conductive pathway and hence its influence on improved electronic conductivity. The effect of the evaporation rate on the

microstructure has been investigated which suggests the existence of distinct aggregation mechanisms. It is found that the spontaneous aggregation with a low evaporation rate is the optimum processing strategy to get the high quality microstructure, and this strategy requires a strong nanoparticle/solvent attractive force. If the nanoparticle/solvent attractive interaction is weak, nanoparticles tend to be isolated by solvents and the evaporation is the only driving force to make an integral conductive network in the electrode. In this case, the evaporation rate plays a subtle rule of determining the microstructure because both high and low evaporation rate reduce the conductive interfacial area ratio. The volume fraction of the active material has been shown to affect the conductive pathway formation between the active material and conductive additive.

The 2D computational model has been used to investigate the influence of processing attributes on the microstructure evolution of a typical lithium-ion battery electrode. Particularly, the impacts of the slurry mixing sequence, the morphology of active material nanoparticles, and the temperature condition on the resultant electrode microstructure have been assessed. The effects of mixing sequences and nanoparticle morphologies are concluded in the phase map. Small-sized nanoparticles are preferred to produce the high conductive interfacial area ratio, and the cubic is the optimal morphology to form a desirable microstructure with a favorable electronic diffusion pathway. The effect of the mixing sequence on the electrode microstructure is investigated. Compared with one-step mixing sequence, stepwise sequences significantly increase the conductive interfacial area ratio. Both the constant temperature condition and temperature-increasing condition are performed in the electrode

processing simulation. It is found that the temperature condition does not significantly affect the conductive interfacial area ratio. However, the temperature condition can subtly affect the homogeneity of the binder distribution. Taking conductive interfacial area ratio and binder distribution into consideration, in the constant temperature condition, the two-step mixing sequence is preferred to produce a high-quality microstructure for an electrode slurry composed by small-sized cubical nanoparticles; while in the temperature-increasing condition, the multi-step-1 mixing sequence is preferred to produce a high-quality microstructure for an electrode slurry composed by small-sized cubical nanoparticles.

The CGKMC model is extended to a pseudo (1+1)D model to study the influence of processing attributes on microstructure representative of an electrode film in LIB. In particular, the electrode film microstructure affected by drying temperature and the length of semi-flexible single chain binder is illustrated by the CGLG model. It is found that the geometric properties of the dried film are significantly affected by the operating temperature and the binder length. For electrode film with cubical active material nanoparticles, the mean thickness increases as binder length increases if the film is dried by the lower temperature, but the mean thickness decreases as binder length increases if the film is dried by the higher temperature. It is found that the topography of the film surface is significantly affected by drying temperature and binder length. The film with micropores can be achieved by using the lower drying temperature, and the depth of pores tends to increases as binder length increases. For film processed by the higher drying temperature, the roughness increase can also be obtained by increasing the binder

length. However, there are no micropores on the surface of electrode film processed by the higher temperature. The conformation of binder in the dried film is investigated in the present study. The end-to-end distance *vs.* binder length still follows the power law as single chain polymer without interaction with other species. However, the conformation of binder is straightened more or less due to the strong attractive interaction between the nanoparticle and the binder molecule. Additionally, the normalized end-to-end distance demonstrates that the shorter binder is straighter in the dried film. Present computations predict that drying temperature predominantly affects nanoparticle aggregation, and the lower temperature is beneficial for help conductive additive coat on active materials to reduce the electronic conductivity. Additionally, the low drying temperature can restrict binder molecules migrating to the surface of the electrode film, which is helpful for improving the mechanical stability of the electrode microstructure. The effect of active nanoparticle shape on electrode microstructure is also assessed in the present study. Compared with cubical active nanoparticles, spherical active nanoparticles does not affect the geometric properties of electrode film significantly. For electrode film contacting spherical active nanoparticles, the lower drying temperature is preferred to keep binder molecules in the electrode microstructure to improve the mechanical stability.

Although the present 2D and pseudo (1+1)D mesoscale models have been successfully applied to elucidate interparticle interactions and drying conditions on the microstructure evolution during LIB electrode processing, and the findings of the model is validated by experimental observations. However, there still some limitations in the

present model. The present model should be extended to a 3D model to more accurately represent the drying process. In addition, the current 2D model neglects the variation of the particle size and assume that the particle size is constant. However, the particle size distribution also affects the aggregation behavior. Furthermore, the gas bubble can form in the bulk phase during the drying process, and the current (1+1)D model neglect this phenomenon. The present model uses dimensionless energies to describe the solvent chemical potential and interactions between particles, hence the physical time cannot be derived from the KMC method. Atomistic simulation is a possible tool to obtain the interaction energies and solvent chemical potential. The extended mesoscale model is expected to combine with first-principle calculations or molecular dynamics to observe new physics during the electrode processing.

7.2 Polysulfide Adsorption and Li2S Film Formation on Electrode Surface

The chemical reactions of insoluble lithium polysulfides on crystal Li_2S surfaces are studied by a first-principles approach. Our simulations demonstrate that stoichiometric (111) and (110) surfaces are the most stable ones around the cell voltage of the Li-S battery. Geometric properties of Li_2S_x molecules adsorption on crystal Li_2S stable surfaces are predicted in this study. It is found that Li_2S_x (x = 1, 2) adsorption on Li_2S surfaces is an exothermic reaction, and Li_2S molecule adsorption releases more energy than Li_2S_2 adsorption. Li_2S (110) surface is more active to interact with Li_2S_x molecules because of the stronger adsorption energy. Electronic structures demonstrate that adsorbates interact with substrates via strong covalent bonds, and the electron transfer from adsorbates to substrates is not observed. The growth mechanism of

thermodynamically stable surfaces is investigated in this study. The result predicts that Li_2S direct deposition on the substrate is energetically more favorable than the Li_2S_2 deposition/reduction process.

The interaction mechanism between Li_2S_x (x = 1,2) and graphene substrate is studied by first-principles calculations. It is found that the adsorption energy of Li_2S molecule on graphene is smaller than that on crystalline Li_2S surface. It can be inferred that Li_2S prefers to adsorb on the pre-deposited Li_2S film in the Li-S battery cathode during the discharge. However, Li_2S adsorption on fresh graphene is still energetically favored. The formation of Li_2S film on the graphene is also studied and the energy profile is calculated. It is found that the formation of Li_2S film is an exothermic process. Defected Li_2S (111) layer will form on the graphene first, and then it will be converted to a perfect Li_2S (111) layer with introducing more Li_2S molecules to the deposited Li_2S layer.

The first-principles approach is used to evaluate silicene as promising cathode material to immobilize discharge products in Li-S batteries. Computational results show that silicene can strongly attract Li_2S_x (x = 1, 2, 4) molecules via chemical bonds. Geometric structures and electronic structures demonstrate that silicene can facilitate the dissociation of PSs and the reduction from S_4^{2-} to S_2^{2-} and S_2^{2-} to S^{2-}. The effect of dopants on PSs adsorption is investigated. It is found that N-doped silicene can further facilitate the adsorption and reduction of intermediate products Li_2S_4 as well as Li_2S_2. Hence silicne-based cathode is an attractive candidate for trapping PSs and mitigating shuttle effect. The atomistic structure evolution of Li_2S layer formation on silicene is

also studied. It is found that Li_2S (110) plane first forms on silicene, and then the L_2S (110) layer is converted to Li_2S (111) layer with introducing more Li_2S molecules to the pre-deposited Li_2S layer. The Li_2S layer interacts with silicene via strong chemical bonds. The energy profile demonstrates that the formation of Li_2S layer on silicene is energetically favorable.

DFT simulations reveal new insights regarding the formation of a Li_2S film on Li anode surfaces of Li-S batteries. DFT analyses shows details of Li_2S molecular adsorption on Li (110) and Li (111) surfaces with energies of -3.22 eV and -3.57 eV respectively, which denote the strong interaction between adsorbate and substrate also confirmed by the difference charge density that shows chemical bonds formation between S atoms and Li atoms from the anode surface. For the Li (110) surface, a Li_2S film with a Li_2S (110)-like structure is predicted to form first and then the structure of the Li_2S film is converted to a distorted Li_2S (111) plane until the Li (110) surface is fully covered. For the Li (111) surface, $(Li_2S)_n$ clusters form on the surface first and a perfect Li_2S (111) plane appears finally. Both the interaction energy analysis and electronic structure analysis suggest that the Li_2S film interact with the Li anode surface via strong chemical bonds and the decomposition of Li_2S film is difficult.

Based on mechanism of Li_2S film formation, a mesoscale interfacial model is developed to study the Li-S cathode surface passivation caused by Li_2S precipitation. The effects S^{2-} concentration and temperature on surface passivation are investigated. It is found that the relatively low S^{2-} concentration can slower the surface passivation. The surface passivation can also be deferred by controlling the temperature. At low-

temperature condition, adsorbed Li_2S molecules will be frozen on the cathode surface and desorption events are difficult to happen, in which case the cathode surface will be passivated very fast. As the temperature increases, pre-adsorbed Li_2S molecules are more active to desorb from the surface hence only a few stable nucleation seeds can form on the cathode surface. Compared with the low temperature, the coverage growth rate is slower at a higher temperature. However, if the temperature is over 60 ℃, the fast diffusion of Li_2S on cathode surface also speeds up the lateral growth of Li_2S film. Thereby, the cathode surface also suffers from fast surface passivation when the temperature is higher than 60 ℃.

The current mesoscale interfacial model only explicitly considers the chemical reactions (*i. e.* Li_2S adsorption and desorption). However, as discussed in Chapter VI, Li-S battery experience complicate multistep electrochemical reactions (from S_8 to S^{2-} with PSs as intermediate products) during the discharge process. The kinetic rates of these electrochemical reactions determines the concentration of S^{2-} in the electrolyte and they also directly affect the discharge performance (*i.e.* discharge voltage and capacity). The current model should be extended to explicitly consider these multistep electrochemical reactions to study how the morphology evolution of Li_2S film growth affects the performance of the Li-S battery. The outcomes of the advanced model are expected to point out guidelines for achieving high performance by controlling electrochemical reactions, PS-cathode interactions and operating temperature.

In addition, the present mesoscale interfacial model assumed that the cathode substrate is ideally flat and the surface passivation is the only reason that can stop the

discharge process. It is worth pointing out that the Li-S battery cathode is always a porous structure. The growth of Li_2S film near the inlet of pores can close these pores, therefore electrochemical reactions will stop due to the consumption of Li^+. In this case, the active material cannot be completely utilized, which leads to a capacity loss. The mesoscale model need be developed to simulate the Li_2S film formation and growth at a single pore level to identify which is the predominant effect (surface passivation or pore blockage) on the capacity loss.

REFERENCES

1. Tachan, Z., S. Rühle, and A. Zaban, *Dye-sensitized solar tubes: A new solar cell design for efficient current collection and improved cell sealing.* Solar Energy Materials and Solar Cells, 2010. **94**(2): p. 317-322.
2. Zhou, L., *Progress and problems in hydrogen storage methods.* Renewable and Sustainable Energy Reviews, 2005. **9**(4): p. 395-408.
3. Lu, L., H. Yang, and J. Burnett, *Investigation on wind power potential on Hong Kong islands—an analysis of wind power and wind turbine characteristics.* Renewable Energy, 2002. **27**(1): p. 1-12.
4. Etacheri, V., et al., *Challenges in the development of advanced Li-ion batteries: a review.* Energy & Environmental Science, 2011. **4**(9): p. 3243-3262.
5. Christensen, J., et al., *A critical review of Li/air batteries.* Journal of the Electrochemical Society, 2011. **159**(2): p. R1-R30.
6. Manthiram, A., Y. Fu, and Y.-S. Su, *Challenges and prospects of lithium–sulfur batteries.* Accounts of chemical research, 2012. **46**(5): p. 1125-1134.
7. Tarascon, J.M., *Key challenges in future Li-battery research.* Philosophical Transactions of the Royal Society a-Mathematical Physical and Engineering Sciences, 2010. **368**(1923): p. 3227-3241.
8. Tarascon, J.M. and M. Armand, *Issues and challenges facing rechargeable lithium batteries.* Nature, 2001. **414**(6861): p. 359-367.

9. Armand, M. and J.M. Tarascon, *Building better batteries.* Nature, 2008. **451**(7179): p. 652-657.

10. Wang, Y. and J.Y. Lee, *Molten salt synthesis of tin oxide nanorods: morphological and electrochemical features.* The Journal of Physical Chemistry B, 2004. **108**(46): p. 17832-17837.

11. Yan, D., et al., *A novel pineapple-structured Si/TiO2 composite as anode material for lithium ion batteries.* Journal of Alloys and Compounds, 2014. **609**: p. 86-92.

12. Chen, N., et al., *LiFe(MoO4)2 as a Novel Anode Material for Lithium-Ion Batteries.* ACS applied materials & interfaces, 2014. **6**(13): p. 10661-6.

13. Feng, J.K., et al., *Synthesis of nanosized cadmium oxide (CdO) as a novel high capacity anode material for Lithium-ion batteries: influence of carbon nanotubes decoration and binder choice.* Electrochimica Acta, 2014. **129**: p. 107-112.

14. Courtney, I.A. and J. Dahn, *Key Factors Controlling the Reversibility of the Reaction of Lithium with SnO2 and Sn2 BPO 6 Glass.* Journal of The Electrochemical Society, 1997. **144**(9): p. 2943-2948.

15. Zhou, X., Y. Zou, and J. Yang, *Periodic structures of Sn self-inserted between graphene interlayers as anodes for Li-ion battery.* Journal of Power Sources, 2014. **253**: p. 287-293.

16. Xu, Y., et al., *Uniform nano-Sn/C composite anodes for lithium ion batteries.* Nano letters, 2013. **13**(2): p. 470-474.

17. Qin, J., et al., *Graphene Networks Anchored with Sn@ Graphene as Lithium Ion Battery Anode.* ACS nano, 2014. **8**(2): p. 1728-1738.

18. Pol, V.G., et al., *Sonochemical Deposition of Sn, SnO2 and Sb on Spherical Hard Carbon Electrodes for Li-Ion Batteries.* Journal of The Electrochemical Society, 2014. **161**(5): p. A777-A782.

19. Zhou, H., et al., *Enhanced Electrocatalytic Performance of One-Dimensional Metal Nanowires and Arrays Generated via an Ambient, Surfactantless Synthesis.* The Journal of Physical Chemistry C, 2009. **113**(14): p. 5460-5466.

20. Alia, S.M., et al., *Platinum-Coated Nickel Nanowires as Oxygen-Reducing Electrocatalysts.* ACS Catalysis, 2014. **4**(4): p. 1114-1119.

21. Cherepy, N.J., et al., *Ultrafast studies of photoexcited electron dynamics in γ- and α-Fe2O3 semiconductor nanoparticles.* The Journal of Physical Chemistry B, 1998. **102**(5): p. 770-776.

22. Rowsell, J.L.C., V. Pralong, and L.F. Nazar, *Layered lithium iron nitride: A promising anode material for Li-ion batteries.* Journal of the American Chemical Society, 2001. **123**(35): p. 8598-8599.

23. Wang, Z., Q. Su, and H. Deng, *Single-layered V 2 O 5 a promising cathode material for rechargeable Li and Mg ion batteries: an ab initio study.* Physical Chemistry Chemical Physics, 2013. **15**(22): p. 8705-8709.

24. Akimoto, J., Y. Gotoh, and Y. Oosawa, *Synthesis and Structure Refinement of LiCoO2Single Crystals.* Journal of Solid State Chemistry, 1998. **141**(1): p. 298-302.

25. Belov, D. and M.-H. Yang, *Investigation of the kinetic mechanism in overcharge process for Li-ion battery.* Solid State Ionics, 2008. **179**(27–32): p. 1816-1821.

26. Amatucci, G.G., J.M. Tarascon, and L.C. Klein, *Cobalt dissolution in LiCoO2-based non-aqueous rechargeable batteries.* Solid State Ionics, 1996. **83**(1–2): p. 167-173.

27. Zhou, J. and P.H.L. Notten, *Studies on the degradation of Li-ion batteries by the use of microreference electrodes.* Journal of Power Sources, 2008. **177**(2): p. 553-560.

28. Daniel, C., *Materials and processing for lithium-ion batteries.* Jom, 2008. **60**(9): p. 43-48.

29. Li, J.L., C. Daniel, and D. Wood, *Materials processing for lithium-ion batteries.* Journal of Power Sources, 2011. **196**(5): p. 2452-2460.

30. Liu, G., et al., *Effects of Various Conductive Additive and Polymeric Binder Contents on the Performance of a Lithium-Ion Composite Cathode.* Journal of the Electrochemical Society, 2008. **155**(12): p. A887-A892.

31. Liu, G., et al., *Optimization of acetylene black conductive additive and PVDF composition for high-power rechargeable lithium-ion cells.* Journal of the Electrochemical Society, 2007. **154**(12): p. A1129-A1134.

32. Liu, G., et al., *Particles and Polymer Binder Interaction: A Controlling Factor in Lithium-Ion Electrode Performance.* Journal of the Electrochemical Society, 2012. **159**(3): p. A214-A221.

33. Zheng, H.H., et al., *Cooperation between Active Material, Polymeric Binder and Conductive Carbon Additive in Lithium Ion Battery Cathode.* Journal of Physical Chemistry C, 2012. **116**(7): p. 4875-4882.

34. Zheng, H.H., et al., *Correlationship between electrode mechanics and long-term cycling performance for graphite anode in lithium ion cells.* Journal of Power Sources, 2012. **217**: p. 530-537.

35. Li, J.L., et al., *Optimization of LiFePO4 Nanoparticle Suspensions with Polyethyleneimine for Aqueous Processing.* Langmuir, 2012. **28**(8): p. 3783-3790.

36. Li, J.L., et al., *Lithium Ion Cell Performance Enhancement Using Aqueous LiFePO4 Cathode Dispersions and Polyethyleneimine Dispersant.* Journal of the Electrochemical Society, 2013. **160**(2): p. A201-A206.

37. Cho, J., Y.J. Kim, and B. Park, *LiCoO2 cathode material that does not show a phase transition from hexagonal to monoclinic phase.* Journal of the Electrochemical Society, 2001. **148**(10): p. A1110-A1115.

38. Lee, J.T., et al., *A novel and efficient water-based composite binder for LiCoO2 cathodes in lithium-ion batteries.* Journal of Power Sources, 2007. **173**(2): p. 985-989.

39. Lee, J.T., et al., *Aqueous processing of lithium-ion battery cathodes using hydrogen peroxide-treated vapor-grown carbon fibers for improvement of electrochemical properties.* Journal of Materials Science, 2007. **42**(24): p. 10118-10123.

40. Zhang, W.J., et al., *Effect of slurry preparation and dispersion on electrochemical performances of LiFePO4 composite electrode.* Ionics, 2011. **17**(5): p. 473-477.

41. Lahaye, J., M.J. Wetterwald, and J. Messiet, *Electrolyte Absorption Capacity of Conducting Carbon-Blacks Used in Leclanche Type Batteries.* Journal of Applied Electrochemistry, 1984. **14**(1): p. 117-122.

42. Takahashi, M., et al., *Reaction behavior of LiFePO< sub> 4</sub> as a cathode material for rechargeable lithium batteries.* Solid State Ionics, 2002. **148**(3): p. 283-289.

43. Kim, J., et al., *Direct carbon-black coating on LiCoO2 cathode using surfactant for high-density Li-ion cell.* Journal of Power Sources, 2005. **139**(1-2): p. 289-294.

44. Zhang, W.M., et al., *Carbon Coated Fe3O4 Nanospindles as a Superior Anode Material for Lithium-Ion Batteries.* Advanced Functional Materials, 2008. **18**(24): p. 3941-3946.

45. Li, J., C. Daniel, and D.L. Wood, *Cathode Manufacturing for Lithium-Ion Batteries*, in *Handbook of Battery Materials, Second Edition*. 2011. p. 939-960.

46. Ge, G.L. and L. Brus, *Evidence for spinodal phase separation in two-dimensional nanocrystal self-assembly.* Journal of Physical Chemistry B, 2000. **104**(41): p. 9573-9575.

47. Tang, J., G.L. Ge, and L.E. Brus, *Gas-liquid-solid phase transition model for two-dimensional nanocrystal self-assembly on graphite.* Journal of Physical Chemistry B, 2002. **106**(22): p. 5653-5658.

48. Rabani, E. and S.A. Egorov, *Interactions between passivated nanoparticles in solutions: Beyond the continuum model.* Journal of Chemical Physics, 2001. **115**(8): p. 3437-3440.

49. Rabani, E. and S.A. Egorov, *Solvophobic and solvophilic effects on the potential of mean force between two nanoparticles in binary mixtures.* Nano Letters, 2002. **2**(1): p. 69-72.

50. Vancea, I., et al., *Front instabilities in evaporatively dewetting nanofluids.* Physical Review E, 2008. **78**(4).

51. Rabani, E., et al., *Drying-mediated self-assembly of nanoparticles.* Nature, 2003. **426**(6964): p. 271-274.

52. Sztrum-Vartash, C.G. and E. Rabani, *Lattice Gas Model for the Drying-Mediated Self-Assembly of Nanorods.* Journal of Physical Chemistry C, 2010. **114**(25): p. 11040-11049.

53. Franco, A.A., *Multiscale modelling and numerical simulation of rechargeable lithium ion batteries: concepts, methods and challenges.* Rsc Advances, 2013. **3**(32): p. 13027-13058.

54. Li, C.C. and J.H. Jean, *Effects of ethylene glycol, thickness, and B2O3 on PVA distribution in dried BaTiO3 green tape.* Materials Chemistry and Physics, 2005. **94**(1): p. 78-86.

55. Jean, J.H. and H.R. Wang, *Organic distributions in dried alumina green tape.* Journal of the American Ceramic Society, 2001. **84**(2): p. 267-272.

56. Nan, C.Y., et al., *Size and shape control of LiFePO4 nanocrystals for better lithium ion battery cathode materials.* Nano Research, 2013. **6**(7): p. 469-477.

57. Damasceno, P.F., M. Engel, and S.C. Glotzer, *Predictive self-assembly of polyhedra into complex structures.* Science, 2012. **337**(6093): p. 453-457.

58. Ye, X., et al., *Competition of shape and interaction patchiness for self-assembling nanoplates.* Nature chemistry, 2013. **5**(6): p. 466-473.

59. Yang, C.Y., et al., *Performance study of the LiCoO2/graphite system.* Journal of Power Sources, 1997. **68**(2): p. 440-442.

60. Kim, K.M., et al., *Effect of mixing sequences on the electrode characteristics of lithium-ion rechargeable batteries.* Journal of power sources, 1999. **83**(1): p. 108-113.

61. Li, J.L., et al., *Optimization of multicomponent aqueous suspensions of lithium iron phosphate (LiFePO4) nanoparticles and carbon black for lithium-ion battery cathodes.* Journal of Colloid and Interface Science, 2013. **405**: p. 118-124.

62. Lee, G.-W., et al., *Effect of slurry preparation process on electrochemical performances of LiCoO< sub> 2</sub> composite electrode.* Journal of Power Sources, 2010. **195**(18): p. 6049-6054.

63. Huang, Y.P., et al., *Excellent electrochemical performance of LiFe0. 4Mn0. 6PO4 microspheres produced using a double carbon coating process.* J. Mater. Chem. A, 2014. **2**(44): p. 18831-18837.

64. Scrosati, B. and J. Garche, *Lithium batteries: Status, prospects and future.* Journal of Power Sources, 2010. **195**(9): p. 2419-2430.

65. Bruce, P.G., L.J. Hardwick, and K.M. Abraham, *Lithium-air and lithium-sulfur batteries.* MRS Bulletin, 2011. **36**(07): p. 506-512.

66. G. Girishkumar, B.M., A. C. Luntz, S. Swanson, and W. Wilcke, *Lithium-Air Battery: Promise and Challenges.* J. Phys. Chem. Lett., 2010. **1**(14): p. 2193-2203.

67. Wadia, C., P. Albertus, and V. Srinivasan, *Resource constraints on the battery energy storage potential for grid and transportation applications.* Journal of Power Sources, 2011. **196**(3): p. 1593-1598.

68. Cairns, E.J. and P. Albertus, *Batteries for electric and hybrid-electric vehicles.* Annu Rev Chem Biomol Eng, 2010. **1**: p. 299-320.

69. Barchasz, C., et al., *Novel positive electrode architecture for rechargeable lithium/sulfur batteries.* Journal of Power Sources, 2012. **211**(0): p. 19-26.

70. Yang, Y., et al., *High-capacity micrometer-sized Li2S particles as cathode materials for advanced rechargeable lithium-ion batteries.* Journal of the American Chemical Society, 2012. **134**(37): p. 15387-15394.

71. Eithiraj, R., et al., *First-principles study of electronic structure and ground-state properties of alkali-metal sulfides–Li2S, Na2S, K2S and Rb2S.* physica status solidi (b), 2007. **244**(4): p. 1337-1346.

72. Viswanathan, V., et al., *Electrical conductivity in Li2O2 and its role in determining capacity limitations in non-aqueous Li-O2 batteries.* The Journal of chemical physics, 2011. **135**(21): p. 214704.

73. Hayashi, A., et al., *Rechargeable lithium batteries, using sulfur-based cathode materials and Li< sub> 2</sub> S–P< sub> 2</sub> S< sub> 5</sub> glass-ceramic electrolytes.* Electrochimica acta, 2004. **50**(2): p. 893-897.

74. Zhou, Y., et al., *Electrochemical reactivity of Co–Li< sub> 2</sub> S nanocomposite for lithium-ion batteries.* Electrochimica acta, 2007. **52**(9): p. 3130-3136.

75. Debart, A., et al., *Reactivity of transition metal (Co, Ni, Cu) sulphides versus lithium: The intriguing case of the copper sulphide.* Solid State Sciences, 2006. **8**(6): p. 640-651.

76. Jeon, B.H., et al., *Preparation and electrochemical properties of lithium–sulfur polymer batteries.* Journal of power sources, 2002. **109**(1): p. 89-97.

77. Meunier, V., et al., *Ab initio investigations of lithium diffusion in carbon nanotube systems.* Physical Review Letters, 2002. **88**(7).

78. Luo, G.X., J.J. Zhao, and B.L. Wang, *First-principles study of transition metal doped Li2S as cathode materials in lithium batteries.* Journal of Renewable and Sustainable Energy, 2012. **4**(6).

79. Yang, Y., G.Y. Zheng, and Y. Cui, *Nanostructured sulfur cathodes.* Chemical Society Reviews, 2013. **42**(7): p. 3018-3032.

80. Seh, Z.W., et al., *Sulphur–TiO2 yolk–shell nanoarchitecture with internal void space for long-cycle lithium–sulphur batteries.* Nature communications, 2013. **4**: p. 1331.

81. Wang, H., et al., *Graphene-wrapped sulfur particles as a rechargeable lithium–sulfur battery cathode material with high capacity and cycling stability.* Nano letters, 2011. **11**(7): p. 2644-2647.

82. Ji, X., K.T. Lee, and L.F. Nazar, *A highly ordered nanostructured carbon-sulphur cathode for lithium-sulphur batteries.* Nat Mater, 2009. **8**(6): p. 500-506.

83. Ji, X., et al., *Stabilizing lithium–sulphur cathodes using polysulphide reservoirs.* Nat Commun, 2011. **2**: p. 325.

84. Zheng, G., et al., *Hollow Carbon Nanofiber-Encapsulated Sulfur Cathodes for High Specific Capacity Rechargeable Lithium Batteries.* Nano Letters, 2011. **11**(10): p. 4462-4467.

85. Li, C.-C. and Y.-W. Wang, *Binder distributions in water-based and organic-based LiCoO2 electrode sheets and their effects on cell performance.* Journal of The Electrochemical Society, 2011. **158**(12): p. A1361-A1370.

86. Shenhar, R., T.B. Norsten, and V.M. Rotello, *Polymer-Mediated Nanoparticle Assembly: Structural Control and Applications.* Advanced Materials, 2005. **17**(6): p. 657-669.

87. Akcora, P., et al., *Anisotropic self-assembly of spherical polymer-grafted nanoparticles.* Nat Mater, 2009. **8**(4): p. 354-359.

88. Sun, S., et al., *Polymer Mediated Self-Assembly of Magnetic Nanoparticles.* Journal of the American Chemical Society, 2002. **124**(12): p. 2884-2885.

89. Lee, B.-R. and E.-S. Oh, *Effect of Molecular Weight and Degree of Substitution of a Sodium-Carboxymethyl Cellulose Binder on Li4Ti5O12 Anodic Performance.* The Journal of Physical Chemistry C, 2013. **117**(9): p. 4404-4409.

90. Tasić, N., et al., *Effect of binder molecular weight on morphology of TiO2 films prepared by tape casting and their photovoltaic performance.* Science of Sintering, 2012. **44**(3): p. 365-372.

91. Mikhaylik, Y.V. and J.R. Akridge, *Polysulfide shuttle study in the Li/S battery system.* Journal of the Electrochemical Society, 2004. **151**(11): p. A1969-A1976.

92. Liu, Z., et al., *Li2S Film Formation on Lithium Anode Surface of Li–S batteries.* ACS applied materials & interfaces, 2016. **8**(7): p. 4700-4708.

93. He, G., X.L. Ji, and L. Nazar, *High "C" rate Li-S cathodes: sulfur imbibed bimodal porous carbons.* Energy & Environmental Science, 2011. **4**(8): p. 2878-2883.

94. Wang, H.L., et al., *Graphene-Wrapped Sulfur Particles as a Rechargeable Lithium-Sulfur Battery Cathode Material with High Capacity and Cycling Stability.* Nano Letters, 2011. **11**(7): p. 2644-2647.

95. Zheng, G.Y., et al., *Hollow Carbon Nanofiber-Encapsulated Sulfur Cathodes for High Specific Capacity Rechargeable Lithium Batteries.* Nano Letters, 2011. **11**(10): p. 4462-4467.

96. Zheng, G., et al., *Amphiphilic Surface Modification of Hollow Carbon Nanofibers for Improved Cycle Life of Lithium Sulfur Batteries.* Nano Letters, 2013. **13**(3): p. 1265-1270.

97. Zhang, Q., et al., *Understanding the Anchoring Effect of Two-Dimensional Layered Materials for Lithium–Sulfur Batteries.* Nano letters, 2015. **15**(6): p. 3780-3786.

98. Liu, Z., et al., *Adsorption of insoluble polysulfides Li 2 S x (x= 1, 2) on Li 2 S surfaces.* Physical Chemistry Chemical Physics, 2015. **17**(14): p. 9032-9039.

99. Gerber, L.C., et al., *3-Dimensional Growth of Li2S in Lithium–Sulfur Batteries Promoted by a Redox Mediator.* Nano letters, 2015.

100. Franco, A.A. and K.-H. Xue, *Carbon-based electrodes for lithium air batteries: scientific and technological challenges from a modeling perspective.* ECS Journal of Solid State Science and Technology, 2013. **2**(10): p. M3084-M3100.

101. Karim, A., et al., *Diffusion of small two-dimensional Cu islands on Cu(111) studied with a kinetic Monte Carlo method.* Physical Review B, 2006. **73**(16): p. 165411.

102. Righi, M.C., et al., *Combined ab initio and kinetic Monte Carlo simulations of C diffusion on the root 3X root 3 beta-SiC(111) surface.* Physical Review B, 2005. **71**(7): p. 075303.

103. Wang, L.G. and P. Clancy, *Kinetic Monte Carlo simulation of the growth of polycrystalline Cu films.* Surface Science, 2001. **473**(1-2): p. 25-38.

104. Wang, Z.Y., Y.H. Li, and J.B. Adams, *Kinetic lattice Monte Carlo simulation of facet growth rate.* Surface Science, 2000. **450**(1-2): p. 51-63.

105. Galloway, G.J. and G.J. Ackland, *Molecular dynamics and object kinetic Monte Carlo study of radiation-induced motion of voids and He bubbles in bcc iron.* Physical Review B, 2013. **87**(10): p. 104106.

106. Domain, C., C.S. Becquart, and L. Malerba, *Simulation of radiation damage in Fe alloys: an object kinetic Monte Carlo approach.* Journal of Nuclear Materials, 2004. **335**(1): p. 121-145.

107. Deng, L., et al., *Morphology, dimension, and composition dependence of thermodynamically preferred atomic arrangements in Ag-Pt nanoalloys.* Faraday Discussions, 2013. **162**: p. 293-306.

108. Deng, L., et al., *Au-Ag Bimetallic Nanoparticles: Surface Segregation and Atomic-Scale Structure.* Journal of Physical Chemistry C, 2011. **115**(23): p. 11355-11363.

109. Franco, A.A., et al., *Pt x Co y Catalysts Degradation in PEFC Environments: Mechanistic Insights I. Multiscale Modeling.* Journal of The Electrochemical Society, 2009. **156**(3): p. B410-B424.

110. Drews, T.O., R.D. Braatz, and R.C. Alkire, *Coarse-grained kinetic Monte Carlo simulation of copper electrodeposition with additives.* International Journal for Multiscale Computational Engineering, 2004. **2**(2): p. 313-327.

111. Li, X., et al., *Effect of additives on shape evolution during electrodeposition I. Multiscale simulation with dynamically coupled kinetic Monte Carlo and moving-boundry finite-volume codes.* Journal of The Electrochemical Society, 2007. **154**(4): p. D230-D240.

112. Yu, J., et al., *Kinetic Monte Carlo Study of Ambipolar Lithium Ion and Electron–Polaron Diffusion into Nanostructured TiO2.* The Journal of Physical Chemistry Letters, 2012. **3**(15): p. 2076-2081.

113. Methekar, R.N., et al., *Kinetic Monte Carlo Simulation of Surface Heterogeneity in Graphite Anodes for Lithium-Ion Batteries: Passive Layer Formation.* Journal of the Electrochemical Society, 2011. **158**(4): p. A363-A370.

114. Kriston, A., et al., *Development of a Full Layer Pore-Scale Model for the Simulation of Electro-Active Material Used in Power Sources.* Journal of the Electrochemical Society, 2014. **161**(8): p. E3235-E3247.

115. Liu, Z. and P.P. Mukherjee, *Microstructure evolution in lithium-ion battery electrode processing.* Journal of The Electrochemical Society, 2014. **161**(8): p. E3248-E3258.

116. Crivoi, A. and F. Duan, *Evaporation-induced formation of fractal-like structures from nanofluids.* Physical Chemistry Chemical Physics, 2012. **14**(4): p. 1449-1454.

117. Zeng, H., et al., *Exchange-coupled nanocomposite magnets by nanoparticle self-assembly.* Nature, 2002. **420**(6914): p. 395-398.

118. Lin, Y., et al., *Nanoparticle Assembly and Transport at Liquid-Liquid Interfaces.* Science, 2003. **299**(5604): p. 226-229.

119. Jin, B., et al., *Effect of different carbon conductive additives on electrochemical properties of LiFePO4-C/Li batteries.* Journal of Solid State Electrochemistry, 2008. **12**(12): p. 1549-1554.

120. Li, H., et al., *A high capacity nano-Si composite anode material for lithium rechargeable batteries.* Electrochemical and Solid State Letters, 1999. **2**(11): p. 547-549.

121. Vancea, I., et al., *Front instabilities in evaporatively dewetting nanofluids.* Physical Review E, 2008. **78**(4): p. 041601.

122. Hong, J.K., J.H. Lee, and S.M. Oh, *Effect of carbon additive on electrochemical performance of LiCoO2 composite cathodes.* Journal of Power Sources, 2002. **111**(1): p. 90-96.

123. Zhu, M., J. Park, and A.M. Sastry, *Particle Interaction and Aggregation in Cathode Material of Li-Ion Batteries: A Numerical Study.* Journal of the Electrochemical Society, 2011. **158**(10): p. A1155-A1159.

124. Barai, P. and P.P. Mukherjee, *Stochastic Analysis of Diffusion Induced Damage in Lithium-Ion Battery Electrodes.* Journal of the Electrochemical Society, 2013. **160**(6): p. A955-A967.

125. Kunduraci, M. and G.G. Amatucci, *The effect of particle size and morphology on the rate capability of 4.7 VLiMn1.5+delta Ni0.5-delta O4 spinel lithium-ion battery cathodes.* Electrochimica Acta, 2008. **53**(12): p. 4193-4199.

126. Pascual, L., et al., *Effect of the thermal treatment on the particle size and electrochemical response of LiCr0.2Mn1.8O4 spinel.* Journal of the Electrochemical Society, 2005. **152**(2): p. A301-A306.

127. Maul, T., et al., *Simulation Modelling Study of Self-Assembled Nanoparticle Coatings for Retinal Implants.* Journal of Bionic Engineering, 2013. **10**(1): p. 65-76.

128. Hintennach, A. and P. Novák, *Influence of surfactants and viscosity in the preparation process of battery electrodes containing nanoparticles.* Physical Chemistry Chemical Physics, 2009. **11**(41): p. 9484-9488.

129. Stein IV, M. and P.P. Mukherjee, *Effect of Evaporation in Electrode Processing.* 2015: p. in preparation.

130. Haji-Akbari, A., et al., *Packing and self-assembly of truncated triangular bipyramids.* Physical Review E, 2013. **88**(1): p. 012127.

131. Liu, Z., V. Battaglia, and P.P. Mukherjee, *Mesoscale Elucidation of the Influence of Mixing Sequence in Electrode Processing.* Langmuir, 2014. **30**(50): p. 15102-15113.

132. Wang, G., et al., *Sn/graphene nanocomposite with 3D architecture for enhanced reversible lithium storage in lithium ion batteries.* Journal of Materials Chemistry, 2009. **19**(44): p. 8378-8384.

133. Wall, F.T. and F. Mandel, *Macromolecular dimensions obtained by an efficient Monte Carlo method without sample attrition.* The Journal of Chemical Physics, 1975. **63**(11): p. 4592-4595.

134. Sztrum, C.G., O. Hod, and E. Rabani, *Self-assembly of nanoparticles in three-dimensions: Formation of stalagmites.* The Journal of Physical Chemistry B, 2005. **109**(14): p. 6741-6747.

135. Korgel, B.A., et al., *Assembly and Self-Organization of Silver Nanocrystal Superlattices: Ordered "Soft Spheres"*. The Journal of Physical Chemistry B, 1998. **102**(43): p. 8379-8388.

136. Kletenik-Edelman, O., et al., *Drying-mediated hierarchical self-assembly of nanoparticles: A dynamical coarse-grained approach.* The Journal of Physical Chemistry C, 2008. **112**(12): p. 4498-4506.

137. Hiemenz, P.C. and T.P. Lodge, *Polymer Chemistry, Second Edition*. 2007: Taylor & Francis.

138. Kohn, W. and L.J. Sham, *Self-Consistent Equations Including Exchange and Correlation Effects.* Physical Review, 1965. **140**(4A): p. 1133.

139. Jones, R.O. and O. Gunnarsson, *The Density Functional Formalism, Its Applications and Prospects.* Reviews of Modern Physics, 1989. **61**(3): p. 689-746.

140. Car, R. and M. Parrinello, *Unified Approach for Molecular-Dynamics and Density-Functional Theory.* Physical Review Letters, 1985. **55**(22): p. 2471-2474.

141. Payne, M.C., et al., *Iterative minimization techniques for ab initio total-energy calculations: molecular dynamics and conjugate gradients.* Reviews of Modern Physics, 1992. **64**(4): p. 1045-1097.

142. Kresse, G. and J. Hafner, *Ab initio molecular dynamics for open-shell transition metals.* Physical Review B, 1993. **48**(17): p. 13115.

143. Kresse, G. and J. Furthmüller, *Efficient iterative schemes for ab initio total-energy calculations using a plane-wave basis set.* Physical Review B, 1996. **54**(16): p. 11169-11186.

144. Kresse, G. and D. Joubert, *From ultrasoft pseudopotentials to the projector augmented-wave method.* Physical Review B, 1999. **59**(3): p. 1758-1775.

145. Blochl, P.E., *Projector Augmented-Wave Method.* Physical Review B, 1994. **50**(24): p. 17953-17979.

146. Perdew, J.P., K. Burke, and M. Ernzerhof, *Generalized gradient approximation made simple.* Physical review letters, 1996. **77**(18): p. 3865.

147. Monkhorst, H.J. and J.D. Pack, *Special Points for Brillouin-Zone Integrations.* Physical Review B, 1976. **13**(12): p. 5188-5192.

148. Momma, K. and F. Izumi, *VESTA 3 for three-dimensional visualization of crystal, volumetric and morphology data.* Journal of Applied Crystallography, 2011. **44**(6): p. 1272-1276.

149. Hummelshøj, J., A. Luntz, and J. Nørskov, *Theoretical evidence for low kinetic overpotentials in Li-O2 electrochemistry.* The Journal of chemical physics, 2013. **138**(3): p. 034703.

150. Barghamadi, M., A. Kapoor, and C. Wen, *A Review on Li-S Batteries as a High Efficiency Rechargeable Lithium Battery.* Journal of The Electrochemical Society, 2013. **160**(8): p. A1256-A1263.

151. Feng, Z., et al., *Unravelling the role of Li< sub> 2</sub> S< sub> 2</sub> in lithium-sulfur batteries: A first principles study of its energetic and electronic properties.* Journal of Power Sources, 2014.

152. Buehrer, W., et al., *Lattice-Dynamics and the Diffuse Phase-Transition of Lithium Sulfide Investigated by Coherent Neutron-Scattering.* Journal of Physics-Condensed Matter, 1991. **3**(9): p. 1055-1064.

153. Lide, D.R., *Standard thermodynamic properties of chemical substances.* CRC Handbook of Chemistry and Physics, 2007. **5**.

154. Bruce, P.G., et al., *Li-O2 and Li-S batteries with high energy storage.* Nature materials, 2012. **11**(1): p. 19-29.

155. Nagao, M., A. Hayashi, and M. Tatsumisago, *High-capacity Li 2 S–nanocarbon composite electrode for all-solid-state rechargeable lithium batteries.* Journal of Materials Chemistry, 2012. **22**(19): p. 10015-10020.

156. Zhang, K., et al., *Ultrasmall Li2S Nanoparticles Anchored in Graphene Nanosheets for High-Energy Lithium-Ion Batteries.* Sci. Rep., 2014. **4**.

157. Kao, J., *Li2S2 and Li2S: an ab initio study.* Journal of Molecular Structure, 1979. **56**(0): p. 147-152.

158. Wang, L., et al., *A quantum-chemical study on the discharge reaction mechanism of lithium-sulfur batteries.* Journal of Energy Chemistry, 2013. **22**(1): p. 72-77.

159. Tang, W., E. Sanville, and G. Henkelman, *A grid-based Bader analysis algorithm without lattice bias.* Journal of Physics-Condensed Matter, 2009. **21**(8).

160. Ji, X. and L.F. Nazar, *Advances in Li-S batteries.* Journal of Materials Chemistry, 2010. **20**(44): p. 9821-9826.

161. Grimme, S., et al., *A consistent and accurate ab initio parametrization of density functional dispersion correction (DFT-D) for the 94 elements H-Pu.* The Journal of chemical physics, 2010. **132**(15): p. 154104.

162. Zhang, Q., et al., *Understanding the Anchoring Effect of Two-dimensional Layered Materials for Lithium-sulfur Batteries.* Nano letters, 2015.

163. Liu, Z., et al., *Adsorption of insoluble polysulfides Li2Sx (x = 1, 2) on Li2S surfaces.* Physical Chemistry Chemical Physics, 2015. **17**(14): p. 9032-9039.

164. Wallace, D.C., *Thermodynamics of crystals*. 1998: Courier Corporation.

165. Zheng, S., et al., *In situ formed lithium sulfide/microporous carbon cathodes for lithium-ion batteries.* ACS nano, 2013. **7**(12): p. 10995-11003.

166. Elazari, R., et al., *Rechargeable lithiated silicon–sulfur (SLS) battery prototypes.* Electrochemistry Communications, 2012. **14**(1): p. 21-24.

167. Wu, H., et al., *Stable cycling of double-walled silicon nanotube battery anodes through solid-electrolyte interphase control.* Nature nanotechnology, 2012. **7**(5): p. 310-315.

168. Liang, X., et al., *Improved cycling performances of lithium sulfur batteries with LiNO3-modified electrolyte.* Journal of Power Sources, 2011. **196**(22): p. 9839-9843.

169. Xiong, S.Z., et al., *Characterization of the solid electrolyte interphase on lithium anode for preventing the shuttle mechanism in lithium-sulfur batteries.* Journal of Power Sources, 2014. **246**: p. 840-845.

170. Aurbach, D., et al., *On the Surface Chemical Aspects of Very High Energy Density, Rechargeable Li-Sulfur Batteries.* Journal of the Electrochemical Society, 2009. **156**(8): p. A694-A702.

171. Zhang, S.S., *Role of LiNO3 in rechargeable lithium/sulfur battery.* Electrochimica Acta, 2012. **70**: p. 344-348.

172. Azimi, N., et al., *Fluorinated electrolytes for Li-S battery: suppressing the self-discharge with an electrolyte containing fluoroether solvent.* Journal of The Electrochemical Society, 2015. **162**(1): p. A64-A68.

173. Gordin, M.L., et al., *Bis (2, 2, 2-trifluoroethyl) Ether As an Electrolyte Co-solvent for Mitigating Self-Discharge in Lithium–Sulfur Batteries.* ACS applied materials & interfaces, 2014. **6**(11): p. 8006-8010.

174. Zhang, Q.F., et al., *Understanding the Anchoring Effect of Two-Dimensional Layered Materials for Lithium-Sulfur Batteries.* Nano Letters, 2015. **15**(6): p. 3780-3786.

175. Li, Z. and L. Yin, *Nitrogen-Doped MOF-Derived Micropores Carbon as Immobilizer for Small Sulfur Molecules as a Cathode for Lithium Sulfur*

Batteries with Excellent Electrochemical Performance. ACS Applied Materials & Interfaces, 2015. **7**(7): p. 4029-4038.

176. Xiao, S., et al., *Polyurethane-derived N-doped porous carbon with interconnected sheet-like structure as polysulfide reservoir for lithium–sulfur batteries.* Journal of Power Sources, 2015. **293**: p. 119-126.

177. Pang, Q., et al., *A Nitrogen and Sulfur Dual-Doped Carbon Derived from Polyrhodanine@Cellulose for Advanced Lithium–Sulfur Batteries.* Advanced Materials, 2015. **27**(39): p. 6021-6028.

178. Hou, T.-Z., et al., *The formation of strong-couple interactions between nitrogen-doped graphene and sulfur/lithium (poly)sulfides in lithium-sulfur batteries.* 2D Materials, 2015. **2**(1): p. 014011.

179. Yang, J., et al., *Novel nitrogen-doped hierarchically porous coralloid carbon materials as host matrixes for lithium–sulfur batteries.* Electrochimica Acta, 2015. **159**: p. 8-15.

180. Qiu, Y., et al., *Highly Nitridated Graphene–Li2S Cathodes with Stable Modulated Cycles.* Advanced Energy Materials, 2015. **5**(23): p. n/a-n/a.

181. Niu, S., et al., *A carbon sandwich electrode with graphene filling coated by N-doped porous carbon layers for lithium-sulfur batteries.* Journal of Materials Chemistry A, 2015. **3**(40): p. 20218-20224.

182. Ding, K., et al., *Ternary-layered nitrogen-doped graphene/sulfur/ polyaniline nanoarchitecture for the high-performance of lithium-sulfur batteries.* Journal of Materials Chemistry A, 2015. **3**(15): p. 8022-8027.

183. Zhang, S., et al., *A high energy density Li2S@C nanocomposite cathode with a nitrogen-doped carbon nanotube top current collector*. Journal of Materials Chemistry A, 2015. **3**(37): p. 18913-18919.

184. Zhao, Y., et al., *A Free-Standing Sulfur/Nitrogen-Doped Carbon Nanotube Electrode for High-Performance Lithium/Sulfur Batteries.* Nanoscale research letters, 2015. **10**(1): p. 1-6.

185. Sun, F., et al., *High efficiency immobilization of sulfur on nitrogen-enriched mesoporous carbons for Li–S batteries.* ACS applied materials & interfaces, 2013. **5**(12): p. 5630-5638.

186. Sun, X.G., et al., *Lithium–Sulfur Batteries Based on Nitrogen-Doped Carbon and an Ionic-Liquid Electrolyte.* ChemSusChem, 2012. **5**(10): p. 2079-2085.

187. Qiu, Y., et al., *High-rate, ultralong cycle-life lithium/sulfur batteries enabled by nitrogen-doped graphene.* Nano letters, 2014. **14**(8): p. 4821-4827.

188. Song, J., et al., *Nitrogen-Doped Mesoporous Carbon Promoted Chemical Adsorption of Sulfur and Fabrication of High-Areal-Capacity Sulfur Cathode with Exceptional Cycling Stability for Lithium-Sulfur Batteries.* Advanced Functional Materials, 2014. **24**(9): p. 1243-1250.

189. Qiu, Y., et al., *High-Rate, Ultralong Cycle-Life Lithium/Sulfur Batteries Enabled by Nitrogen-Doped Graphene.* Nano Letters, 2014. **14**(8): p. 4821-4827.

190. Zhou, G., et al., *High-Performance Lithium-Sulfur Batteries with a Self-Supported, 3D Li2S-Doped Graphene Aerogel Cathodes.* Advanced Energy Materials, 2015.

191. Xie, Y., et al., *Effect of Boron-Doping on the Graphene Aerogel Used as Cathode for the Lithium–Sulfur Battery.* ACS Applied Materials & Interfaces, 2015. **7**(45): p. 25202-25210.

192. Song, J., et al., *Advanced Sulfur Cathode Enabled by Highly Crumpled Nitrogen-doped Graphene Sheets for High-Energy-Density Lithium-Sulfur Batteries.* Nano letters, 2016. **16**(2): p. 864-870.

193. Song, J., et al., *Strong Lithium Polysulfide Chemisorption on Electroactive Sites of Nitrogen-Doped Carbon Composites For High-Performance Lithium–Sulfur Battery Cathodes.* Angewandte Chemie International Edition, 2015. **54**(14): p. 4325-4329.

194. Zhu, P., et al., *Mechanism of Enhanced Carbon Cathode Performance by Nitrogen Doping in Lithium–Sulfur Battery: An X-ray Absorption Spectroscopic Study.* The Journal of Physical Chemistry C, 2014. **118**(15): p. 7765-7771.

195. Liang, X., A. Garsuch, and L.F. Nazar, *Sulfur Cathodes Based on Conductive MXene Nanosheets for High-Performance Lithium–Sulfur Batteries.* Angewandte Chemie, 2015. **127**(13): p. 3979-3983.

196. Seh, Z.W., et al., *Two-dimensional layered transition metal disulphides for effective encapsulation of high-capacity lithium sulphide cathodes.* Nat Commun, 2014. **5**.

197. Seyed-Talebi, S.M., I. Kazeminezhad, and J. Beheshtian, *Theoretical prediction of silicene as a new candidate for the anode of lithium-ion batteries.* Physical Chemistry Chemical Physics, 2015. **17**(44): p. 29689-29696.

198. Liu, G., et al., *Is silicene stable in O2?—First-principles study of O2 dissociation and O2-dissociation–induced oxygen atoms adsorption on free-standing silicene.* EPL (Europhysics Letters), 2014. **106**(4): p. 47001.

199. Guo, X.-X., et al., *First-principles calculations study of Na adsorbed on silicene.* Applied Surface Science, 2015. **341**: p. 69-74.

200. Lin, X. and J. Ni, *Much stronger binding of metal adatoms to silicene than to graphene: A first-principles study.* Physical Review B, 2012. **86**(7): p. 075440.

201. Vogt, P., et al., *Silicene: compelling experimental evidence for graphenelike two-dimensional silicon.* Physical review letters, 2012. **108**(15): p. 155501.

202. Dysart, A.D., et al., *Towards Next Generation Lithium-Sulfur Batteries: Non-conventional Carbon Compartments/Sulfur Electrodes and Multi-scale Analysis.* Journal of The Electrochemical Society, 2015. **Under review**.

203. Tang, W., E. Sanville, and G. Henkelman, *A grid-based Bader analysis algorithm without lattice bias.* Journal of Physics Condensed Matter, 2009. **21**(8).

204. Sanville, E., et al., *Improved grid-based algorithm for Bader charge allocation.* Journal of Computational Chemistry, 2007. **28**(5): p. 899-908.

205. Henkelman, G., A. Arnaldsson, and H. Jónsson, *A fast and robust algorithm for Bader decomposition of charge density.* Computational Materials Science, 2006. **36**(3): p. 354-360.

206. Zhang, S., et al., *Recent Advances in Electrolytes for Lithium-Sulfur Batteries.* Advanced Energy Materials, 2015. **5**(16).

207. Neugebauer, J. and M. Scheffler, *Adsorbate-substrate and adsorbate-adsorbate interactions of Na and K adlayers on Al (111).* Physical Review B, 1992. **46**(24): p. 16067.

208. Michaelides, A., et al., *General Model for Water Monomer Adsorption on Close-Packed Transition and Noble Metal Surfaces.* Physical Review Letters, 2003. **90**(21): p. 216102.

209. Dysart, A., et al., *Towards Next Generation Lithium-Sulfur Batteries: Non-conventional Carbon Compartments/Sulfur Electrodes and Multi-scale Analysis.* Physical Chemistry Chemical Physics, 2015. **Under review**.

210. Chen, Y.-X. and P. Kaghazchi, *Metalization of Li2S particle surfaces in Li-S batteries.* Nanoscale, 2014. **6**(22): p. 13391-13395.

211. Cuisinier, M., et al., *Sulfur speciation in Li–S batteries determined by operando X-ray absorption spectroscopy.* The Journal of Physical Chemistry Letters, 2013. **4**(19): p. 3227-3232.

212. Ghaznavi, M. and P. Chen, *Sensitivity analysis of a mathematical model of lithium–sulfur cells: Part II: Precipitation reaction kinetics and sulfur content.* Journal of Power Sources, 2014. **257**: p. 402-411.

213. Xiao, J., et al., *Following the Transient Reactions in Lithium–Sulfur Batteries Using an In Situ Nuclear Magnetic Resonance Technique.* Nano letters, 2015. **15**(5): p. 3309-3316.

214. Cunningham, P., S. Johnson, and E. Cairns, *Phase Equilibria in Lithium-Chalcogen Systems II. Lithium-Sulfur.* Journal of The Electrochemical Society, 1972. **119**(11): p. 1448-1450.

215. Grande, L., et al., *The lithium/air battery: still an emerging system or a practical reality?* Advanced materials, 2015. **27**(5): p. 784-800.

216. Dominko, R., et al., *Analytical Detection of Polysulfides in the Presence of Adsorption Additives by Operando X-Ray Absorption Spectroscopy.* The Journal of Physical Chemistry C, 2015.

217. Cañas, N.A., et al., *In-situ X-ray diffraction studies of lithium–sulfur batteries.* Journal of Power Sources, 2013. **226**: p. 313-319.

218. Park, H., H.S. Koh, and D.J. Siegel, *First-Principles Study of Redox End Members in Lithium–Sulfur Batteries.* The Journal of Physical Chemistry C, 2015. **119**(9): p. 4675-4683.

219. Weeks, J.D. and G.H. Gilmer, *Dynamics of crystal growth.* Adv. Chem. Phys, 1979. **40**(489): p. 157-227.

220. Dysart, A.D., et al., *Towards Next Generation Lithium-Sulfur Batteries: Non-Conventional Carbon Compartments/Sulfur Electrodes and Multi-Scale Analysis.* Journal of The Electrochemical Society, 2016. **163**(5): p. A730-A741.

221. Drews, T.O., et al., *Stochastic simulation of the early stages of kinetically limited electrodeposition.* Journal of The Electrochemical Society, 2006. **153**(6): p. C434-C441.

222. Liu, Z., et al., *Mesoscale elucidation of laser-assisted chemical deposition of Sn nanostructured electrodes.* Journal of Applied Physics, 2015. **117**(21): p. 214301.

223. Fan, F.Y., W.C. Carter, and Y.M. Chiang, *Mechanism and Kinetics of Li2S Precipitation in Lithium–Sulfur Batteries.* Advanced Materials, 2015. **27**(35): p. 5203-5209.

224. Gallant, B.M., et al., *Influence of Li 2 O 2 morphology on oxygen reduction and evolution kinetics in Li–O 2 batteries.* Energy & Environmental Science, 2013. **6**(8): p. 2518-2528.

225. Kim, D.-H., et al., *First-principles study on charge transport mechanism of lithium sulfide (Li2S) in lithium-sulfur batteries.* Chemistry–An Asian Journal, 2016. **in press**: p. DOI: 10.1002/asia.201600007.

226. Luo, G., J. Zhao, and B. Wang, *First-principles study of transition metal doped Li2S as cathode materials in lithium batteries.* Journal of Renewable and Sustainable Energy, 2012. **4**(6): p. 063128.

227. Hummelshøj, J.S., et al., *Communications: Elementary oxygen electrode reactions in the aprotic Li-air battery.* The Journal of chemical physics, 2010. **132**(7): p. 071101.

228. Radin, M.D., C.W. Monroe, and D.J. Siegel, *How dopants can enhance charge transport in Li2O2.* Chemistry of Materials, 2015. **27**(3): p. 839-847.

229. Timoshevskii, V., et al., *Improving Li2O2 conductivity via polaron preemption: An ab initio study of Si doping.* Applied Physics Letters, 2013. **103**(7): p. 073901.

230. Geng, W.T., B.L. He, and T. Ohno, *Grain Boundary Induced Conductivity in Li2O2.* The Journal of Physical Chemistry C, 2013. **117**(48): p. 25222-25228.

231. Mistry, A. and P.P. Mukerjee, *Demystifying Discharge Limitations in Lithium-Sulfur Batteries.* 2016: p. In preparation

232. Mikhaylik, Y.V. and J.R. Akridge, *Low temperature performance of Li/S batteries.* Journal of The Electrochemical Society, 2003. **150**(3): p. A306-A311.

233. Akridge, J.R., Y.V. Mikhaylik, and N. White, *Li/S fundamental chemistry and application to high-performance rechargeable batteries.* Solid state ionics, 2004. **175**(1): p. 243-245.

234. Huang, J.-Q., et al., *Entrapment of sulfur in hierarchical porous graphene for lithium–sulfur batteries with high rate performance from− 40 to 60 C.* Nano Energy, 2013. **2**(2): p. 314-321.

235. Nevers, D.R., et al., *The Effect of Carbon Additives on the Microstructure and Conductivity of Alkaline Battery Cathodes.* Journal of The Electrochemical Society, 2014. **161**(10): p. A1691-A1697.

236. Martin, M.A., et al., *Morphological Influence in Lithium-Ion Battery 3D Electrode Architectures.* Journal of The Electrochemical Society, 2015. **162**(6): p. A991-A1002.